The Dissertation Committee for Cameron David Peebles Certifies that this is the approved version of the following dissertation:

CONFORMATIONAL SWITCHING WITHIN AROMATIC, ELECTRON DONOR AND ACCEPTOR SUPRAMOLECULAR ARCHITECTURES

Committee:

Brent L. Iverson, Supervisor

Eric V. Anslyn

Christopher J. Ellison

David A. Vanden Bout

C. Grant Willson

Yan J. Zhang

CONFORMATIONAL SWITCHING WITHIN AROMATIC, ELECTRON DONOR AND ACCEPTOR SUPRAMOLECULAR ARCHITECTURES

by

Cameron David Peebles, B.A.

Dissertation

Presented to the Faculty of the Graduate School of

The University of Texas at Austin

in Partial Fulfillment

of the Requirements

for the Degree of

Doctor of Philosophy

The University of Texas at Austin

May 2015

Dedication

To Lianna and my family

Acknowledgements

First off, I would like to thank Brent Iverson for his support and kindness throughout the past five years. His wisdom and insight on how to approach science (and life) has helped me develop as a scientist and a philosopher.

Thank you to the Iverson group past and present. Their continued support, inspiration and knowledge played a pivotal role in developing the story in the proceeding pages of this dissertation. For that I am ever grateful. Maybe more importantly, they (as well as honorary Iverson members) provided much needed relief from lab involving numerous trips to and from the Crown and downtown Austin.

Thank you to the Willson, Anslyn and Sessler groups for the generous use of lab instrumentation (without which many pages of this dissertation would not have been possible) but also for all the intellectual aid I received along the way.

Lastly, thank you to Lianna and my family. Thank you my wonderful family for visiting me in Texas, for always being encouraging and for always being filled with love. Lianna, you have been my partner in this since the beginning. I love you and I look forward to our life together.

CONFORMATIONAL SWITCHING WITHIN AROMATIC, ELECTRON DONOR AND ACCEPTOR SUPRAMOLECULAR ARCHITECTURES

Cameron David Peebles, Ph.D.

The University of Texas at Austin, 2015

Supervisor: Brent L. Iverson

The Iverson group has utilized favorable interactions between aromatic units in the development of highly ordered amphiphilic foldamers, two-component liquid crystal assemblies and pseudo-DNA assemblies. The above materials are made by taking advantage of the complementary electrostatic interactions between derivatives of electron-rich 1,5-dialkoxynaphthalene (DAN) and derivatives of electron-deficient 1,4,5,8-naphthalenetetracarboxylic diimide (NDI).

This dissertation describes the theme of dynamic conformational switching within the context of aromatic stacking interactions. Specifically, this work focuses on switching between an aromatic electron-rich and aromatic electron-deficient alternating stacking geometry and an aromatic electron-rich self stacking geometry. While much of this work can be partially explained using classical notions of aromatic stacking (Hunter and Sanders), a new theory explaining aromatic stacking interactions (Wheeler and Houk) is highlighted which better explains the conformational switching behavior.

Chapter 2 elucidates the aggregated structure of two amphiphilic foldamers that irreversibly undergo thermally induced conformational changes to form self-supporting hydrogels.

The thermodynamics and morphologies of the foldamer aggregates are similar to amyloid aggregates, the misfolded state of proteins associated in numerous neurodegenerative diseases. Chapter 3 discusses the synthesis and time dependent polymorphism of four conjugated aromatic monoalkoxynaphthalene-naphthalimide (MAN-NI) dyads. Interestingly, two dyads displayed a NI-NI stacking geometry upon slower evaporation from solution and a NI-MAN stacking geometry upon faster evaporation from solution. Chapter 4 further investigates the properties of MAN-NI dyads and demonstrates one of dyads displays solvatochromic, thermochromic, vapochromic and mechanochromic stimuli responsive behaviors. Using applied external stimuli the dyad is thought to undergo a conformational change from an NI-NI stacking geometry to a NI-MAN stacking geometry. Chapter 5 details initial investigations into MAN-NI polymers for liquid crystal polymers and organic electronic materials. Four polymers were synthesized and characterized and found to display liquid crystal mesophase textures at room temperature. Additionally, the electronic behavior of the polymers suggests they may be useful candidates for optoelectronic applications.

Overall, this work sheds considerable light on the ability of aromatic materials to under conformational changes in solution and in the solid state as a consequence of favorable direct, electrostatic interactions between the aromatic units.

Table of Contents

List of Tables

List of Figures

List of Schemes

CHAPTER 1

Molecular Self-Assembly via Non-Covalent Interactions

1.1 NON-COVALENT INTERACTIONS FROM BIOLOGY TO MATERIALS

When thinking about non-covalent self-assembly, one should think about three things: *order*, *interactions* and *function*. The *order* in macromolecular (whether in biological or material) systems derives from smaller components assembling into larger, more ordered components. Compared to strong interactions between atoms (covalent bonds), relatively weaker non-covalent *interactions* are responsible for the assembly of these smaller components. Once the self-assembled components are fully converted into a more ordered structure, the structure can *function*. The foremost standard for self-assembly can be found in nature within the complex organization of deoxyribonucleic acid (DNA). Although the core nucleic acids are composed of covalent bonds, the folding and assembly of the structure is facilitated by non-covalent interactions, such as electrostatic, van der Waals and hydrophobic interactions (Figure 1.1).

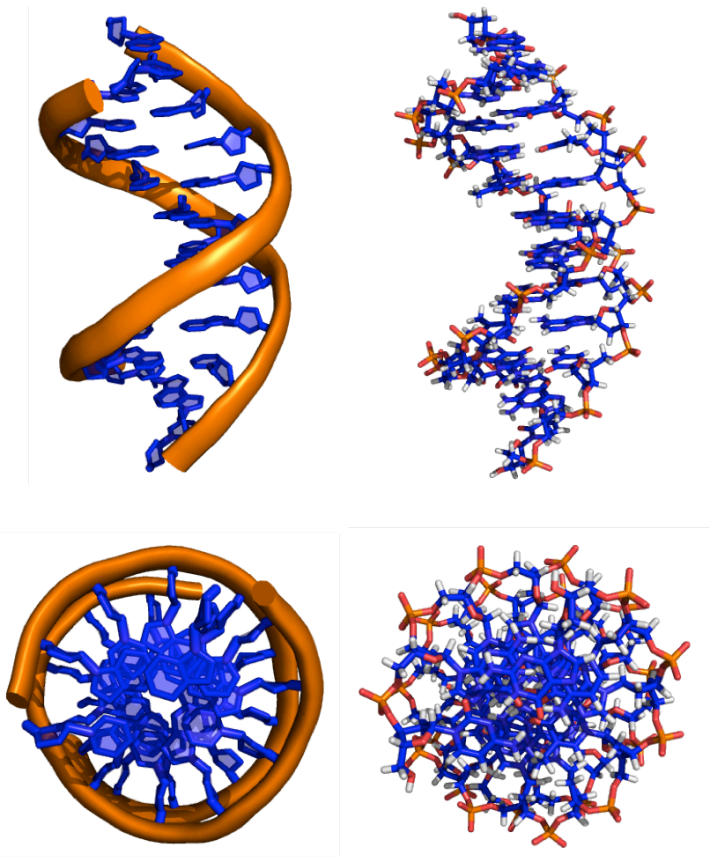

Figure 1.1 Cartoon (left) and stick (right) images of (a) the side view and (b) the top down view of the DNA double helix.

Proteins, systems that easily exceed DNA in terms of their structurally complexity, also need to abide by the same concepts stated in the previous paragraph in order to perform their biological functions. Initially, amino acid sequences are folded into protein secondary structures (α-helix and β-sheet formations) typically characterized by specific patterns of hydrogen bonds between amide bonds of the amino acid residues (Figure 1.2). The final geometric shapes of proteins that give it biological function, tertiary and quaternary structures, are brought together by hydrogen bonding in conjunction with several other non-covalent interactions such as electrostatic, van der Waals, metal coordination and hydrophobic interactions. It is only when strands of amino acids are precisely organized into fully folded proteins that they are able to perform functions such as tissue repair or catalysis.

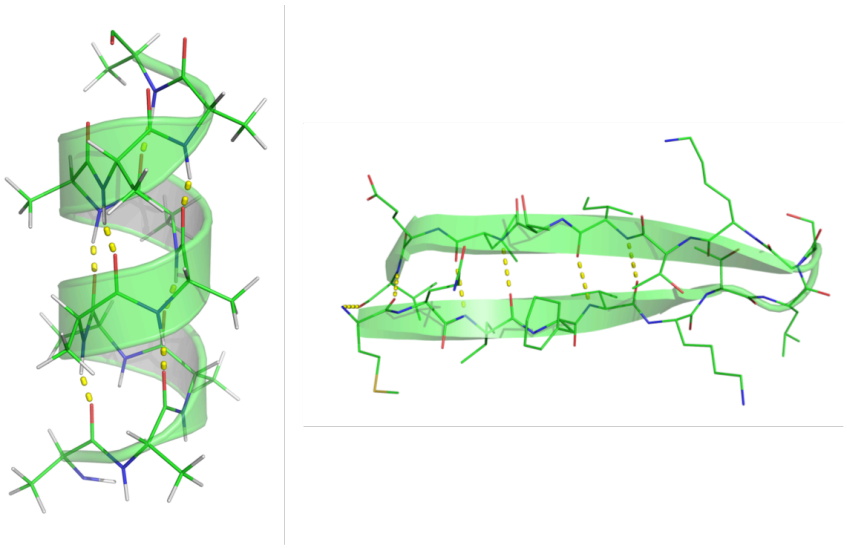

Figure 1.2 Representative α-helix (left) and β-sheet (right) protein secondary structures. Hydrogen bonds between amino acid residues are shown in yellow.

The strength of the average hydrogen bond between amides in a peptide backbone is a mere ~20-25 kJ/mol^{-1} when compared to the strength of a C-C bond (~350 kJ/mol^{-1}) (1); however, when many of these relatively weak interactions are present they reinforce each other. For example, the collective strength of many hydrogen bonds is responsible for the incredible strength of Kevlar (Figure 1.3).

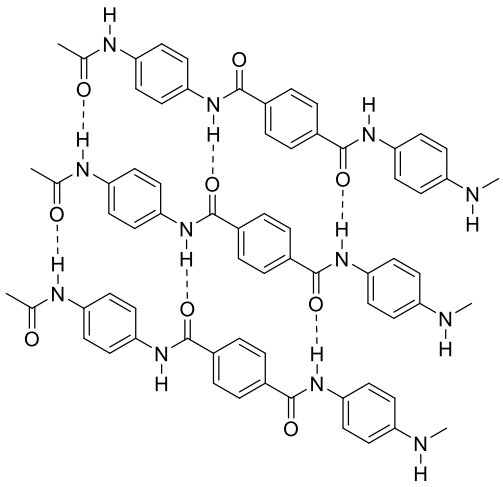

Figure 1.3 Molecular structure of Kevlar with hydrogen bonds shown as dashed lines.

Borrowing from nature, research groups have utilized the organizational motifs inherent in proteins and other biological systems in the assembly of macromolecular structures. Complex uses of non-covalent interactions are present in systems ranging from self-assembling bio-derived polymers to self-assembling DNA metallocages and beyond.

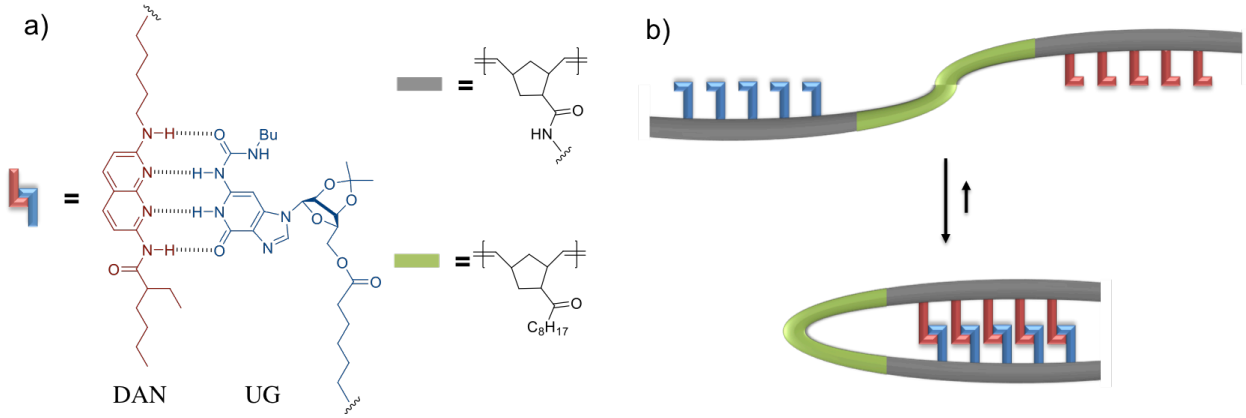

Figure 1.4 (a) Molecular structures and (b) schematic assembly of a triblock copolymer by Romulus and Weck (2013) (2). Even at low concentrations, the intramolecular assembly of a triblock copolymer was facilitated by complementary hydrogen bonds between diaminonaphthyridine (red) and ureidoguanosine (blue).

Recently Romulus and Weck (2013) utilized the complementary hydrogen bonding recognition pair diaminonaphthyridine-ureidoguanosine (DAN-UG) in the self-assembly of a single-chain polymer (2). The norbornene-based DAN and UG monomers (red and blue, respectively) were polymerized with an inert norbornene monomer (green) as a triblock copolymer (Figure 1.4a). Even in dilute concentrations (100 x 10^{-6} M), ^{1}H NMR and dynamic light scattering studies showed that single polymer chains were intramolecularly associating due to the recognition and strength of DAN-UG hydrogen bonding (Figure 1.4b).

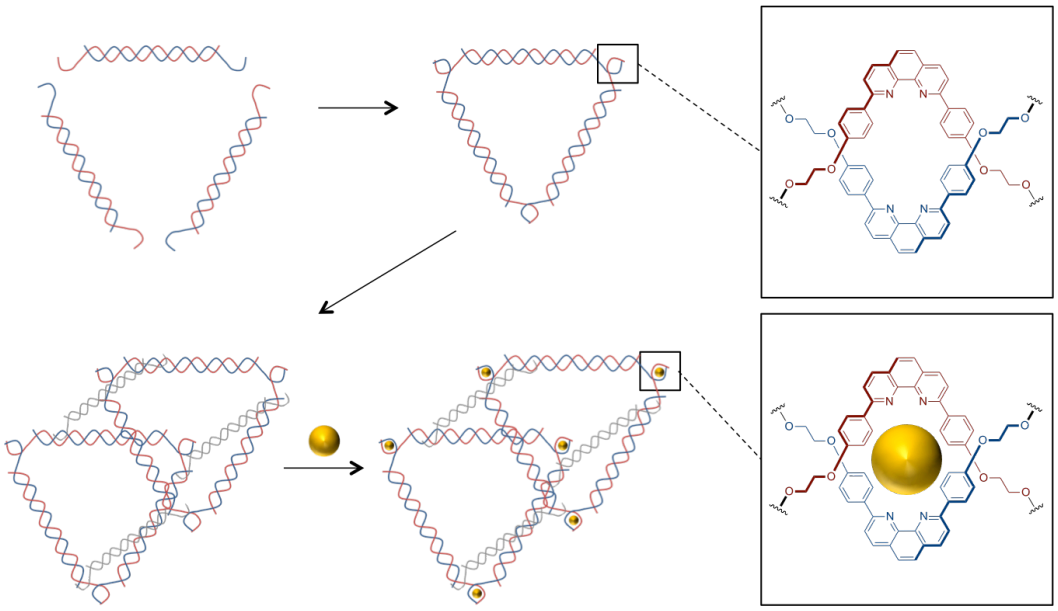

Figure 1.5 Cages of oligonucleotides, or DNA metallocages, are constructed through well-designed metal-tetraamine coordination sides. Double stranded DNA (red and blue) strands are end-capped with aryl amine functionalities (top expansion). Coordination of the aryl amines to a metal (bottom expansion) facilitates the formation of well-defined 3D cages.

Coordination of monomeric or polymeric systems to metals is an established route to structurally complex designs. In 2009, Sleiman *et al*. demonstrated the formation of numerous metallated DNA 3D nanocages, a relatively new class of molecules that could serve as potential stimuli-responsive host structures for biomolecules or nanomaterials (3). In their design (Figure 1.5), three strands of oligonucleotides (red and blue) are brought together forming a nitrogen-rich coordination site for metals (top-right). Upon further linking two sets of the triangular oligonucleotides together (using grey oligonucleotides strands) a triangular prism is formed with six pre-organized sites for transition metal binding (bottom-right).

With the previous section outlining the potential of non-covalent interactions to direct the intra- or inter-molecular assembly of unordered units into more ordered complexes another non-covalent interaction should be introduced: aromatic-aromatic interactions. The innate material properties of aromatic units have led them to be highly researched in the formation of molecular machines, organic electronic devices and bio-inspired materials. To enhance the use of aromatic

stacking interactions in literature, further investigations into how to induce morphological changes between stacked aromatic units are necessary.

1.2 Stacking Interactions and Geometries

As previously mentioned, interactions between aromatic groups play a critical stabilizing role in many naturally occurring systems such as the DNA double helix and proteins. For example, the so-called tryptophan zipper motif can greatly stabilize β-hairpin peptides due to the interactions between four tryptophan residues (4). In amyloidogenic peptides, it has been suggested that the order and directionality of interactions between aromatic groups play a dominant role in the fibril assembly process (5, 6). On the synthetic side, nanostructures composed of interacting aromatic constituents have shown great potential for optoelectronic devices (7), *n*/*p*-type semiconductors (8, 9) and organic electronic devices (10).

To better exploit interactions between aromatic groups in the biological sciences (incorporation of non-natural, aromatic residues into proteins; designed secondary and tertiary structure, artificial DNA's) and materials sciences (for better charge mobility or optoelectronic uses), a deeper understanding of these interactions between aromatic groups is necessary. It is the goal of this Chapter to provide a qualitative description of how electrostatics and desolvation energies dictate aromatic interaction geometries, followed by examples from the literature that illustrate folding, assembly and finally conformational switching behavior.

1.2.1 Hunter and Sanders "Polar/pi" model

A predictive understanding of aromatic stacking geometry was put forth by Hunter and Sanders in the 1990s that was based upon the overall polarization of the aromatic pi electron cloud (11). This approach, known as the "polar/pi" model, uses an analysis of quadrupole-quadrupole interactions between aromatic molecules to rationalize or predict why some aromatics might exhibit herringbone arrangements or off-set parallel stacking geometries while

certain electron-rich and electron-deficient aromatics tend toward alternating face-centered stacking (Figure 1.6).

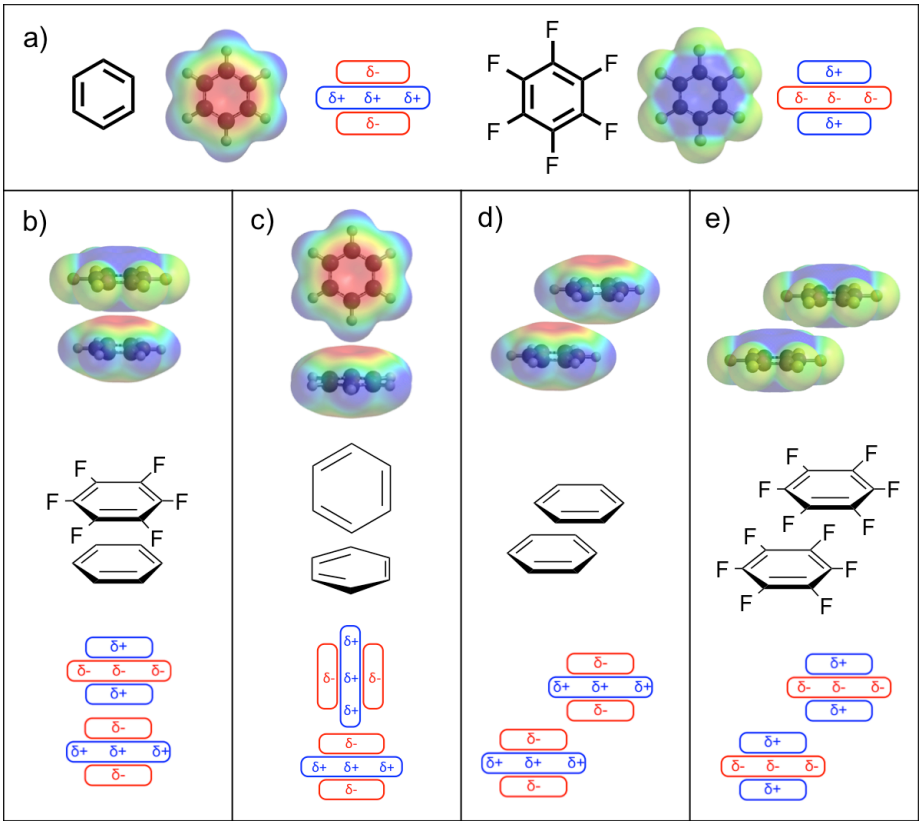

Figure 1.6 The "polar/pi" model of aromatic stacking. (a) Electron-rich benzene (left) and electron-deficient hexafluorobenzene (right). Typical stacking modes include (b) face-centered stacking between electron-rich and electron-deficient aromatics, (c) edge-to-face stacking between electron-rich aromatics, (d) offset face-to-face stacking between electron-rich aromatics and (e) offset face-to-face stacking between electron-deficient aromatics. Electrostatic potential maps were generated in Spartan 08 using the DFT B3LYP G-31* method.

The quadrupole moment inherent in aromatic molecules is derived from the amount of pi electron density located both above and below an aromatic ring plane and any counterbalancing charge around the ring periphery. For underivatized aromatics, this amounts to a region of more negative charge both above and below the ring plane (also referred to as the aromatic core), with a region of more positive charge around the periphery. Strongly electron-withdrawing groups on

the ring can remove so much electron density from the pi cloud that the quadrupole moment is inverted, having a more positive central region and a more negative region associated with the electron withdrawing groups. Benzene, the prototypical aromatic, is electron-rich along its central top and bottom surface (core) and electron-deficient around its periphery (see Figure 1.6a). Hexafluorobenzene, on the other hand, displays a somewhat inverted quadrupole moment, having a relatively electron-deficient aromatic core and an electron-rich periphery associated with the fluorine atoms (Figure 1.6a). The calculated quadrupole moments of benzene and hexafluorobenzene are -29.0×10^{-40} C m^2 and 31.7×10^{-40} C m^2, respectively (12). Based largely on overall quadrupole moments, aromatics are classified according to the nature of their core. For example, benzene would generally be referred to as an electron-rich aromatic, while hexafluorobenzene would be described as electron-deficient.

The "polar/pi" model predicts that when two relatively electron-rich benzene molecules interact, they will maximize complementary quadrupole-quadrupole interactions by stacking in an off-set parallel or an edge-to-face (so-called herringbone) geometry, a prediction that is confirmed experimentally (13). Note that in the case of electron-rich aromatics such as benzene, a face-centered stacking geometry is predicted to be less favorable due to the repulsion that would occur upon bringing two electron-rich aromatic core surfaces together. On the other hand, the interaction of benzene with the electron deficient hexafluorobenzene is predicted to occur with an alternating face-centered stacked geometry that maximizes the complementarity of the quadrupole moments between the relatively electron-rich core and electron-deficient periphery of benzene being attracted to the relatively electron-deficient core and electron-rich periphery of hexafluorobenzene, a geometry that has been confirmed in the solid state (14, 15).

1.3.2 Houk and Wheeler "local, direct interaction" model

Some nice early experimental work by Rashkin and Waters used a molecular-rotation system to probe interactions between substituted aromatic rings (16). In addition to noticing that

polarization played a role in the interaction of the rings, they suggested that direct, electrostatic interactions between the substituents on the periphery of both rings should be considered to be an important factor driving stacking geometry.

Direct complementary interactions between aromatic substituents was examined closely by Wheeler and Houk looking at the interaction energies between substituted face-centered stacked benzene dimers (17). Importantly, they found that the substituted benzene face-centered stacked dimer interaction energies are not dominated by interactions between the aromatic cores of the substituted benzene rings, as similar trends in interaction energies were replicated in the interaction between an H-X unit and the unsubstituted-benzene ring (see Figure 1.7).

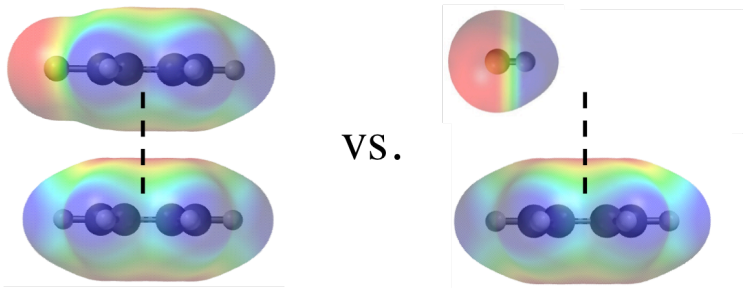

Figure 1.7 Computational work by Wheeler and Houk (17) demonstrated that the interaction energies between monosubstituted-benzene rings and unsubstituted-benzene rings (left) are equivalent to the interaction energies between H-X and unsubstituted-benzene rings (right). Electrostatic potential maps for the pairs of dimers were generated in Spartan 08 using the DFT B3LYP G-31* method.

Experimental work by Houk *et al*. (18) and further computational work by Wheeler (19, 20) has helped refine this model and painted an alternative picture for predicting the preferred interaction geometries between two or more aromatic units. The model, referred to as the "local, direct interaction" model, (19) theorizes that the local, direct through-space interactions between polarized moieties on the periphery of stacked aromatic units drive the aromatic stacking geometry.

This work, as well as work by Sherill and co-workers, (21, 22, 23, 24) Snyder *et al*., (25) Lee *et al*., (26) and Grimme (27) has helped underscore the importance of electrostatic interactions between the substituent of one aromatic ring with a second aromatic ring.

1.2.3 Aromatic Interactions in the solid state

Dialkoxy naphthalene (DAN) and naphthalenetetracarboxylicacid diimide (NDI) are the central focus of the following dissertation. DAN is a prototypical electron-rich aromatic, and NDI is a prototypical electron deficient aromatic. The electrostatic potentials for DAN and NDI are dominated by the electron-donating alkoxy and electron-withdrawing imide carbonyl groups, respectively (see Figure 1.8a). An important aspect of the DAN and NDI structures is that they are roughly the same size, a parameter that is more important in the solid state.

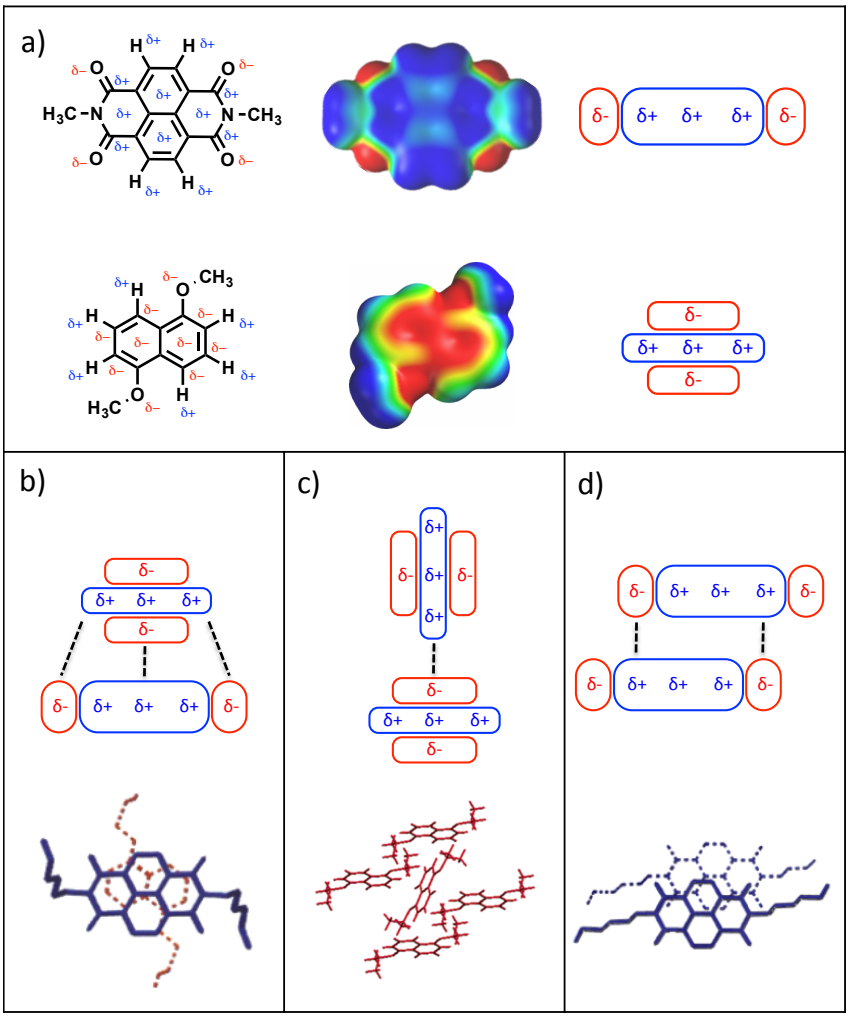

Figure 1.8 (a) Structure, electrostatic potential maps and cartoon representations of NDI (top) and DAN (bottom); (b) Donor-acceptor complex between face-centered stacked DAN-NDI; (c) Herringbone DAN-DAN stacking; (d) Off-set parallel NDI-NDI stacking. Electrostatic potential maps were generated in Spartan 08 using the DFT B3LYP G-31* method. Single crystal structures from (28) and (29).

In the solid state and in solution, mixtures of DAN and NDI are observed to stack in an alternating, face-centered geometry as expected for complementary electron-rich and electron-deficient aromatics (see Figure 1.8b). The face-centered stacking geometry and corresponding pi orbital mixing result in a charge-transfer (CT) absorbance band and characteristic red-purple color seen when the colorless DAN and NDI are mixed. An alternative terminology refers to electron-rich aromatics such as DAN as a donor (D) and electron-deficient aromatics such as NDI as an acceptor (A) in complexes that exhibit charge-transfer behavior. The charge-transfer

absorbance occurs when an electron from the HOMO on the donor transfers to the LUMO of the adjacent acceptor aromatic.

DAN self-stacks in a herringbone arrangement (Figure 1.8c), while NDI is observed to stack in an off-set parallel fashion (Figure 1.8d). Examination of the NDI-NDI self-stack reveals close contact between the carbonyl O atom of one NDI and the carbonyl C atom of the adjacent NDI unit, likely providing a qualitative explanation for the observed solid state geometry.

The key insight from this analysis is that the four polarized carbonyls of NDI provide for two distinct stacking geometries with aromatic molecules. With electron-rich aromatics like DAN, alternating face-centered stacking is observed, while an off-set parallel stacking mode is seen when NDI interacts with itself.

1.2.4 Aromatic Interactions in solution

Up until now, only complementary electrostatic interactions have been discussed as modulating the interactions between relatively electron-rich and electron-deficient aromatic units, but a new consideration arises when discussing interactions between aromatic groups in strongly interacting solvents such as water; solvation/desolvation effects. The key question, then, is how do both solvation/desolvation and complementary electrostatic interactions contribute to the overall geometry and strength of the interaction when two aromatic units are placed in a range of solvents?

Cubberley and Iverson sought to answer this question by determining the association constants of DAN and NDI, individually as well as mixed, in solvents of varying polarities (28). ^{1}H NMR was used to determine the binding affinities of tetraethylene glycol-substituted DAN and triethylene glycol-substituted NDI monomers (Figure 1.9a). In particular, Figure 1.9b shows the observed interaction energies between DAN-DAN, NDI-NDI and DAN-NDI as a function of solvent polarity. The most obvious trend is that upon increasing solvent polarity, the interaction energies between aromatic units all increased suggesting that solvation/desolvation effects are

the dominant energetic parameter in polar solvents. In other words, desolvation of hydrophobic aromatic faces in more polar solvents appears to be the dominant energetic component driving association.

a)

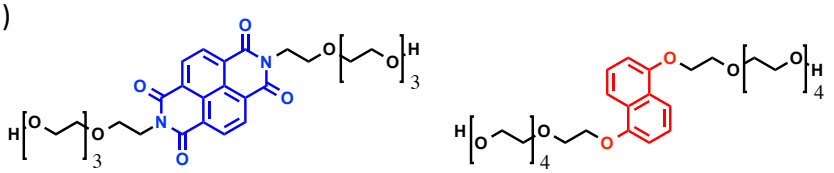

b)

Solvent	DAN-DAN	NDI-NDI	DAN-NDI
$CDCl_3$	-*	-*	2
acetone-d_6	1	1	8
CD_3CN	1	3	11
CD_3OD	1	8	30
D_2O	20	245	2045

Figure 1.9 (a) NDI (left) and DAN (right) monomers used for the ^{1}H NMR study; (b) Summary of association constants collected by Cubberley and Iverson (2001) in solvents of varying polarity (28). *Calculated association constants undeterminable within error range.

However, solvation/desolvation alone cannot explain all the data. Note the large difference in interaction energies between DAN-NDI and DAN-DAN/ NDI-NDI, yet both DAN and NDI have hydrophobic surfaces of roughly the same size. Revisiting the solid-state structures of DAN and NDI in Figure 1.8 provides a reasonable explanation for the observed relative association constants. While the main driving force for association is desolvation of the hydrophobic aromatic faces in highly polar sovlents, electrostatics *dictate the geometry of the interaction and thus the extent of hydrophobic surface overlap upon complexation*. Whereas the DAN-NDI complementary electrostatic interaction maximizes the burial of hydrophobic surfaces by stacking in a face-centered geometry (thus stronger association), the DAN-DAN interaction

occurs in an edge-to-face geometry and buries a minimal amount of hydrophobic surface area, leading to a significantly weaker association. The offset stacking seen with NDI self-assembly results in an intermediate level of buried hydrophobic surface area and correspondingly intermediate association strength (28, 29).

It is worth pointing out that as solvent polarity and presumably the significance of solvation/desolvation effects decrease, the differences between the DAN-DAN, NDI-NDI and DAN-NDI association constants also decrease (Figure 1.9b). This idea should be kept in mind when considering the design and analysis of supramolecular systems and assemblies involving electron-deficient moieties such as NDI. Greater discrimination between stacking modes (*i.e.*, DAN-NDI vs. NDI-NDI) is expected for more polar solvents, and conversely, less discrimination would be expected in solvents of low polarity or the solid state.

1.3 Electron-Rich / Electron-Deficient Systems

Complementary electrostatic interactions between NDI and relatively electron-rich aromatic moieties such as DAN or pyrene have been exploited extensively in the development of catenanes, hetero-duplex forming oligomers and numerous 1D and 2D nanostructures. By itself, NDI is capable of forming highly ordered structures by way of self-associating in off-set parallel stacking geometries.

1.3.1 Ghosh's fibrils and Sander's catenanes

Ghosh *et al*. reported the spontaneous self-assembly of NDI-based bolaamphiphiles in aqueous solution into 2D vesicles that could then be transformed into 2D fibrils upon introducing insoluble, relatively electron-rich pyrene monomers that would insert themselves between two NDI monomeric building blocks (Figure 1.10a) (30). Using similar self-assembling NDI monomeric scaffolds, they also reported the assembly of 1D fibers (31, 32) and 2D vesicles (33) derived from NDI-NDI interactions.

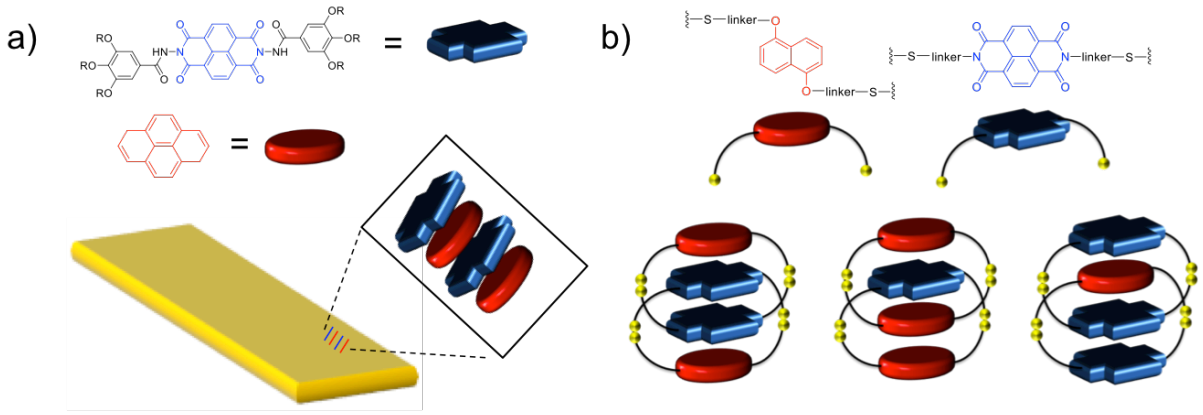

Figure 1.10 Schematic representing the use of face-centered stacking in (a) the formation of D-A 2D fibrils by Molla and Ghosh (30) and (b) the formation of various catenanes by Sanders *et al*. using thiol linkages (34).

The Sanders group has exploited solvaphobic effects in the dynamic combinatorial synthesis of D-A [2]-catenanes as shown in Figure 1.10b (35, 36). Their results have shed light on the formation of DAAD, DADD and ADAA stacked [2]-catenanes, which has challenged the conventional thinking of stacking preference based on a primary consideration of electrostatic complementarity.

1.3.2 Gabriel and Iverson heteroduplexes

Based on the successful development of other folding systems in our group, Gabriel and Iverson designed DAN and NDI oligomers capable of self-assembling into heteroduplexes in water (Figure 1.11a) (37). ^{1}H NMR studies showed that a face-centered DAN-NDI alternate stacking geometry was present in the heteroduplex (Figure 1.11b). Interestingly, as the number of aromatic units in the individual DAN and NDI oligomers was increased from 1 to 4, the resulting heteroduplex binding affinity (K_a) (as determined by ITC) increased proportionately (Figure 1.11c). The 1:1 DAN-NDI hetero-duplex binding model was proven by NMR job plots

as well as PAGE titration experiments. Perhaps most interesting of all, there was a surprising temperature independence of the association constant observed, indicating a high degree of enthalpy-entropy compensation.

a)

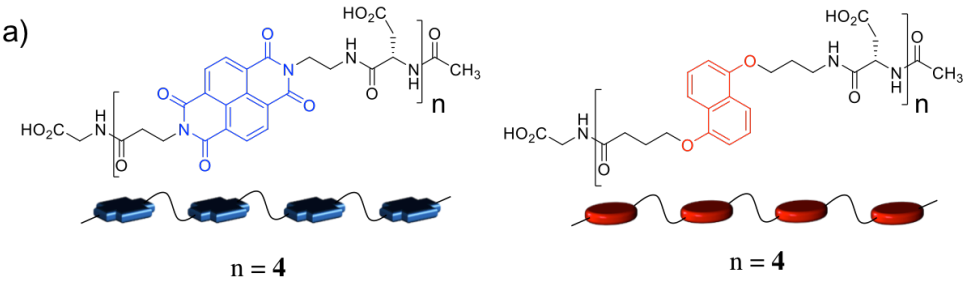

b)

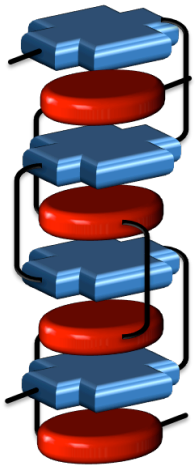

c)

Complex	K_a (M^{-1})	ΔG° (kcal·mol^{-1})	ΔH° (kcal·mol^{-1})	ΔS° (kcal·mol^{-1})
n = **2**	2.7 x 10^3	-5.0	-12.3	-23.0
n = **3**	4.5 x 10^4	-6.8	-17.7	-34.2
n = **4**	3.5 x 10^5	-8.1	-19.3	-35.3

Figure 1.11 Heteroduplex formation in water using face-centered stacked DAN-NDI interactions as found by Gabriel and Iverson (37). (a) NDI oligomer (left) and DAN oligomer (right), (b) 1:1 DAN-NDI heteroduplex and (c) association energies for heteroduplexes **2** – **4** determined by ITC.

1.3.3 Reczek and Iverson water-soluble polymers

Inspired by earlier investigations of DAN and NDI binding affinity in water, Reczek and Iverson sought to make water-soluble DAN and NDI polymers capable of intermolecular association (29). The idea was simple: if such large binding affinities were observed for small oligomers of DAN and NDI strands in water (as presented by Gabriel and Iverson), then much larger affinities should be realized in polymeric DAN and NDI strands. Functionalization of poly(ethylene-*alt*-maleic anhydride) with DAN and NDI monomers yielded polymers **P1** and **P2** that showed slight solubility in basic solutions (Figure 1.12a). Independent of each other, **P1** and **P2** formed clear solutions, but mixing them in a 1:1 ration (at 3% weight in 0.2 M NaOH)

resulted in a purple solution with a CT band at 560 nm consistent with face-center DAN-NDI stacking (Figure 1.12b). AFM and SEM of the polymers revealed that while **P1** and **P2** showed micelle-like deposits and uniform surfaces, respectively, a 1:1 combination of **P1** and **P2** yielded large macrostructures indicative of a polymer network formed upon DAN and NDI association.

Interestingly, extruding a slightly basic solution of **P1** and **P2** through a small aperture into a slightly acidic solution (1 M HCl) produced long fibers up to several centimeters in length. When either **P1** or **P2** were extruded through a small aperture under the same experimental setup no fibers were made. Although the fibers were delicate, meaning that an overall small percentage of DAN and NDI associations were occurring in the fiber, this study helped show that intermolecular association by aromatic-aromatic interactions can serve as a platform for intermolecular assembly.

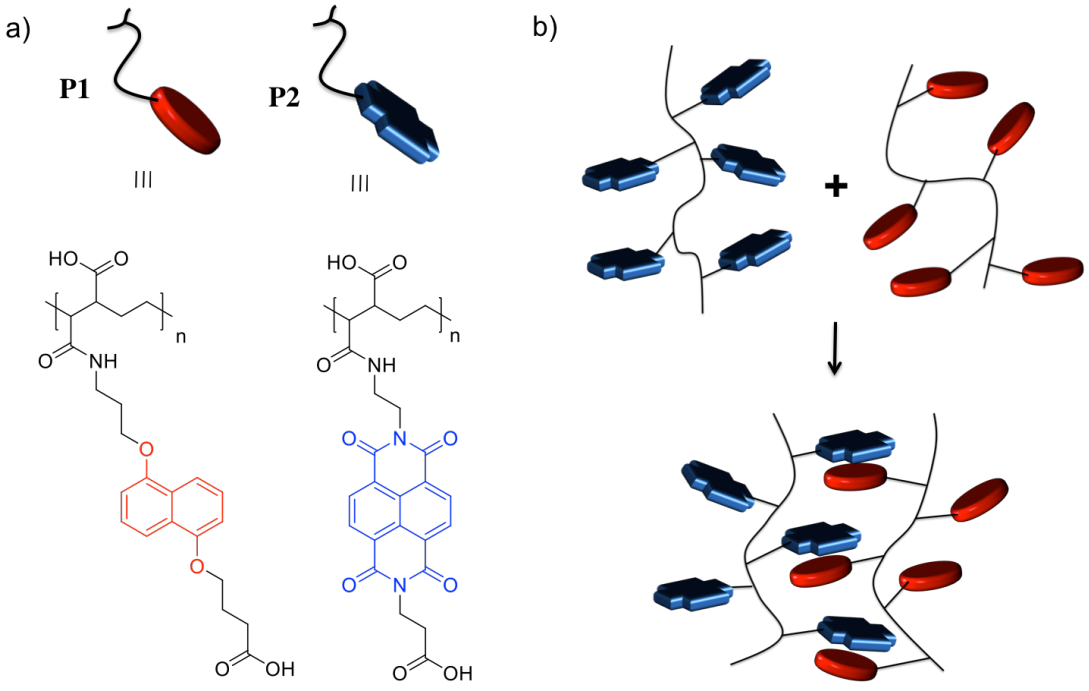

Figure 1.12 Water-soluble DAN and NDI polymers investigated by Reczek and Iverson (38). (a) DAN and NDI polymer structures and (b) the proposed stacking model of DAN and NDI polymers in solution.

1.4 Electron-Deficient/ Electron-Deficient Systems

1.4.1 Alvey and Iverson NDI-donor polymers

In an effort to make semiconducting materials Alvey *et al*. (2012) copolymerized NDI (an increasingly more studied electron acceptor molecule due to its low-lying LUMO energy levels) with several donor monomers of varying HOMO energy levels (benzene, naphthalene, dialkoxynaphthalene, and anthracene) to make several conjugated alternating donor-acceptor polymers (Figure 1.13a-b) (39). Not surprisingly, electrochemical studies revealed the LUMO of all the polymers to be located around -3.75 eV, which was attributed to the strong electron withdrawing character of NDI, even when conjugated to electron-donating substituents. While the LUMO levels of the polymers were more varied, **P11** showed the smallest HOMO-LUMO band gap (1.44 eV) and remains one of the smallest conjugated NDI-donor polymer band gaps to date.

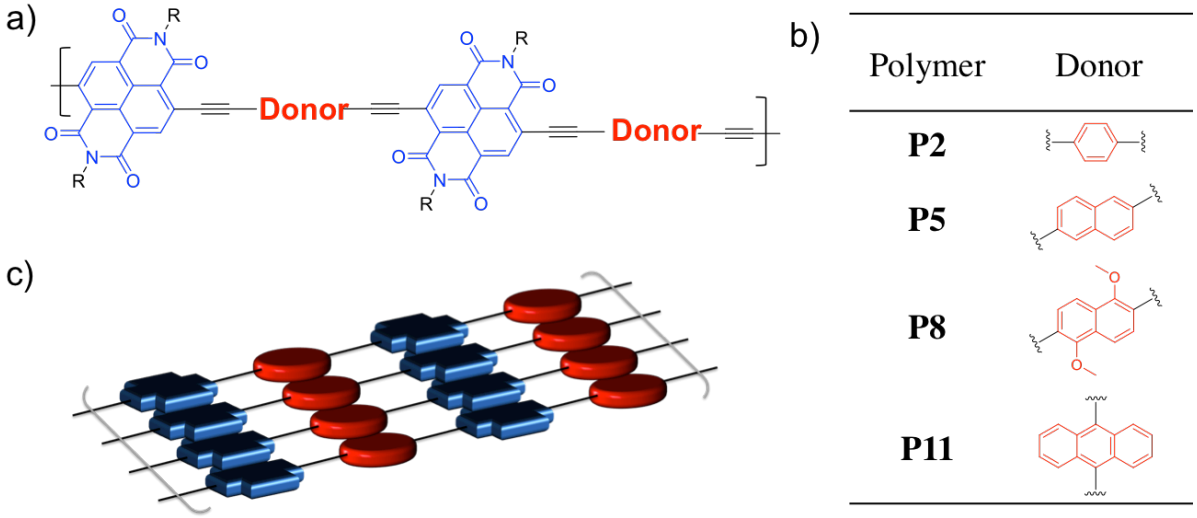

Figure 1.13 Alternating NDI-donor polymers investigated by Alvey and co-workers (39). (a) Structure of polymers, (b) structures of donor groups and (c) proposed NDI-NDI off set stacking of polymers in the solid state.

The stacking morphology of all the polymers was investigated and parallel trends were observed. XRD of the polymer thin films all looked very similar, with large diffraction peaks occurring at *d*-spacings of ~23, ~14, ~4.5 and ~3.5 Å for each of them. Modeling of the polymers proposed that the largest *d*-spacing (~23 Å) was indicative of lamellar-type interdigitated side-chain packing between polymer chains while the smaller *d*-spacings of ~4.5 and ~3.5 Å indicated centroid-centroid and planar NDI-NDI stacking interactions, respectively (Figure 1.13c). The proposed self-association of the NDI aromatic units was attributed to the favored electrostatic interactions between the highly polarized carbonyl carbon-oxygen bond with adjacent NDI units.

1.4.2 Ghosh's, Parquette's and Govindaraju's sheets, cups and fibrils

Using NDI-appended dipeptides, Parquette *et al*. has shown the formation of 1D nanofibrils facilitated by intermolecular NDI-NDI off-set parallel stacking coupled with favorable charged, electrostatic interactions between monomers (40) (*Entry 1*). Intermolecular NDI-NDI off-set parallel stacking was also observed in lysine-based NDI amphiphilic monomers that self-assembled in aqueous solutions to form 1D nanotubes (9) (*Entry 2*) (41) (*Entry 3*).

Ghosh's NDI-forming 2D fibrils and 2D spheres (30) have previously been mentioned (*Entry 4*).

System	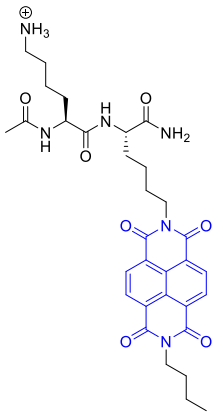	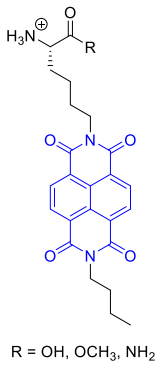 R = OH, OCH_3, NH_2	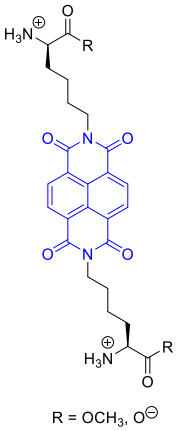 R = OCH_3, $O^{\ominus}$
Entry	*1*	*2*	*3*
Structure made	A	B	B
Reference	(40)	(9)	(41)
System	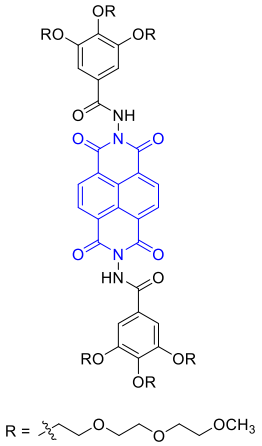 R =	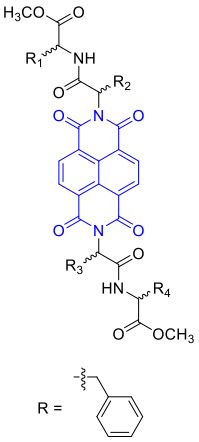 R =	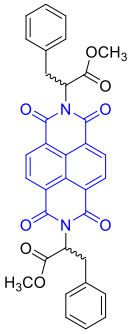
Entry	*4*	*5*	*6*
Structure made	A, C	D	A, C, D
Reference	(30)	(42)	(8)
Where:	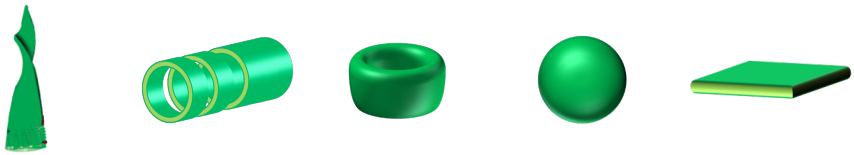		
	A	B	C	D

Table 1.1 Collected structures of NDI-containing systems that form various types of well-defined supramolecular structures.

Govindaraju *et al*. took a different approach to forming highly ordered nanostructures by directly appending either a single, or a strand of, amino acids to the imide of a monomeric NDI unit. A combination of hydrophobic interactions and favorable NDI-NDI off-set parallel stacking interactions led to the formation of conductive 2D nanosheets and nanocups (42) (*Entry 5*) and nanospheres, nanobelts and fractals (8) (*Entry 6*).

Stoddart *et al*. has also employed NDI in the synthesis of switchable donor-acceptor [2]-rotaxanes. In one instance, click chemistry was used to afford a neutral [2]-rotaxane composed of a rigid NDI strand interlocked with 1,5-dinaphthol[38]crown-10 (DN38C10) (43). "Shuttling" of the [2]-rotaxane, that is the electrochemically-driven switching interaction between the DN38C10 unit and the NDI and triazole rings, was proposed based on CV and spectroelectrochemsitry analysis. In another instance, DN38C10 was shown to "shuttle" between electron-deficient NDI and 4,4'-bipyridinium aromatic units even with a sterically bulky tetraarylmethane moiety between the units (44).

1.5 Electron-Rich/ Electron-Deficient to Electron-Deficient/ Electron-Deficient Switching

As illustrated, there are many highly ordered systems that form supramolecular assemblies composed of either alternating stacking between NDI and an electron rich aromatic such as DAN, or NDI-NDI self-assembly. There is now a growing list of interesting systems containing NDI that are capable of conformational switching between different stacking geometries. In the following pages, several of these systems are described.

1.5.1 Matile's synthetic ion channel

The conformational change of static, monofunctional synthetic ion channels into more complex multifunctional channels that can open and close in response to external stimuli is a maturing area of supramolecular chemistry. In 2005, Matile *et al*. introduced a ligand-gated

synthetic ion channel incorporating NDI units that open in response to intercalating guest molecules (see Figure 1.14) (45). The design uses four linear "stave-like" monomers, incorporating *p*-octiphenyl rigid-rod scaffolds appended with NDI units, which assemble into cylindrical, barrel-stave pores. The pore is closed initially due to the conformational twisting of the *p*-octiphenyl scaffold to accommodate NDI-NDI interactions between aromatic groups, favorable hydrogen-bonding and side chain steric crowding. In this position, one can envision J-type NDI-aggregates, but slightly mismatched, with the NDI faces off-set in a twisted, parallel fashion to one another.

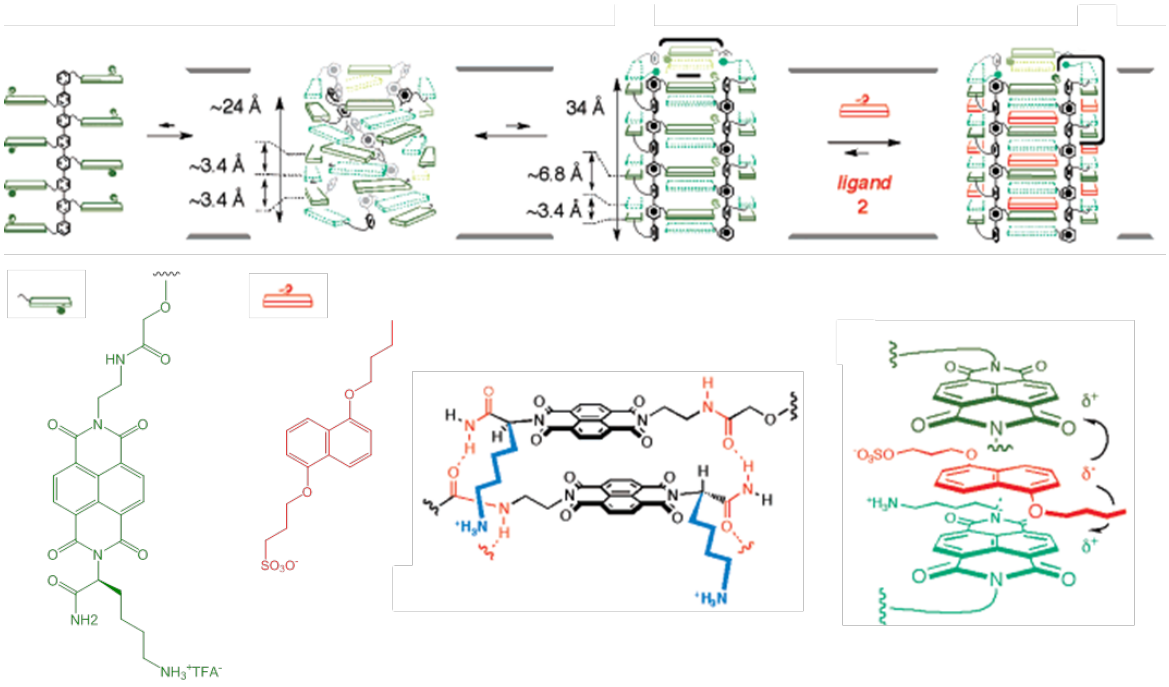

Figure 1.14 The assembly and later opening of the pi-helix structure into the pi-barrel pore upon intercalation of DAN monomers is shown at top. Structures of the NDI (green) and DAN (red) aromatic units are shown at bottom left while modeled NDI-NDI, off-set parallel displaced interactions in the pi-helix structure and DAN-NDI face-centered interactions in the pi-barrel pore structure are shown at bottom right. Adapted with permission from (45). Copyright (2005) American Chemical Society.

Addition of DAN monomer into the solution leads to the intercalation of DAN in between NDI units, eliminating the twist and opening the ion channel, as corroborated using the

exciton chirality method in CD studies (46). The open ion channel has the characteristic red-purple color due to a strong CT absorbance derived from alternating DAN-NDI stacking. This "ligand-gating" provides a dramatic example of how the two stacking geometries of NDI, off-set stacking with itself, and face-centered stacking with DAN, can be exploited to modulate supramolecular properties.

This design was later incorporated into a vesicular membrane to act as an electron-transport pathway and an ion channel (47). Photoexcitation of the system transports an electron from an electron-source outside the membrane to the embedded pi-helix structure and to a final acceptor in the membrane. Addition of DAN monomer opens the pi-helix structure into a synthetic ion channel which then facilitates hydroxide ion transport through the membrane.

1.5.2 Ghosh's self-sorting DAN and NDI monomers

In 2010, Molla, Das and Ghosh used a trade-off between hydrogen bonding and interactions between DAN and NDI monomers to facilitate both the alternate and segregated stacking of these monomers in solution (see Figure 1.15*)* (48). To this extent, DAN and NDI monomers were synthesized with complementary and non-complementary hydrogen-bonding motifs and then mixed in non-polar solvent.

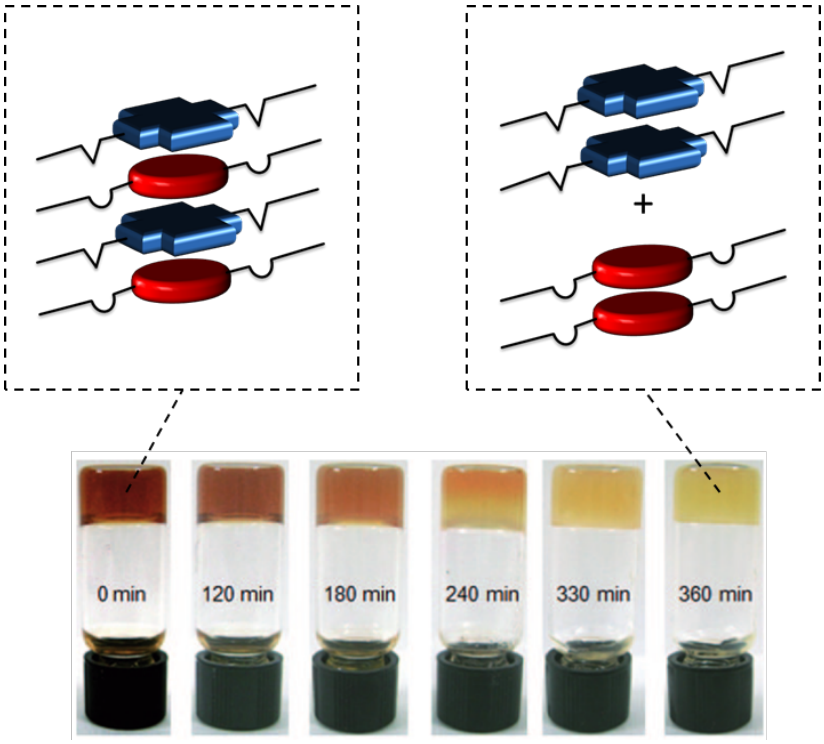

Figure 1.15 The transition from a DAN-NDI face-centered, alternating assembly to segregated DAN-DAN and NDI-NDI self-sorted assemblies is schematically shown. NDI monomers are represented as blue squares while DAN monomers are represented as red ovals. Non-complementary hydrogen bonds are represented by the interaction of different colored spheres (yellow and green), while complementary hydrogen bonds are represented by interactions of the same colored spheres. Adapted with permission from (48). Copyright (2005) John Wiley and Sons.

The absence of a charge-transfer absorbance when the DAN and NDI monomers containing *non-complementary* hydrogen-bonding motifs were mixed together suggested the monomers were forming segregated, self-assembled stacks. This segregated assembly was theorized due to the complementary hydrogen bonding between like monomers (DAN-DAN and NDI-NDI) overriding the preference for alternating stacking (DAN-NDI). Consistent with this hypothesis, mixing of DAN and NDI monomers with *complementary* hydrogen-bonding units resulted in a strong CT absorbance, indicative of alternating DAN-NDI stacking.

Further refinement of the DAN and NDI monomer units allowed for a time-dependent reorganization of the DAN and NDI monomers from an alternate, stacked DAN-NDI assembly to segregated stacked assemblies while both being gels (10, 49). In a similar conclusion, they

proposed that interactions between aromatic groups in the kinetically stable alternate stacked assembly would reorganize so that stronger hydrogen-bonding interactions could occur in the thermodynamically favored segregated stacked assemblies.

1.5.3 Reczek and Alvey DAN and NDI liquid crystals

Previous work in the Iverson group has also used the complementarity of DAN and NDI monomers to generate highly colored mesophases (29). Melting of mixtures of DAN and NDI derivatives yielded a red-purple color indicative of the characteristic aromatic D-A CT absorbance. This color, along with UV-Vis, single crystal and variable temperature XRD data, provided strong evidence that an alternating, face-centered stacked geometry of DAN and NDI molecules was occurring in the columnar liquid crystal mesophase. The same red color was observed in the crystalline phase for many of these mixtures suggesting that little reorganization occurred between the mesophase-to-crystalline phase transition.

In some cases, however, melting of specific DAN and NDI monomers (Figure 1.16a) gave a red-colored mesophase, but upon cooling produced a dramatic thermochromic change to a yellow-colored crystalline solid (see Figure 1.16b). An interesting feature of the mixtures exhibiting thermochromic behavior is that the transition occurs without any detectable change the macroscopic morphology of the solid (see Figure 1.16b). Later work sought to further explore the thermochromic behavior, focused on side chain interactions between the DAN and NDI monomers (50). These results confirm that manipulating side chain interactions in a systematic way between DAN and NDI monomers can lead to highly tunable mesophases as well as controllable thermochromism. Detailed characterization of the mesophase and crystalline phase using single crystal analysis and XRD patterning revealed that the thermochromic transition in these mixtures involves a shift from alternating DAN-NDI stacking geometry (liquid crystal mesophase) to NDI-NDI off-set parallel self-stacking (crystalline phase) (Figure 1.16d-e).

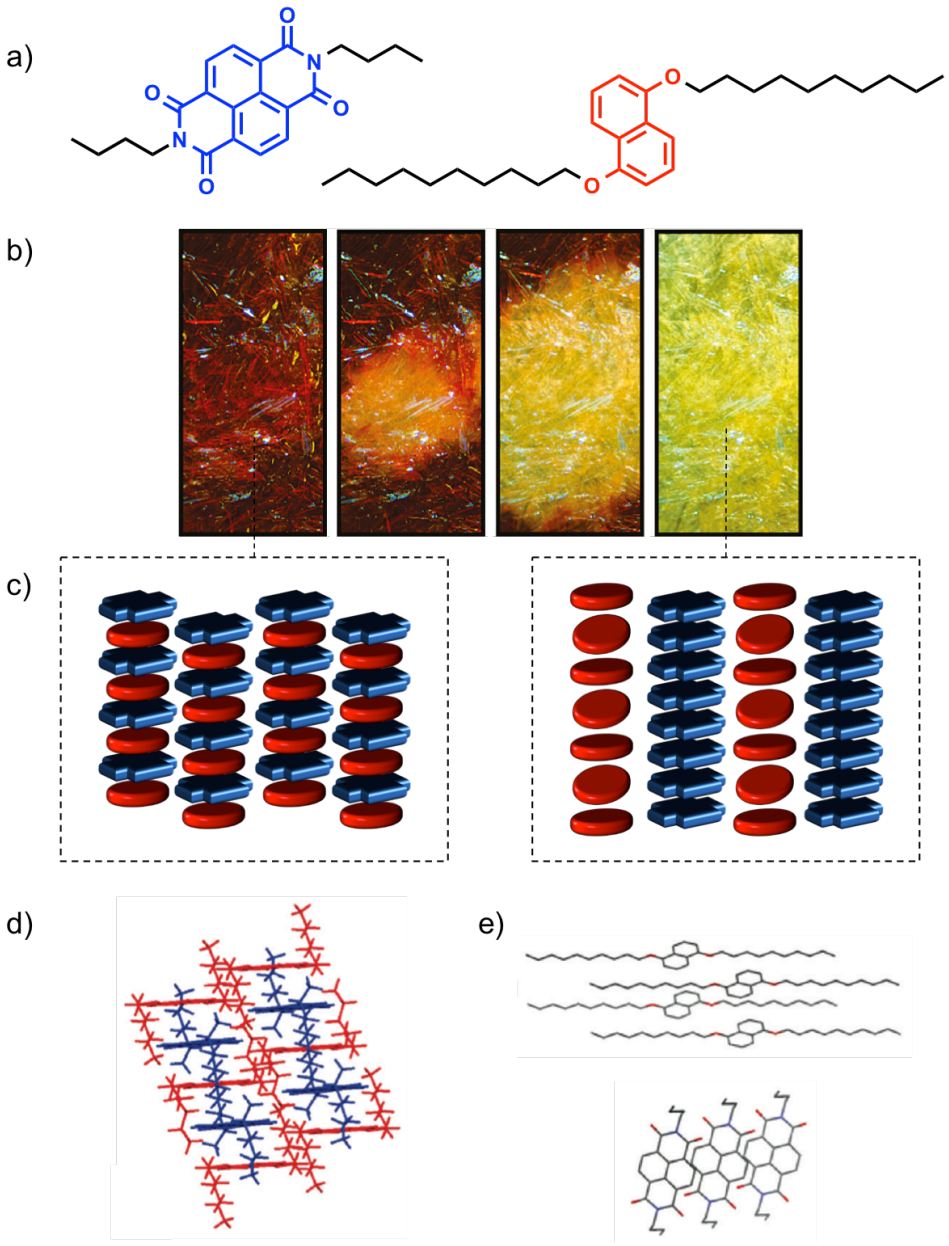

Figure 1.16 (a) Structures of NDI (left) and DAN (right) monomers; (b) Optical microscope images showing the transition from mesophase (red) to crystalline phase (yellow). Notice that the macromolecular morphology remains intact through the transition; (c) Scheme showing the self-sorting behavior of the DAN (red) and NDI (blue) monomers; (d) Face-centered DAN-NDI stacking in the mesophase; (e) DAN herringbone (top) and NDI off-set parallel (bottom) stacking in the crystalline phase. Adapted with permission from (50). Copyright (2010) American Chemical Society.

1.6 OTHER NDI PROPERTIES

1.6.1 Core-substitution

Core-substituted NDIs (cNDIs) have been studied extensively over the past 10-15 years. Recent improvements in the synthesis of brominated or chlorinated cNDIs have made the NDI "toolbox" even larger than it was previously (see Figure 1.17). The ability to append electron-donating (-OR, -NHR) or electron-withdrawing (-CN, $-SO_3$) substituents not only affects the color of the molecules (due to "push-pull" chromophores in the case of electron-donating substituents) but also imparts significant changes to the redox properties of the cNDIs. While electron-donating substituents lowers the HOMO-LUMO gap and increases the HOMO and LUMO energies electron-withdrawing substituents raises the HOMO-LUMO gap and lowers the HOMO and LUMO energies (51). For instance, the HOMO and LUMO energy levels for cNDIs appended with two amino groups to the core versus two cyano groups are -5.45 and -3.40 and -7.50 and -4.50 eV, respectively (52).

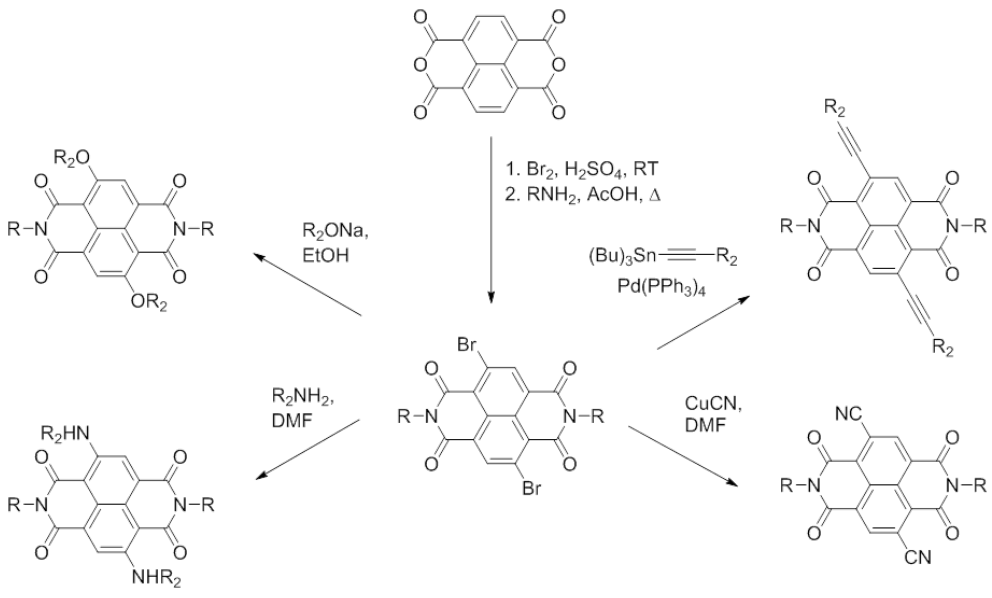

Figure 1.17 Synthetic routes to various core-substituted NDIs.

1.6.2 Circular dichroism spectroscopy

Circular dichroism (CD) spectroscopy of NDIs in a non-chiral state gives no signal, even if there is association in H- or J-type aggregates that are stacked in a parallel fashion (where the transition moment between the aromatic units is 0°). However, in a chiral environment where helicity is imparted in the NDI stacks strong bisignate exciton-coupled CD (ECCD) can be observed (see Figure 1.18). In short, ECCD can discriminate between CD-silenced parallel-stacked NDI aggregation and CD-active helical NDI aggregation (46). More so, depending on the sign of the first bisignate curve (or Cotton effect), left-handed M (the lower energy transition is negative) or right-handed P (the lower energy transition is positive) helicity can be assigned to the stacking.

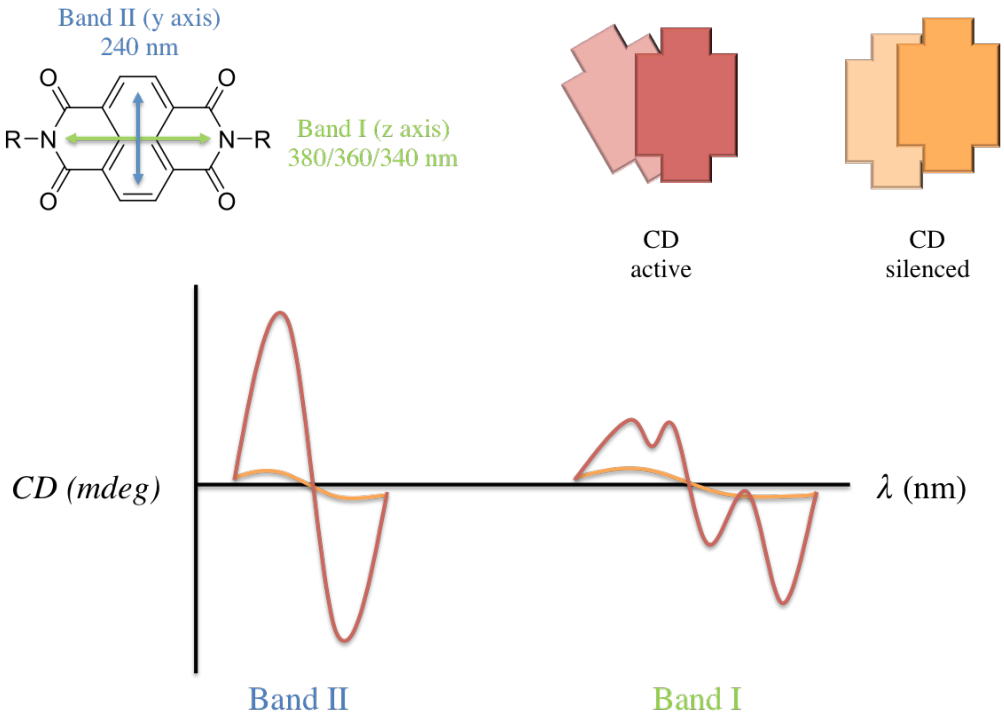

Figure 1.18 Exciton coupling of two twisted NDI chromophores yields bisignate CD cotton effects for both vibrational bands (Band I and Band II) of NDI (red CD trace). When NDIs are stacked in a non-twisted parallel fashion (orange CD trace) they are CD silent and show minimal Cotton effects. The M helicity of the NDI is indicated in the negative sign of the first Cotton effect.

1.7 Overview of Aromatic Donor-Acceptor Interactions

At this point, the authors feel it necessary to include a couple more examples of molecular switching systems, even if they do not fit into the scope of this review, due to their importance in the field of supramolecular chemistry. While Stoddart's NDI-containing [2]-rotaxanes were briefly mentioned, his work with paraquat-containing molecular switches demonstrates the progress that has been made towards implementing these devices in molecular electronics (53). Sauvage *et al*. has also made important contributions to molecular machines using transition metal complexes as elements of rotaxanes and catenanes (54).

NDI has proven to be an important supramolecular building block in large part because it can adopt two different but entirely predictable stacking geometries; alternating face-centered stacks with complementary electron-rich aromatic moieties such as DAN and an off-set parallel self-stacking mode. These insights allow a systematic manipulation of stacking geometry and therefore properties of assemblies. Taking advantage of these two distinct states has generated several interesting systems capable of conformation switching ranging from artificial ion channels to synthetic amyloid analogues and even mesophases capable of dramatic thermochromism. Moving forward, the scientific community can expect a number of new and exciting applications of NDI and its analogues, limited only by our imaginations.

The remainder of this dissertation will further investigate the conformational switching phenomenon displayed by NDI.

CHAPTER 2

Conformational switching in donor-acceptor foldamers

2.1 CHAPTER SUMMARY

2.1.1 Introduction

Chapter 1 described the theory behind aromatic stacking interactions and geometries and outlined several approaches to highly ordered 2D and 3D molecular structures that can be realized using these non-covalent interactions. Previous work in the Iverson group has explored the stability of DAN-NDI donor-acceptor amphiphilic foldamers in aqueous solvent and observed interesting thermally-induced hydrogelation effects. Chapter 2 describes our efforts to elucidate the aggregated hydrogel state of the foldamer and propose a model for how the aggregation process proceeds.

2.1.2 Goals

The aim of this chapter is to elucidate the structure of an aggregated state of a DAN-NDI donor-acceptor amphiphilic foldamer. The goal is to further investigate this highly ordered structure by way of microscopy and elucidate the aggregate morphology.

2.1.3 Approach

Three amphiphilic foldamers (a tetramer, hexamer and octamer) were synthesized, heated to the aggregated hydrogel state and investigated by circular dichroism and UV-Vis spectroscopy. The structure of the hydrogel state was investigated by TEM and AFM. A structure of the aggregate was proposed with analogies to the amyloid formation process.

2.1.4 Results

Three amphiphilic donor-acceptor foldamers were synthesized and the aggregated state of these foldamers were explored by UV-Vis, CD, AFM and TEM. While the tetramer and hexamer formed 1D nanofibrils upon heating to the aggregated state, the octamer did not form a self-supporting hydrogel. Our findings indicate that the aromatic DAN-NDI interactions of the original foldamer undergoes transformation to a fibrillar assembly with aromatic NDI-NDI stacked interactions. These structural insights could help inform new molecular designs and increase our understanding of the fibrillar assembly and aggregation process in aqueous solution.

2.2 BACKGROUND

The importance of protein folding in the scheme of molecular self-assembly was previously shown in Chapter 1. For a protein to function, it must correctly self-assemble into well-defined tertiary and quaternary structures while keeping their native residues intact. However, if the folding process fails and the protein becomes misfolded, this incorrect protein folding can possibly lead to the formation of highly ordered aggregates. There are more than twenty neurodegenerative diseases, most famous of which are Alzheimer's, Huntington's, Creutzfeldt-Jakob, Parkinson's disease and type II diabetes, where irreversible protein misfolding is directly associated with the disease. In these protein misfolding diseases, the highly ordered aggregates are known as amyloid fibrils and form as a result of the irreversible conformational change of globular proteins into self-assembled, highly ordered β-sheet-rich fibrillar structure.

Two classes of molecules are able to exhibit amyloid formation: globular proteins that exist as folded or partially folded species and then undergo a transformation into fibrillar structures, and polypeptides without globular structure which then aggregate into ordered fibrils. For both classes, the initial monomeric state overcomes an entropic barrier while assembling into an insoluble, more thermodynamically stable fibril aggregate (Scheme 2.1) (55). Both classes of

amyloid forming molecules are initially monomeric in solution, but as the initial structures reorder and nucleation-dependent self-assembly commences, "one-dimensional crystallization" occurs (56, 57, 58). Nucleation of partially unfolded or monomeric oligomers of the protein or polypeptide produces protofilaments (more soluble oligomeric assemblies than insoluble mature fibrils). Whether the "immature" fibrils are considered to be more toxic than the mature fibrils is still a point of controversy in the amyloid community (59).

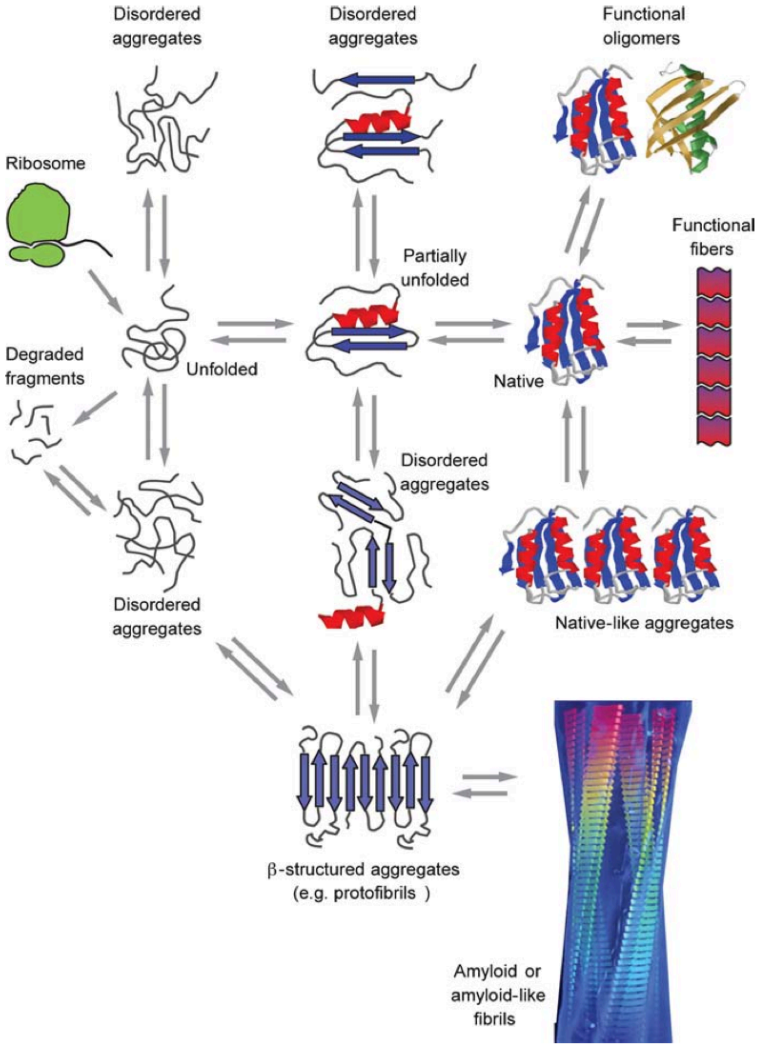

Scheme 2.1 A schematic of the amyloid formation process. Starting from functional oligomers and natively folded proteins, many conformational pathways towards amyloid formation are possible (60).

Amyloidogenic proteins are composed of a diverse array of amino acid sequences and prior to forming amyloid fibrils these sequences may organize into a range of secondary structures (α-helix, β-sheet,) or partially unfolded states (60, 61). However, the morphological and structural similarities between the various amyloid-forming fibrils likely indicate a common mechanism of their formation (62).

Attractive interactions between hydrophobic surfaces on protofilament strands have been strongly linked to the merging of protofilament strands into multistranded fibril precursors which then go on to form mature fibril aggregates (63). The generic amyloid shape, the cross β-strand, is a robust shape that is easily able to form repetitive hydrogen bonds with other cross β-strands (64, 65). This enables the linear addition of strands together in the formation of protofilaments (61). A model proposed by Petkova *et al*. used hydrophobic interactions to show the merging of two $A\beta_{1\text{-}40}$ cross β-strand units (the likely causative agent associated with Alzheimer's disease) wherein the C-terminal hydrophobic residues are sequestered on the interior of a dimer unit juxtaposing the more hydrophilic N-terminal residues on the exterior (Figure 2.1a) (64). This model has been further corroborated by numerous research groups (Figure 2.1b) (66, 67, 60, 62).

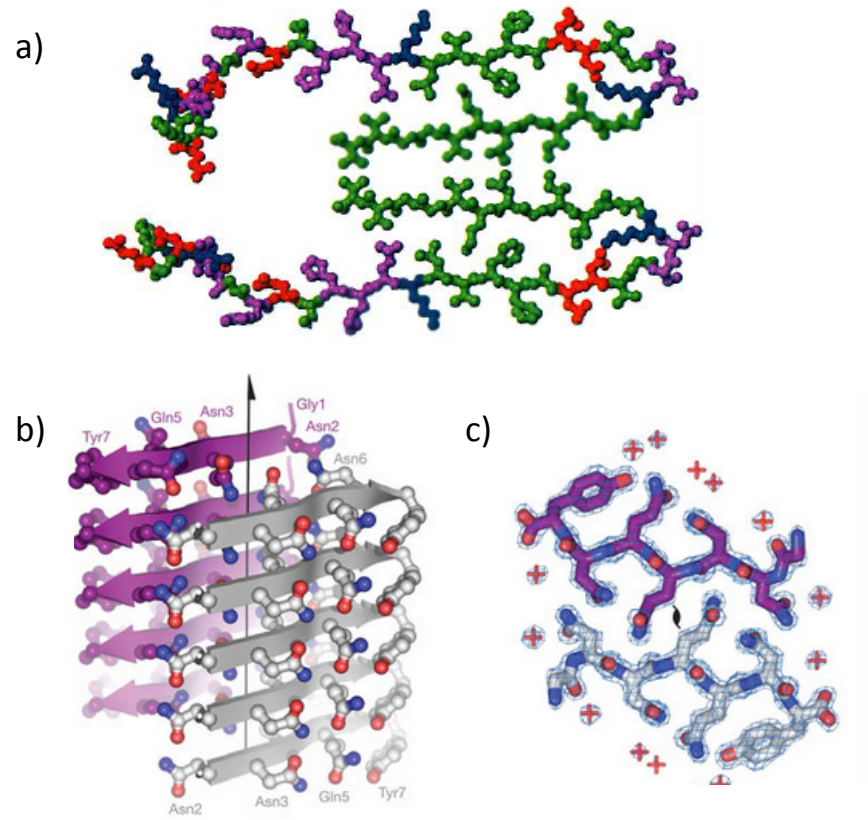

Figure 2.1 Proposed extended β-strands of amyloid fibrils. (a) Cross-section of an $A\beta_{1-40}$ fibril with hydrophobic residues in the interior of the fibril and hydrophilic residues on the fibril's exterior (64), (b) Structure of the fibril forming GNNQQNY peptide, a small segment from the yeast protein Sup35 (65) and (c) top-view view of (b) showing the difference in electrostatic charge between the fibril interior and exterior.

The structure of amyloid fibrils has been extensively studied. While TEM images can provide information about the width and length of fibrils (after negative staining), typically they cannot give information regarding the handedness or 3D morphology of the fibrils (68, 62). To accomplish this high-resolution scanning using SEM, STM and AFM have been used and found to be very suitable for determining helicity and fibril height (69). Visualization of $A\beta_{1-40}$ (68, 70, 71), β-lactoglobulin (62), hen lysozyme (68) and SAA_{1-12} (68) amyloid aggregates using TEM and AFM show they form fibrils with easily identifiable helical twists.

It has been suggested that the order and directionality of stacked aromatic residues in amyloidogenic peptides (*i.e.*, tyrosine, tryptophan, phenylalanine) and *de novo* designed peptides can act as a thermodynamic driving force for the formation of amyloid and amyloid-like fibril assembly (41, 5, 6, 72). The aromatic component to these *de novo* designed peptides comes from aromatic amino acids phenylalanine and tyrosine. Tenidis *et al*. studied the short peptides FGAIL and NFGAIL, penta- and hexa-peptide sequences found within a longer 37 amino acid sequence called islet amyloid polypeptide (IAPP) which is associated with type II diabetes (73). Not only did they see that these substantially shorter peptides formed amyloid fibrils structurally similar to their parent peptide sequences, but that dropping phenylalanine from the shorter sequences resulted in no amyloid fibril formation. Table 2.1 below lists reported shorter sequences of longer amyloid forming peptides that still form amyloid fibrils similar to their parent peptides. A systematic study performed by Gazit *et al*. (2001) demonstrated that in short (7 amino acid) peptide fragments substituting phenylalanine out of the sequence for non-aromatic amino acids took away a peptides ability to form fibril aggregate (72).

Parent peptide	Disease	Shorter sequence	Reference
Medin	Aortic medial amyloid	N<u>F</u>GSVQ	(74)
		N<u>F</u>GSV	(74)
Type II diabetes	Islet amyloid polypeptide	N<u>F</u>GAIL	(73)
		N<u>F</u>LVH	(73)
Human calcitonin	Medullary thyroid carcinoma	D<u>F</u>NK<u>F</u>	(75)
		D<u>F</u>NK	(75)
β-amyloid peptide	Alzheimer's	KLV<u>FF</u>AE	(76)
Sup35p	Yeast prion protein	GNNQQN<u>Y</u>	(77)

Table 2.1 Amyloid fibril forming peptide sequences derived from longer peptide sequences. Aromatic amino acids (tryphophan and phenylalanine) are underlined.

Chapter 1 briefly highlighted ordered supraomlecular systems composed of NDI-NDI off-set parallel stacking. In some of these examples (Table 1.1, *Entry 1*,*4*,*5*,*7*) hydrophobic and favorable electrostatic interactions between NDI-appended peptide monomers resulted in the formation of 1D fibrils. Circular dichroism of these aggregates suggested that adjacently stacked NDIs were slightly twisted relative to one another. This was corroborated when AFM studies revealed the fibrils had regular helicities. Interestingly, although the two systems are quite different, the fibril morphology and structure of the NDI-peptide fibril aggregates was similar to the morphology and structure of amyloid fibrils.

In 1995 Scott Lokey developed the first abiotic molecule to self-assemble into a defined secondary structure in water using aromatic interactions (78). These foldamers were initially called *aedamers* (*a*romatic *e*lectron *d*onor-*a*cceptor folda*mers*). Solid-phase chemistry was used to link amino acid-like DAN and NDI monomers (both with aspartic acid side chains) in an

alternating fashion to yield foldamer **1** as shown in Figure 2.2a. In aqueous solution **1** was shown to fold intramolecularly in on itself forming a pleated structure such that the DAN and NDI aromatic faces were in a face-centered stacked orientation (Figure 2.2b). This not only minimized their exposure to solvent, but also maximized favorable electrostatic interactions. Due to the DAN-NDI face-centered stacking geometry, mixing of atomic orbitals occurs leading to a CT complex with a characteristic red-purple color. Furthermore, while UV-Vis spectroscopy showed hypochromism (or the decrease in absorption of light by a chromophore) upon comparing **1** to its monomeric counterparts upfield shifts in the ^{1}H NMR spectra of **1** were also suggestive of a pleated structure.

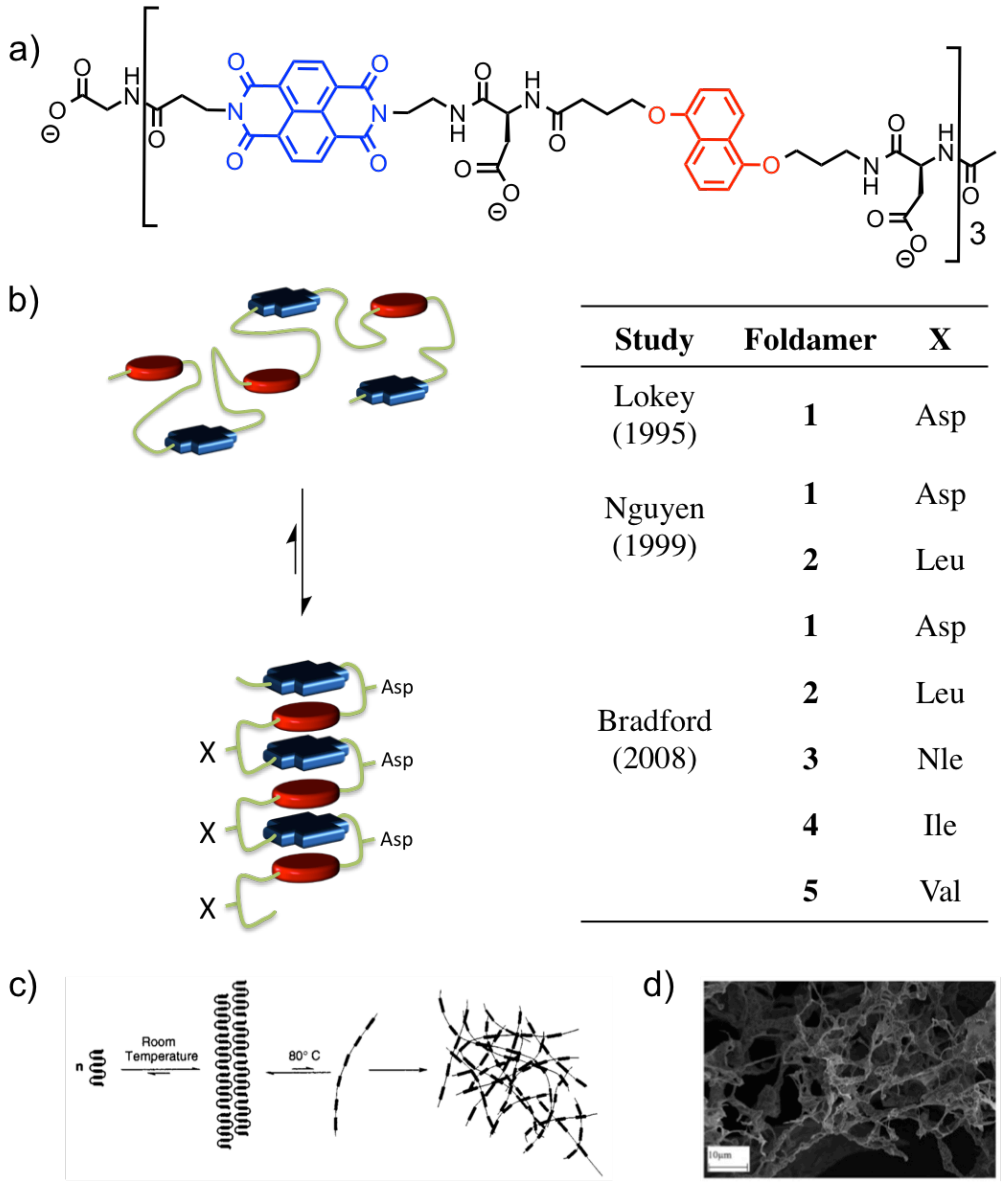

Study	Foldamer	X
Lokey (1995)	**1**	Asp
Nguyen (1999)	**1**	Asp
	2	Leu
Bradford (2008)	**1**	Asp
	2	Leu
	3	Nle
	4	Ile
	5	Val

Figure 2.2 Aromatic donor-acceptor foldamers synthesized by the Iverson group. (a) Generic structure of the hexameric aromatic donor-acceptor foldamer; (b) Cartoon representation of face-centered stacked DAN-NDI foldamer assembly mechanism in aqueous solutions (blue unit = NDI, red unit = DAN) showing the type of foldamer derivatives realized; (c) Proposed aggregation mechanism of **2** (79); (d) SEM images of the highly ordered network of aggregated **2** (80). Asp = aspartic acid, Leu = leucine, Nle = norleucine, Ile = isoleucine, Val = valine. Adapted with permission from (79) and (80). Copyright (1999) and (2008) American Chemical Society.

Encouraged by Lokey's results, Nguyen and Iverson derivatized the basic structure of **1** by replacing three of the aspartic acid residues with hydrophobic leucine residues (79). This yielded structurally amphiphilic foldamer **2** that has similarities to the luecine zipper motif found in proteins. Interestingly, upon heating an aqueous solution of **2** at 80 °C the CT absorbance disappeared and the foldamer solution formed an aggregated, self-supporting hydrogel. In addition, the hydrogelation was shown to be nucleation-dependent. Heating **1** at the same temperature did not show any hydrogelation effect indicating that amphilicility is a requirement for hydrogel formation. Nguyen proposed a model of aggregation wherein the foldamer structure unfolds upon heating and subsequently becomes entangled to create a highly disordered network with other unfolded foldamers (Figure 2.2c).

Further modification of the foldamer structure by Bradford and Iverson afforded amphiphilic foldamers **3** - **5** containing constitutional isomers isoleucine, norleucine and valine to probe how changes in hydrophobicity affected folding behavior (see Figure 2.2b) (80). Prior to heating, **3** - **5** exhibited UV-Vis spectra characteristic of the alternatively stacked, pleated structures of **1** and **2**. Consistent with **2**, norleucine and isoleucine foldamer derivatives (**3** and **4**, respectively) both formed self-supporting hydrogels at 80 °C with subsequent loss of the CT absorbance band after heating. Examination of the aggregated hydrogel state of **2** - **4** by circular dichroism (CD) revealed that the aggregated state was actually due to *highly ordered intermolecular assembly*. These findings were corroborated by SEM images of the aggregates that showed highly ordered web-like morphologies as seen in Figure 2.2d! This behavior was seen as being conceptually analogous to the amyloid formation process in proteins.

2.3 RESULTS

2.3.1 Foldamer Selection and Synthesis

In addition to amphiphilic foldamer **2**, two additional foldamers were synthesized: a tetramer derivative and an octamer derivative (see Figure 2.3). For the rest of this Chapter the

foldamer derivatives will be referred to as **2h** (hexamer), **2t** (tetramer) and **2o** (octamer). The foldamer derivatives were synthesized using Fmoc solid phase peptide synthesis chemistry using monomers that were previously reported (80).

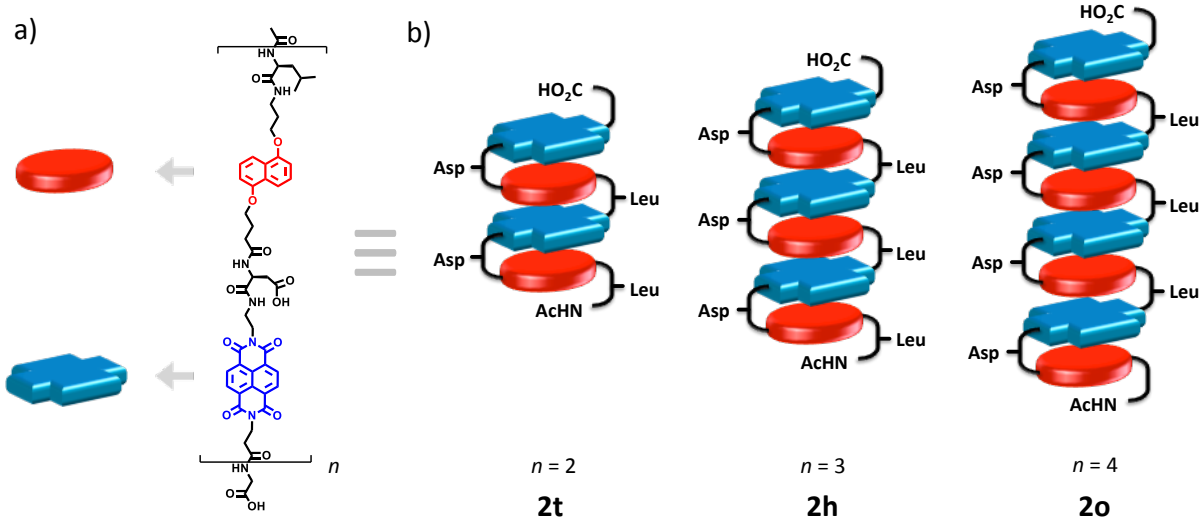

Figure 2.3 (a) Structure of amphiphilic foldamers and (b) cartoon representations of tetramer (**2t**), hexamer (**2h**) and octamer (**2o**) in the pleated structure (Asp = aspartic acid, Leu = leucine).

2.3.2 Hydrogelation

As expected, heating a 2.0 mM solution (~ 0.50 weight %) of **2h** at 80 °C for 90 minutes yielded a self-supporting hydrogel with subsequent loss of the purple CT absorbance band. Pleasantly, heating **2t** (2.0 mM solution) at 80 °C for 90 minutes formed a self-supporting hydrogel with subsequent loss of the CT band. Attempts to form self-supporting hydrogels of **2o** at multiple concentrations (0.1 to 4.0 mM) over multiple temperatures (60 to 80 °C) and times (1.5 to 24 hrs) were unsuccessful.

2.3.3 UV-Visible Spectroscopy

UV-Vis spectra of **2h** prior to heating showed a broad CT band in the visible region (λ_{max} 526 nm) and several peaks in the UV region indicative of electronic transitions across the NDI long axis (300, 360, 380 nm) (Figure 2.4a). Disappearance of the CT band after heating occurs along with a slight decrease in hypochromism in the far-UV region. Foldamer **2t** showed a similar UV-Vis spectrum prior to heating, with peaks at 300, 359 and 380 nm in the far-UV and a broad CT band (λ_{max} 526 nm) in the visible region (Figure 2.4b). Heating of **2t** also resulted in loss of the CT band, with a slight decrease in hypochromism in the far-UV. Foldamer **2o** showed similar UV-Vis peaks at 298, 364 and 382 nm in the far-UV and a broad CT band (λ_{max} 529 nm) in the visible region with a slight decrease in hypochromism observed in the far-UV. In conrast, heating **2o** did not result in disappearance of the CT band (Figure 2.4c)

The appearance of a new peak after heating, formerly a shoulder, at 219 (**2h**), 223 (**2t**) and 221 nm (**2o**) was thought to correspond to electronic transitions across the NDI short axis. To investigate the origin of this peak, aqueous-soluble DAN and NDI derivatives were synthesized and titration experiments were conducted. DAN monomer was titrated into a solution of NDI monomer and UV-Vis spectra of varying equivalents of the monomers were collected (Figure 2.5). UV-Vis spectra of only NDI in solution showed peaks at 231, 359 and 379 nm while UV-Vis spectra of only DAN in solution showed peaks at 221 and 294 nm. Upon titration of DAN into a solution of NDI a peak corresponding to electronic transitions across the NDI short axis at 232 nm was overtaken by a peak at 222 nm corresponding to DAN electronic transitions.

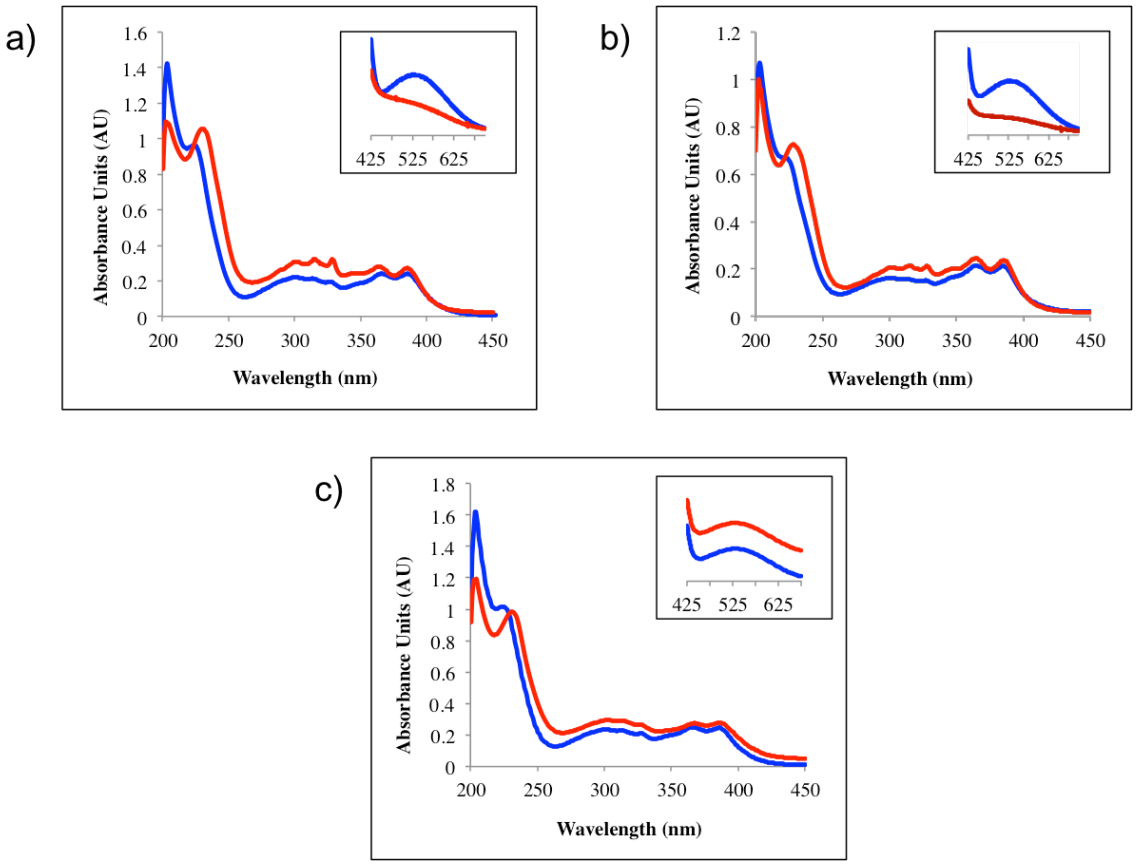

Figure 2.4 UV and Visible spectra of (a) **2h**, (b) **2t** and (c) **2o** before (blue) and after (red) heating at 80 °C for 90 min. Inset spectra show the visible region of the foldamers. Foldamer concentrations are 15 μM and 2.0 mM in a 50 mM sodium phosphate buffer for UV and Visible spectroscopy, respectively.

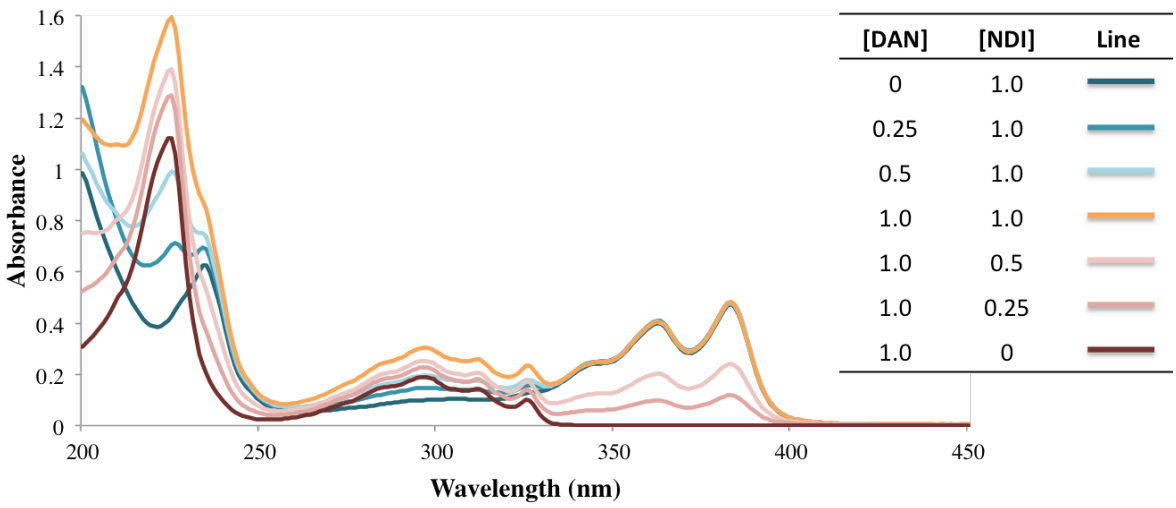

Figure 2.5 DAN and NDI monomer titration experiment. Concentration (in mM) ratios of DAN and NDI are given in the table. As the ratio of DAN to NDI increases to 1:1, peak corresponding to electronic transitions across NDI short axis (232 nm) becomes a shoulder of larger peak at 223 nm corresponding to electronic transitions across DAN.

2.3.4 Circular Dichroism

Investigation of foldamers **2h**, **2t** and **2o** by CD showed minimal signals in the near UV and none in the far UV prior to heating. The three foldamer solutions were then heated to 80 °C for 90 min to facilitate the aggregation process. After heating, strong bisignate couplet signals appeared for **2h** and **2t**, with the null occurring at 215 and 235 nm, respectively, indicative of exciton Cotton effects along the NDI y-polarized (short) transition axis (Figure 2.6a-b) (81, 46). For **2o**, a large negative CD peak was observed at 235 nm, however, no bisignate signal was observed (Figure 2.6c). Moderate signals at 325, 360, and 390 nm also appeared for **2h**, while **2t** gave moderate signals at 310, 353, and 390 nm. Both of these correspond to electronic transitions along the NDI z-polarized (long) transition axis. Although a slightly enhanced signal was observed for **2o** at 326 nm after heating, no other signals similar to those observed for **2h** and **2t** were seen. When the UV spectra are compared to the CD spectra, the newly emerged peak in the

aggregated state of foldamers **2h** and **2t** nearly intercept the null of the bisignate Cotton effects. (Figure 2.7a-b).

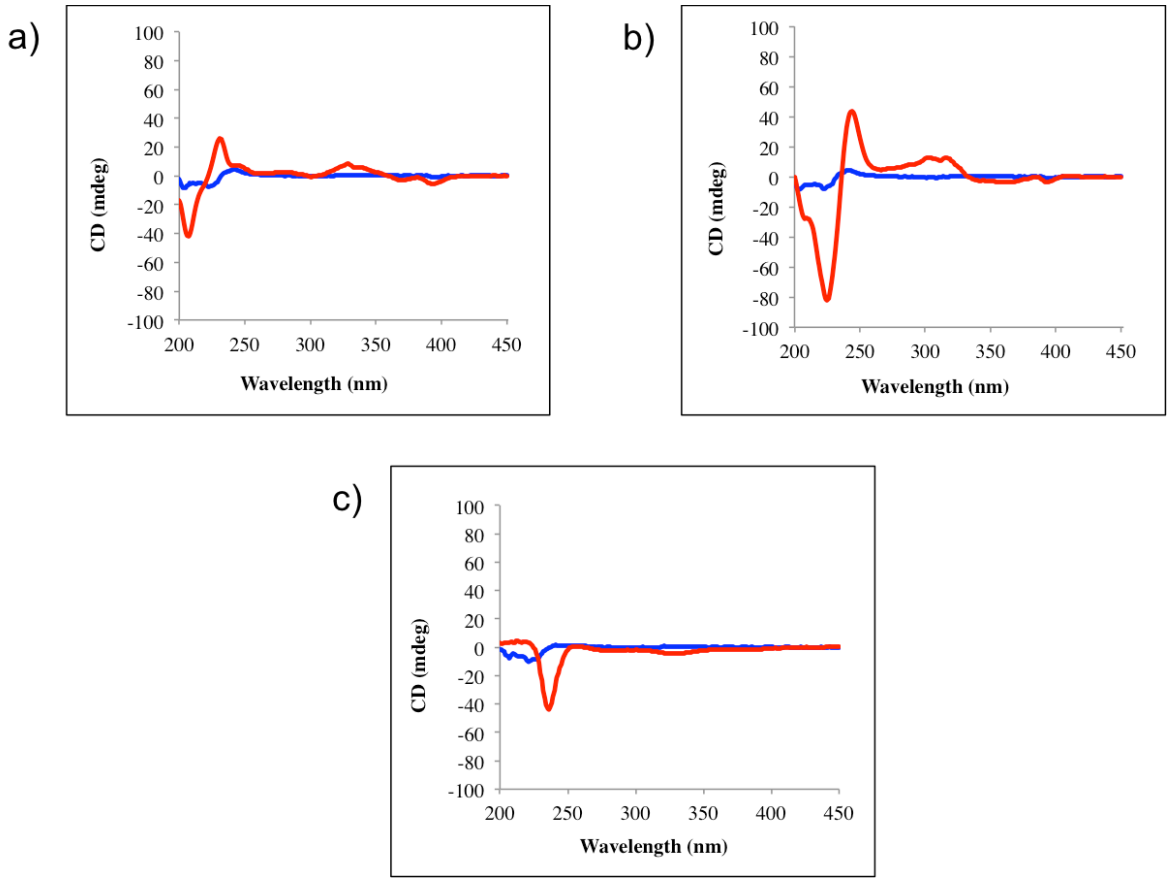

Fixure 2.6 CD spectra of (a) **2h**, (b) **2t** and (c) **2o** before (blue) and after (red) heating at 80 °C for 90 min. Foldamer concentrations are 0.2 mM in a 50 mM sodium phosphate buffer.

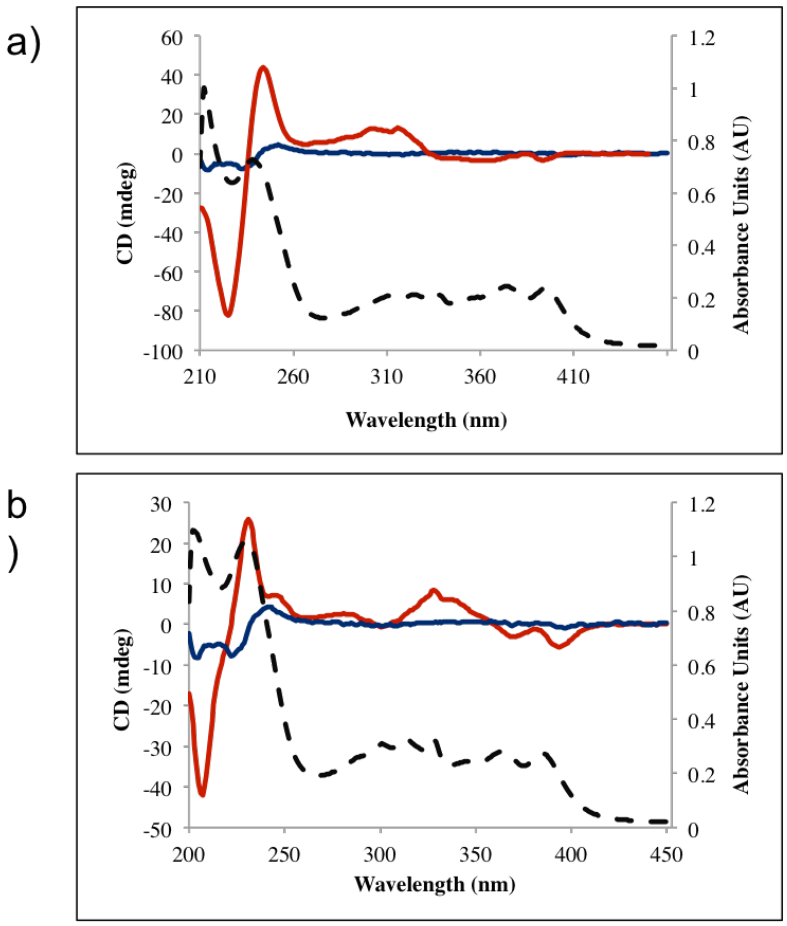

Figure 2.7 CD spectra of foldamers overlaid on UV spectra of foldamers. (a) Overlay for **2h** and (b) overlay for **2t**. CD before heating (blue line), and CD after heating (red line), UV after heating (dashed black line).

2.3.5 Transmission Electron Microscopy

To our surprise, 1D fibrils were observed by transmission electron microscopy (TEM) after heating solutions of **2h** and **2t** to the aggregated state and staining with 2% uranyl acetate. No fibrils were observed for **2o** after heating at multiple temperatures and times. Importantly, fibril formation was also observed in the same samples used for CD analysis proving the existence of highly ordered aggregation in the CD spectra. As shown in Figure 2.8, negatively stained aggregated samples revealed fibrils with uniform widths up to a micrometer in length for **2h** and **2t** (Figure 2.8a-b). While TEM images of **2h** showed fibrils with a diameter of 10.5 ± 1

nm, **2t** revealed fibrils of 7.5 ± 1 nm in diameter. As shown by TEM, the fibrils tend to "stick to" and "wrap around" each other, indicating some extent of inter-fibril interaction (Figure 2.8c-d). The presence of 1D fibrils indicates the requirement for 1D growth in the aggregated foldamer structure.

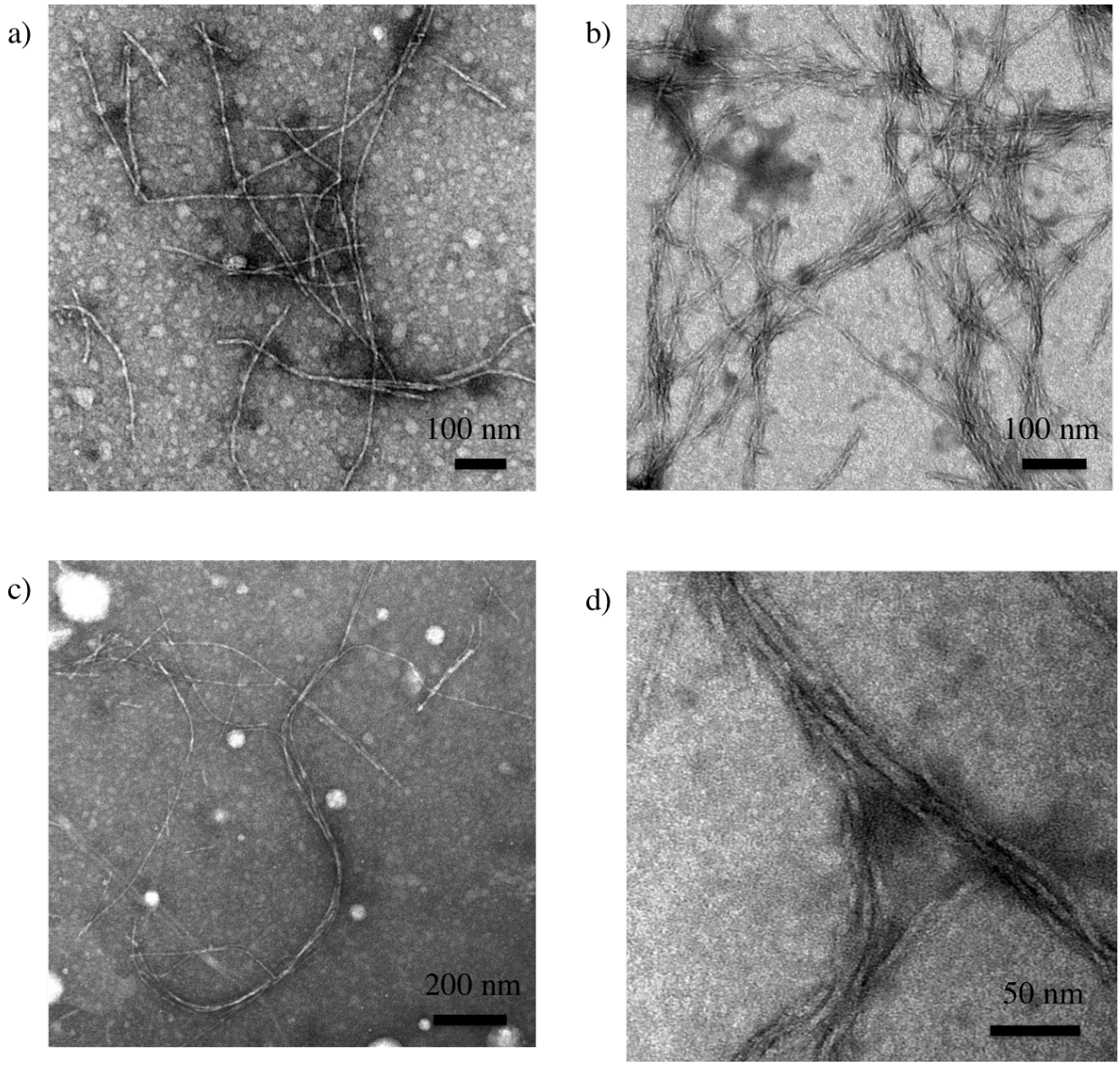

Figure 2.8 TEM images of foldamers (2% uranyl acetate staining on carbon/Formvar grid). (a) TEM of **2h**, (b) TEM of **2t**. "Stick-and-wrap" behavior of (c) **2h** and (d) **2t**.

2.3.6 Atomic Force Microscopy

In order to gain additional insight into the fibril morphology, tapping-mode atomic force microscopy (AFM) was utilized. Deposition of the foldamer aggregates onto freshly cleaved mica revealed 1D fibrils similar to those observed by TEM for **2h** and **2t**. Both foldamer aggregates showed fibrils with regular helicity with a pitch of ~170 nm for **2h** and ~150 nm for **2t** (Figure 2.9a-b). While **2h** had a height profile of 5.5 ± 1 nm, **2t** showed a height profile of 4 ± 1 nm, both approximately one-half of the fibril width observed by respective TEM images. An additional AFM phase image for **2h** is shown in Figure 2.9c while a 3D topography image of **2h** is shown in Figure 2.9d. Differences in fibril width between TEM and AFM may be attributed to compression of the aggregate sample by the AFM tip or due to AFM tip and/or cantilever geometry (41, 62).

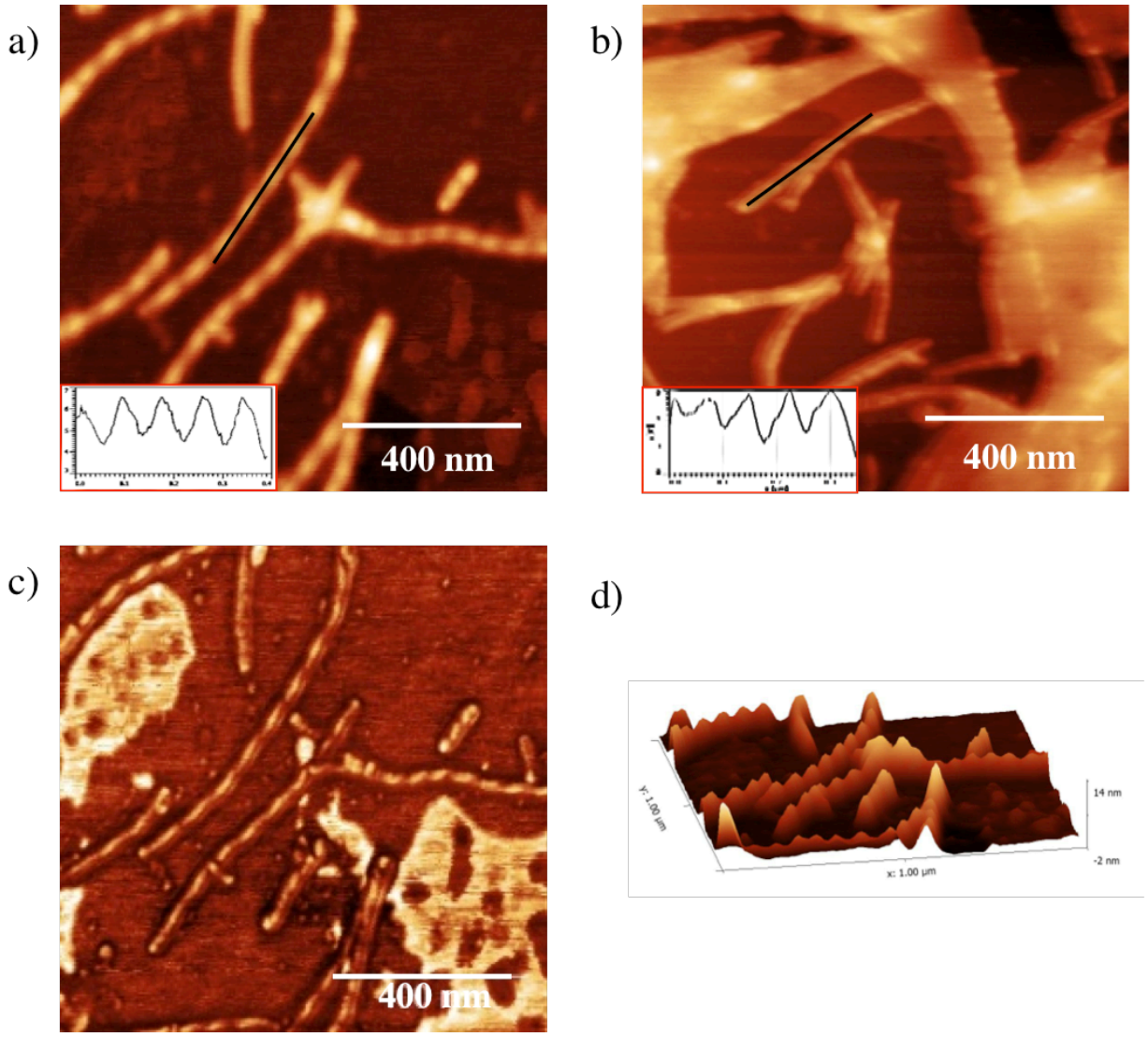

Figure 2.9 AFM images of foldamers (freshly cleaved mica). (a) AFM of **2h**, (b) AFM of **2t**, (c) phase image of (a) which better shows the helicity of the fibrils, (d) 3D image of **2h** nicely illustrating the helical pitch along the fibril backbone.

2.3.7 Seeding Experiments

Seeding experiments of **2t** and **2o** were performed in order to determine if foldamer length had any effect on catalyzing the conformational change of the foldamers at lower temperatures. Previous seeding-experiments were done on **2h** derivatives and revealed intermediate aggregated structures (80). Seeding room temperature foldamer solutions with 10% w/v pre-aggregated (or in the case of **2o**, pre-heated) material followed by 14 day wait period at 27 °C again gave a level of intermediate aggregation. Prior to heating, all foldmaers looked

similar with minimal signals in the far- UV and no signals in the near-UV regions. After 14 days with pre- aggregated material, higher amplitude signals were observed for all foldmaers in the far-UV but no signals were seen in the near-UV (Figure 2.10a-c). Interestingly, CD spectra of aggregated **2h** and **2t** looked similar while that of aggregated **2o** differs in both the near- and far-UV regions. While **2t** shows a strong positive bisignate exciton effect (null at 235 nm) in the far-UV, **2o** shows a negative signal centered at 230 nm. The near-UV of **2t** shows similar Exciton Cotton effects as **2h** (positive signal at 320 nm, negative signals at 360 and 390 nm).

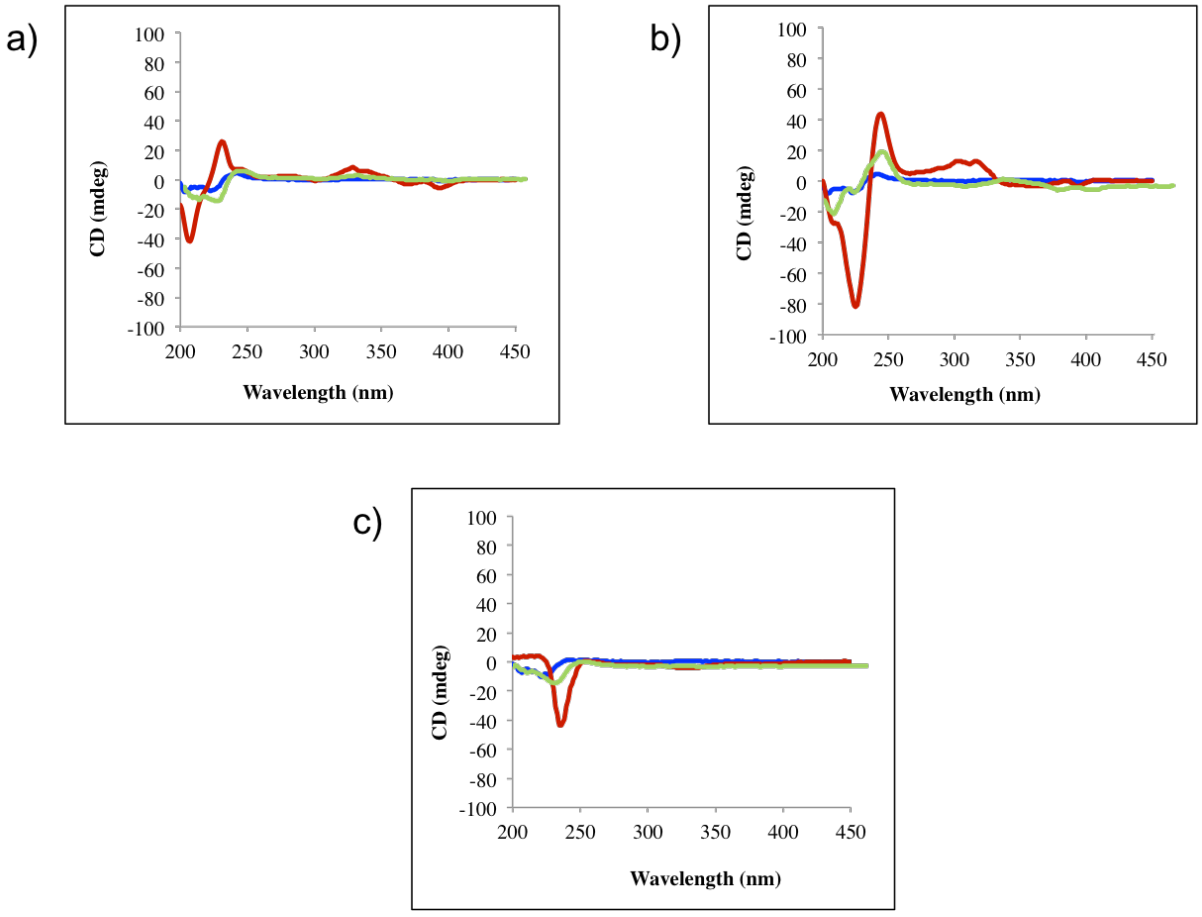

Figure 2.10 CD spectra of foldamers (a) **2h**, (b) **2t** and (c) **2o** before heating (blue), after heating at 80 C for 90 min (red) and after 14 days at 27 °C with 10% (w/v) pre-aggregated material (green).

2.3.8 Solid State NMR

Further attempts to investigate the foldamer aggregate were performed using solid state (SS) ^{13}C and ^{1}H magic angle spinning (MAS) NMR. Samples were prepared by heating 2.0 mM solutions of **2h** in the typical buffer solution within glass NMR tubes. After formation of the hydrogel, the glass tubes were pulled close and SS NMR data was collected by Dr. Vladimir Bakhmutov at Texas A&M University. Unfortunately, long term (2 day) pulse ^{13}C NMR and ^{1}H MAS NMR experiments did not yield any signals representative of our foldamer system (Figure 2.11a-d).

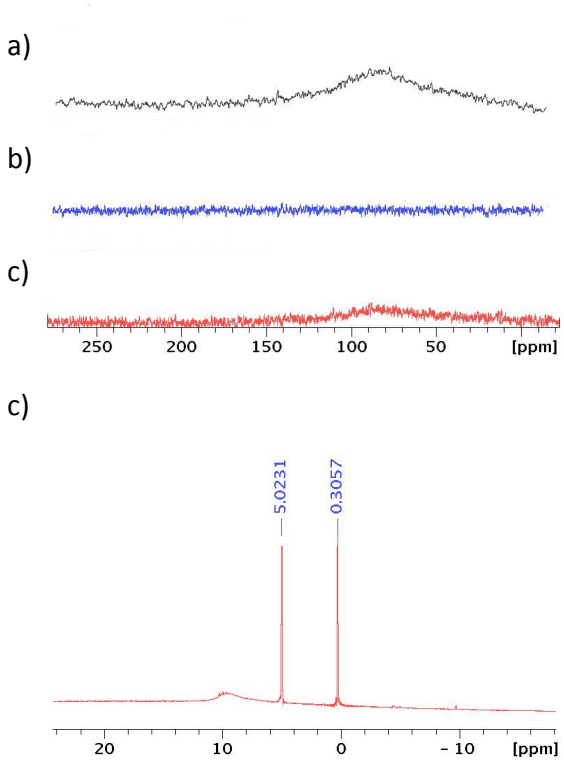

Figure 2.11 ^{13}C MAS NMR spectra recorded at a spinning rate of 2 kHz. (a) ^{13}C MAS spectrum with direct excitation of ^{13}C nuclei (the wide line is coming from the NMR probe), (b) ^{13}C Cross-polarization MAS spectrum, (c) ^{13}C MAS spectrum without ^{1}H decoupling, (d) ^{1}H MAS NMR spectrum. Samples were heated to the hydrogel state and run in 50 mM sodium phosphate buffer.

2.3.9 X-Ray Diffraction

Inspired by insightful X-Ray diffraction (XRD) patterns of 1D fibrils formed from NDI-peptide aggregation by Shao and Parquette (2010) (82) XRD studies of the foldamers were performed. Samples were prepared by centrifuging hydrogel solutions of **2h** with subsequent deposition of the collected solid material onto quartz slides. Unfortunately, only a large, broad diffraction from 20 - 40 two-theta (characteristic of an amorphous material) was observed (Figure 2.12). Several attempts to collect diffraction data on more concentrated samples did not yield any useful results.

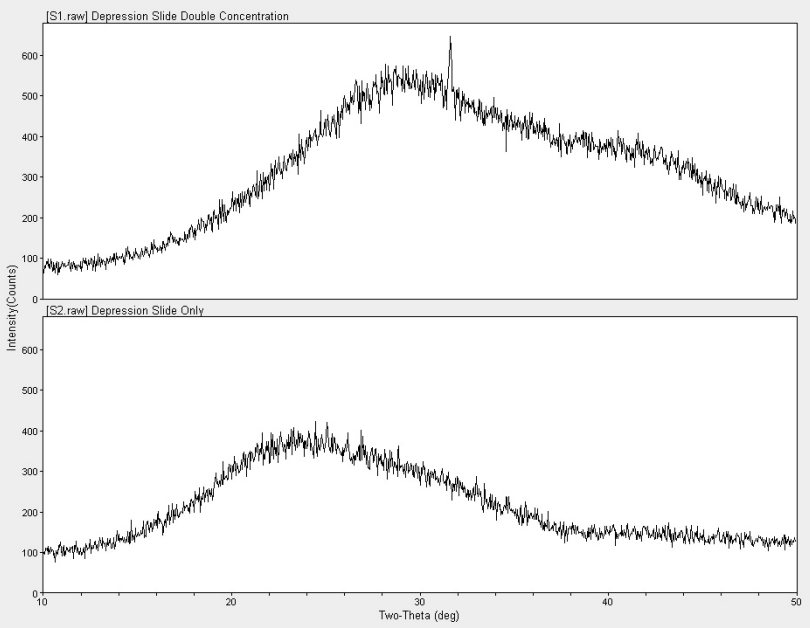

Figure 2.12 X-Ray diffraction pattern of **2h** on quartz giving unresolved peaks.

2.4 DISCUSSION

2.4.1 Fibril Morphology

When the UV spectra are compared to the CD spectra, the newly emerged peak in the aggregated state of foldamers **2h** and **2t** nearly intercept the null of the bisignate Cotton effects, strongly indicative of NDI self-assembly (Figure 2.7a-b) (43, 81, 86). In systems composed of

self-assembling NDI monomers or NDI-containing peptides, this overlap of the bisignate Cotton effect in the near-UV is representative of off-set stacked NDI-NDI assembly (40, 41, 81, 82, 83).

The fibril twisting observed by AFM is consistent with helical, off-set parallel-displaced NDI-NDI interactions seen in previous work with NDI monomers (40, 82). Importantly, the measured fibril widths of 11 nm and 7.5 nm are each in agreement with the calculated extended lengths of **2h** and **2t**, respectively. Coincidentally, the twisted-ribbon fibril morphology of the foldamer aggregate is similar to that of a twisted-ribbon structure often found in aggregated amyloid proteins (62, 68, 84).

Off-set parallel displaced NDI-NDI interactions leading to highly ordered aggregates have been shown in numerous studies using CD spectroscopy of NDI monomers (40, 82, 9, 41, 30, 31, 32, 8, 85, 45, 86). As stated previously, it has been suggested that the order and directionality of aromatic stacking interactions in amyloidogenic peptides and *de novo* designed peptides can act as a thermodynamic driving force for the formation of amyloid and amyloid-like fibril assembly (5, 6, 87). Also interesting is the requirement for amphiphilicity in the formation of one-dimensional fibril-containing structures as seen in both abiotic and biotic systems (88). Based on this information, it is proposed that while aromatic NDI-NDI interactions facilitate 1D fibril growth in the aggregated structure, the amphiphilic nature of the molecule contributes to the thermodynamic driving force for fibril formation.

2.4.2 Proposed model

A proposed model for the foldamer aggregated structure and formation based on the bisignate CD signal, the 1D fibrils observed by TEM and the fibril twisted-ribbon shape by AFM is proposed in Figure 2.13. Upon heating, unfolding of the foldamer DAN-NDI pleated aromatic structure occurs, as evidenced by disappearance of the CT band. Reorganization of the core aromatics in the aggregated structure into a stable fibril is believed to be initiated by NDI-NDI off-set parallel-displaced stacking the between NDI units of the two oligomers. More unfolded

oligomers assemble as the nucleation process continues, so that a relatively stable ribbon is formed. Assembly continues in one-dimension, leading to an amphiphilic ribbon structure in which all hydrophobic leucines organize on one surface and the hydrophilic aspartates are arranged on the other (Figure 2.13a). Based on the amyloid fibril assembly, it is proposed that dimerization of the sheets occurs to sequester the hydrophobic leucine surfaces on the interior of a pseudo bilayer assembly, juxtaposing the hydrophilic aspartates on the exterior (Figure 2.13b). The assembled duplex ribbon grows in length until it becomes the fully assembled fibril observed in the TEM and AFM studies. The spatial organization of the DAN units in the fibril structure are presently not proposed because there is no direct spectroscopic data that defines their relative orientations.

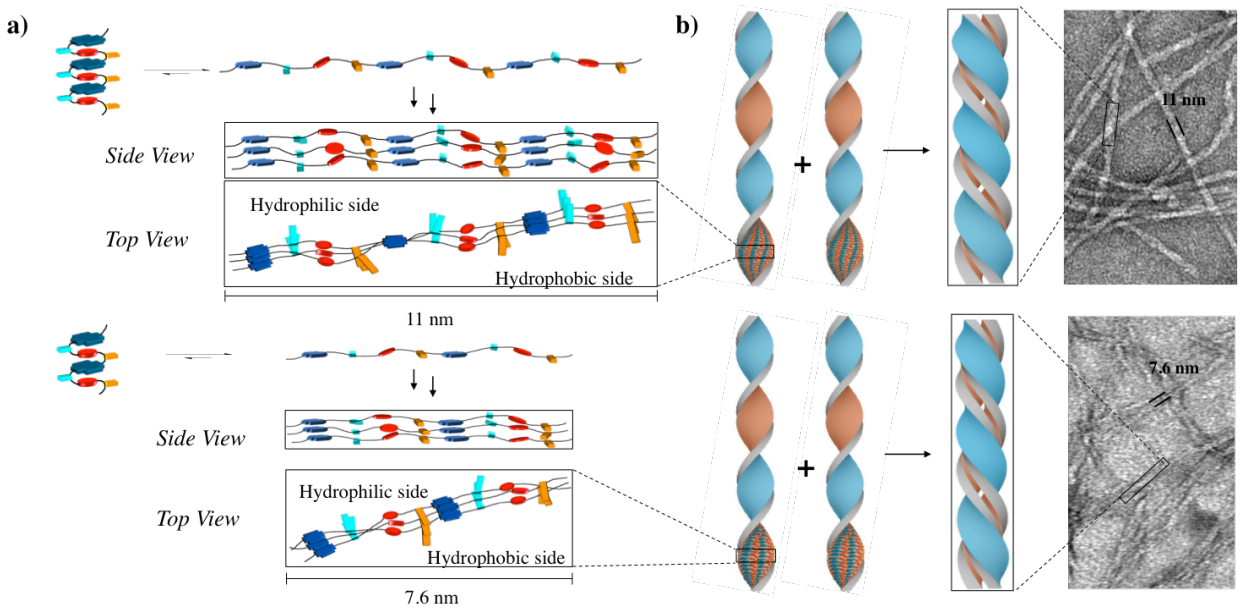

Figure 2.13 Proposed model (**2h** top, **2t** bottom) describing how the pleated amphiphilic foldamer undergoes a conformational change to self-assembled one-dimensional fibrils (89). (a) Upon heating, unfolding of the pleated DAN-NDI structure (light blue and orange rectangles represent aspartate and leucine side chains, respectively) occurs to form a new structure that self-assembles around offset NDI-NDI stacking. The resulting ribbon has a hydrophilic side and a hydrophobic side; (b) Dimerization of the amphiphilic ribbons is proposed to sequester the hydrophobic leucine face on the interior and juxtaposes the hydrophilic aspartate face on the exterior of the fibril.

2.4.3 Length Dependence

Foldamers **2t**, **2h**, and **2o** were designed to investigate the activation energy required for hydrogelation. The lack of hydrogelation seen with 2o at 80 °C may indicate that higher temperatures are needed. Unfortunately, 100 °C is the highest the foldamer solutions (due to the aqueous solvent) can be heated but the fact prolonged times at elevated temperatures did not cause **2o** hydrogelation is also interesting. In light of our proposed aggregation model, the inability of **2o** to form fibrils is most likely because the activation energy for unstacking of the aromatic DAN-NDI face-centered interactions is not reached at 80 °C as shown by the CT band still being present. Based on the large negative Cotton effect observed in the CD of heated **2o**, however, some intermediate aggregate is likely to be forming.

2.4.4 Requirements for fibril formation

It appears that at least three features are required for an abioitic molecule to exhibit the kind of conformational switching, reminiscent of amyloid fibril formation, observed here. First, there must be a kinetically stable initial folded structure that is based largely on intramolecular interactions. In the case of amphiphilic foldamer 1, the kinetically folded structure is based on intramolecular alternating DAN-NDI stacks. Second, there must be an alternative aggregated state possible that involves an unfolded conformation. For **2h**, it has now been shown that this alternative mode of aggregation between unfolded chains involves NDI-NDI interactions. Third, there must be amphiphilicity present so that this alternative mode of interchain aggregation leads to formation of both a hydrophobic face and a hydrophilic face in the growing aggregate.

Stabilization of the fibril comes when two of the hydrophobic faces interact to create a fully desolvated hydrophobic interior and hydrophilic outer faces in a pseudo bilayer arrangement. One could propose that it is the desolvation of the considerable hydrophobic interior of the growing fibrillar assembly that provides the ultimate driving force for the

thermodynamic stability of the fibril. Note there is likely a length dependence to this stability that explains why nucleation kinetics (i.e. a lag in fibril formation upon heating) is a hallmark of this process. During the lag (nucleation) phase, intermediates form and disassemble until the critical length is achieved, after which the fibril forms by quickly adding unfolded chains to each end of the now thermodynamically stable structure.

2.5 CONCLUSIONS

The face-centered geometry observed in the amphiphilic foldamer prior to heating is correctly predicted by the work of Wheeler when one considers the maximization of complementary interactions between the relatively electron-rich DAN oxygen atoms and relatively electron-deficient NDI carbonyl carbon atoms in the stacked structure. The same considerations also predict strong complementary interactions between the highly polarized carbonyls of two off-set stacked NDI molecules, i.e. the carbonyl oxygen of one NDI carbonyl interacting with the carbonyl carbon of the adjacent NDI.

This unique proposed conformational switching process - from an aromatic DAN-NDI foldamer to an aromatic NDI-NDI fibril-forming aggregate - illustrates a new model of self-assembly behaviour. Nevertheless, this proposed desolvation model can be seen as analogous to the proposed dimerization of $A\beta_{1\text{-}40}$ cross stand β-sheets described earlier (64). Interestingly, for our aggregated amphiphilic foldamer structure and for proteins and polypeptides in the amyloid state, there exists a strong requirement to shield the more hydrophobic residues on the interior of a two-strand dimer while juxtaposing the more hydrophilic residues in the solvent-exposed exterior. In this light, our material bridges the gap between biotic proteins and polypeptides that form amyloid and synthetically derived, abiotic molecules that form highly ordered 1D fibril aggregates.

2.6 EXPERIMENTAL

General methods

All commercially available chemicals were purchased from Aldrich, Fisher Scientific or Novabiochem/EMD/Merck unless otherwise indicated. ^{1}H and ^{13}C NMR spectra were taken on a Varian Unity Plus 400 spectrometer at 400 MHz in $CDCl_3$ or d_6-DMSO. All amphiphilic foldamer purification was done on a Waters HPLC system equipped with a 2996 photodiode array detector and Grace-Vydac C18 peptide semi-preparatory reverse phase column. Transition electron microscopy (TEM) was performed on a FEI Tecnai microscope operating at 80 kV. Circular dichroism (CD) was done on a Jasco J-815 circular spectropolarimeter. Atomic force microscopy (AFM) was taken on a Digital Instruments Dimension 3100 atomic force microscope with silicon tips (NSC14/AIBS, MicroMasch) in tapping mode.

UV-Vis spectroscopy

Ultraviolet-Visible (UV-Vis) spectroscopy was performed on a Perkin-Elmer Lambda 35 spectrophotometer. Foldamer solutions (50uM for UV; 0.2mM for Vis) were observed in a 50mM sodium phosphate buffer with 100mM NaCl added and pH adjusted to 7.0. A 1 cm cuvette was used and initial spectra were observed at room temperature (27°C). Samples were then heated in a 80°C oil bath for 2 hours, cooled at room temperature for 30 min and then final spectra were recorded. All samples were filtered using a 0.45 μm nylon filter prior to recording spectra.

Circular Dichroism

Circular dichroism (CD) experiments were performed on a Jasco J-815 circular spectropolarimeter and all spectra were collected using a 1mm quartz cell. Samples (0.2m) were dissolved in a 50mM sodium phosphate buffer with 100mM NaCl, pH adjusted to 7.0 and initial spectra were recorded at 27°C. Samples were then heated to 80°C for 90 min using a Jasco-equipped Peltier temperature controller and final spectra were recorded after allowing the

samples to cool to room temperature for 30 min. All samples were filtered using a 0.45 μm nylon filter prior to recording spectra.

Atomic Force Microscopy

Atomic force microscopy (AFM) was taken on a Dimension 3100 atomic force microscope with silicon tips (NSC14/AIBS, MicroMasch) in tapping mode. Samples were prepared by allowing a drop of the foldamer aggregated solution to dry on mica plates overnight.

Transmission Electron Microscopy

Transmission electron microscopy (TEM) images were obtained using a FEI Tecnai microscope operating at 80 kV. Samples were prepared by placing a drop of the aggregated foldamer solution onto 400 mesh carbon coated copper Formvar grids (Electron Microscopy Sciences, Inc.) for 5 minutes. Removal of the remaining solution after 5 minutes was followed by addition of a 2% uranyl acetate solution for negative staining. After allowing the stain to sit for 2 minutes it was removed and the sample was allowed to dry before analysis.

Solid Phase Peptide Synthesis

All amphiphilic foldamers were all synthesized using standard Fmoc-based solid phase peptide synthesis protocols. Our starting resin was Fmoc Wang resin and our monomers (3eq.) were Fmoc-Asp(OtBu)-NDI-CO_2H and Fmoc-Leu-DAN-CO_2H utilizing PyBOP (3 eq.) as a coupling additive and DIPEA (6 eq.) as base in NMP. Fmoc deprotection was performed using a 20% (v/v) piperidine solution in DMF. Capping with acetic anhydride (1:1 Ac_2O: CH_2Cl_2) was performed after each monomer coupling step. Cleavage of the crude foldamer off the resin was performed with a 95:5 TFA/H2O solution. RP-HPLC purification of the crude foldamers was performed on a Waters HPLC system equipped with a 2996 photodiode array detector and Grace-Vydac C18 peptide semi-preparatory reverse phase column. Mobile phase solution consisted of a gradient of 25% B to 40% B over 60 minutes, where A is 10mM ammonium

acetate buffer (pH 5.6) and B is 100% acetonitrile. Compound elution was monitored at a UV wavelength of 298nm. After lyopholization, purified foldamers were de-salted using Waters C-18 Sep-Pak cartridges.

Synthesis of Fmoc-Asp(OtBu)-NDI-CO_2H and Fmoc-Leu-DAN-CO_2H

Synthesis of the starting monomers for Fmoc-based solid phase synthesis, Fmoc-Asp(OtBu)-NDI-CO_2H and Fmoc-Leu-DAN-CO_2H, were synthesized and characterized according to previously published literature (80).

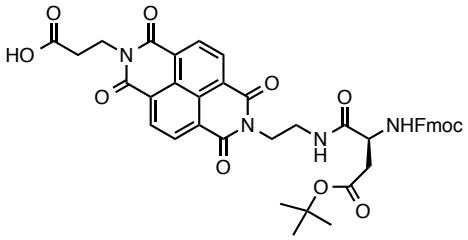

^{1}H NMR (400 MHz, DMSO-d_6): 8.54 (s, 4H), 7.70 (d, 2H), 7.57 (m, 1H), 7.37 (t, 4H), 7.26 (m, 4H), 4.35 (m, 10H), 3.15 (m, 2H), 2.96 (dd, 2H), 2.81 (dd, 2H), 1.45 (s, 9H).

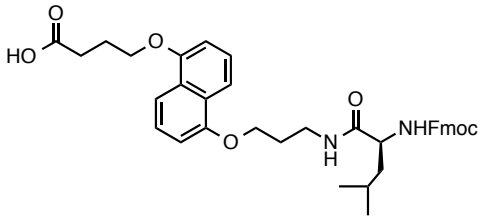

^{1}H NMR (400 MHz, DMSO-d_6): 8.05 (t, 1H), 7.88 (d, 2H), 7.72 (m, 4H), 7.50 (d, 1H), 7.34 (m, 5H), 6.93 (dd, 2H), 4.30 (m, 4H), 4.14 (m, 4H), 4.01 (m, 1H), 2.09 (q, 2H), 1.99 (q, 2H), 1.28 (t, 4H), 0.86 (m, 6H).

Tetrameric amphiphilic foldamer (2t)

The tetramer was synthesized using Fmoc-DAN-Leu-CO_2H and Fmoc-Asp(OtBu)-NDI-CO_2H monomers and followed the above stated protocol for standard Fmoc-based solid phase synthesis and RP-HPLC purification. Ac(Leu-DAN-Asp-NDI)$_2$Gly-CO_2H. ESI-HRMS (negative mode) calculated for $C_{96}H_{103}N_{13}O_{27}$ (M+2H): m/z 934.460, found 934.500.

Hexameric amphiphilic foldamer (2h)

The hexamer was synthesized using Fmoc-DAN-Leu-CO_2H and Fmoc-Asp(OtBu)-NDI-CO_2H monomers and followed the above stated protocol for standard Fmoc-based solid phase synthesis and RP-HPLC purification. Ac(Leu-DAN-Asp-NDI)$_3$Gly-CO_2H. ESI-HRMS (positive mode) calculated for $C_{142}H_{151}N_{19}O_{39}$ (M+2H): m/z 1374.911, found 1374.523.

Octameric amphiphilic foldamer (2h)

The octamer was synthesized using Fmoc-DAN-Leu-CO_2H and Fmoc- Asp(OtBu)-NDI-CO_2H monomers and followed the above stated protocol for standard Fmoc- based solid phase synthesis and RP-HPLC purification. Ac(Leu-DAN-Asp-NDI)$_4$Gly-CO_2H. ESI-HRMS (negative mode) calculated for $C_{188}H_{199}N_{25}O_{55}$ (M-2H)+: m/z 1811.361, found 1811.171.

Synthesis of monomers for UV spectroscopy titrations

Aqueous-soluble DAN and NDI monomers were synthesized and characterized according to previously published literature (90).

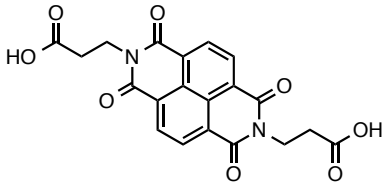

^{1}H NMR (400 MHz, DMSO-d_6): 8.68 (s, 4H), 4.28 (t, 4H), 2.63 (t, 4H).

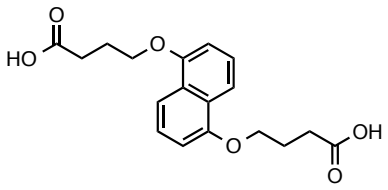

^{1}H NMR (400 MHz, DMSO-d_6): 9.90 (s, 2H), 7.55 (d, 2H), 7.19 (d, 2H), 6.82 (d, 2H), 4.23 (t, 4H), 2.42 (t, 4H), 2.13 (m, 4H).

CHAPTER 3

Head-to-tail to head-to-head solid-state polymorphism in aromatic monoalkoxynaphthalene (MAN)- naphthalimide (NI) conjugated dyads

3.1 CHAPTER SUMMARY

3.1.1 Introduction

Chapter 2 described the thermally-induced conformational change of a DAN-NDI donor-acceptor foldamer to a NDI-NDI acceptor-acceptor fibril aggregate. Using the theory of aromatic interactions described in Chapter 1, the fibril formation was rationalized due to favorable complementary electrostatic interactions between adjacent aromatic units. Chapter 3 seeks to exploit the propensity of aromatic molecules to undergo conformational switching and insert this trait into aromatic conjugated monoalkoxynaphthalene (MAN)- naphthalimide (NI) dyads. This chapter describes the solid-state polymorphism of four MAN-NI dyads and the elucidation of their packing morphologies in both head-to-tail (MAN-NI) and tail-to-tail (NI-NI) conformations.

3.1.2 Goals

The aim of this chapter is to explore the solid-state time-dependent polymorphism of four conjugated donor-acceptor dyads. The effect of the monoalkoxynaphthalene donor orientation and length of the side chains are under investigation as is the structural morphology of the two polymorphs.

3.1.3 Approach

Four donor-acceptor dyads were synthesized and their structural morphology as a result of both relatively slow and fast evaporation from solution was investigated by way of single crystal analysis and powder X-Ray diffraction (PXRD). When single crystal analysis could not be performed, modeling of the dyads based on PXRD and single crystal studies of similar dyads aided in proposing molecular structures.

3.1.4 Results

Four donor-acceptor dyads were synthesized and their packing in the solid-state from either slower (10-20 days) or faster (1-2 days) evaporation from solvent was investigated using single crystal X-ray analysis and powder X-ray diffraction. Two of the dyads exhibited tail-to-tail (A-A) packing upon slower evaporation from solvent and head-to-tail (D-A) packing upon faster evaporation from solvent. A combination of single crystal analysis and XRD patterns were used to create models wherein a packing model for the other two dyads is proposed. Our findings suggest that while side chain interactions in asymmetric aromatic dyads can play an important role in enforcing segregated D-A dyad assembly, slowly evaporating symmetrically substituted aromatic dyads allows for favorable electrostatic interactions between the aromatic moieties to facilitate the organization of the dyads in the solid-state.

3.2 BACKGROUND

The efficiency of organic material devices, such as organic light-emitting diodes (OLEDs) and organic field-effect transistors (OFETs), is intrinsically tied to the morphology of an electron donor (D) and electron acceptor (A) in the active layer of the device (91, 92, 93). When blends of D and A are cast in the active layer, non-covalent interactions, such as van der Waals interactions, charge transfer and other electrostatic interactions, play a role in defining

their supramolecular order (92). Figure 3.1 shows an ideal representation of a D/A bulk heterojuntion layer.

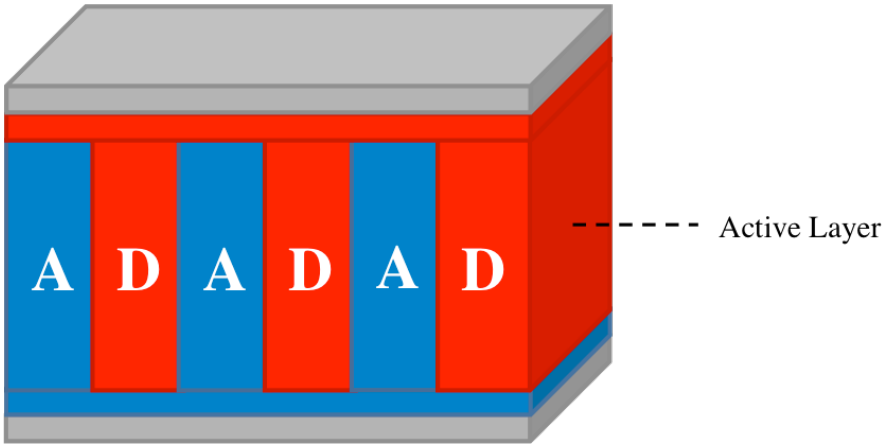

Figure 3.1 Ideal active layer of a D/A bulk heterojunction for optimal efficiency in organic material devices.

While bicontinuous D and A regions are crucial for device efficiency, D-A charge transfer complexes often occur leading to poor charge carrier mobility. Another morphologically-controllable alternative to D and A blends are covalently linked D-A dyads, representing one of the simpler "bottom-up" methods for obtaining long-range order in the active layer of organic material devices (see Figure 3.2) (91, 94, 95). While mixed stacks of dyads are not useful for electron transfer, segregated stacks can lead to continuous electron transport.

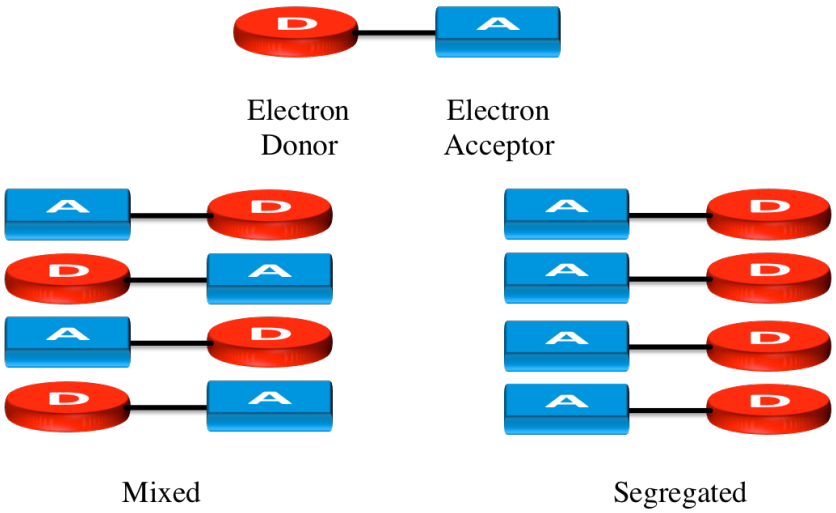

Figure 3.2 Packing arrangements of D-A dyads showing mixed and segregated stacking.

A myriad of D-A dyads have been synthesized and studied and are shown in Table 3.1. While Müllen and co-workers primarily focus on dyads composed of hexa-*peri*-hexabenzocoronene (HBC) linked to perylenetetracarboxy-diimide (PDI) and –monoimide (PMI) (92, 94, 96, 97, 98), Aidi and co-workers have developed amphiphilic oligothiophene-C_{60} (99) and HBC-C_{60} dyads (100). Venkataraman and co-workers have studied amphiphilic naphthalimide (NI)–naphthyl (101) and naphthalene diimide (NDI)-quaterthiophene (QT) D-A dyads (102) while Würthner *et al*. studied the effects of hydrogen bonding on the assembly of oligo(p-phenylene vinylenes) (OPVs) and perylene bisimides (PERYs) into *p-n* heterojunctions (103).

Donor-Acceptor Dyad	Ref.	Donor-Acceptor Dyad	Ref.
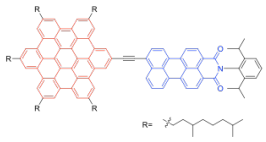	(97)	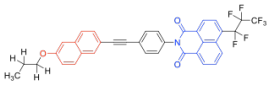	(101)
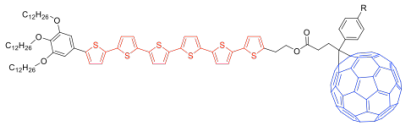	(99)	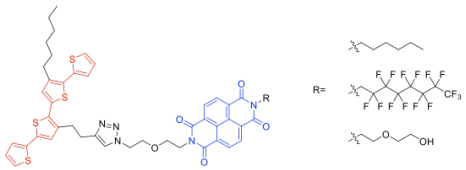	(102)
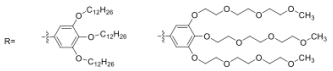		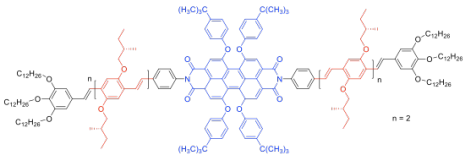	(103)
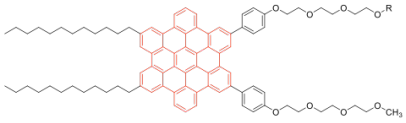	(100)	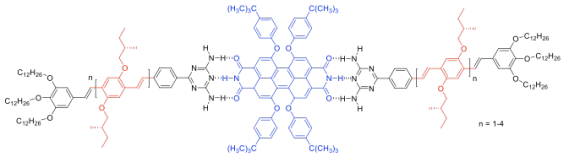	(103)
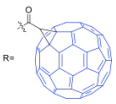			

Table 3.1 Various D-A dyads and triads showing the diversity of structures and aromatic units. Donor components are shown in red while acceptor components are shown in blue.

Several strategies have been used to direct segregated stacking in bulk heterojunction structures (see Figure 3.3). In 2007, Benanti, Saejueng and Venkataraman designed D-A dyads that took advantage of the immiscibility of hydrocarbon and fluorocarbon side chains appended to aromatic moieties to induce segregated D-A domains composed of aromatic acceptor-acceptor stacking between the NI units (101). More recent work by Aida and co-workers utilized a similar immiscible side chain scaffold to promote the D-A segregation of D-A dyads into a lamellar stacking arrangement (99) and coaxial nanotubes (100). Taking a simpler route to achieve segregated stacking, Samorì *et al*. used a technique called solvent induced precipitation to form fibers composed of D-A dyads (94).

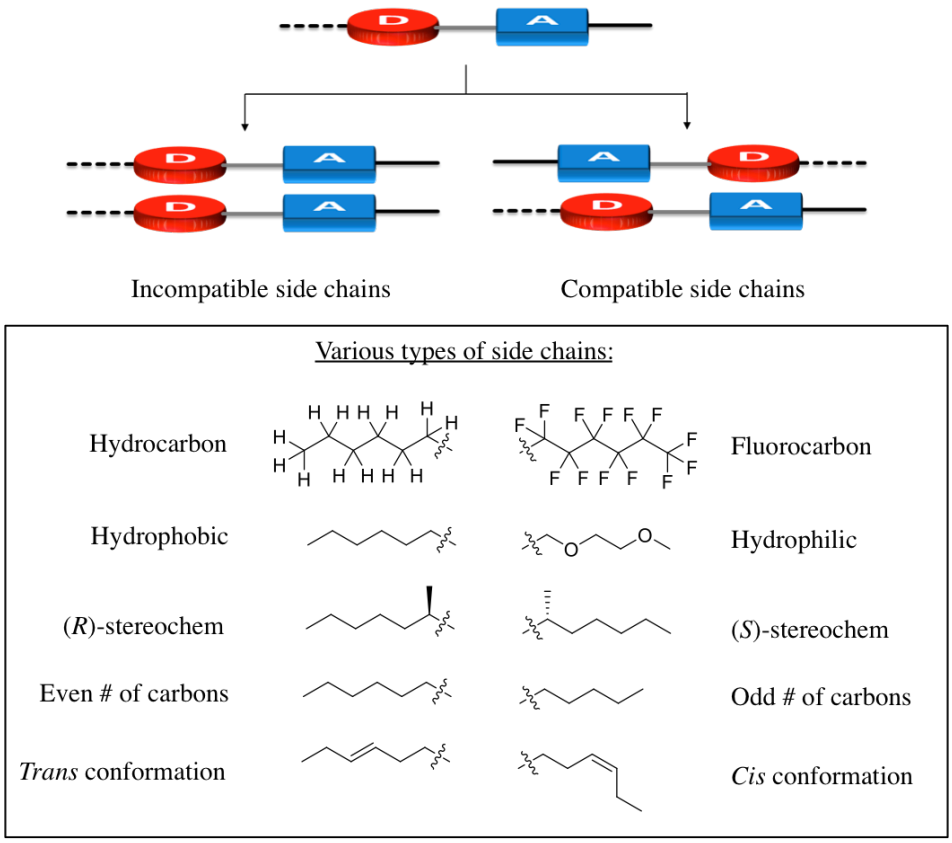

Figure 3.3 Numerous D-A systems have employed dyads with asymmetric side chain derivatives to aid in the orientation of the aromatic cores. By using side chains that are incompatible segregated D-A stacks are obtainable.

Non-covalent interactions play decisive roles in defining highly ordered architectures such as foldamers (104), catenanes (105, 106), rotaxanes (107, 108) and materials with interesting electronic properties (94, 96, 99). In most of these systems, a careful interplay of solvaphobic interactions coupled with complementary electrostatic interactions between aromatics drive the system assembly. For a more in depth analysis of molecular self-assembly using non-covalent interactions refer to Chapter 1.

Polymorphism, or the ability of one molecule to form two or more distinct crystal structures, is a well-documented phenomenon and is influenced by numerous parameters such as additives and solvent (109). Conformational twisting (110) and *cis*-to-*trans* conformational

switching (111, 112, 113) are examples of solvent induced polymorphism observed in small molecules. Work by Myerson *et al*. explored the effect of solvent evaporation rate on the polymorphism of glycine crystals and found that a slower evaporation time lead to the more stable polymorph of glycine (114). To our knowledge, however, the solid-state polymorphism of conjugated aromatic D-A dyads using slower and faster evaporation rates has not yet been reported.

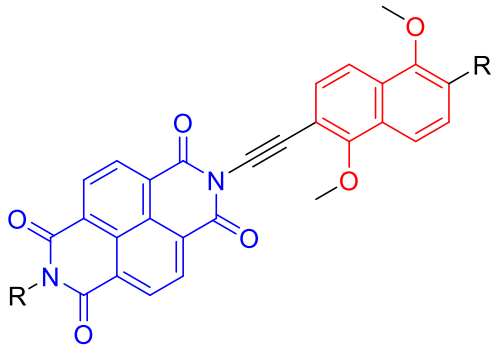

Figure 3.4 Previously attempted DAN-NDI conjugated aromatic donor-acceptor dyad.

Previous work in our group had attempted to synthesize a D-A dyad from ynimide funcionalized NDI as shown in Figure 3.4 (115). However, the synthesis was unsuccessful and thus a new system was devised in order to look at the assembly of D-A dyads in the solid state.

For the first time, the present work examines the ability of conjugated aromatic D-A dyads with symmetric side chains to exhibit solid-state polymorphism as a function of time during the solid formation process. More specifically, while single crystal X-ray and XRD analyses revealed head-to-tail D-A stacking for all four of the D-A dyads derived from fast evaporation, relatively slow evaporation lead to a tail-to-tail A-A packing geometry in two cases.

3.3 RESULTS

3.3.1 Synthesis and electrostatic potential maps

A series of four dyads bearing shorter and longer alkyl chains were synthesized via Sonogashira couplings between aromatic naphthalimide (NI) and monoalkoxynaphthalene (MAN) units in order to test the influence of chain length and orientation on solid state packing. In particular, both 2,6- and 1,4-position substituted MAN units were synthesized containing either one or eight carbon chains (Figure 3.5a).

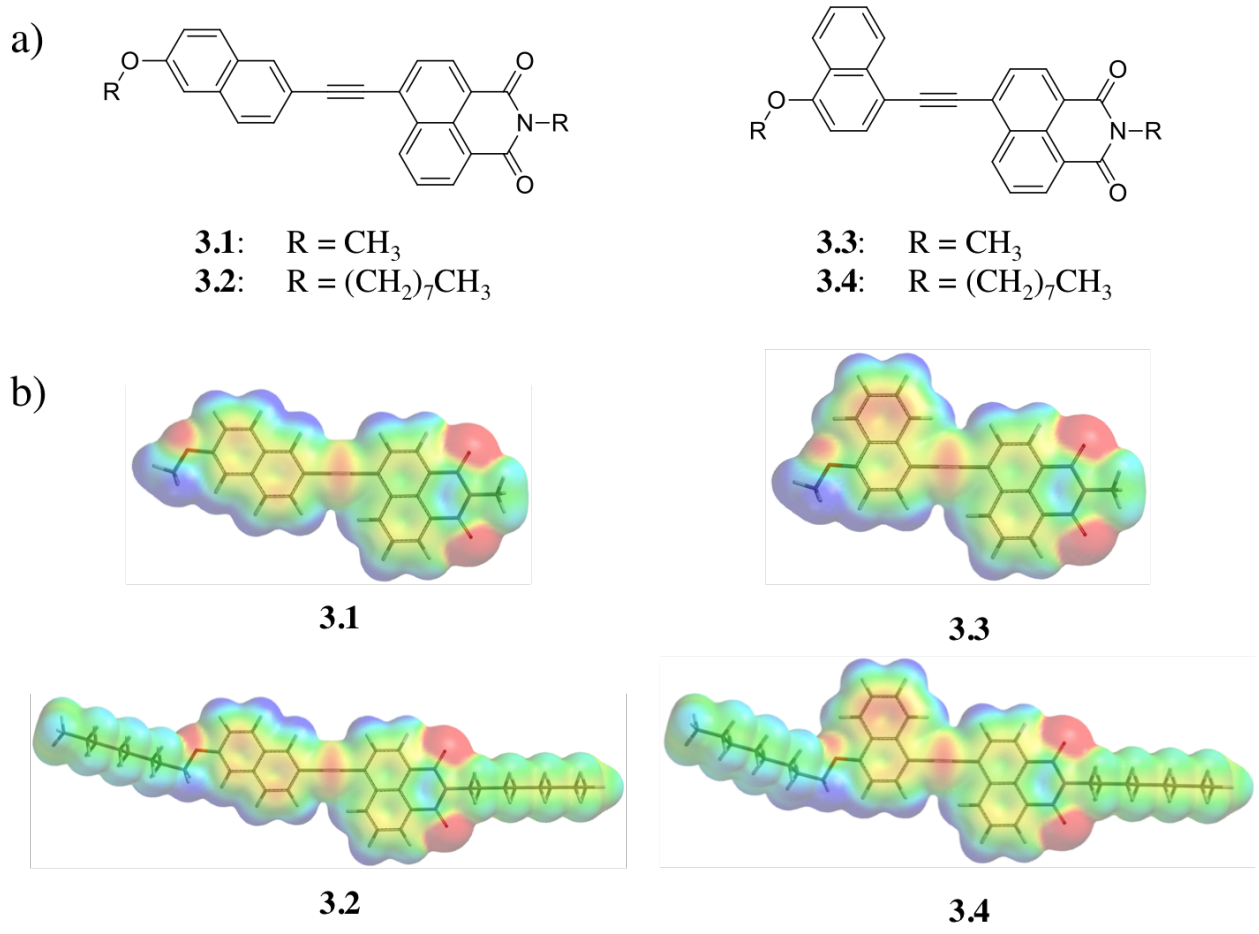

Figure 3.5 (a) Structures and (b) electrostatic potential maps of dyads **1** - **4** generated in Spartan 08 using the DFT B3LYP G-31* method.

Electrostatic potential maps of dyads **3.1** – **3.4** are shown in Figure 3.5b. The most striking feature of all the dyads is the strong polarization of the NI carbonyl bonds, rendering the

carbonyl oxygen atoms electron-rich while leaving the carbonyl carbon atoms relatively electron-deficient. One might anticipate intuitively that the NI portion would be significantly more electron-deficient relative to the MAN portion than what is seen in Figure 3.5b. Although there is a difference, the overall electronic similarities seen near the center of each aromatic unit are attributable, at least in part, to delocalization of the MAN electron-density onto the NI unit through the alkyne linker (116, 117).

In order to determine the dyad packing in the solid state, various conditions were used to grow crystals of the dyads. Powder XRD patterns of those crystals were then obtained and compared to XRD patterns obtained from either slower or faster evaporation from toluene. The packing structure of the dyads, even for those without a crystal structure, could then be compared based on the two sets of XRD data.

3.3.2 Single crystal analysis

Crystals suitable for structural analysis were grown from either slower (20 days for **3.1**, 10 days for **3.4**) or faster (1 day for **3.1**) evaporation from solvent systems that were empirically found to be capable of growing high quality crystals. "Fast" crystals of dyad **3.1** were grown from chloroform while "slow" crystals of dyad **3.1** and **3.4** were grown from 1:1:1 Toluene:MeOH:Ethyl Acetate and 1:1:1 DCM:MeOH:Acetone, respectively. For the remainder of this chapter the dyads will be referred to as follows:

Faster evaporated dyads	*Slower* evaporated dyads
3.1f	**3.1s**
3.2f	**3.2s**
3.3f	**3.3s**
3.4f	**3.4s**

Typically, ~5.0 mg of dyad was placed in a scintillation vial and dissolved in 10 mL of solvent. For slower evaporations the vials were partially closed while faster evaporations were performed without a cap. Numerous attempts at growing high quality crystals of dyads **3.2** and **3.3** gave at best hair-like solids that did not refract.

3.3.2.1 Dyad 3.1

Dyad **3.1** was found to form two distinct crystals as a function of crystal growth time and solvent system: a head-to-tail (MAN-NI aromatic interaction) crystal after faster evaporation from chloroform and a head-to-head (NI-NI aromatic interaction) crystal after slower evaporation from 1:1:1 Toluene:MeOH:Ethyl Acetate. The head-to-tail crystal resulting from fast evaporation is nearly planar and exhibits stacking in which the MAN portion of one dyad stacks in a face-centered fashion with the NI portion of another (Figure 3.6). The NI portion of the aforementioned dyad is situated directly above the NI portion of another dyad (Figure 3.7a). While the NI-MAN centroid-centroid distance is 3.73 Å, the NI-NI centroid-centroid distance is 4.0 Å. The plane-to-plane distance between the stacked dyad layers is 3.33 Å. Within the same column, the dyads are ~55° offset along the dyad short-axis. The bond lengths between C14≡C15 (1.198 Å), C5-C14 (1.431 Å) and C15-C16 (1.428 Å) are relatively short suggesting delocalization between the NI and MAN unit (118) and are all within standard bond lengths for other NI-containing systems (119, 120). The head-to-tail dyad pairs reside in rows that do not show any overlap between dyads of either row (Figure 3.7b). Looking down the crystallographic A-axis reveals that each row can be divided further into columns (Figure 3.7c). Bond lengths within the NI dicarboximide ring are typical and are in good agreement with bond lengths in other NI-containing systems (119, 120).

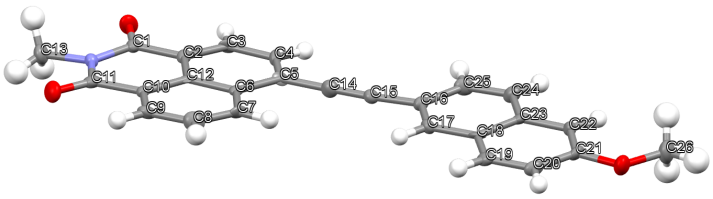

Figure 3.6 Structure of **3.1f** showing the atom-numbering scheme with ellipsoids scaled at the 50% probability level. A molecule of chloroform has been removed from the asymmetric unit for clarity.

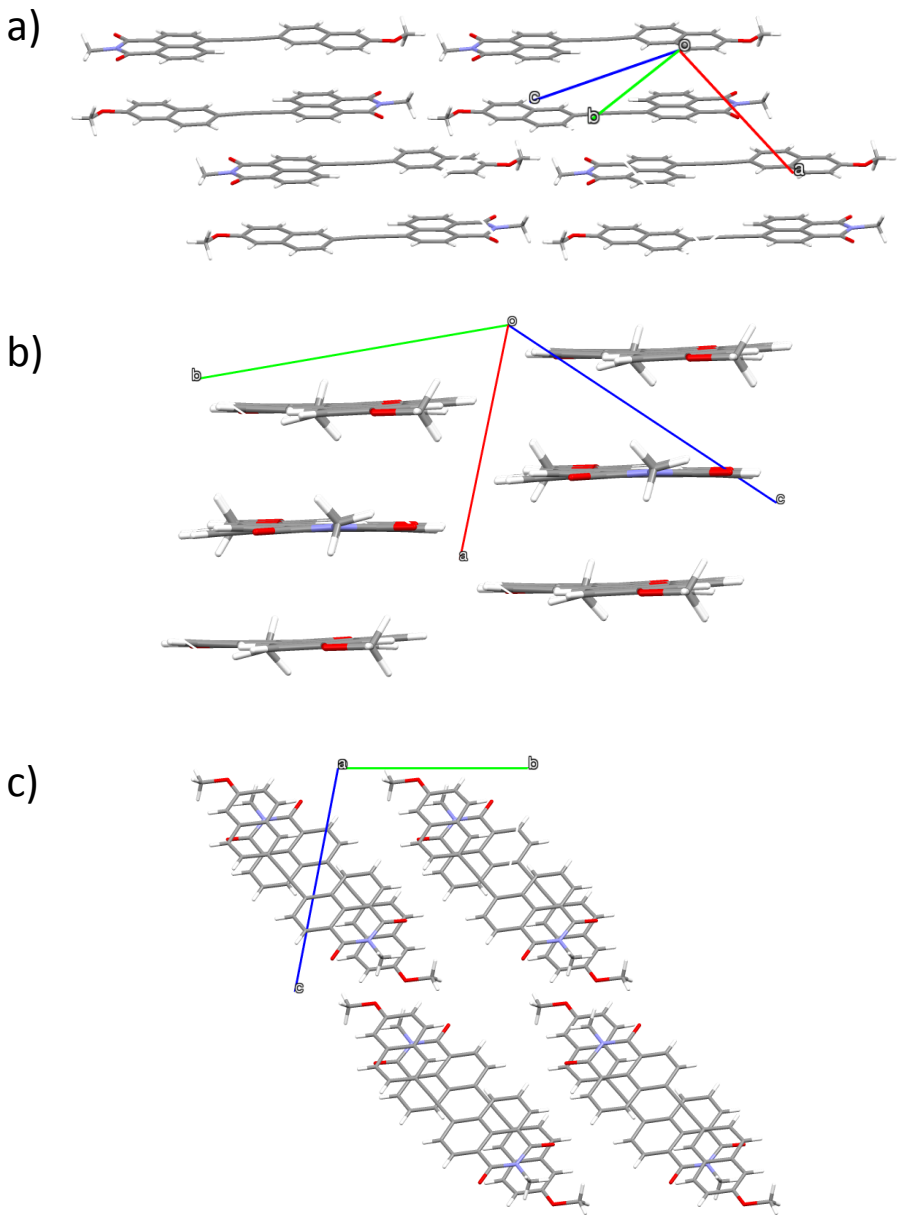

Figure 3.7 Crystal structure of **3.1f** showing (a) Head-to-tail, MAN-NI packing occurs between dyads directly above each other while NI-NI interactions occurs between adjacent pairs; (b) side view of crystal packing showing rows of non-interacting dyads; and (c) view down crystallographic A-axis shows details of crystal packing.

When evaporated more slowly from 1:1:1 Toluene:MeOH:Ethyl Acetate, **3.1s** displayed a nearly planar relationship between the NI and MAN units with the dyads packing in a tail-to-tail fashion (Figure 3.8).

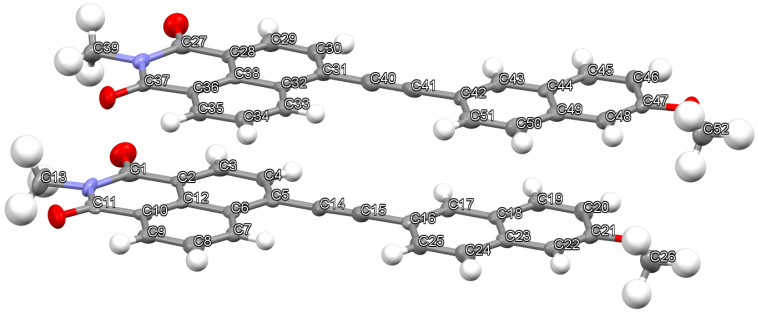

Figure 3.8 Asymmetric unit of **3.1s** showing the atom-numbering scheme with ellipsoids scaled at the 50% probability level. A molecule of toluene was removed from the unit for clarity.

While the plane-to-plane distance between dyads is slightly larger (3.36 Å compared to 3.33 Å when quickly evaporated), the dyads are ~20° off-set from each other along the dyad short-axis in the same column (Figure 3.9a). The NI-NI centroid-centroid distance for the pair of dyads in the asymmetric unit is 3.72 Å while the NI-NI centroid-centroid distance between asymmetric units is 3.76 Å. The bond lengths between both molecules in the asymmetric cell are C14≡C15 (1.191 Å) and C41≡C40 (1.200 Å), C5-C14 (1.423 Å) and C31-C40 (1.420 Å), and C15-C16 (1.444 Å) and C41-C42 (1.425 Å) are all relatively short suggesting delocalization between the NI and MAN unit (118). Again, all bond lengths within the NI unit are consistent with those previously seen in NI-containing systems (119, 120). Rows of non-interacting dyads are shown in Figure 3.9b. Interestingly, extended columns of aromatic-aromatic (NI-NI) interactions occur in the more slowly evaporated crystal (Figure 3.9c), unlike what was observed in the crystal obtained upon more rapid evaporation described above.

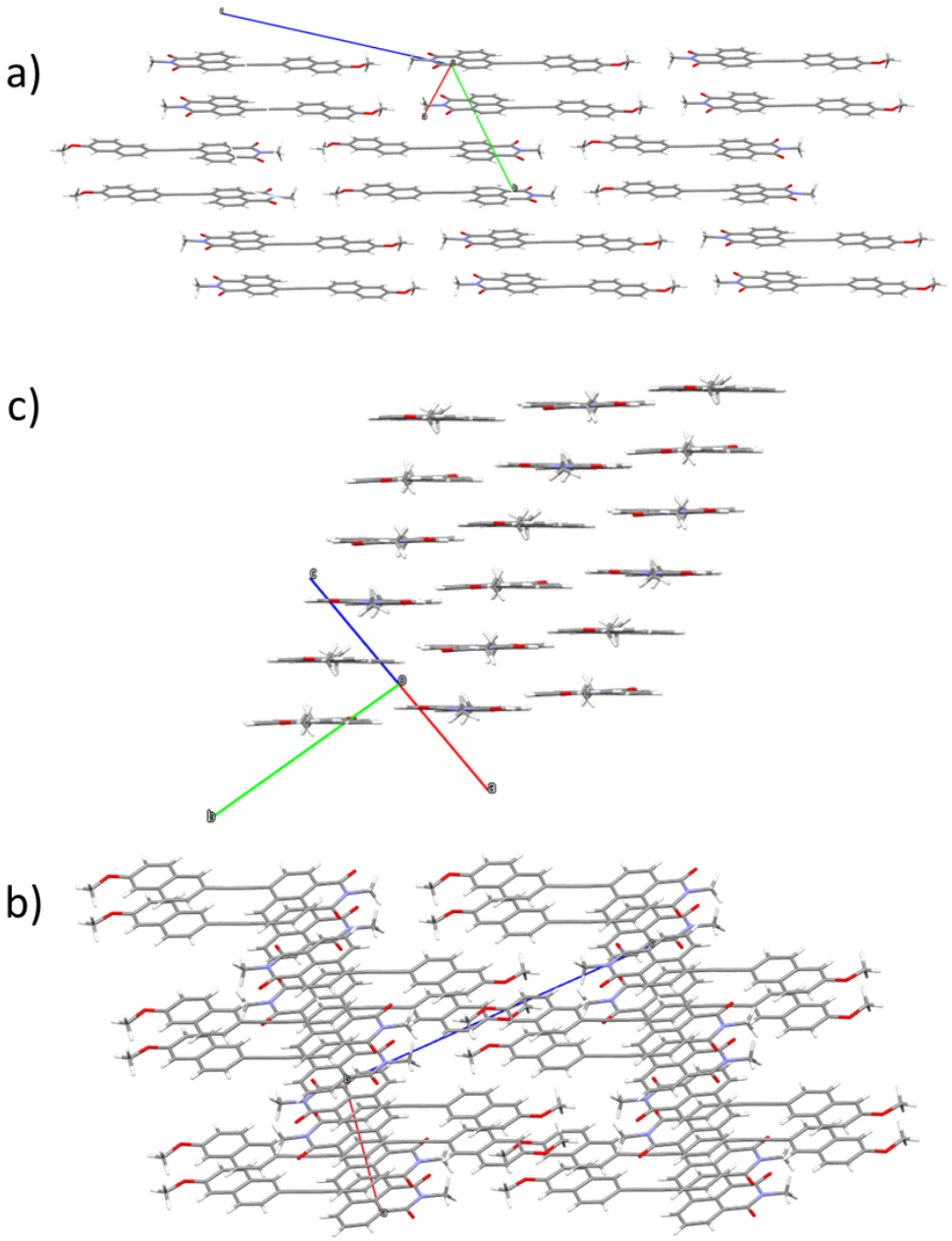

Figure 3.9 Crystal structure of **3.1s** showing (a) tail-to-tail, NI-NI packing occurs between two dyad molecules situated in one asymmetric unit; (c) side view of crystal packing showing rows of non-interacting dyads; and (b) NI-NI aromatic interactions among columns as viewed from crystallographic C-axis.

3.3.2.2 Dyad 3.4

The crystal structure of dyad **3.4** produced upon slower evaporation from 1:1:1 DCM:MeOH:Acetone also reveals a tail-to-tail (A-A) stacking geometry, with the NI unit being nearly coplanar with the MAN unit (Figure 3.10).

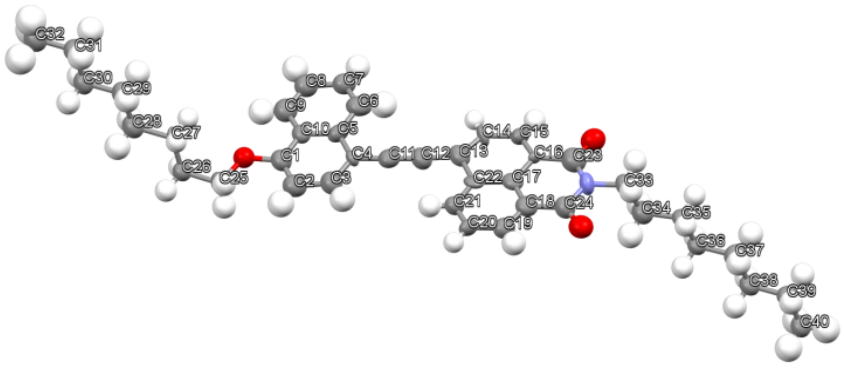

Figure 3.10 Structure of **3.4s** showing the atom-numbering scheme with ellipsoids scaled at the 30% probability level.

As shown in Figure 3.11a, the dyads are packed in an off-set parallel-displaced fashion with the NI portions of adjacent dyads stacking on top of each other. The plane-to-plane distance is 3.36 Å and the stacked dyads show an off-set angle of ~45° along the dyad long-axis. The NI-NI centroid-centroid distance is 4.73 Å. Unsurprisingly, the bond lengths between C11≡C12 (1.220), C4-C11 (1.414) and C12-C13 (1.435) are all relatively short suggesting delocalization between the NI and MAN unit (118). Looking down the crystallographic C-axis, adjacent columns of stacked dyads exist in the same conformation, however, the orientation of the stacks are rotated 90° relative to every other stack (Figure 3.11b). Adjacent columns of stacked dyad **3.4** pack with octyl side chains interdigitated in a lamellar fashion (Figure 3.11c).

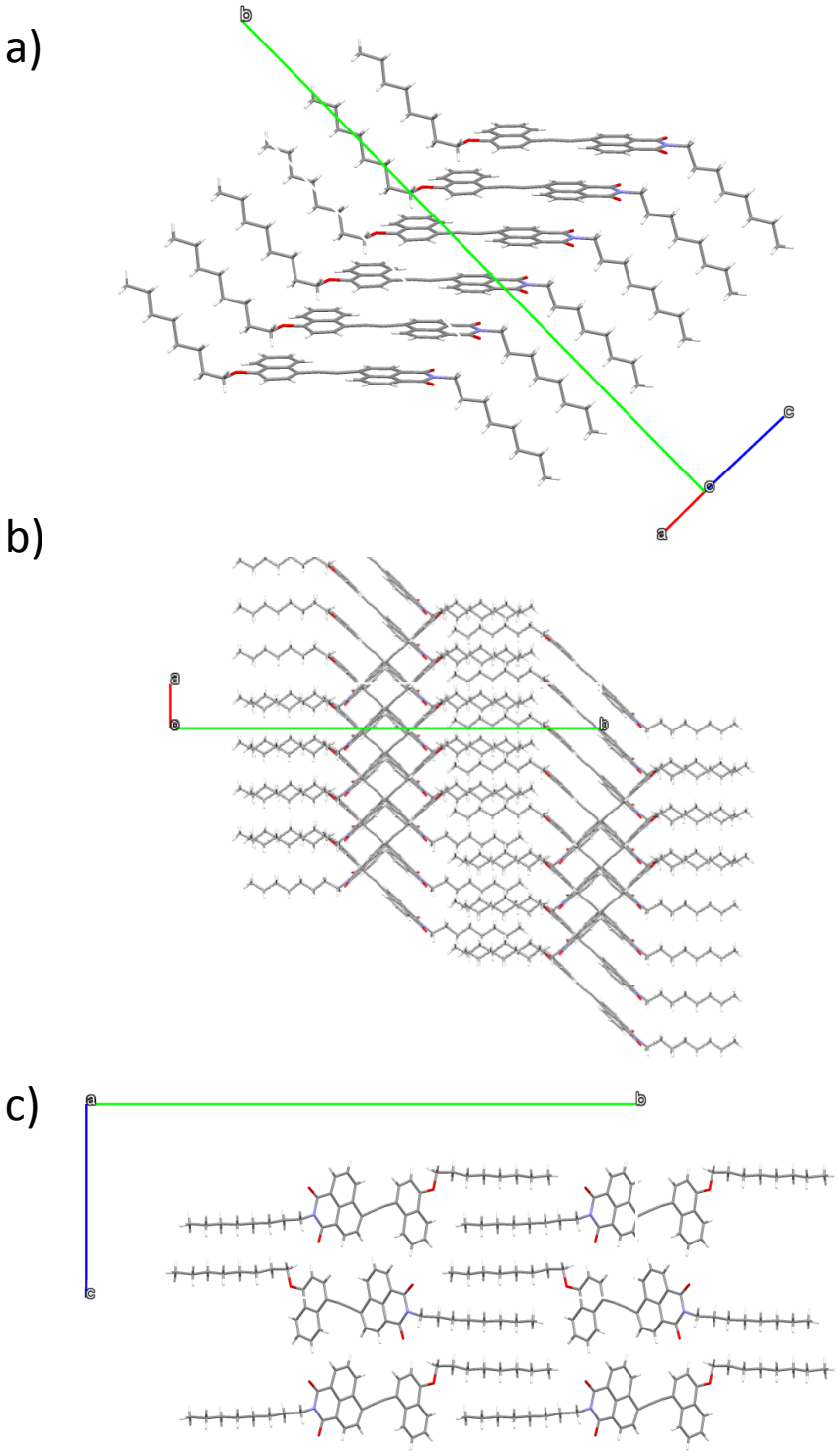

Figure 3.11 Crystal structure of **3.4s** showing (a) off-set parallel-displaced packing between adjacent aromatic NI units; (b) orthogonal crystal packing between rows of stacked dyads along the C-axis; and (c) interdigitated sidechains among rows reminiscent of lamellar structure along the A-axis.

3.3.3 Powder X-ray diffraction (XRD)

Because high quality single crystals could not be obtained for each dyad, powder XRD was performed on dyads **3.1** – **3.4** to gain insight into their molecular packing morphology. XRD patterns were collected on each dyad after having been relatively slowly (10 - 15 days for **3.1s**, **3.2s**, **3.3s**, **3.4s**) and more quickly (1 day for **3.1f**, **3.2f**, **3.3f**, **3.4f**) evaporated from toluene. Typically, ~ 5.0 mg of dyad was dissolved in 10 mL of toluene. Although numerous solvents and longer (30 days) evaporation times were tested to give rise to the more slowly formed polymorphs, all attempts only resulted in the one polymorph for **3.2** and **3.3**. Toluene was chosen due to its relatively high boiling point and its ability to solubilize all four dyads. Initial evaporations from DCM, and other lower boiling point solvents, occurred too quickly (< 4 days) and did not allow for a longer time-scale evaporation. Most importantly, using the same solvent for each powder sample insured that any differences in structure are not the result of solvent interactions, but rather reflect the influence of evaporation time.

3.3.3.1 XRD - single crystal by various solvents

For calibration purposes, XRD of the dyad crystals used for single crystal analyses were compared to XRD patterns of the same dyads quickly or slowly evaporated from toluene (see Figure 3.12). For **3.4s** and both **3.1f** and **3.1s**, the XRD patterns are the same between the single crystals that were grown from different solvents and from the powders obtained via evaporation strictly from toluene. Therefore, although different solvents were used to obtain the crystals for single crystal analysis, it is assumed that the obtained crystals had the same molecular morphology as the powders obtained via evaporation from toluene. The XRD data has thus established an important structural link between materials obtained by either faster or slower evaporation that is at least partially independent of solvent composition, at least in these specific cases.

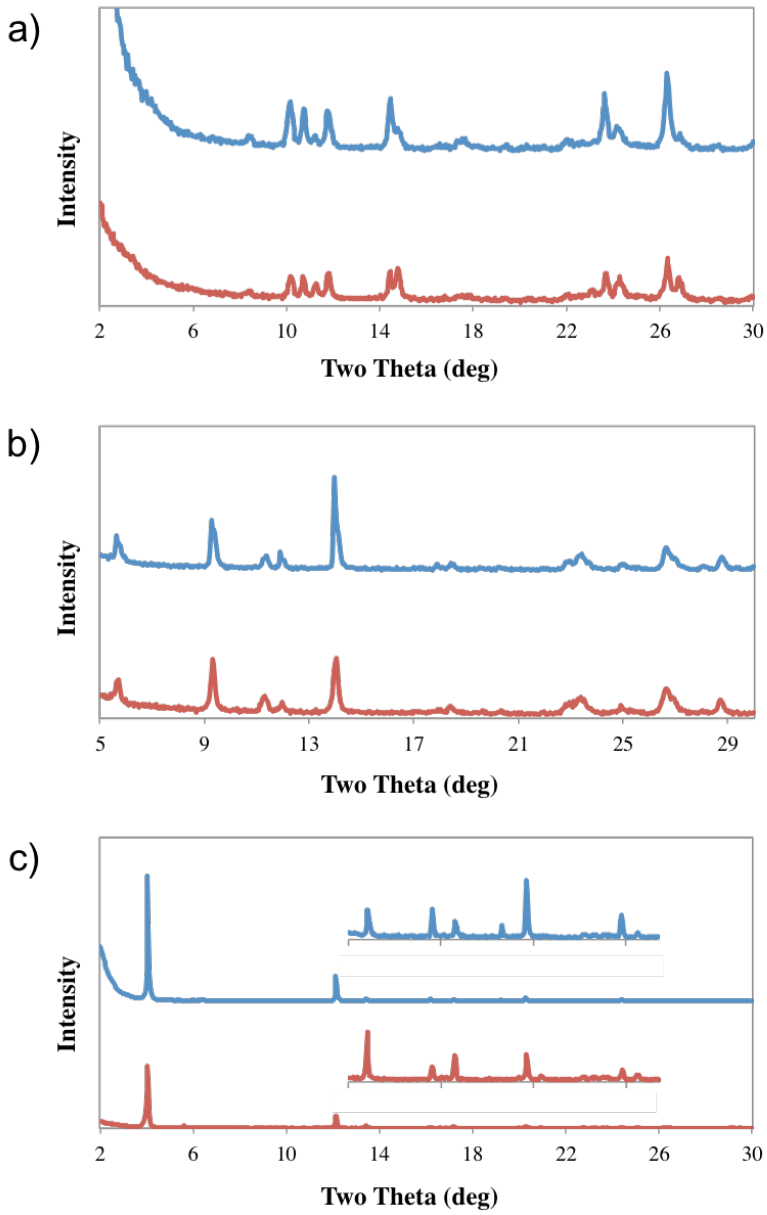

Figure 3.12 Comparisons of XRD patterns between dyad single crystals grown from various solvents (top, blue lines) and powders of dyads evaporated from toluene (bottom, red lines). Inset graph shows a magnified XRD pattern. (a) Dyad **3.1f**. (b) Dyad **3.1s**. (c) Dyad **3.4s**.

3.3.3.2 XRD – powders by toluene evaporation

Powder XRD patterns for dyads **3.1** – **3.4** after slower and faster evaporation from toluene are shown in Figure 3.13. For dyad **3.1**, the slower and faster evaporated powders show patterns that can be easily distinguished from one another. Dyad **3.4** also shows two distinct patterns between the evaporated powders obtained from relatively slow and fast evaporation conditions. Interestingly, dyads **3.2** and **3.3** show very similar diffraction patterns between their respective powders produced upon slower and faster evaporation.

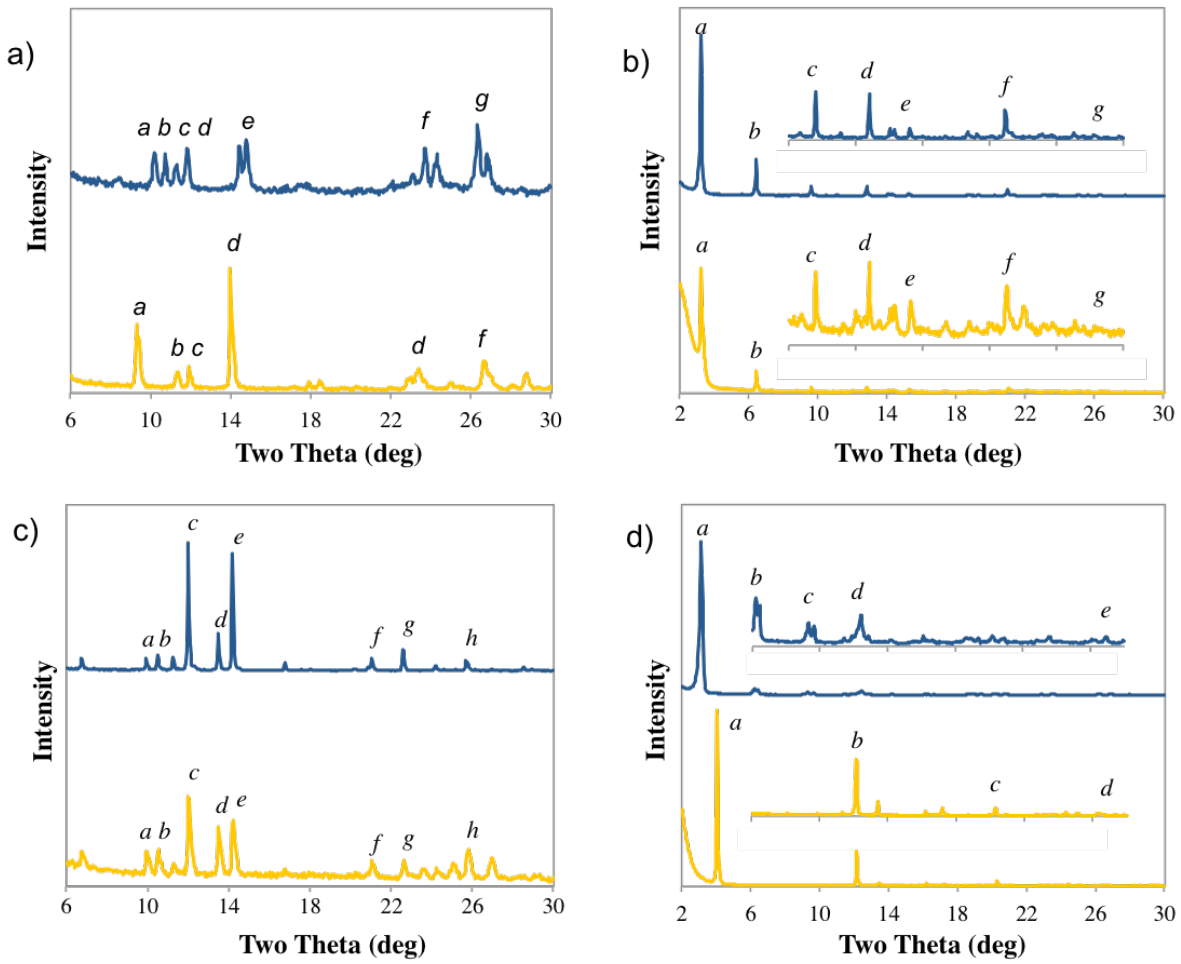

	d-spacings (in Å)							
	Dyad **3.1**		Dyad **3.2**		Dyad **3.3**		Dyad **3.4**	
Peak	Faster	Slower	Faster	Slower	Faster	Slower	Faster	Slower
a	8.7	9.5	27.6	27.5	8.9	8.9	28.3	21.9
b	8.3	7.8	13.8	13.8	8.4	8.4	14.2	7.3
c	7.9	7.4	9.2	9.2	7.4	7.4	9.1	4.4
d	7.5	6.3	6.9	6.9	6.6	6.6	7.1	3.4
e	6.0	3.7	5.8	5.8	6.3	6.2	3.4	
f	3.7	3.4	4.2	4.2	4.3	4.2		
g	3.4		3.5	3.5	3.7	3.7		
h					3.4	3.5		

Figure 3.13 Powder XRD patterns obtained from toluene for (a) dyad **3.1**, (b) dyad **3.2**, (c) dyad **3.3** and (d) dyad **3.4** are shown with peaks labeled and their corresponding *d*-spacing values listed in the accompanying table. Relatively slower evaporated dyads are shown on the bottom (in orange) while relatively faster evaporated dyads are shown on top (in blue). Inset graphs show magnified XRD patterns.

3.4 Discussion

3.4.1 Dyad proposed packing morphologies

3.4.1.1 Dyad 3.1

The XRD *d*-spacing values for **3.1f** nicely match up with patterns found in the associated quickly evaporated crystal structures (see Figure 3.14). For the more quickly evaporated crystal structure, *d*-spacing values of 3.4 and 4.0 Å (similar to 3.7 Å found by XRD) represent the interplanar distances between the dyads and centroid-centroid distances between NI units, respectively (101, 121, 122, 123, 124, 125, 126). Single crystal distances of 8.4 and 8.6 Å were also found to be in good agreement with XRD *d*-spacing values (8.3 and 8.7 Å, respectively).

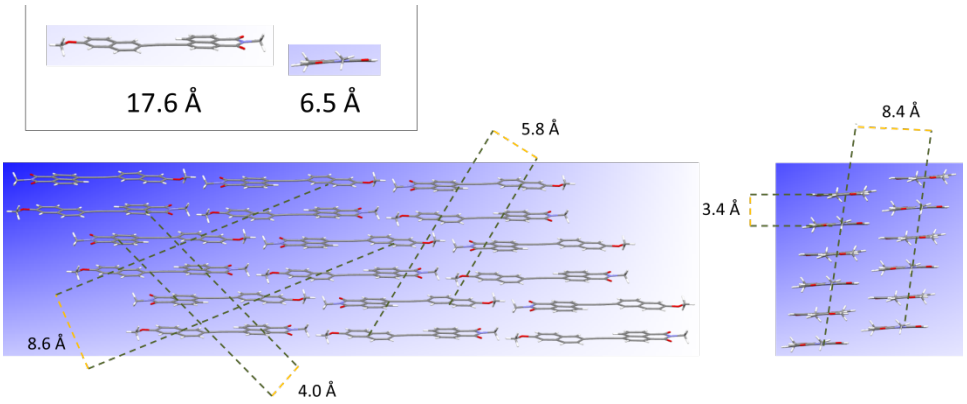

Figure 3.14. Dyad **3.1f** crystal structure with important XRD *d*-spacing values highlighted.

The crystal structure of **3.1s** shows spacing distances that are also in good agreement with the XRD *d*-spacing values (see Figure 3.15). While XRD *d*-spacings of 3.4, 7.8 and 9.5 Å exactly match patterns from the crystal structure, a *d*-spacing value of 6.3 Å closely resembles the 6.2 Å value from the crystal structure.

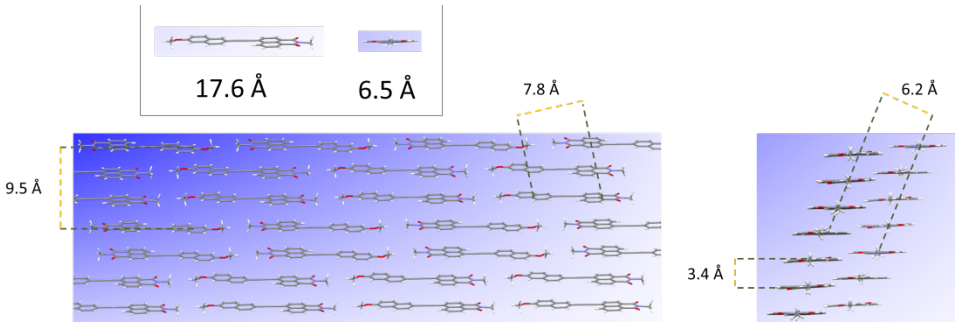

Figure 3.15 Dyad **3.1s** crystal structure with important XRD *d*-spacing values highlighted.

3.4.1.2 Dyad 3.2

Both the fast and slow evaporation of dyad **3.2** from toluene gave similar powder XRD patterns (Figure 3.13b). Proposed interdigitation of the dyad octyl chains in a lamellar-fashion corresponds to a distance (27.5 Å) that is shorter than the distance across the dyad diagonal structure (33.5 Å). 1 2 The proposed packing model therefore incorporates lamellar-type packing and uses the crystal structure of dyad **3.1** to arrange dyad **3.2** in a similar head-to-tail (D-A) stacking geometry (see Figure 3.16a). The observed *d*-spacings of 9.2 and 13.8 Å were then incorporated into our proposed model to give a final molecular packing similar to that of dyad **3.4f**. A *d*-spacing at 3.5 Å is also in good agreement with previously reported values for aromatic-aromatic stacking interactions (101, 121, 122, 123, 124, 125, 126).

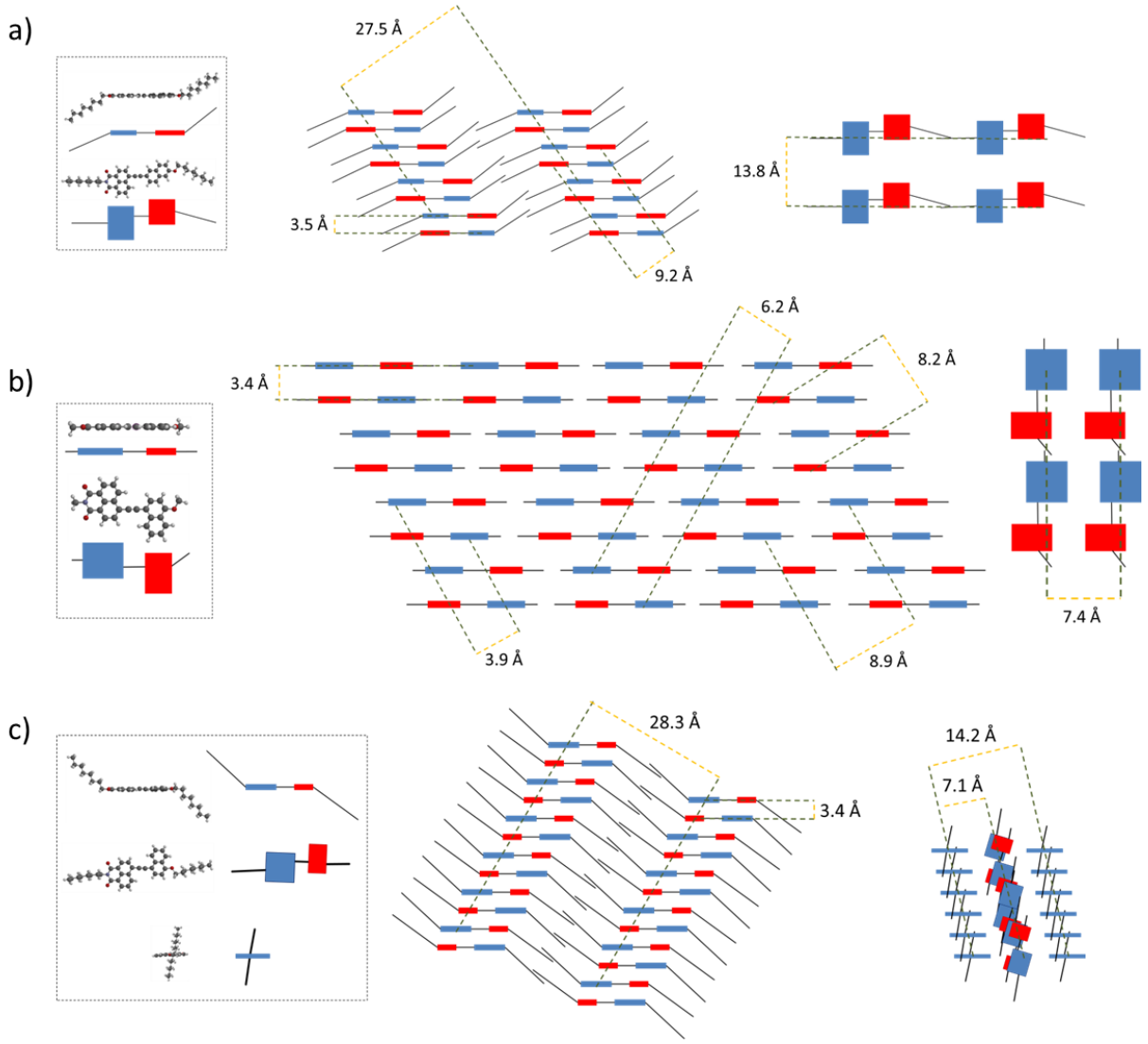

Figure 3.16 Proposed molecular packing for (a) dyad **3.2**, (b) dyad **3.3**, and (c) dyad **3.4f**. Important XRD *d*-spacing values are highlighted for each model. Scale representations of the dyads are shown in the dashed boxes (blue and red represent the NI and MAN portion of the dyad, respectively) and only represent that dyad. The middle sections show the side view of packing while the right sections show the top-down packing view.

3.4.1.3 Dyad 3.3

Both the fast and slow evaporation of dyad **3.3** from toluene gave very similar powder XRD patterns suggesting that, like dyad **3.2**, the solid produced by dyad **3.3** is isomorphic for

both evaporation times (see Figure 3.13c). Note that the XRD patterns for dyad **3.3** are similar to the XRD patterns observed for dyad **3.1f** (see Figure 3.13a). As a result, it is proposed that in both the faster and slower evaporation solids, dyad **3.3** is ordered in a head-to-tail (D-A) fashion, similar to the crystal structure of dyad **3.1f** (see Figure 3.16b). In the proposed model for dyad **3.3**, a plane-to-plane distance of 3.4 Å fits the observed XRD *d*-spacing while a *d*-spacing at 7.4 Å represent the distance between the centers of the dyad rows. The *d*-spacing at 3.4 Å is in agreement with previously reported values for aromatic-aromatic stacking interactions (101, 121, 122, 123, 124, 125, 126). Further *d*-spacings can be identified in Figure 3.16b which support the proposed model of molecular packing for dyad **3**.

3.4.1.4 Dyad 3.4

While single crystals suitable for X-ray analysis were only obtained for dyad **3.4** when the sample was evaporated slowly, XRD results showed that two distinct molecular packing arrangements exist between the quickly and slowly evaporated solids as shown in Figure 3.13c. For the slowly evaporated structure, a *d*-spacing of 21.9 Å nicely fits an interdigitated lamellar packing as scene in the obtained crystal structure (see Figure 3.17). Further *d*-spacings of 3.4 and 4.2 Å (which is very similar to a *d*-spacing of 4.2 Å found by XRD) represent interplanar distances between the dyads and centroid-centroid distances between NI units, respectively.

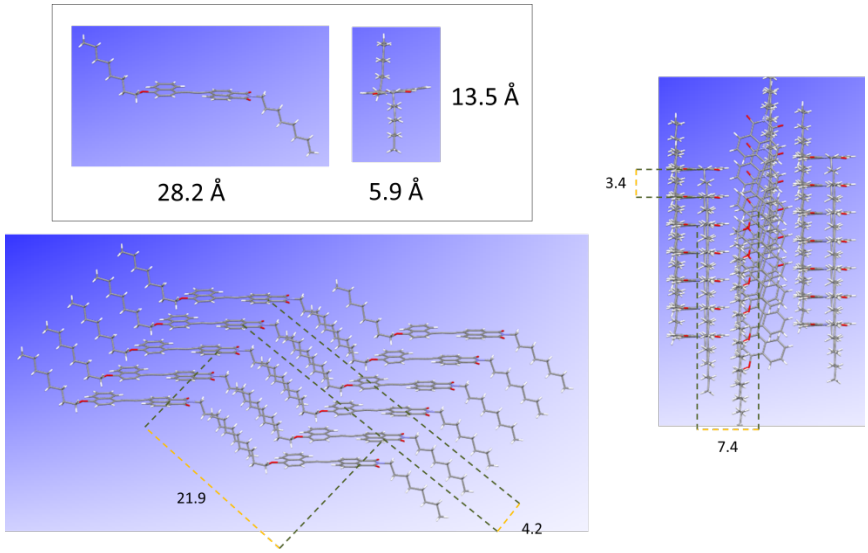

Figure 3.17 Dyad **3.4s** crystal structure with important XRD *d*-spacing values highlighted.

For dyad **3.4f**, an intense diffraction peak at 2θ = 3.1° corresponds to a *d*-spacing of 28.3 Å suggesting that the side chains are also packing in an interdigitated lamellar (127, 128) as proposed in our packing model in Figure 3.16c. Note that given the diagonal length of dyad **3.4** is 31.3 Å between the terminal carbons on the alkyl chains, this packing model makes sense according to the lamellar structure that was observed in the dyad **3.4s** structure. In good agreement with the proposed model, *d*-spacings of 7.1 and 14.2 Å represent symmetric planes found within the proposed packing model. The *d*-spacing at 3.4 Å is in good agreement with the interplanar distance typically found between pairs of stacked NI-NI (101, 121, 122) and NDI-NDI (123, 124, 125, 126) aromatic units.

3.4.2 DFT calculations

DFT calculations of the dyad electrostatic potentials gave some level of insight as to why the head-to-head NI-NI (A-A) packing state could be observed for dyads **3.1s** and **3.4s**. It is assumed, based on the computational work of Wheeler, that favorable geometries between aromatic portions of adjacently stacked molecules in a solid will be largely directed by favorable,

direct through-space interactions between polarized moieties on the periphery of aromatic units (129). Consistent with this idea, in the tail-to-tail A-A stacked geometry observed here for the more slowly evaporated samples of **3.1s** and **3.4s**, the relatively electron-rich carbonyl oxygen of the NI aromatic unit resides directly above the relatively electron-deficient carbonyl carbon atoms of the NI portion on an adjacent dyad (see Figures 3.18a-c).

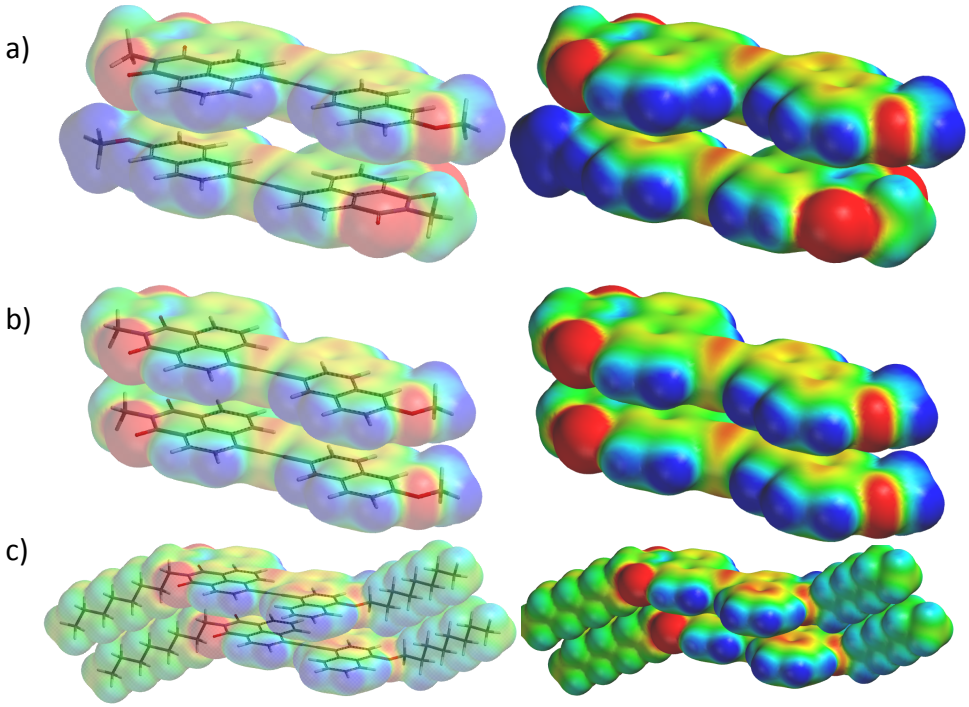

Figure 3.18 Electrostatic potential maps showing the favorable electrostatic interactions between adjacent dyads for (a) dyad **3.1f**, (b) dyad **3.1s** and (c) dyad **3.4s**. Generated in Spartan using the DFT B3LYP G-31* method.

3.5 CONCLUSIONS

Overall, our results indicate that in conjugated aromatic D-A dyads, solid-state polymorphic molecular assembly can be achieved depending on the evaporation rate of the dyad from solvent. Single-crystal X-ray crystallography combined with powder XRD revealed that

two of the four dyads displayed polymorphic behavior and stacked in a tail-to-tail NI-NI (A-A) fashion when more slowly evaporated from solvent while exhibiting head-to-tail MAN-NI (D-A) stacking when more quickly evaporated from solvent. Apparently, the length of the alkyl chain appended to the dyads did not direct the molecular packing of the aromatic units, nor did the alkoxy substitution geometry (at the 2,6- or 1,4-position) of the MAN aromatic unit, although these parameters are obviously important factors in the details of the packing geometries seen. Interestingly, the two dyads (**3.2** and **3.3**), that displayed only one type of packing following evaporation at either rate gave XRD patterns predicted to derive from head-to-tail (D-A) stacking. Thus, while all the dyads could stack in a head-to-tail D-A fashion, only **3.1** and **3.4** could produce a solid with stacking in a tail-to-tail A-A fashion, but only when evaporated more slowly.

It is tempting to assume that slower evaporation necessarily leads to the more stable (thermodynamic) polymorph, indicating that tail-to-tail (A-A) stacking of our dyads is more favorable than head-to-tail (D-A) stacking due to better electrostatic complementarity in the head-to-head geometry. While intuitively pleasing, such an assumption is dangerous for at least two reasons. First, the present results only consider room temperature crystal and powder formation, so overall thermodynamics have not been firmly established. Second, solvent is present in the single crystals of dyad **3.1**. Therefore, assuming the presence of solvent molecules in other samples, solvent molecules distributed differently in the various crystals and solids could have a strong influence over lattice energies, introducing significant interactions that are not consistent between samples. Chapter 4 explores the thermodynamic considerations of the dyads in a more thorough fashion.

Taken together, our data verifies that evaporation time should be considered when producing solids from aromatic dyads. In particular, segregated stacks of D and A units, predicted to have favorable electronic properties, were produced at longer evaporation times.

3.6 EXPERIMENTAL

General Methods

All reagents used were purchased from Sigma Aldrich or Fisher Scientific unless otherwise noted. $PdCl_2(PPh_3)_2$ and Cu(I) were purchased from STREM. All solvents were dried over molecular sieves prior to use. If necessary, reagents were recrystallized prior to use following reported literature. ^1H and ^{13}C NMR spectra were taken on a Varian Unity Plus 400 spectrometer at 400 MHz. All chemical shifts (δ) are reported in ppm and all coupling constants (J) are reported in Hz. All NMR chemical shifts are reported relative to the residual solvent peak. Melting points were taken on a melting point apparatus.

X-ray Crystallography

X-ray crystallography was performed on a Nonius Kappa CCD diffractometer using a Bruker AXS Apex II detector and a graphite monochromator with MoKα radiation (λ = 0.71075Å). Specific instrumentation details for each obtained single crystal are located in the supplemental section. Specific single crystal data for dyads **3.1f**, **3.1s** and **3.4s** can be found in the Appendix.

Powder X-Ray Diffraction

X-ray powder diffraction (XRD) patterns were obtained with a Scintag X1 theta–theta diffractometer equipped with a Cu X-ray tube and a solid-state X-ray detector set to count Cu Kα radiation. Samples were prepared by placing the solid dyads onto a zero background quartz plate sample holder.

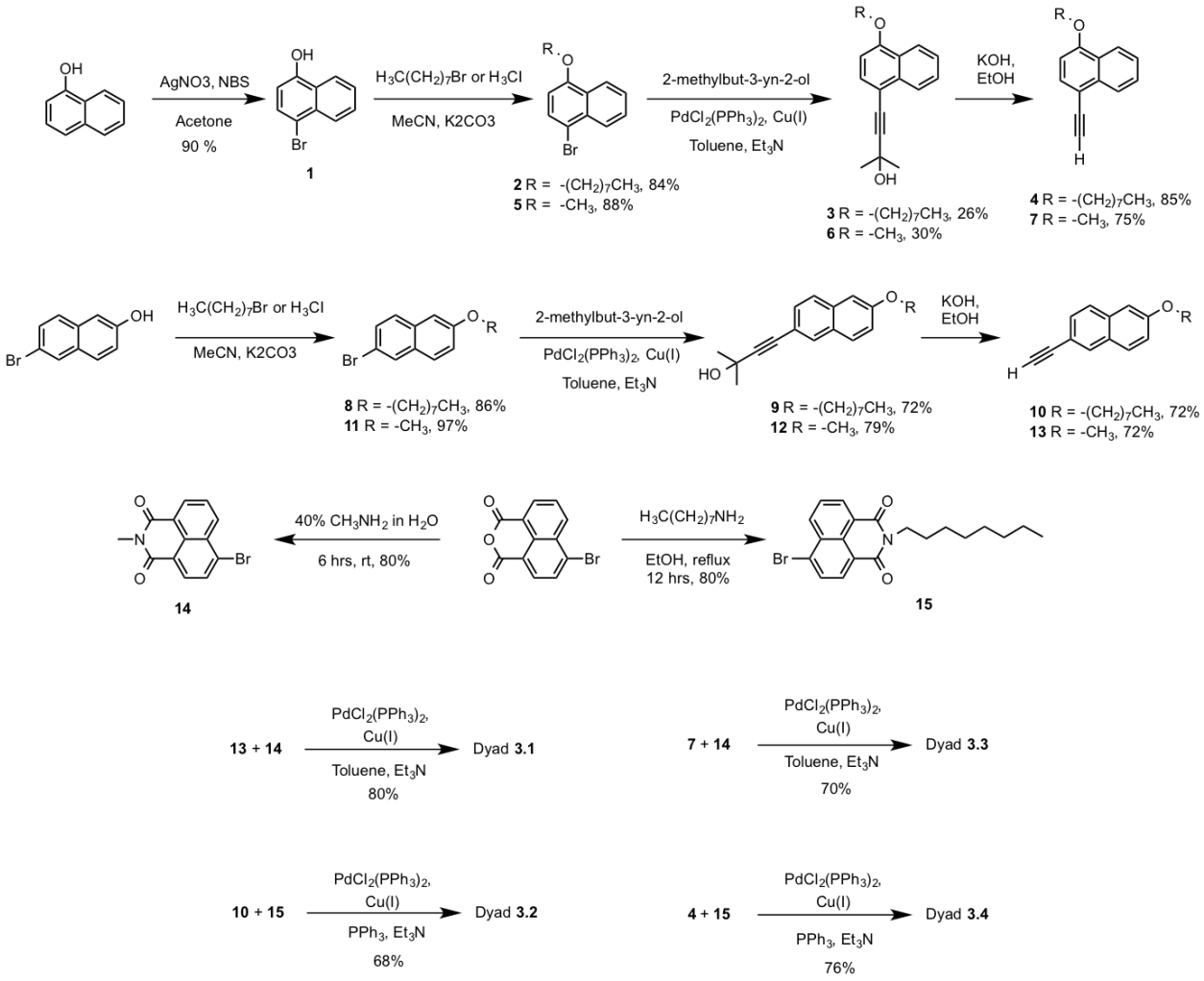

Scheme 3.1 Synthesis of dyads **3.1** – **3.4**.

4-bromonaphthalen-1-ol (1): To a solution of 1-naphthol (10.0g, 69.4 mmol) in dry acetonitrile (70 mL) was added freshly recrystallized NBS (12.4 g, 7.1 mmol) in several portions at room temperature over 30 min. After complete addition of the NBS, the reaction was allowed to stir at room temperature for an addition 4 hrs. The reaction solution was then poured into H_2O (50 mL) and extracted with diethyl ether twice (50 mL). The organic layers were then combined and washed with H_2O (3 x 300 mL) and sat. NaCl (3 x 300 mL) and dried over Na_2SO_4. Filtration and removal of diethyl ether by rotary evaporation yielded the crude product which was then subjected to column chromatography (20%/80% DCM/hexanes to 100% DCM) to yield **1** as an

off-white powder after rotary evaporation (13.9 g, 62.3 mmol, 90% yield). ^{1}H NMR ($CDCl_3$, 400 MHz): δ 8.20 (t, 2H, *J* = 8 Hz), 7.60 (m, 3H), 6.69 (d, 1H, *J* = 8 Hz), 5.27 (s, 1H). ^{13}C NMR ($CDCl_3$, 400 MHz): δ 151.32, 132.82, 129.51, 128.00, 127.25, 127.19, 126.17, 122.27, 113.59, 109.31. CI-HRMS (pos. ion): Calc. for $C_{10}H_7BrO$ 221.9675, found 221.9682. MP: 112-115 °C.

1-bromo-4-(octyloxy)naphthalene (2): To a solution of **1** (3.0 g, 13.5 mmol) in dry acetonitrile (80 mL) was added dry K_2CO_3 (5.5 g, 40 mmol) and 1-bromooctane (3.0 mL, 16.1 mmol) and the solution was allowed to relux overnight. After removing the acetonitrile by rotary evaporation, the crude mixture was dissolved in DCM (100mL) and the K_2CO_3 removed using a celite plug which was then rinsed with DCM (500 mL). The crude solution was then absorbed onto silica, which was then then subjected to column chromatography (100% hexanes) to yield **2** as a clear oil (3.8 g, 11.3 mmol, 84% yield). ^{1}H NMR ($CDCl_3$, 400 MHz): δ 8.30 (d, 1H, *J* = 8 Hz), 8.16 (d, 1H, *J* = 1 Hz), 7.65 (d, 1H, *J* = 8 Hz), 7.6 (tt, 1H, *J* = 4 Hz, *J* = 4 Hz), 7.52 (tt, 1H, *J* = 4 Hz, *J* = 4 Hz), 6.67 (d, 1H, *J* = 8 Hz), 4.11 (t, 2H, *J* = 8 Hz), 1.93 (q, 2H, *J* = 12 Hz, *J* = 8 Hz, *J* = 1 Hz), 1.55 (q, 3H, *J* = 12 Hz, *J* = 8 Hz, *J* = 1 Hz), 1.31 (m, 9H), 0.90 (t, 3H, *J* = 8 Hz). ^{13}C NMR ($CDCl_3$, 400 MHz): δ 155.58, 134.35, 131.24, 127.32, 125.88, 125.68, 125.59, 122.49, 112.11, 97.11, 80.65, 68.42, 66.08, 31.97, 31.91, 29.53, 29.40, 29.33, 26.38, 22.82, 14.27. CI-HRMS (pos. ion): Calc. for $C_{18}H_{23}BrO$ 334.0932 , found 334.0929.

2-methyl-4-(4-(octyloxy)naphthalen-1-yl)but-3-yn-2-ol (3): To a stirring solution of **2** (1.8 g, 5.3 mmol) in triethylamine (40 mL) was added 2-methyl-3-butyn-2-ol (0.8 mL, 7.6 mmol) and Argon was bubbled through the solution for 5 min. After degasing the solution, Cu(I) (50 mg, 5 mol %), PPh_3 (150 mg, 5 mol %) and PdCl2(PPh3)2 (380 mg, 5 mol %) were added and the reaction was brought to 90 °C and left for 20 hrs. The reaction was then filtered, washed with diethyl ether (100 mL) and concentrated by rotary evaporation. DCM was then added (300 mL) and the organic solution was washed with H_2O (3 x 300mL), 1N HCl (3 x 300mL), H_2O (3 x 300mL) and sat. NaCl (3 x 300 mL). The organic layer was then dried over Na_2SO_4, loaded onto

silica and concentrated by rotary evaporation. The crude material was purified by column chromatography (50%/50% DCM/Hexanes) and concentrated by rotary evaporation to yield **3** as a brown oil (450 mg, 1.4 mmol, 26% yield). ^{1}H NMR ($CDCl_3$, 400 MHz): δ 8.24 (dd, 2H, *J* = 4 Hz, *J* = 0.5 Hz), 7.57 (dd, 2H, *J* = 8 Hz, *J* = 1 Hz), 7.50 (dd, 1H, *J* = 8 Hz, *J* = 1 Hz), 6.72 (d, 1H, *J* = 8 Hz), 4.12 (t, 2H, *J* = 4 Hz), 2.86 (d, 1H, *J* = 4 Hz), 1.92 (q, 2H, *J* = 12 Hz, *J* = 8 Hz, *J* = 1 Hz), 1.73 (s, 6H), 1.57 (q, 2H, *J* = 12 Hz, *J* = 8 Hz, *J* = 1 Hz), 1.31 (m, 8H), 0.91 (t, 3H, *J* = 4 Hz). ^{13}C NMR ($CDCl_3$, 400 MHz): δ 162.74, 155.53, 134.32, 131.20, 127.29, 125.87, 125.65, 125.56, 122.46, 112.12, 104.23, 97.17, 80.57, 68.39, 66.01, 31.95, 31.89, 29.51, 29.38, 29.31, 26.36, 22.80, 14.25. CI-HRMS (pos. ion): Calc. for $C_{23}H_{30}O_2$ 338.2240, found 338.2253.

1-ethynyl-4-(octyloxy)naphthalene (4): To a round bottom flask containing **3** (450 mg, 1.3 mmol) was added finely ground KOH pellets (250 mg, 4.5 mmol) and toluene (10 mL). The reaction was then refluxed for 9 hrs and upon cooling the KOH was filtered, washed using DCM, and concentrated under reduced pressure. Purification of the crude material by column chromatography (50%/50% DCM/Hexanes) yielded **4** as a brown oil (322.2 mg, 1.1 mmol, 85% yield). ^{1}H NMR ($CDCl_3$, 400 MHz): δ 8.30 (dd, 2H, *J* = 4 Hz, *J* = 0.5 Hz), 7.66 (d, 1H, *J* = 8 Hz), 7.57 (dd, 1H, *J* = 8 Hz, *J* = 1 Hz), 7.51 (dd, 1H, *J* = 8 Hz, *J* = 1 Hz), 6.75 (d, 1H, *J* = 8 Hz), 4.13 (t, 2H, *J* = 4 Hz), 3.38 (s, 1H), 1.93 (q, 2H, *J* = 12 Hz, *J* = 8 Hz, *J* = 1 Hz), 1.56 (q, 2H, *J* = 12 Hz, *J* = 8 Hz, *J* = 1 Hz), 1.31 (m, 10H), 0.90 (t, 3H, *J* = 4 Hz). ^{13}C NMR ($CDCl_3$, 400 MHz): δ 155.95, 134.61, 132.13, 127.49, 125.93, 125.78, 125.57, 122.53, 111.58, 104.20, 68.47, 31.99, 29.53, 29.41, 29.32, 26.39, 22.83, 14.27. CI-HRMS (pos. ion): Calc. for $C_{20}H_{24}O$ 280.1827, found 280.1827.

1-bromo-4-methoxynaphthalene (5): To a solution of **1** (3.0 g, 13.5 mmol) in dry acetonitrile (80 mL) was added dry K_2CO_3 (5.5 g, 40 mmol) and methyl iodide (1.2 mL, 16.1 mmol) and the solution was allowed to relux overnight. After removing the acetonitrile by rotary evaporation, the crude mixture was dissolved in DCM (100mL) and the K_2CO_3 removed using a celite plug

which was then rinsed with DCM (500 mL). The crude solution was then absorbed onto silica, which was then then subjected to column chromatography (100% hexanes) to yield **5** as a clear oil (2.89 g, 11.8 mmol, 88% yield). ^{1}H NMR ($CDCl_3$, 400 MHz): δ 8.32 (dd, 1H, J = 4 Hz, J = 1 Hz), 8.23 (dd, 1H), 7.58 (m, 3H), 6.67 (dd, 1H, J = 4 Hz, J = 1 Hz), 3.97 (s, 3H). ^{13}C NMR ($CDCl_3$, 400 MHz): δ 155.29, 132.48, 129.54, 127.84, 126.92, 126.86, 126.02, 122.51, 113.30, 104.56, 55.73. CI-HRMS (pos. ion): Calc. for $C_{11}H_9BrO$ 235.9836, found 235.9840.

4-(4-methoxynaphthalen-1-yl)-2-methylbut-3-yn-2-ol (6): To a stirring solution of **5** (1.0 g, 4.2 mmol) in triethylamine (40 mL) was added 2-methyl-3-butyn-2-ol (0.7 mL, 6.6 mmol) and Argon was bubbled through the solution for 5 min. The reaction was then filtered, washed with diethyl ether (100 mL) and concentrated by rotary evaporation. DCM was then added (300 mL) and the organic solution was washed with H_2O (3 x 300mL), 1N HCl (3 x 300mL), H_2O (3 x 300mL) and sat. NaCl (3 x 300 mL). The organic layer was then dried over Na_2SO_4, loaded onto silica and concentrated by rotary evaporation. The crude material was purified by column chromatography (50%/50% DCM/Hexanes) and concentrated by rotary evaporation to yield **6** as a brown oil (300 mg, 1.25 mmol, 30% yield). ^{1}H NMR ($CDCl_3$, 400 MHz): δ 8.28 (d, 2H, J = 8 Hz), 7.58 (d, 2H, J = 8 Hz), 7.49 (dd, 1H, J = 8 Hz, J = 0.5 Hz), 6.67 (d, 1H, J = 8 Hz), 3.94 (s, 3H), 1.76 (s, 6H). ^{13}C NMR ($CDCl_3$, 400 MHz): δ 155.83, 134.17, 131.02, 127.26, 125.82, 125.67, 125.28, 122.24, 112.41, 103.45, 97.29, 80.39, 65.89, 55.53, 31.80, 31.61. CI-HRMS (pos. ion): Calc. for $C_{16}H_{16}O_2$ 240.1145, found 240.1151.

1-ethynyl-4-methoxynaphthalene (7): To a round bottom flask containing **6** (300 mg, 1.2 mmol) was added finely ground KOH pellets (250 mg, 4.5 mmol) and toluene (10 mL). The reaction was then refluxed for 9 hrs and upon cooling the KOH was filtered, washed using DCM, and concentrated under reduced pressure. Purification of the crude material by column chromatography (50%/50% DCM/Hexanes) yielded **7** as a brown oil (179.5 mg, 0.9 mmol, 75% yield). ^{1}H NMR ($CDCl_3$, 400 MHz): δ 8.35 (dd, 2H, J = 16 Hz, J = 4 Hz), 7.72 (d, 1H, J = 8 Hz),

7.65 (tt, 1H, *J* = 8 Hz), 7.56 (tt, 1H, J = 8 Hz), 6.75 (d, 1H, *J* = 8 Hz), 4.00 (s, 3H), 3.45 (s, 1H). ^{13}C NMR ($CDCl_3$, 400 MHz): δ 156.36, 134.50, 132.02, 127.53, 125.91, 125.86, 125.35, 122.38, 111.08, 103.45, 82.21, 80.43, 55.66. CI-HRMS (pos. ion): Calc. for $C_{13}H_{10}O$ 182.0731, found 182.0736.

2-bromo-6-(octyloxy)naphthalene (8): To a solution of 6-bromo-2-naphthol (1.0 g, 4.5 mmol) in dry acetonitrile (45 mL) was added dry K_2CO_3 (3 g, 21.7 mmol) and 1-bromo octane (1.0 mL, 5.7 mmol) and the reaction was heated to reflux overnight. After allowing the reaction to cool, it was poured into H_2O (200 mL) and extracted twice with diethyl ether (2 x 100 mL). The organic layers were combined, washed with H_2O (3 x 300 mL) and sat. NaCl (3 x 300mL) and dried over MgSO4. Filtration and then removal of the solvent by rotary evaporation yielded **8** as a white crystalline (1.18 g, 3.6 mmol, 86%). ^{1}H NMR ($CDCl_3$, 400 MHz): δ 7.90 (d, 1H, *J* = 1 Hz), 7.63 (d, 1H, *J* = 8 Hz), 7.58 (d, 1H, *J* = 8 Hz), 7.49 (dd, 1H, *J* = 8 Hz, *J* = 1 Hz), 7.16 (dd, 1H, *J* = 8 Hz, *J* = 1 Hz), 7.08 (d, 1H, *J* = 4 Hz), 4.05 (t, 2H, *J* = 4 Hz), 1.85 (q, 2H, *J* = 12 Hz, *J* = 8 Hz, *J* = 1 Hz), 1.50 (q, 2H, *J* = 12 Hz, *J* = 8 Hz, *J* = 1 Hz), 1.31 (m, 8H), 0.91 (t, 3H, *J* = 8 Hz). ^{13}C NMR ($CDCl_3$, 400 MHz): δ 157.55, 133.24, 130.04, 129.75, 129.64, 128.53, 128.46, 120.22, 116.61, 68.23, 31.98, 29.53, 29.41, 29.35, 2625, 22.82, 14.27. CI-HRMS (pos. ion): Calc. for $C_{18}H_{23}BrO$ 334.0932, found 334.0932. MP: 35-40 °C.

2-methyl-4-(6-(octyloxy)naphthalen-2-yl)but-3-yn-2-ol (9): To a stirring solution of **8** (1.8 g, 5.3 mmol) in triethylamine (40 mL) was added 2-methyl-3-butyn-2-ol (0.8 mL, 7.6 mmol) and Argon was bubbled through the solution for 5 min. After degasing the solution, Cu(I) (50 mg, 5 mol %), PPh_3 (150 mg, 5 mol %) and PdCl2(PPh3)2 (380 mg, 5 mol %) were added and the reaction was brought to 90 °C and left for 20 hrs. The reaction was then filtered, washed with diethyl ether (100 mL) and concentrated by rotary evaporation. DCM was then added (300 mL) and the organic solution was washed with H_2O (3 x 300mL), 1N HCl (3 x 300mL), H_2O (3 x 300mL) and sat. NaCl (3 x 300 mL). The organic layer was then dried over Na_2SO_4, loaded onto

silica and concentrated by rotary evaporation. The crude material was purified by column chromatography (50%/50% DCM/Hexanes) and concentrated by rotary evaporation to yield **9** as a pale, yellow solid (1.27 g, 3.8 mmol, 72% yield). ^{1}H NMR ($CDCl_3$, 400 MHz): δ 7.86 (s, 1H), 7.64 (dd, 2H, *J* = 16 Hz, *J* = 4 Hz), 7.43 (dd, 1H, *J* = 8 Hz, *J* = 1 Hz), 7.15 (dd, 1H, *J* = 8 Hz, *J* = 1 Hz), 7.07 (d, 1H, *J* = 1 Hz), 4.04 (t, 2H, *J* = 4 Hz), 2.42 (s, 1H), 1.84 (q, 2H, *J* = 12 Hz, *J* = 8 Hz, *J* = 1 Hz), 1.67 (s, 6H), 1.50 (q, 2H, *J* = 12 Hz, *J* = 8 Hz, *J* = 1 Hz), 1.31 (m, 8H), 0.92 (t, 3H, *J* = 8 Hz). ^{13}C NMR ($CDCl_3$, 400 MHz): δ 157.86, 134.21, 131.39, 129.25, 129.03, 128.37, 126.76, 119.76, 117.54, 106.56, 93.47, 82.75, 68.15, 65.76, 31.93, 31.68, 29.48, 29.36, 29.29, 26.20, 22.77, 14.23 CI-HRMS (pos. ion): Calc. for $C_{23}H_{30}O_2$ 338.2240, found 338.2247. MP: 70-72 °C.

2-ethynyl-6-(octyloxy)naphthalene (10): To a round bottom flask containing **9** (400 mg, 1.2 mmol) was added finely ground KOH pellets (250 mg, 4.5 mmol) and toluene (10 mL). The reaction was then refluxed for 12 hrs and upon cooling the KOH was filtered, washed using DCM, and concentrated under reduced pressure. Purification of the crude material by column chromatography (50%/50% DCM/Hexanes) yielded **10** as a clear oil (241 mg, 0.86mmol, 72% yield). ^{1}H NMR ($CDCl_3$, 400 MHz): δ 7.91 (s, 1H), 7.67 (dd, 2H, *J* = 16 Hz, *J* = 4 Hz), 7.49 (dd, 1H, *J* = 8 Hz, *J* = 1 Hz), 7.16 (dd, 1H, *J* = 12 Hz, *J* = 1 Hz), 7.09 (d, 1H, *J* = 1 Hz), 4.04 (t, 2H, *J* = 2 Hz), 3.11 (s, 1H), 1.85 (q, 2H, *J* = 12 Hz, *J* = 8 Hz, *J* = 1 Hz), 1.50 (m, 2H), 1.31 (m, 10H), 0.91 (t, 3H, *J* = 8 Hz) ^{13}C NMR ($CDCl_3$, 400 MHz): δ 158.11, 134.56, 132.18, 129.35, 129.17, 128.30, 126.88, 119.92, 116.87, 106.59, 84.39, 68.20, 31.96, 29.51, 29.39, 29.32, 26.23, 22.80, 14.24. CI-HRMS (pos. ion): Calc. for $C_{20}H_{24}O$ 280.1827, found 280.1829.

2-bromo-6-methoxynaphthalene (11): To a solution of 6-bromo-2-naphthol (4.0 g, 17.9 mmol) in dry DMF (30 mL) was added dry K_2CO_3 (4.9 g, 45 mmol) and methyl iodide (2.8 mL, 45 mmol) and the reaction was heated to 100°C overnight). After allowing the reaction to cool, it was poured into H_2O (200 mL) and extracted twice with diethyl ether (2 x 100 mL). The organic

layers were combined, washed with H_2O (3 x 300 mL) and sat. NaCl (3 x 300mL) and dried over MgSO4. Filtration and then removal of the solvent by rotary evaporation yielded **11** as a white solid (4.1 g, 17.36 mmol, 97%). ^{1}H NMR ($CDCl_3$, 400 MHz): δ 7.92 (d, 1H, *J* = 1 Hz), 7.63 (dd, 2H, *J* = 12 Hz, *J* = 8 Hz), 7.50 (dd, 1H, *J* = 8 Hz, *J* = 1 Hz), 7.16 (dd, 1H, *J* = 12 Hz, *J* = 2 Hz), 7.09 (d, 1H, *J* = 4 Hz), 3.92 (s, 3H). ^{13}C NMR ($CDCl_3$, 400 MHz): δ 157.85, 133.03, 129.99, 129.64, 129.60, 128.48, 128.35, 119.76, 117.00, 105.72, 55.33. CI-HRMS (pos. ion): Calc. for $C_{11}H_9BrO$ 235.9836, found 235.9836. MP: 103-105 °C.

4-(6-methoxynaphthalen-2-yl)-2-methylbut-3-yn-2-ol (12): To a stirring solution of **11** (1.0 g, 4.2 mmol) in triethylamine (30 mL) was added 2-methyl-3-butyn-2-ol (0.7 mL, 6.6 mmol) and Argon was bubbled through the solution for 5 min. After degasing the solution, Cu(I) (50 mg, 5 mol %) and PdCl2(PPh3)2 (300 mg, 5 mol %) were added and the reaction was brought to 90 °C and left for 20 hrs. The reaction was then filtered, washed with diethyl ether (100 mL) and concentrated by rotary evaporation. DCM was then added (300 mL) and the organic solution was washed with H_2O (3 x 300mL), 1N HCl (3 x 300mL), H_2O (3 x 300mL) and sat. NaCl (3 x 300 mL). The organic layer was then dried over Na_2SO_4, loaded onto silica and concentrated by rotary evaporation. The crude material was purified by column chromatography (50%/50% DCM/Hexanes) and concentrated by rotary evaporation to yield **12** as a pale, yellow solid (0.776 g, 3.3 mmol, 79% yield). ^{1}H NMR ($CDCl_3$, 400 MHz): δ 7.87 (s, 1H), 7.66 (t, 2H, *J* = 8.0 Hz), 7.43 (dd, 1H, *J* = 8.0 Hz, *J* = 1.0 Hz), 7.15 (dd, 1H, *J* = 8 Hz, *J* = 4 Hz), 7.09 (d, 1H, *J* = 1 Hz), 3.92 (s, 3H), 1.66 (s, 6H). ^{13}C NMR ($CDCl_3$, 400 MHz): δ 158.40, 134.21, 131.46, 129.40, 129.17, 128.52, 126.87, 119.52, 117.72, 105.88, 93.48, 82.75, 65.86, 55.48, 53.57, 31.72 CI-HRMS (pos. ion): Calc. for $C_{16}H_{16}O_2$ 240.1150, found 240.1151. MP: 111-113 °C.

2-ethynyl-6-methoxynaphthalene (13): To a round bottom flask containing **12** (218 mg, 1.2 mmol) was added finely ground KOH pellets (250 mg, 4.5 mmol) and toluene (15 mL). The reaction was then refluxed for 12 hrs and upon cooling the KOH was filtered, washed using

DCM, and concentrated under reduced pressure. Purification of the crude material by column chromatography (50%/50% DCM/Hexanes) yielded **13** as a clear oil (157 mg, 0.86mmol, 72% yield). ^{1}H NMR ($CDCl_3$, 400 MHz): δ 7.96 (s, 1H), 7.69 (t, 2H, *J* = 8 Hz), 7.51 (dd, 1H, *J* = 8 Hz, *J* = 1 Hz), 7.17 (dd, 1H, *J* = 8 Hz, *J* = 1 Hz), 7.10 (d, 1H, *J* = 4 Hz), 3.92 (s, 3H), 3.12 (s, 1H). ^{13}C NMR ($CDCl_3$, 400 MHz): δ 158.25, 134.19, 131.89, 129.13, 128.96, 128.10, 126.63, 119.31, 116.74, 105.56, 84.02, 76.53, 55.14. CI-HRMS (pos. ion): Calc. for $C_{13}H_{10}O$ 182.0732, found 182.0734. IR: 3279, 3067, 2924, 2858, 1626, 1587, 1500, 1462, 1387, 1266, 1210, 1200, 1029, 910, 852, 818. MP: 95-110 °C.

6-bromo-2-methyl-1H-benzo[de]isoquinoline-1,3(2H)-dione (14): To a round-bottom flask containing 4-bromo-1,8-naphthalic anhydride (1.0 g, 3.6 mmol) was added methyl amine (10.0 mL, 40% solution in H_2O) and the reaction was allowed to sir for 6 hrs at room temperature. The reaction solution was then filtered and the precipitate washed with H_2O. The filtrate was then dissolved in hot ethanol, filtered, and the mother liquor stored at 0 °C overnight to yield **14** as an off-white, fluffy powder after filtration (600 mg, 2.9 mmol, 80% yield). ^{1}H NMR ($CDCl_3$, 400 MHz): δ 8.65 (d, 1H, *J* = 8 Hz), 8.55 (d, 1H, *J* = 8 Hz), 8.40 (d, 1H, *J* = 8 Hz), 8.03 (d, 1H, *J* = 8 Hz), 7.84 (d, 1H, *J* = 8 Hz), 7.82 (dd, 1H, *J* = 8 Hz, *J* = 1 Hz), 3.55 (s, 3H). ^{13}C NMR ($CDCl_3$, 400 MHz): δ 163.92, 133.39, 132.11, 131.29, 131.20, 130.68, 130.40, 128.92, 128.18, 123.05, 122.19, 27.23. CI-HRMS (pos. ion): Calc. for $C_{13}H_8BrNO_2$ 288.9738, found 288.9739. MP: 183-186 °C.

6-bromo-2-octyl-1H-benzo[de]isoquinoline-1,3(2H)-dione (15): To a solution of 4-bromo-1,8-naphthalic anhydride (2.0 g, 7.2 mmol) in ethanol (20 mL) was added 1-octylamine (2.39 mL, 8.6 mmol) and the solution was brought to relux for 12 hrs. After the reaction was deemed completed by TLC, ethanol was removed by rotary evaporation and the crude product was recrystallized from hot ethanol to give **15** as a pale, yellow solid (2.24 g, 5.76 mmol, 80% yield). ^{1}H NMR ($CDCl_3$, 400 MHz): δ 8.62 (dd, 1H, *J* = 4 Hz, *J* = 1 Hz), 8.52 (dd, 1H, *J* = 4 Hz, *J* = 1

Hz), 8.38 (d, 1H, *J* = 8 Hz), 8.00 (d, 1H, *J* = 8 Hz), 7.81 (dd, 1H, *J* = 8 Hz, *J* = 1 Hz), 4.15 (t, 2H, *J* = 8 Hz), 1.70 (q, 2H, *J* = 12 Hz, *J* = 8 Hz, *J* = 1 Hz), 1.26 (m, 10H), 0.86 (t, 3H, *J* = 8 Hz). ^{13}C NMR ($CDCl_3$, 400 MHz): δ 163.68, 163.66, 133.72, 132.09, 131.28, 131.18, 130.69, 130.26, 129.08, 128.17, 123.17,122.41, 40.77, 31.95, 29.46, 29.35, 28.22, 27.27, 22.78, 14.23. CI-HRMS (pos. ion): Calc. for $C_{20}H_{22}BrNO_2$ 387.0833, found 387.0830. MP: 80-84 °C.

6-((6-methoxynaphthalen-2-yl)ethynyl)-2-methyl-1H-benzo[de]isoquinoline-1,3(2H)-dione (Dyad 3.1): To a solution of **14** (400 mg, 1.38 mmol) in dry toluene (2 mL) was added dry triethylamine (14 mL) and **13** (251.3 mg, 1.38 mmol). Argon was bubbled through the solution for 5 min. To this solution was added Cu(I) (13 mg, 5 mol %) and $PdCl_2(PPh_3)_2$ (49 mg, 5 mol %) and the reaction was heated to 90°C for 12 hrs. After allowing the reaction to cool, the reaction was filtered to obtain the product which was rinsed with H_2O and dried under vacuum. The orange product was then taken up in hot toluene and activated charcoal was added to the hot solution. Filtration of the activated charcoal followed by rotary evaporation to remove the toluene afforded pure **3.1** as an bright orange solid (430 mg, 1.1 mmol, 80% yield). ^{1}H NMR ($CDCl_3$, 400 MHz): δ 8.81 (dd, 1H, *J* = 8 Hz, *J* = 1 Hz), 8.66 (dd, 1H, *J* = 8 Hz, *J* = 1 Hz), 8.58 (d, 1H, *J* = 8 Hz), 8.12 (s, 1H), 7.98 (d, 1H, *J* = 8 Hz), 7.86 (dd, 1H, *J* = 8 Hz, *J* = 1 Hz), 7.78 (d, 2H, *J* = 12 Hz), 7.66 (dd, 1H, *J* = 8 Hz, *J* = 1 Hz), 7.22 (dd, 1H, *J* = 8 Hz, *J* = 1 Hz), 7.16 (d, 1H, *J* = 1 Hz), 3.96 (s, 3H), 3.57 (s, 3H). ^{13}C NMR ($CDCl_3$, 400 MHz): δ 164.48, 164.21, 134.90, 132.71, 132.21, 131.76, 130.75, 130.61, 129.70, 128.93, 128.55, 128.15, 127.53, 127.31, 123.00, 119.96, 117.13, 106.05, 100.21, 86.25, 55.57, 27.22. CI-HRMS (pos. ion): Calc. for $C_{26}H_{17}NO_3$ 391.1208, found 391.1213. MP: 198 °C.

2-octyl-6-((6-(octyloxy)naphthalen-2-yl)ethynyl)-1H-benzo[de]isoquinoline-1,3(2H)-dione (Dyad 3.2): To a solution of **15** (696 mg, 1.8 mmol) in dry triethylamine (20 mL) was added PPh_3 (26 mg, 5 mol %) and **10** (503 mg, 1.8 mmol). Argon was bubbled through the solution for 5 min. To this solution was added Cu(I) (17 mg, 5 mol %) and $PdCl_2(PPh_3)_2$ (128 mg, 10 mol %)

and the reaction was heated to 90°C for 12 hrs. After allowing the reaction to cool, the reaction was concentrated *in vacuo* and purified via column chromatorgraphy (50/50 Hexanes/DCM). Recrystallization of the crude product in toluene yielded **3.2** as a green solid (752.3 mg, 1.2 mmol, 68% yield). ^{1}H NMR ($CDCl_3$, 400 MHz): δ 8.80 (dd, 1H, *J* = 8 Hz, *J* = 1 Hz), 8.65 (dd, 1H, *J* = 8 Hz, *J* = 1 Hz), 8.57 (d, 1H, *J* = 8 Hz), 8.12 (s, 1H), 7.98 (d, 1H, *J* = 8 Hz), 7.86 (dd, 1H, *J* = 8 Hz, *J* = 1 Hz), 7.77 (dd, 2H, *J* = 8 Hz, *J* = 1 Hz), 7.65 (dd, 1H, *J* = 8 Hz, *J* = 1 Hz), 7.21 (dd, 1H, *J* = 8 Hz, *J* = 1 Hz), 7.14 (d, 1H, *J* = 4 Hz), 4.18 (t, 2H, *J* = 8 Hz), 4.10 (t, 2H, *J* = 8 Hz), 1.87 (q, 2H, *J* = 12 Hz, *J* = 8 Hz, *J* = 1 Hz), 1.74 (q, 2H, *J* = 12 Hz, *J* = 8 Hz, *J* = 1 Hz), 1.31 (m, 19H), 0.88 (m, 6H). ^{13}C NMR ($CDCl_3$, 400 MHz): δ 164.20, 163.57, 158.57, 134.98, 132.60, 132.21, 130.74, 130.59, 129.62, 128.86, 128.47, 128.29, 128.04, 127.52, 127.27, 122.08, 120.27, 117.00, 106.78, 105.16, 86.25, 68.35, 40.74, 31.99, 29.51, 29.39, 28.31, 27.33, 26.27, 22.80, 14.26. ESI-HRMS (pos. ion): Calc. for $C_{40}H_{45}NO_3$+Na 610.3297, found 610.3289. MP: 114 °C.

6-((4-methoxynaphthalen-1-yl)ethynyl)-2-methyl-1H-benzo[de]isoquinoline-1,3(2H)-dione (Dyad 3.3): To a solution of **14** (246 mg, 0.85 mmol) in dry toluene (5 mL) was added dry triethylamine (5 mL) and **7** (150.3 mg, 0.82 mmol). Argon was bubbled through the solution for 5 min. To this solution was added Cu(I) (8 mg, 5 mol %) and $PdCl_2(PPh_3)_2$ (30 mg, 5 mol %) and the reaction was heated to 90°C for 12 hrs. After allowing the reaction to cool, the reaction was filtered to obtain the product which was rinsed with H_2O and dried under vacuum. The orange product was then taken up in hot toluene and activated charcoal was added to the hot solution. Filtration of the activated charcoal followed by rotary evaporation to remove the toluene afforded pure **3.3** as an bright orange solid (273.8 mg, 0.6 mmol, 70% yield). ^{1}HNMR ($CDCl_3$, 400 MHz): δ 8.88 (dd, 1H, *J* = 8 Hz, *J* = 1 Hz), 8.68 (dd, 1H, *J* = 8 Hz, *J* = 1 Hz), 8.61 (d, 1H, *J* = 8 Hz), 8.45 (d, 1H, *J* = 8 Hz), 8.35 (d, 1H, *J* = 8 Hz), 8.06 (d, 1H, *J* = 8 Hz), 7.88 (m, 2H), 7.70 (m, 1H), 7.59 (m, 1H), 6.89 (d, 1H, *J* = 8 Hz), 4.09 (s, 2H), 3.59 (s, 2H). ^{13}C NMR ($CDCl_3$, 400 MHz): δ 164.52, 164.25, 157.41, 134.45, 132.45, 131.90, 131.73, 130.74, 130.67, 128.62,

128.02, 127.56, 126.24, 125.91, 125.84, 123.29, 122.87, 121.99, 112.31, 104.04, 98.42, 90.08, 55.99, 46.15, 27.19. CI-HRMS (pos. ion): Calc. for $C_{26}H_{17}NO_3$ 391.1208, found 391.1207. MP: 260 °C.

2-nonyl-6-((4-(octyloxy)naphthalen-1-yl)ethynyl)-1H-benzo[de]isoquinoline-1,3(2H)-dione (Dyad 3.4): To a solution of **15** (117 mg, 0.3 mmol) in dry triethylamine (30 mL) was added PPh_3 (3.7mg, 5 mol %) and **4** (251.3 mg, 1.38 mmol). Argon was bubbled through the solution for 5 min. To this solution was added Cu(I) (3 mg, 5 mol %) and $PdCl_2(PPh_3)_2$ (21.3 mg, 10 mol %) and the reaction was heated to 90°C for 12 hrs. After allowing the reaction to cool, the reaction was filtered to obtain the product which was rinsed with H_2O and dried under vacuum. Recrystallization of the crude product in toluene yielded **3.4** as a yellow solid (134.1 mg, 0.23 mmol, 76% yield). ^{1}H NMR ($CDCl_3$, 400 MHz): δ 8.86 (dd, 1H, *J* = 8 Hz, *J* = 1 Hz), 8.65 (dd, 1H, *J* = 8 Hz, *J* = 1 Hz), 8.58 (d, 1H, *J* = 8 Hz), 8.43 (d,1H, *J* = 8 Hz), 8.37 (d, 1H, *J* = 8 Hz), 8.03 (d, 1H, *J* = 8 Hz), 7.85 (m, 2H), 7.68 (m, 1H), 7.58 (m, 1H), 6.86 (d, 1H, *J* = 8 Hz), 4.20 (m, 4H) 1.97 (q, 2H, *J* = 12 Hz, *J* = 8 Hz, *J* = 1 Hz), 1.73 (q, 2H, *J* = 12 Hz, *J* = 8 Hz, *J* = 1 Hz), 1.59 (q, 2H, *J* = 12 Hz, *J* = 8 Hz, *J* = 1 Hz), 1.32 (m, 15H), 0.89 (m, 6H). ^{13}C NMR ($CDCl_3$, 400 MHz): δ 164.23, 163.97, 156.73, 134.29, 132.66, 132.56, 131.69, 130.64, 128.46, 128.35, 127.92, 127.50, 126.08, 125.81, 125.74, 123.20, 122.87, 121.84, 111.71, 105.16, 104.58, 98.43, 90.01, 68.67, 40.74, 31.99, 29.55, 29.52, 29.42, 29.39, 29.33, 26.40, 22.84, 22.81, 14.26. CI-HRMS (pos. ion): Calc. for $C_{41}H_{47}NO_3$ 587.3399, found 587.3387. MP: 147 °C.

CHAPTER 4

Stimuli responsive behavior and photophysical studies of monoalkoxynaphthalene (MAN)- naphthalimide (NI) conjugated dyads

4.1 CHAPTER SUMMARY

4.1.2 Introduction

Chapter 3 describes the solid-state polymorphism in a series of conjugated donor-acceptor dyads and uses electrostatic arguments presented in Chapter 1 to rationalize their molecular packing. In Chapter 1 the propensity for NDI to self-associate in mixtures of DAN and NDI as a consequence of cooling from a liquid crystalline mesophase was briefly discussed. Chapter 4 looks at the propensity of conjugated donor-acceptor dyads to exhibit solid-state stimuli-responsive behavior and also extends our groups efforts in investigating liquid crystalline mesophases. The solution-state and solid-state photophysical properties are also investigated.

4.1.3 Goals

After thoroughly investigating the polymorphism of four conjugated donor-acceptor dyads in Chapter 3 the goal of this chapter is to explore the interconversion between the two polymorphs of the dyads which may shed light on the thermodynamics of the polymorphs. The solution and solid-state photophysical properties will also be explored.

4.1.4 Approach

The solution-state and solid-state photophysical properties of two dyads were analyzed using UV-Visible and fluorescence spectroscopy. Investigation of the dyad solid-state was carried out using polarized optical microscopy (POM), differential scanning calorimetry (DSC)

and powder X-Ray diffraction (XRD) techniques. To explore the interconversion between the two polymorphs of one dyad several types of stimuli were applied to the dyad in the solid-state.

4.1.5 Results

Two of the dyads, dyads **4.1** and **4.4**, showed a difference in solid-state color between relatively faster (yellow) and slower (yellow-orange or orange) evaporation from solution, while the other dyads, **4.2** and **4.3**, only showed one color (yellow and orange, respectively) for both evaporation rates. The solution-state photophysical properties of dyads **4.2** and **4.4** were investigated and they were found to be solvatochromic. Importantly, dyad **4.4** displayed thermochromic (orange to yellow), mechanochromic (orange to yellow) and vapochromic (yellow to orange) stimuli-responsive behavior in the solid-state with repeatable cycles of color changing. Structural and spectroscopic studies indicated that the stimuli-responsive behavior of dyad **4.4** is the result of a 180° molecular rotation wherein the presumably thermodynamically more stable head-to-head stacked orange crystalline solid interconverts with a head-to-tail stacked soft-crystalline yellow mesophase.

4.2 BACKGROUND

Strongly fluorescent, or luminescent, organic materials whose fluorescence can be finely-tuned show great potential for applications in light-emitting diodes (LEDs) (130), optoelectronic devices (131, 132), and sensing materials (133, 134). One approach attracting increased attention involves the development of molecules that show changes in their photophysical properties upon reversibly switching their solid-state morphology in response to an external stimulus. These materials are called stimuli-responsive and undergo morphological (molecular packing) changes as a result of (but not limited to) changes in temperature (thermochromic) (130, 132, 131, 133, 135, 136, 137, 138, 139, 140, 141), pH (acidchromic) (136, 139), pressure (mechanochromic) (130, 132, 131, 142) and vapor (vapochromic) (132, 135, 136, 139, 140, 142). A few examples

of these stimuli-responsive materials are shown in Figure 4.1. Currently, many of these materials show stimuli-responsive behavior towards only one type of external stimulus, thus new molecular systems responsive to multiple external stimuli are still noteworthy (136, 137, 140).

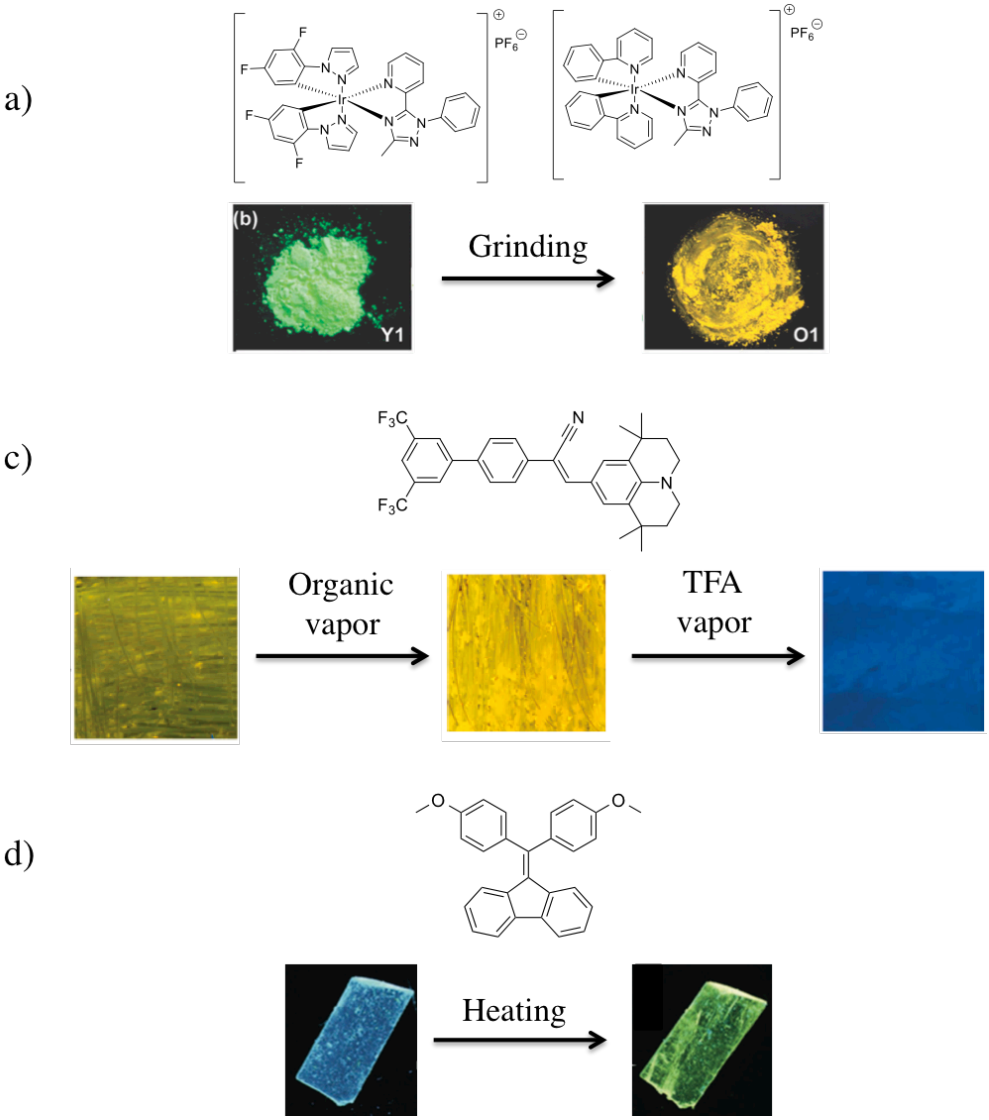

Figure 4.1 Examples of (a) mechanochromism (143), (b) acidochromism and vapochromism (136) and (c) thermochromism (130). Adapted with permission from (143) Copyright (2012) Royal Society of Chemistry, (136) Copyright (2011) American Chemical Society, (130) Copyright (2012) John Wiley and Sons.

Of the types of stimuli-responsive behavior, mechanochromic materials are still uncommon, but are attracting increased attention (134). In contrast to "normal" mechanochromic

materials, whose absorbance properties change with applied force (pressure/grinding), mechanochromic materials whose fluorescence properties change with applied force (mechanoluminescent or piezoluminescent materials) are less common. Applications for these molecules range from mechano-sensors to security papers and damage-indicators. The energetics of mechanochromic materials is typically straightforward: the material state after having been ground or pressed is often associated with a meta-stable state which can be reverted back to the thermodynamic state with additional stimuli that allows morphological changes (heating, solvent fuming, etc.) (144, 145). Stimuli-responsive luminescent organic molecules have been reported in both crystalline (146, 147) and liquid crystalline (134) systems. Variable luminescence between liquid crystal and crystalline phases has also been reported for pi-conjugated materials containing asymmetric side chains (148). Ito *et al*. reported a mechanically-induced single-crystal-to-single-crystal transformation in a material subsequently leading to a luminescent color change (from blue to green) (149).

As demonstrated in Chapters 1-3, there is a delicate balance between NDI stacking in an alternating, face-centered geometry with aromatics such as DAN, and NDI self-stacking in an off-set geometry. For example, Reczek *et al*. demonstrated that derivatives of DAN and NDI monomers mixed in a 1:1 ratio formed mesophases over a range of temperatures that exhibited a dark red color indicative of alternating, face-centered NDI-DAN stacking (29). Interestingly, for several derivatives, upon cooling from the mesophase the dark red color becomes pale yellow or even white due to unstacking of the DAN and NDI monomers into separate microdomains. These domains were shown to be composed of off-set NDI self-stacked monomers and herringbone-stacked DAN monomers (50).

Chapter 3 previously outlined the synthesis and polymorphism of a series of conjugated aromatic monoalkoxynaphthalene (MAN) and naphthalene imide (NI) donor-acceptor (D-A) dyads **4.1** – **4.4** (150) (Figure 4.2). During our investigation of the photophysical properties of dyads **4.1** – **4.4**, dyad **4.4** was discovered to exhibit extensive stimuli-responsive behavior when exposed to heat, pressure and solvent vapor.

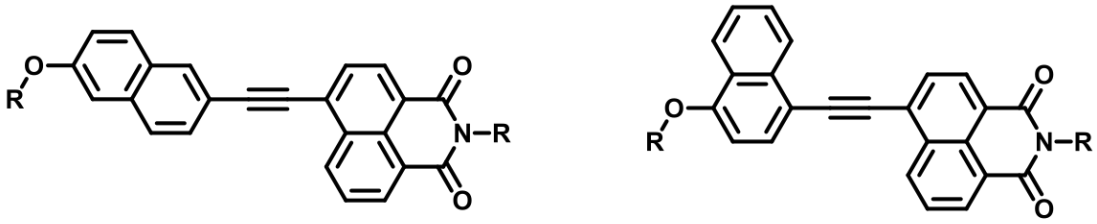

4.1: R = CH_3
4.2: R = $(CH_2)_7CH_3$

4.3: R = CH_3
4.4: R = $(CH_2)_7CH_3$

Figure 4.2 Molecular structures of dyads **4.1** – **4.4**.

4.3 RESULTS

4.3.1 Solution-state photophysical properties

The absorbance spectra and solvent dependence of **4.2** and **4.4** are nearly identical. For **4.2**, structural absorption bands were observed in non-polar *n*-hexane and toluene. Table 4.1 lists all the relevant spectroscopic data for both dyads. A broad absorption band was present for each solvent and the absorption maximum bathochromically shifted with increasing solvent polarity (Figure 4.3a and 4.3c). For **4.4** this shift changed from 403 to 419 nm from *n*-hexane to acetone, and for **4.2** this shift changed from 391 to 403 nm for *n*-hexane to acetone. Interestingly, for both dyads, the absorbance band in DCM was the most bathochromically shifted (see Table 4.1). The width of the peak as well as its solvatochromicity (or increase in Stokes shift upon increasing solvent polarity) is suggestive of an intramolecular charge-transfer (ICT) band. Given the absorption data for both dyads are very similar, one can assume that the geometry of the MAN aromatic core relative to the NI core has only a minor effect on the solution-state photophysical properties of these dyads.

A strong bathochromic shift in emission was observed upon dissolving the dyads in solvents of varying polarity (see Figure 4.3b and 4.3d). Both exhibit decreasing emission intensity upon going from *n*-hexane to acetone (a change in dielectric constant from ε 1.89 to ε

20.7). Note, Figure 4.3 was normalized so the decrease in emission was not visible. The positive solvatochromism of the emission can be seen by the naked eye with the dyads exhibiting a blue fluorescence in *n*-hexane, but a yellow/orange fluorescence in acetone (Figure 4.4a-b). In particular, emission spectra of **4.4** in various solvents revealed a bathochromic shift of 135 nm upon going from *n*-hexane (λ_{max} 444 nm) to acetone (λ_{max} 579 nm) while **4.2** shows a bathochromic shift of 133 nm upon going from *n*-hexane (λ_{max} 426 nm) to acetone (λ_{max} 559 nm). Table 4.2 lists all the relevant emission data for both dyads. While **4.4** reaches farther into the longer wavelengths than **4.2** (579 versus 559 nm, respectively), the latter reaches farther into the shorter wavelengths (426 versus 444 nm, respectively). For both dyads, the emissions exhibited broad, structureless bands in most solvents, with the exception of the highly nonpolar *n*-hexane and toluene that showed some structured bands for both dyads. The large Stokes shift observed upon increasing the solvent polarity suggests that 1) polar solvents substantially stabilize the excited states of the molecules, and 2) the absolute values of the excited state dipole moments are higher than those in the ground states (151, 152).

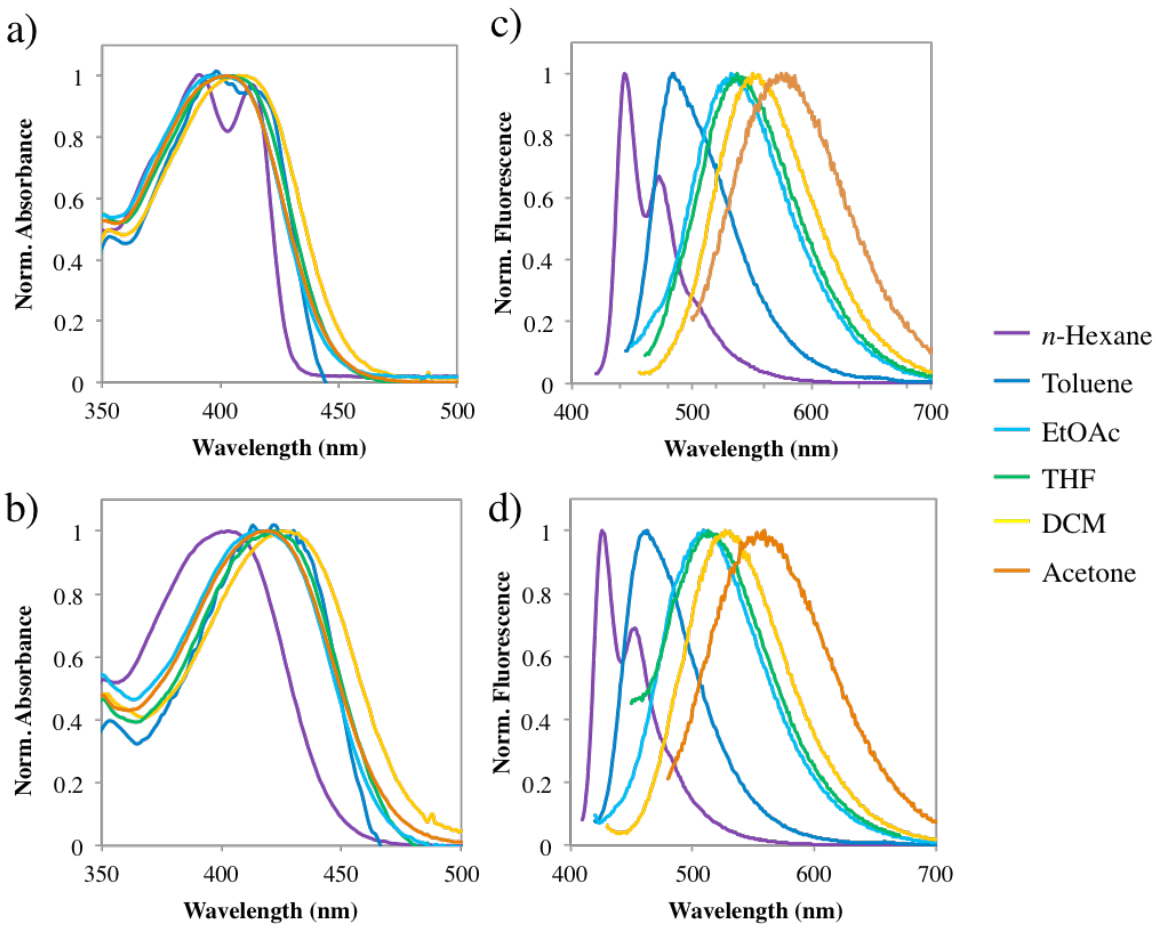

Figure 4.3. Normalized solution-state photophysical properties of **4.2** and **4.4**; (a) **4.2** absorbance spectrum; (b) **4.2** fluorescence spectrum; (c) **4.4** absorbance spectrum; (d) **4.4** fluorescence spectrum. Concentrations for UV-Vis and fluorescence studies were 50 and 20 μM, respectively.

Concentration dependent emission fluorescence measurements were performed in order to verify the mode of electron transfer in the dyad excited states. Plotting the concentration versus emission intensity gave a linear relationship indicating minimal concentration-dependent dyad fluorescence (data not shown). This result, combined with the observed solvent-dependence of both the absorbance and emission, confirms an intramolecular photoinduced-electon transfer (PET) process (rather than a Förster resonance energy transfer (FRET) process).

Solvent	λ_{max} Abs (nm)	λ_{max} Em (nm)	Quantum Yield (Φf)*	μg (D)**	μe (D)***
		4.2			
n-Hexane	391/413	426	0.50	7.39	61.26
Toluene	398/413	463	0.39		
Ethyl Acetate	400	509	0.31		
THF	405	513	0.31		
DCM	408	527	0.26		
Acetone	403	559	0.12		
		4.4			
n-Hexane	403	444	0.31	7.52	54.99
Toluene	422	484	0.22		
Ethyl Acetate	418	538	0.17		
THF	421	533	0.16		
DCM	426	551	0.15		
Acetone	419	579	0.04		

Concentrations for UV-Vis and fluorescence were 50 and 20 μM, respectively. *All absorbances were kept below 0.1 at maximum excitation wavelength. Solid-state fluorescence quantum yields were not determined. **Calculated using the DFT method in Spartan 08 at the B3LYP G-31* level. Ground dipoles for the planar geometries are shown. ***Calculated and extracted using the Lippert-Mataga relationship.

Table 4.1 Solution-state spectroscopic data for **4.2** and **4.4**.

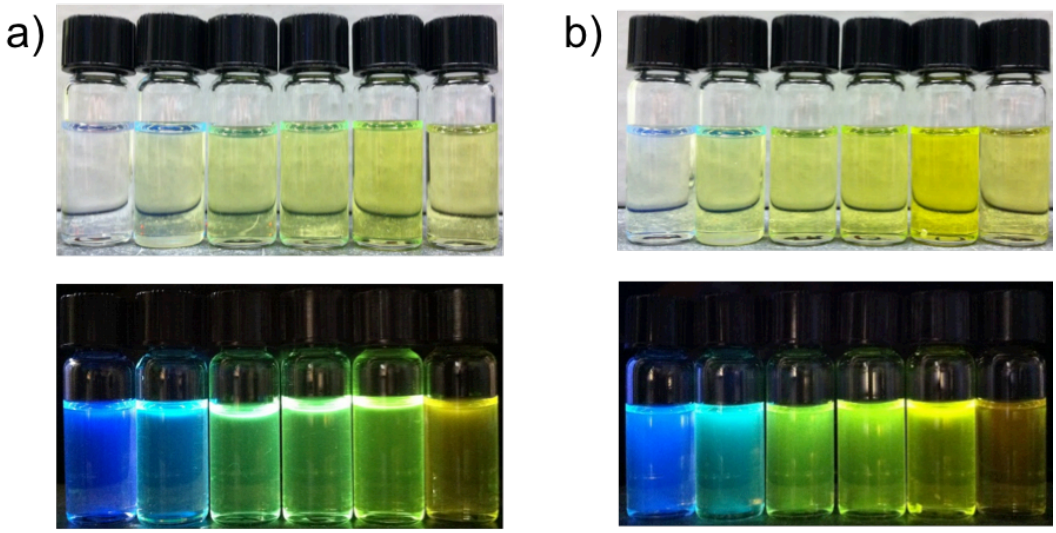

Figure 4.4 Photographs of (a) **4.2** and (b) **4.4** in solution (from *n*-hexane to acetone, left to right) under room light (top) and UV irradiation (bottom).

In order to evaluate the excited state dipole moments of the dyads, a Lippert-Mataga plot was generated. The Lippert-Mataga plot evaluates the relationship between the solvent polarity parameter (Δf) and the Stokes shift of the absorption and emission maxima ($\Delta\bar{\nu}$) using the Lippert-Mataga equation:

$$\bar{\nu}_A - \bar{\nu}_F = \Delta\bar{\nu} = \frac{2(\Delta\mu)^2}{hca^3}\Delta f + \text{constant}$$

where

$$\Delta f = \frac{\varepsilon - 1}{2\varepsilon + 1} + \frac{n^2 - 1}{2n^2 + 1}$$

and

$$a = \frac{3M}{4N\pi d}$$

where $\bar{\nu}_A$ and $\bar{\nu}_F$ are the absorption and fluorescence maxima in wave numbers (cm^{-1}), $\Delta\mu$ is the change in dipole moment ($\mu_{excited} - \mu_{ground}$), h is Plank's constant, c is the velocity of light in

a vacuum, a is the Onsager cavity radius, ε and n are the dielectric constant and refractive index of a solvent, respectively, M is the molecular weight of the molecule, N is Avogadro's number, and d is the density of the molecule (151, 152). Our calculations assume the density of our dyads is 1. For the results shown below the polarity function of the solvents were calculated using the Lippert solvent polarity function.

The calculated Onsager radii for **4.4** and **4.2** were 10.922 and 12.048 Å, respectively. The ground state dipole moments (μgD) were calculated using the DFT method at the B3LYP G-31* level and were found to be 7.52 D and 7.39 D for **4.4** and **4.2**, respectively. Using the Lippert-Mataga relationship, the excited state dipole moments (μeD) for **4.4** and **4.2** were calculated to be 54.99 D and 61.26 D, respectively, which amount to overall dipole changes of 41.81 D and 49.21 D, respectively, upon going from the ground to excited states. These calculations confirm that the excited states of both dyads have a significantly larger dipole moment, consistent with the observed solvatochromatic behavior and our DFT calculations. Quantum fluorescence yields (Φf) were calculated using the comparative method. Standards of 20, 15, 10, 5, and 2.5 μM concentrations were subjected to UV-Vis and fluorescence spectroscopy. Perylene in a solution of cyclohexane (Φf = 0.94) was used as standard due to its similar excitation range (360-420 nm) (153). For both dyads a general decrease in fluorescence quantum yield upon increasing the polarity of the solvent was observed going from 0.31-0.04 for **4.4** and 0.50-0.12 for **4.2** (see Table 1). As can be seen, the fluorescence quantum yields for **4.2** are higher than for **4.4**. Other studies using 4-donor substituted 1,8-naphthalimide derivatives (154, 155) and other dyes (139, 156) exhibit the same decrease in fluorescence quantum yield as a result of increasing solvent polarity.

4.3.2 Known solid-state polymorphism

As detailed in Chapter 3, dyads **4.1** and **4.4** were found to form two distinct forms as a function of crystal growth time. While **4.1f** and **4.4f** displayed a head-to-tail (NI-MAN aromatic

interaction) stacking arrangement upon faster evaporation from solvent, **4.1s** and **4.4f** displayed a tail-to-tail (NI-NI aromatic interaction) stacking arrangement upon slower evaporation (see Figure 4.5a-d).

a) Yellow crystals of **4.1f**

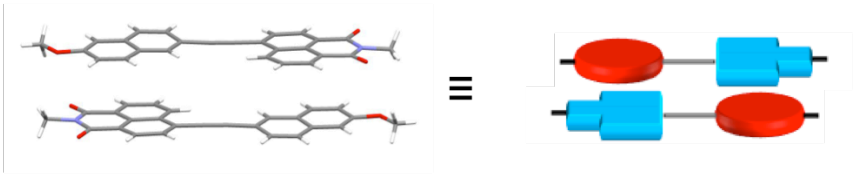

b) Yellow-orange crystals of **4.1s**

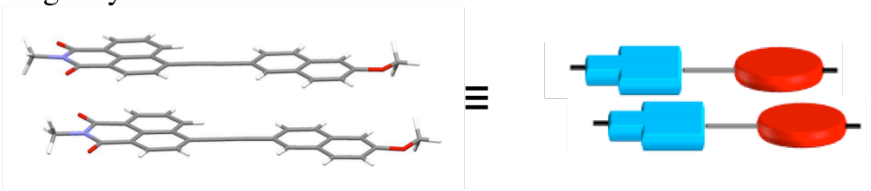

c) Orange crystals of **4.4s**

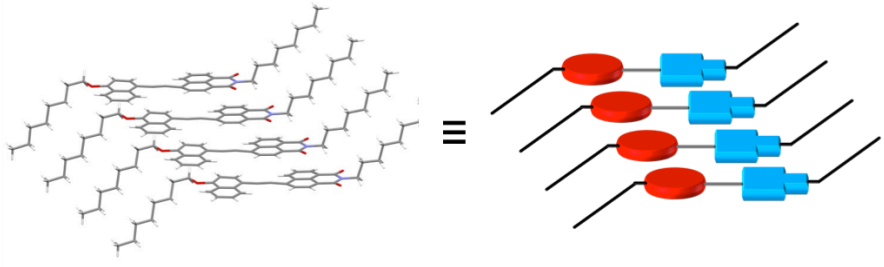

d) Proposed packing model for yellow **4.4f**

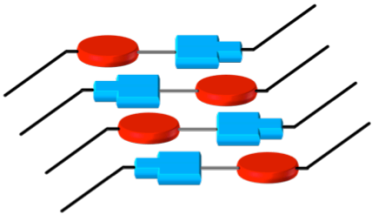

Figure 4.5. Dyad molecular packing based on single crystal X-ray analyses and modeling. (a) Crystal structure and schematic packing of slower evaporated **1f** observed to stack in a head-to-tail orientation. (b) Crystal structure and schematic packing of faster evaporated **1s** observed to stack in a head-to-head orientation. (c) Crystal structure and schematic packing of slower evaporated **4s** observed to stack in head-to-head orientation. (d) Proposed head-to-tail packing of **4f**. In the cartoons, the naphthalimide portion of the dyad is shown in blue and the monoalkoxynaphthalene portion in red. All crystal structures from (150).

Interestingly, while crystals of **4.1f** were yellow with a yellow emission, crystals of **4.1s** were yellow-orange with a yellow emission (Figure 4.6a.). Dyads **4.2** and **4.3**, which each formed only one polymorph, gave yellow and orange solids that gave yellow-green and yellow-orange emissions, respectively (Figure 4.6b-c). Yellow crystals of dyad **4.4f** produced upon slower evaporation displayed a yellow-green emission while **4.4s** orange crystals grown from slower evaporation gave orange-red emission (Figure 4.6e).

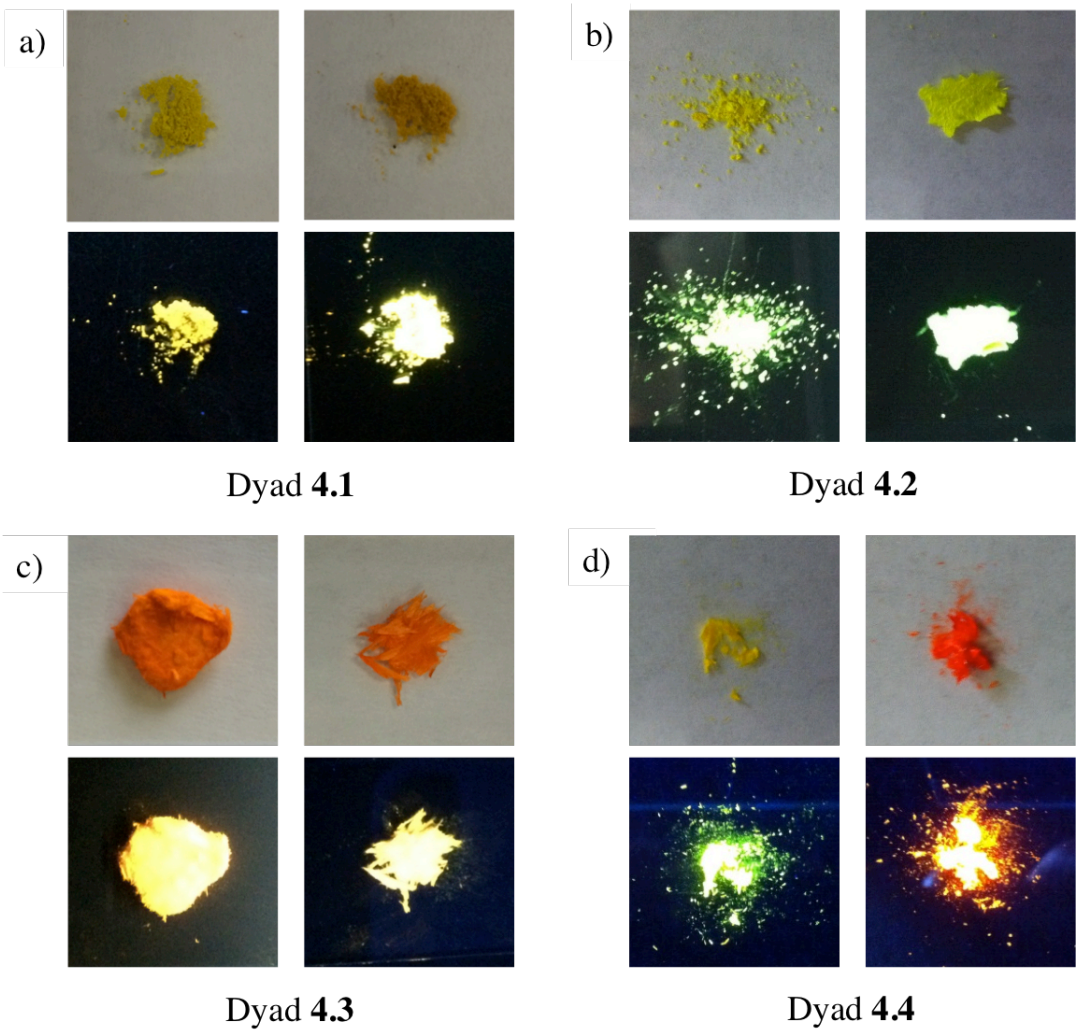

Figure 4.6 Images of dyads **4.1** – **4.4** (a) - (d). Images show the faster evaporated solid (left) and the slower evaporated solid (right).

The remainder of this Chapter will discuss the solid-state photophysical properties of **4.2** and **4.4** and the stimuli-responsive behavior of **4.4**. Although dyad **4.1** was found to form two polymorphs, its potential stimuli-responsive behavior was not investigated due to both polymorphs being difficult to discriminate without using a crystallographic analysis.

4.3.3 Solid-state photophysical properties

The solid-state absorbance and emission spectra for dyads **4.2** and **4.4** are shown in Figure 4.7. Table 4.2 lists all the solid-state spectroscopic data. For both faster and slower evaporated **4.2** an λ_{max} Abs at 398 nm is observed with a small shoulder peak at 350 nm (Figure 4.7a). **4.4f** shows a sharp absorbance peak at 398 nm while **4.4s** shows a peak at 542 nm with a smaller shoulder peak at 480 nm (Figure 4.7c).

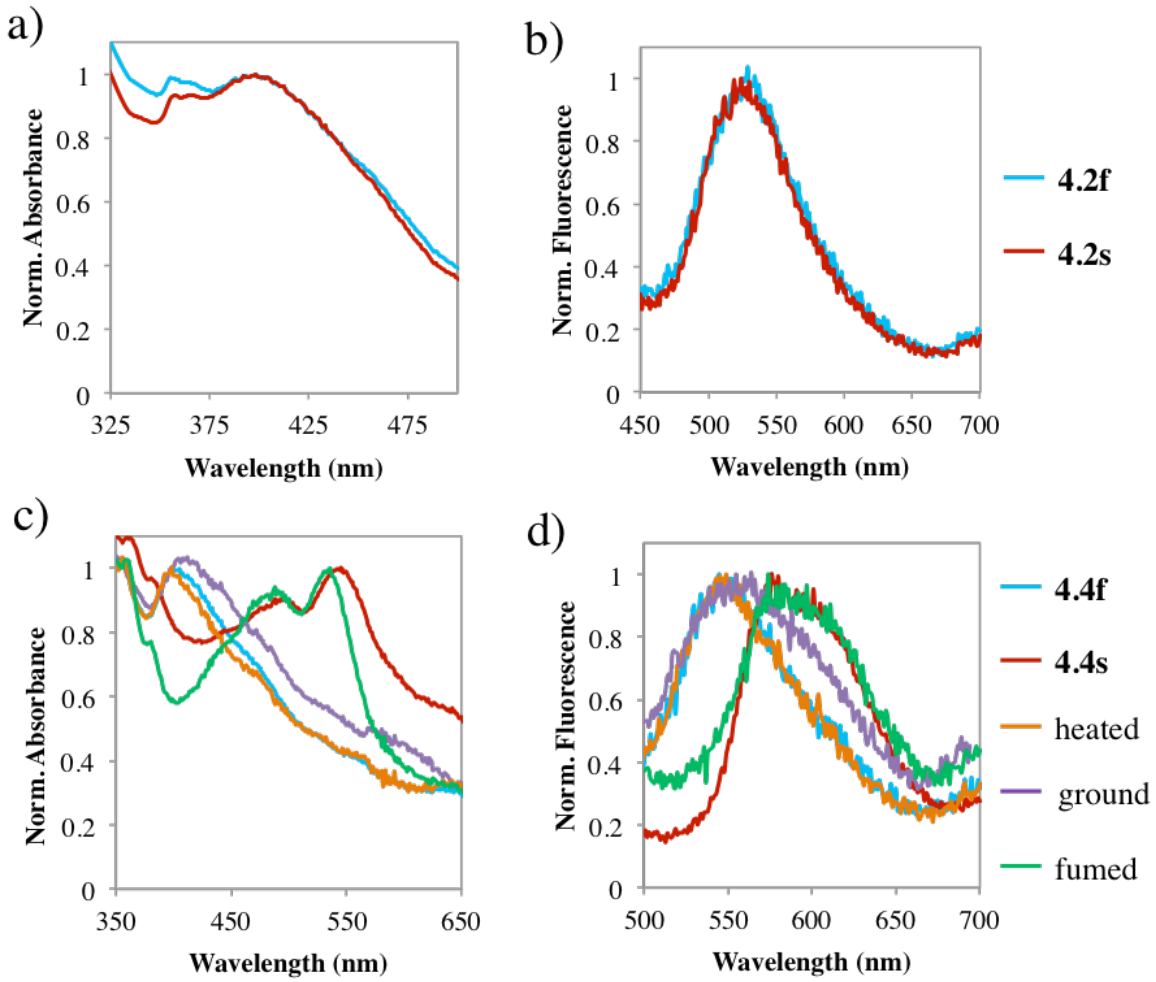

Figure 4.7 Normalized solid-state photophysical properties of **4.2** and **4.4**. (a) **4.2** absorbance spectrum; (b) **4.2** fluorescence spectrum; (c) **4.4** absorbance spectrum; (d) **4.4** fluorescence spectrum.

Solid-state emission spectra for the dyads are displayed in Figure 4.7. The emission spectra for both faster and slower evaporated **2** look nearly identical with the broad λ_{max} Em peaks occurring at 525 and 524 nm, respectively (Figure 4.7b). **4.4f** shows a strong emission at 545 nm while **4.4s** shows an emission peak at 576 nm (Figure 4.7d). Compared to the solution-state optical spectroscopy, the solid-state emission of **4.4f** and **4.4s** occur roughly where the emissions for the dyads in CH_2Cl_2 (551 nm) and acetone (579 nm) occur, respectively.

Condition	λ_{max} Abs (nm)	λ_{max} Em (nm)
	4.2	
Fast Evaporation	398	525
Slow Evaporation	398	524
	4.4	
4.4f	398	545
4.4s	542	576
After heating	398	549
After grinding	404	546
After fuming	536	574

Table 4.2 Solid-state spectroscopic data for **4.2** and **4.4**.

4.3.4 Electronic properties

To get a better understanding of the electronic nature of these dyads, the frontier molecular orbital energy levels for both **4.2** and **4.4** were calculated using the DFT method at the B3LYP G-31* level (shown in Figure 4.8). For each dyad, two geometries were used: a planar geometry, in which the rotation angle between the donor and acceptor moieties is 0° (as observed in the crystal structures for **4.4s**, **4.1f** and **4.1s**, and what **4.2** and **4.4f** are assumed to look like), and a twisted geometry, in which the donor and acceptor moieties are angled 90° to each other. The calculated HOMO and LUMO energy levels are listed in Table 4.3. As shown below, the HOMOs of both dyads in both geometries are similar and resides primarily on the relatively more electron-rich MAN while the LUMOs for both dyads in both geometries are similar and are located primarily on the relatively electron-deficient NI. In the planar conformations, both the HOMOs and LUMOs are slightly delocalized across the alkyne linker while the twisted conformation shows no delocalization of the HOMO and LUMO. This effect is common in

frontier molecular orbital calculations of planar verses twisted aromatic molecules (151, 157, 158). The physical separation between the HOMOs and LUMOs of each dyad is consistent with internal charge-transfer (ICT) and the previously mentioned solvatochromism studies (132, 139). The relative similarities between the HOMO and LUMO energy levels of the dyads indicate that the geometry of the MAN aromatic unit relative to the NI aromatic unit likely plays only a small role in the photophysics of the dyads.

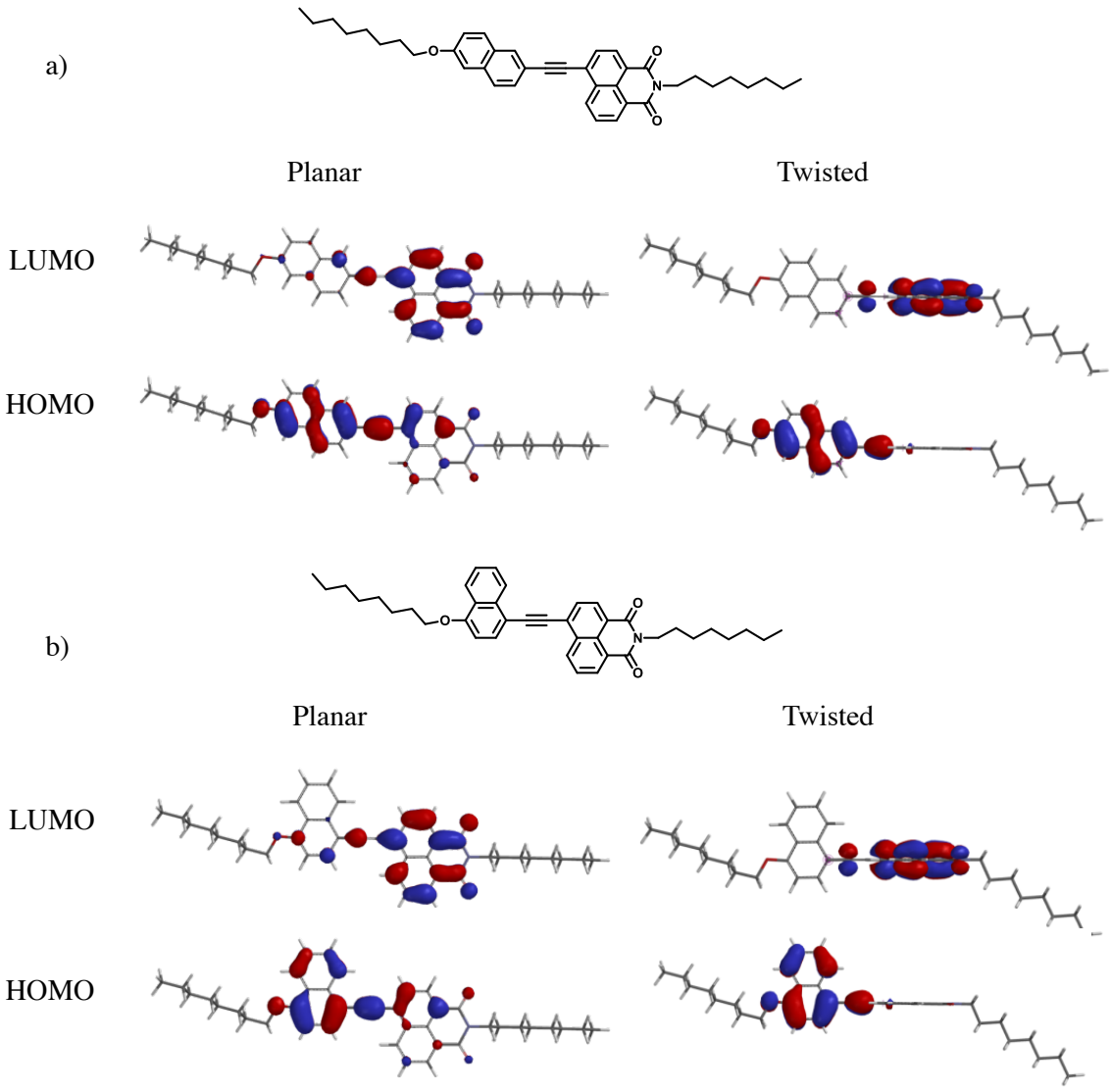

Figure 4.8 Calculated frontier molecular orbitals for (a) **4.2** and (b) **4.4** in planar and twisted geometries using the DFT method in Spartan 08 at the B3LYP G-31* level.

Alkyne Geometry	4.2			4.4		
	HOMO	LUMO	Gap	HOMO	LUMO	Gap
Planar	-5.60	-2.51	3.09	-5.46	-2.48	2.97
Twisted	-5.75	-2.47	3.27	-5.58	-2.46	3.11

Calculated using the DFT method in Spartan 08 at the B3LYP G-31* level. Energies in eV.

Table 4.3 Calculated HOMO and LUMO energy levels for **4.2** and **4.4**.

4.3.5 Thermochromic properties

Upon heating crystals of **4.4s** at 110 °C for 30 seconds, an obvious and dramatic color change from orange to yellow occurred while remaining in a solid phase (Figure 4.9). Importantly, the yellow form did not revert back to the initial orange color for the duration of the study (12 months when stored at room temperature). Heating either **4.2f** or **4.2s** did not result in any color change.

In multiple examples, the thermochromic change from orange to yellow was observed to begin on the edge of the orange crystal, working its way inward, then ending towards the middle. In fact, heating does not change the macroscopic morphology of the original crystal, indicating that reorganization of the dyad packing is occurring at a microdomain level (29, 50).

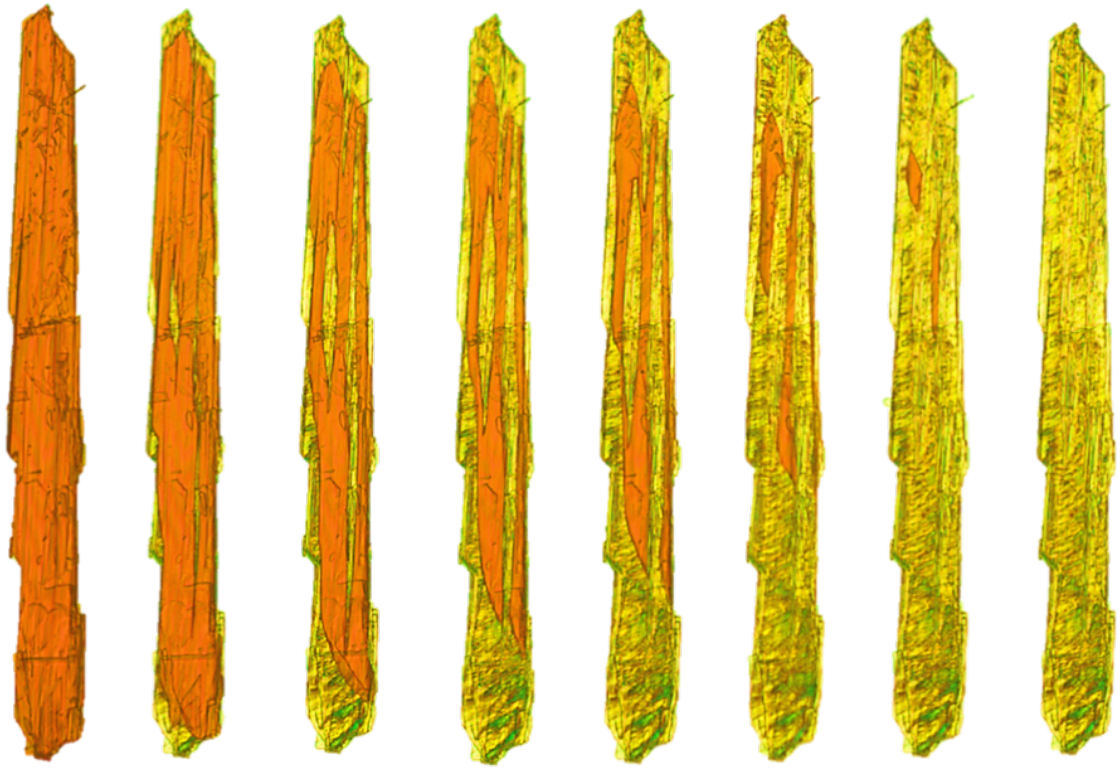

Figure 4.9 Photographs of the thermochromic behavior of **4.4s**. Optical microscope images of heating **4.4s** at 110 °C showing the conversion to a yellow form after 30 seconds without any change in macroscopic morphology of the crystal.

4.3.6 Mechanochromic and vapochromic properties

Upon taking a sample of **4.4s** and grinding it with a pestle, the orange solid turned yellow indicating that the material is mechanochromic (mechanoluminescent) in nature. As shown in Figure 4.10a, the initials for The University of Texas at Austin "UT" were ground into a glass plate covered with orange **4.4s** thus making the initials yellow.

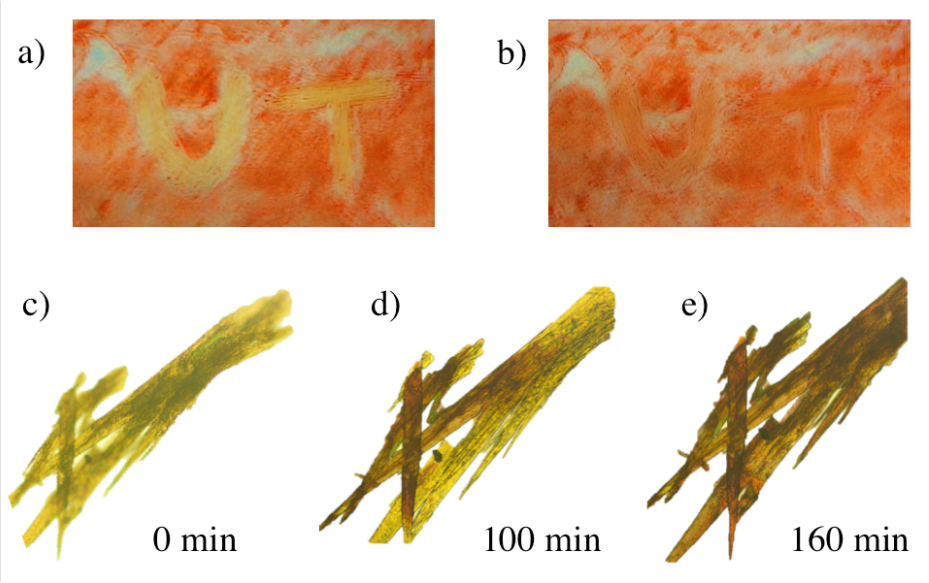

Figure 4.10 Mechanochromic and vapochromic behavior of **4.4**. (a) The initials "UT" appear in yellow after grinding with a glass rod a glass plate coated in **4.4s**. (b) Vapor-fuming of the glass plate shown in (a) reverts the yellow "UT" initials back to orange. (c) – (e) Crystals of **4.4s** were placed on a glass slide and heated at 110 °C and converted to the yellow form. The yellow solid was transferred to a vapor-fuming chamber containing DCM. The glass slide was transferred between the optical microscope and the fuming chamber to collect images of the transformation every 20 minutes. Images captured at time equals 0, 100 and 180 minutes are presented.

Subjecting the glass plate on which "UT" had been mechanically ground to vapor-fuming with CH_2Cl_2 reverted the yellow "UT" letters back to orange (Figure 4.10b). Similarly, subjecting a sample of either the yellow solid formed after grinding **4.4s**, or the yellow solid formed after heating **4.4s,** to vapor-fuming with a 1:1:1 mixture of CH_2Cl_2:MeOH:Acetone at room temperature and ambient pressure yielded orange crystals (or solid in the case of the ground material) after a period of 1 day (overnight). Vapor-fuming of quickly formed solid **4.4f** with 100% CH_2Cl_2 also gave a color change to orange crystals over the course of 1 day (Figure 4.10c-e), however, vapor-fuming with *n*-hexane or MeOH over 1 week did not have any effect on the color of the crystals (stayed yellow).

4.3.7 Shearing and texture properties

Interestingly, when a single crystal of the initially evaporated yellow **4.4f** is sandwiched between two glass slides and a shear force applied the crystal material smeared (Figure 4.11a). As seen in Figure 4.11b, when the same shearing force was applied to crystals of **4.4s** the crystals broke into smaller shards retaining their crystalline form.

Upon drop-casting a solution of **4.4** from CH_2Cl_2 onto a glass slide (leaving a yellow solid after rapid evaporation) and looking at the solid under cross-polarized light using a polarized OM (POM) spherulite-like textures were observed (Figure 4.12a).

With this result in mind, crystals of **4.4s** were heated on a hot plate past their melting point (~130 °C), then allowed to sit at 150 °C for 5 minutes, and then slowly cooled at a rate of 5 °C per minute to room temperature. Investigation of the resulting yellow material under cross-polarized POM revealed spherulite-like textures similar to those shown by drop-casting a solution of **4.4** at room temperature (Figure 4.12b).

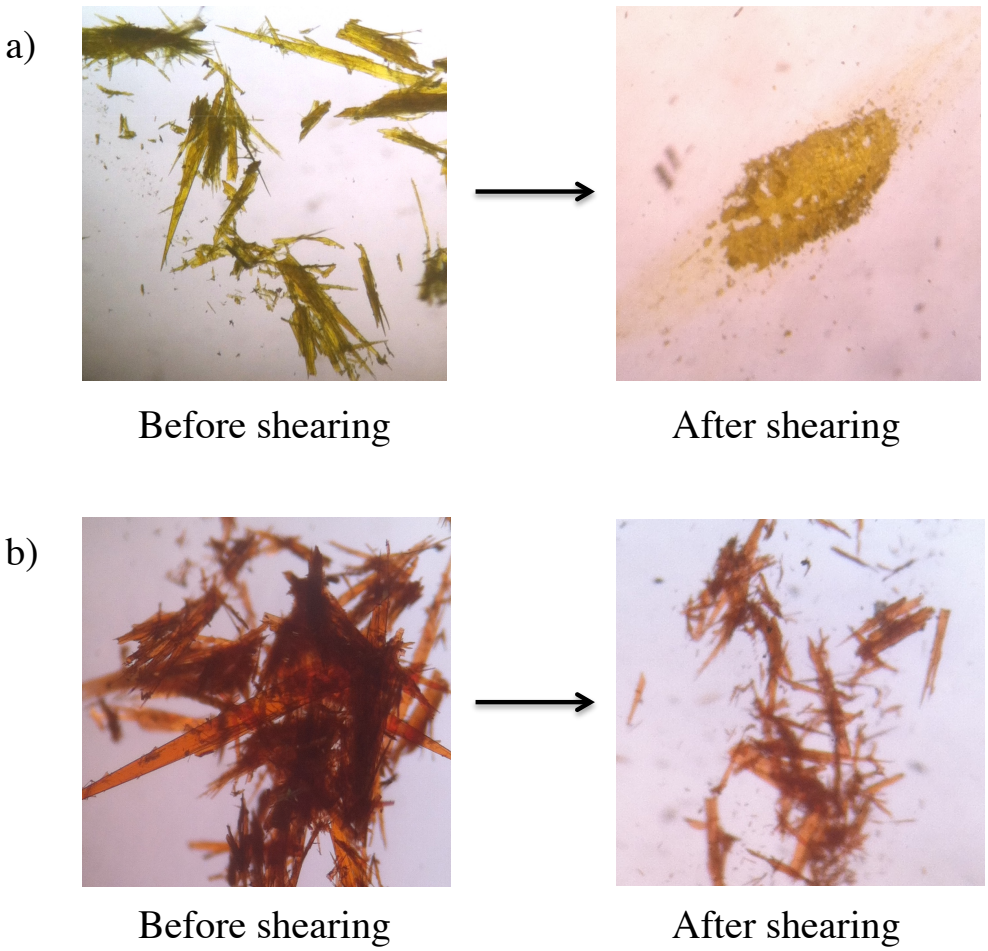

Figure 4.11 Photographs of shearing effects on (a) **4.4f** and (b) **4.4s**. While **4.4f** smears, **4.4s** remains crystalline.

4.3.8 Liquid Crystalline Mesophase Properties

Further investigation of the crystallization process of **4.4** was carried out using a POM. To this end, solid **4.4s** was placed on a microscope slide and subsequently placed on a hot stage attached to the POM and heated to its melt. The sample was then cooled at a rate of 5 °C/min and the crystallization process observed. Surprisingly, at ~ 125 °C, fan-like liquid crystal textures emerged that were characteristic of a Smectic A (SmA) liquid crystalline mesophase (Figure 4.12c). This texture remained until the material was cooled to 115 °C, at which point the SmA texture disappeared.

a) Soft crystalline mesophase after drop-casting

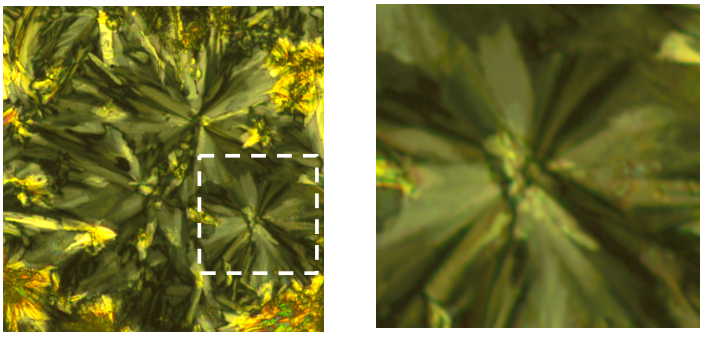

b) Soft crystalline mesophase after cooling from melt

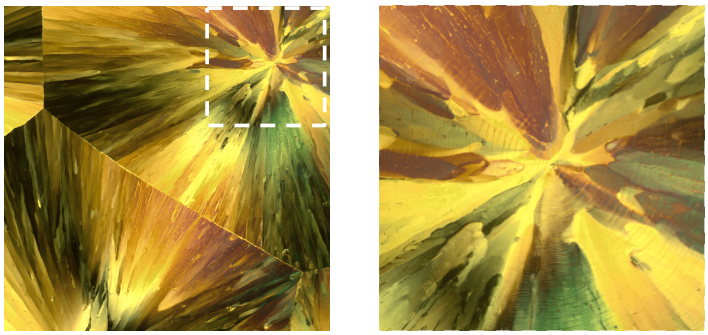

c) Smectic A liquid crystal mesophase

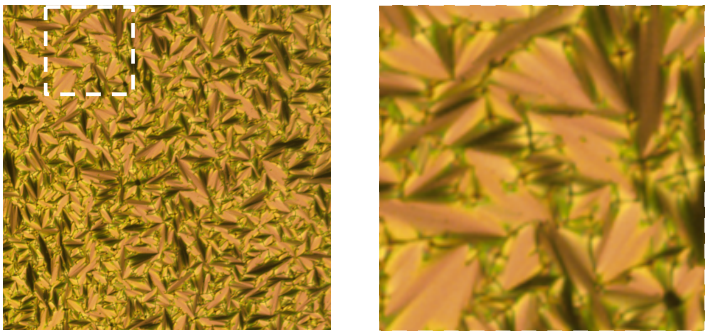

Figure 4.12 Representative POM images of the soft crystalline and liquid crystalline mesophases of **4.4**. (a) Soft crystalline mesophase of **4.4f** after drop-casting on a glass slide at room temperature; (b) Soft crystalline mesophase of **4.4f** after having been slowly cooled from the isotropic state; (c) Fan-like Smectic A textures in the liquid crystalline mesophase state of **4.4** at an elevated temperature. Images on the right are blown-up sections of the white dashed boxes on the left images.

4.3.9 Thermal analysis

Thermal analysis using DSC of **4.4f** showed a large endothermic transition at 133.68 °C (14.85 kJ/mol) corresponding to the melting point of the dyad (Figure 4.13a). The DSC heating trace for **4.4s**, however, showed a broad endothermic peak at 98.39 °C (38.8 kJ/mol) as well as a larger endothermic peak at 132.49 °C (19.5 kJ/mol). Both of these DSC traces can be repeated using the non-crystalline solid material for both the relatively faster and slower evaporated species with the same results in the DSC analysis. The smaller endothermic peak at 98.39 °C is strongly indicative of a phase transition (131, 159, 136, 138, 141, 142).

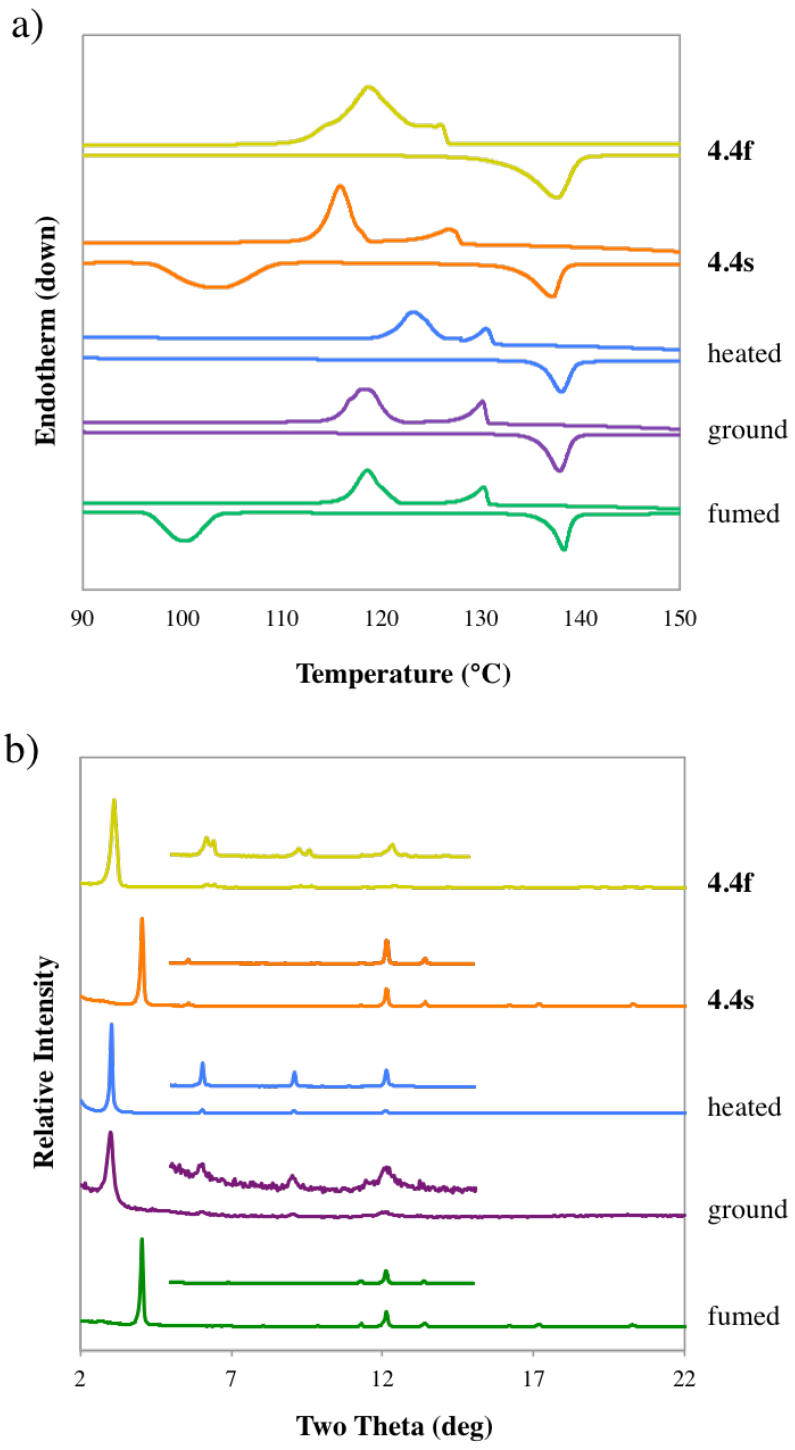

Figure 4.13 (a) DSC traces (scan rate of 5 °C /min) and (b) powder XRD patterns for **4.4f**, **4.4s** and when external stimuli are applied. Sample sizes between 3 – 5 mg were used for DSC analysis at a thermal ramp rate of 5 °C/min.

The yellow solid generated by heating **4.4s** was subjected to XRD and the obtained patterns were nearly identical to those of **4.4f** generated directly by faster evaporation (Figure 4.13a). In agreement with the images of the thermally driven orange to yellow conversion and the DSC trace, this strongly indicates that heating crystalline **4.4s** gives the soft crystalline mesophase **4.4f**.

In addition to DSC measurements, thermal gravitational analysis (TGA) was conducted to verify that the phase transition of **4.4s** to **4.4f** at ~100 °C was the result of only molecular rearrangement of the dyads and not by loss of solvent from the crystal matrix. Figure 4.14 shows the overlap of TGA and DSC curves for heating **4.4s** under the same experimental conditions (thermal ramp of 5 °C/min). While heating from 90 to 110 °C, where the solid phase transition occurs, there was a weight loss of 0.08435% which is comparable to the weight loss observed upon melting from 130 °C to 150 °C (0.09800%) on the same TGA experiment. As mentioned earlier, the crystal structure of **4.4s** did not show any solvent molecules in its crystal lattice. Taken together, these data indicate that the thermal transition from **4.4s** to **4.4f** is not due to removal of solvent from the crystal lattice, but instead rearrangement of dyad molecular packing.

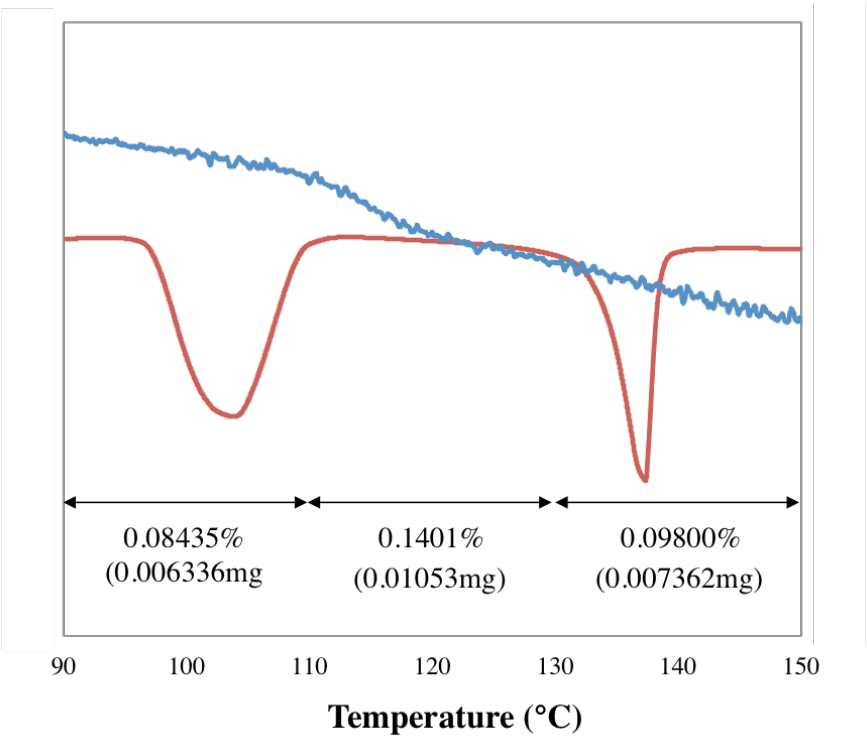

Figure 4.14 TGA (blue line) and DSC (red line) curves for **4.4** with both analyses heating at the same rate (5 °C per minute). The total sample weight for TGA was 7.5120 mg and the % weight loss as a function of temperature (90-110, 110-130 and 130-150 °C) is indicated with the double-sided arrows.

The vapor-fuming generated orange solid was analyzed in a number of ways. Optical spectroscopy revealed an absorbance maximum (536 nm) and fluorescence maximum (574 nm) that match those of **4.4s** (542 and 576 nm, respectively) as shown in Table 4.2.

Thermal analysis of the vapor-fuming generated orange solid looked very similar to that of the slower evaporated **4.4s** and yielded a broad endothermic peak at 98.39°C (45.07 kJ/mol) and a sharp endothermic peak at 134.35 °C (25.58 kJ/mol) representative of a phase transition and the melting point, respectively (Figure 4.13a) (131, 159, 136, 138, 141, 142). Two recrystallization exothermic peaks were also present at 130.21 °C (5.89 kJ/mol) and 122.26 °C (18.37 kJ/mol). Subjecting the vapor-fuming generated orange solid to XRD analysis gave a crystalline pattern that exactly matches that of the **4s** pattern (Figure 4.13b).

The back and forth conversion process of orange to yellow and yellow to orange appears to be entirely reversible. Figure 4.15 shows the maximum emission wavelengths of the solid after repeated cycles of heating and vapor-fuming and indicate that this material can undergo multiple heating-fuming cycles without significant change to the emission spectra of either state.

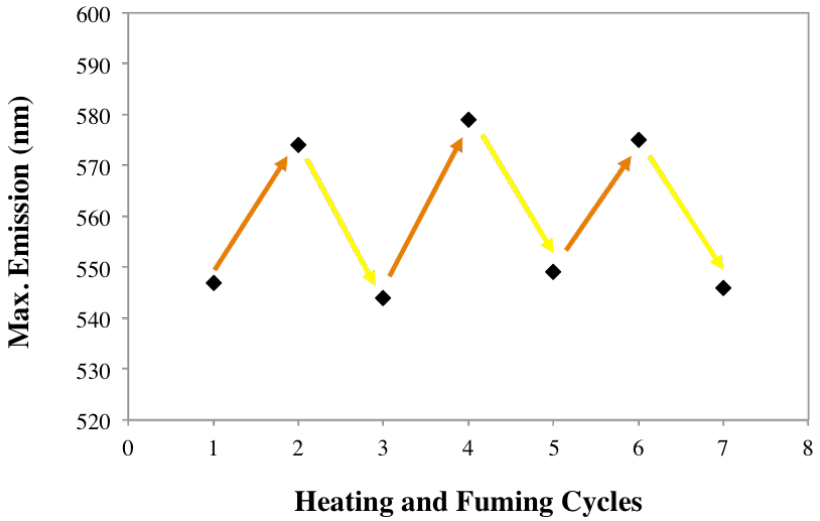

Figure 4.15 Repetitive cycles of heating and fuming **4.4** consistently give nearly the same emission maximum for **4.4f** (545 nm) and **4.4s** (576 nm).

Taken together, these data are entirely consistent with the hypothesis that crystalline orange **4.4s** is regenerated from the yellow **4.4f** by vapor-fuming. Importantly, the fuming process uses the same solvent system (1:1:1 CH_2Cl_2:MeOH:Acetone) as is initially used to generate crystals of **4.4s** suitable for single crystal X-ray analysis. Recall that no solvent molecules are seen in the X-ray analysis of **4.4s**, thus it seems likely that vapor-fuming **4.4f** back to **4.4s** is not the result of introducing solvent molecules into the solid. Additionally, repetitive cycles of heating and vapor-fuming **4.4** gave nearly the same emission maximum as the initially quickly (545 nm) and slowly (576 nm) evaporated **4.4f** and **4.4s**, respectively.

As expected, heating **4.4s** to the isotropic (Iso) state with subsequent cooling (5 °C/min) yielded two exothermic crystallization peaks at 126.84 °C (4.29 kJ/mol) and 119.03 °C (15.94

kJ/mol) with the resulting solid material being yellow (Figure 4.13a). Repeating the heating of **4.4s** using DSC with sequential slow cooling (1 °C/min from 160 °C down to 40 °C) again lead to the formation of **4.4f** with the same exothermic crystallization peaks occurring. The first crystallization event of **4.4f** (the Iso → SmA transition) displays a transition energy of ~5 kJ/mol which matches those of previously reported Iso-SmA transition energies. The second crystallization event (SmA → soft crystalline mesophase) has a transition energy of ~16 kJ/mol which is smaller than both the **4.4s** → **4.4f** (38.8 kJ/mol) and **4.4f** → Iso (19.5 kJ/mol) phase transitions. Powder XRD of this material matched that of both the initially recrystallized yellow solid **4.4f** and the heated and ground yellow solids (data not shown) indicating the structural morphology of the three solids is the same. The previously detailed drop-cast experiments demonstrated that the soft crystalline mesophase observed upon cooling **4.4** from the liquid crystalline mesophase to the soft crystalline mesophase did not retain the LC textures. Importantly, this observation revealed that between ~125 - 115 °C the yellow polymorph **4.4f** is in a liquid crystal mesophase. Upon cooling below ~115 °C **4.4f** undergoes a transition to a soft crystalline mesophase.

4.4 DISCUSSION

4.4.1 Proposed molecular rearrangement

Previously, compounds **4.1** and **4.4** were shown to form two distinct solids as a function of solvent and solvent evaporation time (150). Slower evaporation yielded yellow-orange and orange **4.1s** and **4.4s**, respectively, while faster evaporation gave yellow **4.1f** and **4.4f**. Compounds **4.2** and **4.3** gave only yellow-green solids regardless of evaporation time or solvent used. Solids **4.1f**, **4.1s** and **4.4s** were found to be crystalline. Single crystal X-ray analysis revealed a head-to-head (NI-NI interaction) stacking geometry (See Figure 4.5) for both **4.1s** and **4.4s**. On the other hand, the structure of yellow **4.1f** revealed a head-to-tail (NI-MAN interaction) geometry. Based on powder XRD analysis and detailed modeling it was concluded

that **4.4f** is also stacked in a head-to-tail (NI-MAN) geometry. Therefore, based on structural similarity to **4.1s** and **4.1f**, one can assume that interconversion of **4.1s** and **4.4f** involves a 180° rotation motion that is normal to the long axis of the molecules. Because **4.4f** is a soft crystalline mesophase while **4.4s** is crystalline, interconversion of the two also leads to a change in the dynamic mobility of the molecules after the interconversion. One could imagine the octyl side chains of **4.4f** to be more fluid-like while the aromatic center of the dyad remains crystalline thus imparting both fluid and crystalline characteristics to the polymorph. Nevertheless, it appears that both forms have at least similar packing densities as the gross macroscopic crystal dimensions and morphology do not change significantly upon heating a crystal of **4.4s** to give **4.4f** (Figure 4.9).

4.4.2 Potential differences in dyad color

The different absorbance and emission wavelengths seen in **4.4f** and **4.4s** can be attributed to at least two possible causes. First, based on analogy to the yellow **4.1f** and yellow-orange **4.1s** for which crystal structures are known, it is reasonable to propose that head-to-tail stacking of **4.4f** leads to an electronic environment that dictates shorter wavelength absorption and emission, while the head-to-head stacking of **4.4s** leads to an electronic environment that dictates longer wavelength absorbance and emission (153). Second, for the sake of completeness, the possibility that there is a different amount of twisting of the two aromatic units with respect to each other in **4.4f** vs. **4.4s** cannot be ruled out. The aromatic units are coplanar in the crystal structure of the orange **4.4s**, yellow **4.1f**, and yellow-orange **4.1s**, but evidence for the geometry of **4.4f** is missing. Our DFT calculations (Figure 4.8) predict longer wavelength absorbances and emissions in the case of highly twisted dyad structures, so a twisted structure in **4.4f** could in theory contribute to its photophysical properties although there is no evidence to support such a hypothesis.

4.4.3 Thermodynamic considerations

The presence of two forms of **4.4** that can be interconverted in the solid-state raises interesting thermodynamic questions. From the evaporation time-dependent formation of the two forms, it is intuitive to suggest that since **4.4s** takes longer to form relative to **4.4f** (10 days versus 1 day, respectively), **4.4s** is the thermodynamically more stable state. This assumption is in agreement with Ostwald's step rule (160). A similar view of evaporation-dependent kinetics has been proposed in other systems displaying polymorphic and stimuli-responsive behavior (149, 154). Upon heating **4.4f** to its melt and allowing it to cool at a rate of 5 °C/min, a liquid crystalline mesophase was observed by DSC and POM between ~ 125-115 °C while textures reminiscent of a soft crystalline mesophase was observed by POM upon cooling to room temperature. Powder XRD of the room temperature soft crystalline mesophase material matched that of yellow samples generated using other methods (**4.4** quickly evaporated from solvent, **4.4s** crystals heated without melting, or ground **4.4**), so one can assume that all of these yellow samples of **4.4f** are similarly a soft crystalline mesophase. The picture that emerges is one in which the yellow soft crystalline mesophase **4.4f** is formed faster than **4.4s** upon solvent evaporation, yet once formed, **4.4f** is kinetically trapped in the less stable state at or around room temperature.

Conversion of **4.4s** to the soft crystalline mesophase **4.4f** upon grinding appears to be in line with the behavior of several previously reported materials. In particular, it has been observed that grinding a crystalline state of a mechanochromic material generally leads to a metastable and more amorphous state (136, 138, 139, 141, 142). The conversion of **4.4f** to **4.4s** in the presence of vapor from certain solvents over a 24-hour period is also consistent with previously reported vapochromic systems. In particular, it has generally been observed that exposure to solvent vapor leads to the conversion of a metastable state to a more stable state (136) and/or conversion of a more amorphous state to a more crystalline state (132, 137, 137, 139, 140, 155). Recall that TGA and single crystal experiments revealed that there are no solvent molecules present in the crystal lattice of **4.4s**. Therefore, it can be proposed that the solvent

molecules are only playing a transient role in the crystallization process from the soft crystalline mesophase state of **4.4f**. A reasonable hypothesis is that the solvent molecules from vapor temporarily diffuse at least some extent into the solid and are able to provide a sufficient level of mobility to allow for the slow rearrangement necessary to produce **4.4s**.

In contrast to the observed mechanochromic and vapochromic behaviors, the thermochromic behavior of **4.4s** is counterintuitive and to the best of our knowledge unique among stimuli-responsive materials. One would ordinarily expect heating of a thermochromic solid to facilitate the conversion of a metastable and higher energy form, especially one that is a soft crystalline mesophase such as **4.4f**, to a presumably lower energy form such as **4.4s**, not the reverse as was observed in our study. Indeed, other thermochromic materials generally display a change from a less ordered state to more ordered state (132, 142, 155, 156) or a meta-stable state to lower energy state upon heating (130, 136, 138, 141). It is not clear why heating the presumably lower energy crystalline form of **4.4s**, while staying well below its melting temperature, would lead to the apparent complete conversion to a higher energy form, **4.4f**, especially considering a dramatic 180° reorientation required of at least half the molecules in the solid. Since both **4.4s** and **4.4f** have long-range order, the only conclusion to draw thus far is that there appears to be some structural link between the presence of dynamic motion and enhanced stability of head-to-tail stacking in **4.4f**. The exact nature of that link is currently not known.

4.5 CONCLUSIONS

In summary, the stimuli-responsive behavior of a NI-MAN conjugated dyad **4.4** in which the photophysical properties of the dyad can be switched by heating, grinding and vapor-fuming were detailed. Based on single crystal data, XRD patterns and modeling, the change in the dyad color upon external stimuli is proposed to be based on a 180° rotation relative to the long axis of the molecule. A number of other key questions remain concerning the stimuli-responsive behavior of **4.4**. For example, it is not clear why the head-to-tail assembly seen in **4.1f** and **4.4f**

forms faster relative to head-to-head stacking seen in **4.1s** and **4.4s**. Further, it is unclear why **4.4f**, despite being a soft crystalline mesophase, is prevented from returning to the apparently lower energy **4.4s** crystalline even after extended periods at room temperature (12 months).

4.6 EXPERIMENTAL

General Methods

Detailed procedures for the synthesis of dyads **4.1** – **4.4** were previously reported (150). Absorption spectra were taken on an Agilent 8453 UV-Vis spectrometer (50 μM concentrations for solution-state measurements). Fluorescence spectroscopy was performed on a PTI fluorimeter (100 nM concentrations for solution-state, 0.5 mm slits for solution-state, 2.00 mm slits for solid-state) equipped with a 814 photomultiplier detection system using a 75W xenon short arc lamp. Differential scanning calorimetry (DSC) was performed on a DSC Q100 from TA Instruments Waters (USA) at a scan rate of 5 °C/min under a Nitrogen airflow. Thermal gravitational analysis (TGA) was performed on a TA Instruments-Waters LLC TGA Q500 instrument. Powder X-ray diffraction (XRD) was obtained using a Scintag X1 theta-theta diffractometer equipped with a Cu X-ray tube and solid-state X-ray detector set to count Cu Kα radiation. X-ray crystallography was performed on a Nonius Kappa CCD diffractometer using a Bruker AXS Apex II detector and a graphite monochromator with Mo Kα radiation (λ = 0.71075 Å). Polarized optical microscopy was performed on an Olympus BX60 microscope equipped with a Mettler FP82HT hot stage and Leica digital camera. An ice-water cooling apparatus was attached to the hot stage to maintain a steady cool down rate while analyzing samples.

CHAPTER 5

Initial investigations into monoalkyoxynaphthalene-naphthalimide (MAN-NI) polymers for liquid crystal polymers and organic electronic materials

5.1 CHAPTER SUMMARY

5.1.2 Introduction

Chapter 4 explores the stimuli responsive behavior and liquid crystalline mesophase properties of monoalkyoxynaphthalene-naphthalimide (MAN-NI) dyads. This Chapter describes the initial progress made towards incorporating these dyads as side chain mesogens to polynorbornene main chain polymers. Ultimately, this Chapter serves as a well-developed outline with suggestions for future studies of these dyad-appended polymers.

5.1.3 Goals

The aim of this chapter was to investigate the liquid crystalline and electronic material properties of a set of MAN-NI appended polymers. By making side chain liquid crystal polymers composed of materials previously explored for use in organic electronic devices, these polymers have the potential for several applications down the road.

5.1.4 Approach

Four MAN-NI dyads were synthesized in a similar fashion to those in Chapter 4. However, the dyads were modified to incorporate a norbornene functional group on the MAN portion of the dyad to allow for ring-opening metathesis polymerization of the monomers. The four monomers were then polymerized and the polymers were investigated using POM, DSC, TGA, XRD and CV to establish their liquid crystalline mesophase and electronic properties.

5.1.5 Results

Ring-opening metathesis polymerization yielded four polymers in good yields (~80%) as determined by ^{1}H NMR. The PDI of the four polymers were all around 1.5 while all the polymers showed good thermal stability (~420 °C). Cyclic voltammetry showed the polymers to have LUMO energy levels around -3.3 eV and HOMO energy levels around -5.6 eV similar to other NI-donor polymers in the literature. Investigation of the polymers using POM revealed that three of the four polymers formed liquid crystalline mesophases below their respective glass transition temperatures.

5.2 Background

Liquid crystal polymers (LCPs), materials that combine the mechanical properties of polymers with the anisotropy of liquid crystal mesogens, have gained considerable attraction since their discovery in the late nineteenth century owing to their interesting optical and rheological properties (161). LCPs are used in many applications including high strength fibers, responsive optical materials, liquid crystal displays and nonlinear devices. Investigation of these materials has been directed towards two types of LCPs: “main chain liquid crystal polymers” (MCLCPs) and “side chain liquid crystal polymers” (SCLCPs). In the former the LC mesogen makes up the backbone of the polymer, while in the latter the LC mesogen is appended to the main chain of the polymer (see Figure 5.1).

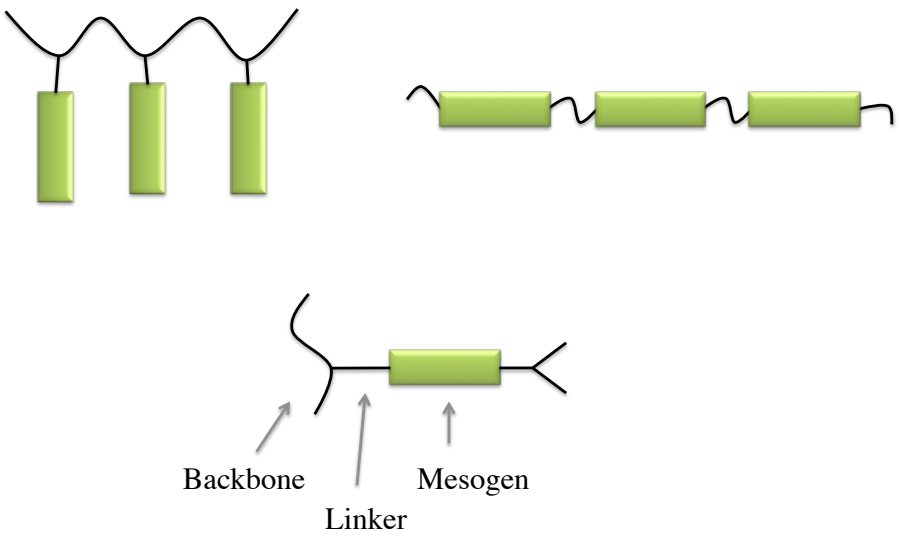

Figure 5.1 Cartoon representations of a (a) side chain liquid crystal polymer, (b) main chain liquid crystal polymer, and (c) important factors that influence SCLCP properties.

Polymer chain backbones are usually disordered and coil-like which is driven by maximization of conformational entropy. Conversely, the aromatic mesogen side chains of LCPs will self-assemble into more ordered structures to maximize their enthalpic interactions (162). To find a balance between the tendency of the polymer backbone to form a random coil and the tendency of aromatic side chains mesogens to align, the length of the linker group between the backbone and the mesogen is usually altered. For SCLCPs, if the mesogen unit is attached directly to the polymer backbone, the motion of the LC mesogen side chain unit is coupled to the polymer backbone, thus prohibiting a liquid crystal mesophase (163). However, if the mesogen is connected to the polymer using a flexible enough linker, the LC mesogen side chains can build up orientational order separate from the polymer (164).

Organic electronic systems comprised of conjugated polymers continue to be attractive materials for electronic, opto-electronic and photovoltaic devices (39). In particular, polymeric systems composed of NI-donors have been used in many applications including *n*-type semiconducting polymers (165) and electrochromic polymers (166) (see Figure 5.2).

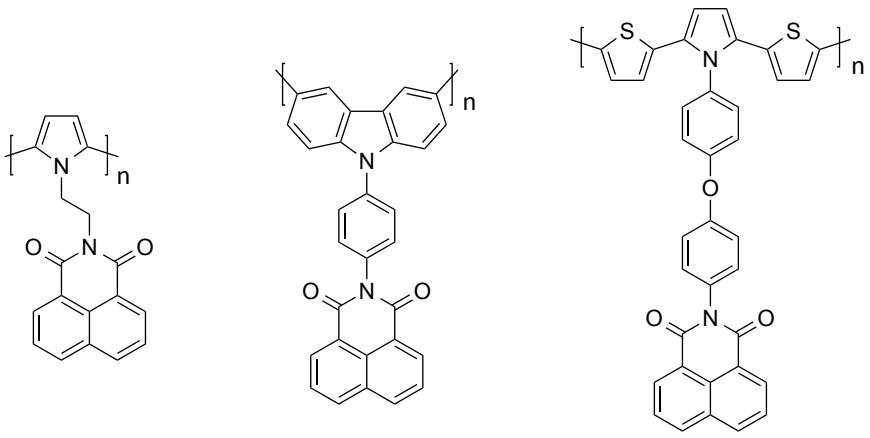

Figure 5.2 Structures of a few NI-donor polymers.

A major challenge in device fabrication for electronic polymers is the alignment of donor and acceptor moieties for efficient charge transfer through the conductive medium. Interestingly, SCLCPs provide materials composed of aromatic mesogen side chains that can be highly ordered due to favorable alignment if properly decoupled from the main chain backbone. Consequently, SCLCPs may be a candidate for organic electronic polymers due to their intrinsic highly ordered behavior (167).

This Chapter discusses the design, synthesis and characterization of four conjugated monoalkyoxynaphthalene-naphthalimide (MAN-NI) polymers and discusses their liquid crystalline and electronic properties.

5.3 RESULTS

5.3.1 Monomer Design

Several important factors influence the properties of SCLCPs including the polymer backbone, mesogen, and linker group. As previously stated, polymer chain backbones are usually disordered and coil-like (which is driven by maximization of conformational entropy), while aromatic mesogen side chains self-assemble into more ordered structures to maximize their enthalpic interaction (162). Norbornene-based polymers offer the advantage of having high thermal stabilities and are typically more solution-processable when compared to polybutadiene

counterparts (168). In addition, polynorbornene polymers have higher conformational flexibilities than polybutadiene polymers. Thus, appended mesogens can be more easily aligned potentially generating more ordered liquid crystalline mesophases (*i.e.*, smectic mesophases vs. less ordered nematic mesophases).

The monomers envisioned for polymerized had the same core design of the dyads discussed in Chapters 3 - 4 and featured a few similarities: 1) a planar design, 2) a relative ease of derivitization, and 3) an easy coupling between the MAN and NI components. To verify that norbornene-based polymer backbone would provide optimal stacking for our proposed mesogens basic modeling was perfroming of two different main chain backbone oligomers using Spartan 08 (Figure 5.3). Computation modeling showed that methyl methacrylate polymerization would cause the distance between side-chain units to be very close, such that potential packing would result in unordered side-chains packing. Calculations using norbornene polymerization showed that the distance between side-chain units would be approximately 3.5 Å in good expectation of what we see in the solid state packing for similar molecules (29, 150). According to the model, the selected spacer length of three carbons allows for enough flexibility between our dyad and the polymer backbone for the dyads to self-assemble via aromatic interactions in a stacked geometry. It is important to note that for the polynorbornene system our modeling of the norbornene monomers all occurred symmetrically (*i.e.*, all monomers were in the same direction and orientation). Experimentally the monomers may polymerize in two different orientations (up-side-down relative to one another) that may put the aromatic units slightly offset to one another.

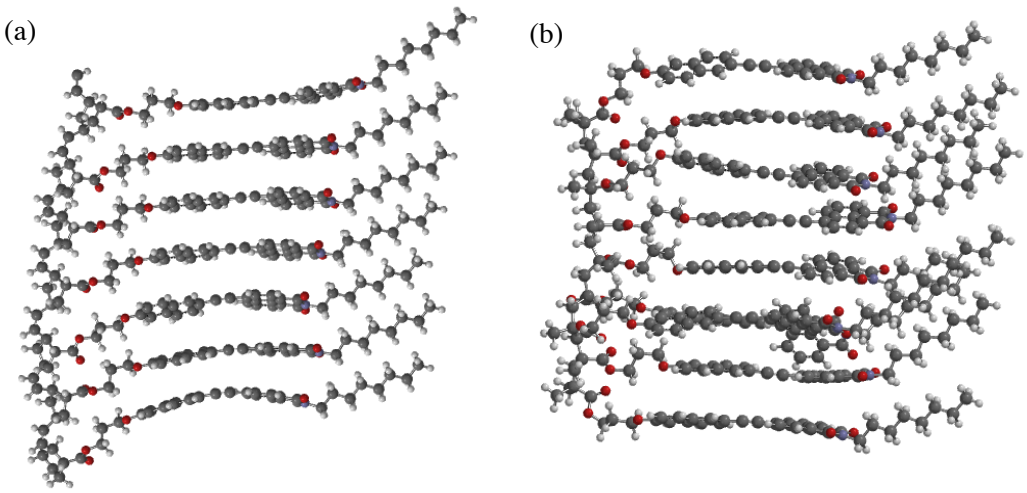

Figure 5.3 Spartan 08 modeling of short oligomers of (a) polynorbornene and (b) poly (methyl methacrylate).

5.3.2 Monomer Synthesis

The two key steps of the synthesis of **M5.1** – **M5.4** were 1) the carboxylic ester formation between the norbornene and MAN components (54 -61% yield) and 2) the Sonogashira coupling between the MAN and NI components (32 – 41% yield). See Figure 5.4 for the monomer structures. To maintain consistency between the polymers, the *endo* monomer was selectively purified (verified by ^{1}H NMR) after attachment of the norbornene functional group. Using only the *endo* conformation would ensure the reaction polymerization kinetics would be solely dependent on the *endo* isomer. ^{1}H NMR of monomers **M5.1** – **M5.4** shows the norbornene olefin peaks as quartets between 5.9 and 6.2 ppm. For **M5.2**, the *exo* isomer was observed at roughly 10% of the *endo* isomer by ^{1}H NMR.

5.3.3 Polymer Synthesis

Polymers **P5.1** – **P5.4** were obtained by conventional ring opening metathesis polymerization (ROMP) and their structures are shown in Figure 5.4. Grubbs 2nd generation

catalysis was used due to its functional group tolerance (169) and polymer yields were obtained ranging from 83 – 89%. Number average (M_n) and weight average (M_w) molecular weight of the polymers were determined using gel permeation chromatography (GPC) with polystyrene as the standard. Table 5.1 shows all the collected polymer physical characterization data. M_n values of the polymers ranged from 221 to 394 kD while the polydispersity indices (PDI) were relatively consistent between 1.38 to 1.56. As expected, ^{1}H NMR of the polymers showed significant broadening of all peaks. Importantly, the two quartet peaks corresponding to the norbornene olefin peaks (5.9 – 6.2 ppm) disappeared while a broad peak at 5.25 ppm appeared for all polymers indicative that all monomers had been successfully polymerized. ^{1}H NMR spectra for **M5.1/ P5.1**, **M5.2/ P5.2** and **M5.3/ P5.3**, **M5.4/ P5.4** are shown in Figures 5.5 and Figure 5.6, respectively.

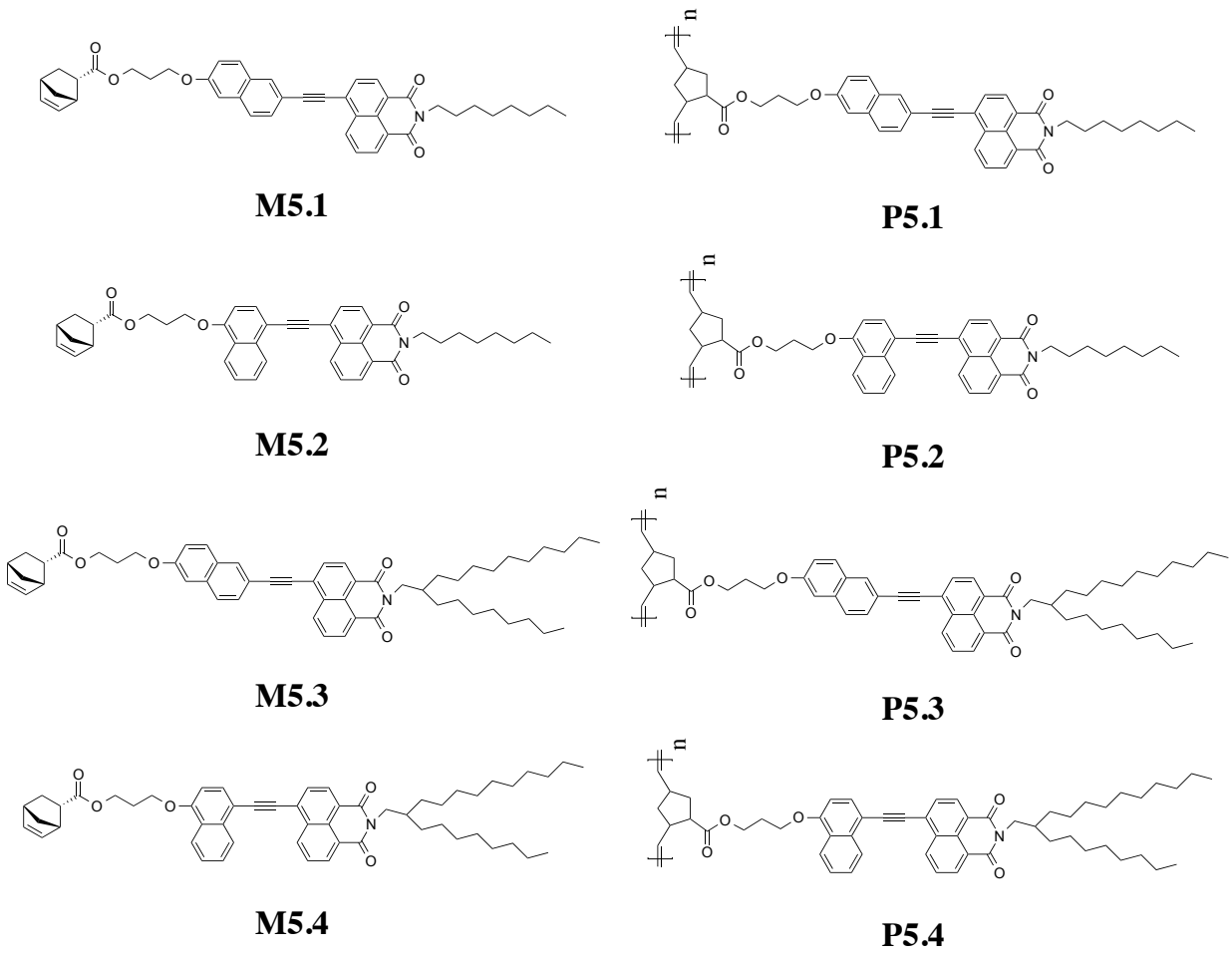

Figure 5.4 Structures of **M5.1** – **M5.4** and **P5.1** – **P5.4**.

Polymer	M_n (kD)*	M_w (kD)*	PDI*	T_g (°C)	Td (°C)**
P5.1	394	602	1.53	99	413
P5.2	289	430	1.49	98	402
P5.3	221	346	1.56	52	417
P5.4	351	484	1.38	45	418

* Polystyrene used as GPC standard. **Td at 5% decomposition.

Table 5.1 Collected polymer physical characteristics.

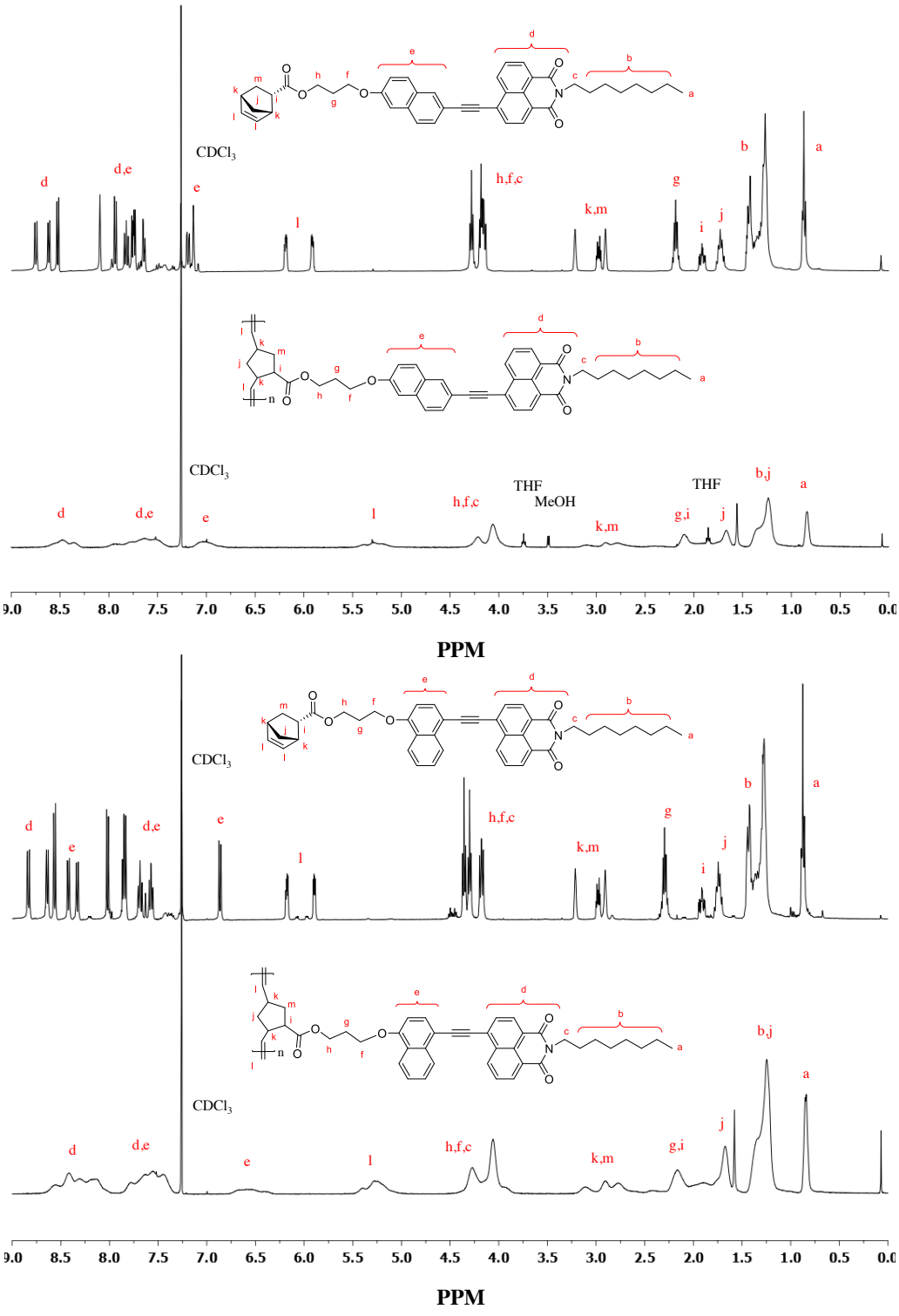

Figure 5.5 ^{1}H NMR spectra of (a) **M5.1** (top) and **P5.1** (bottom) and (b) **M5.2** (top) and **P5.2** (bottom) in $CDCl_3$.

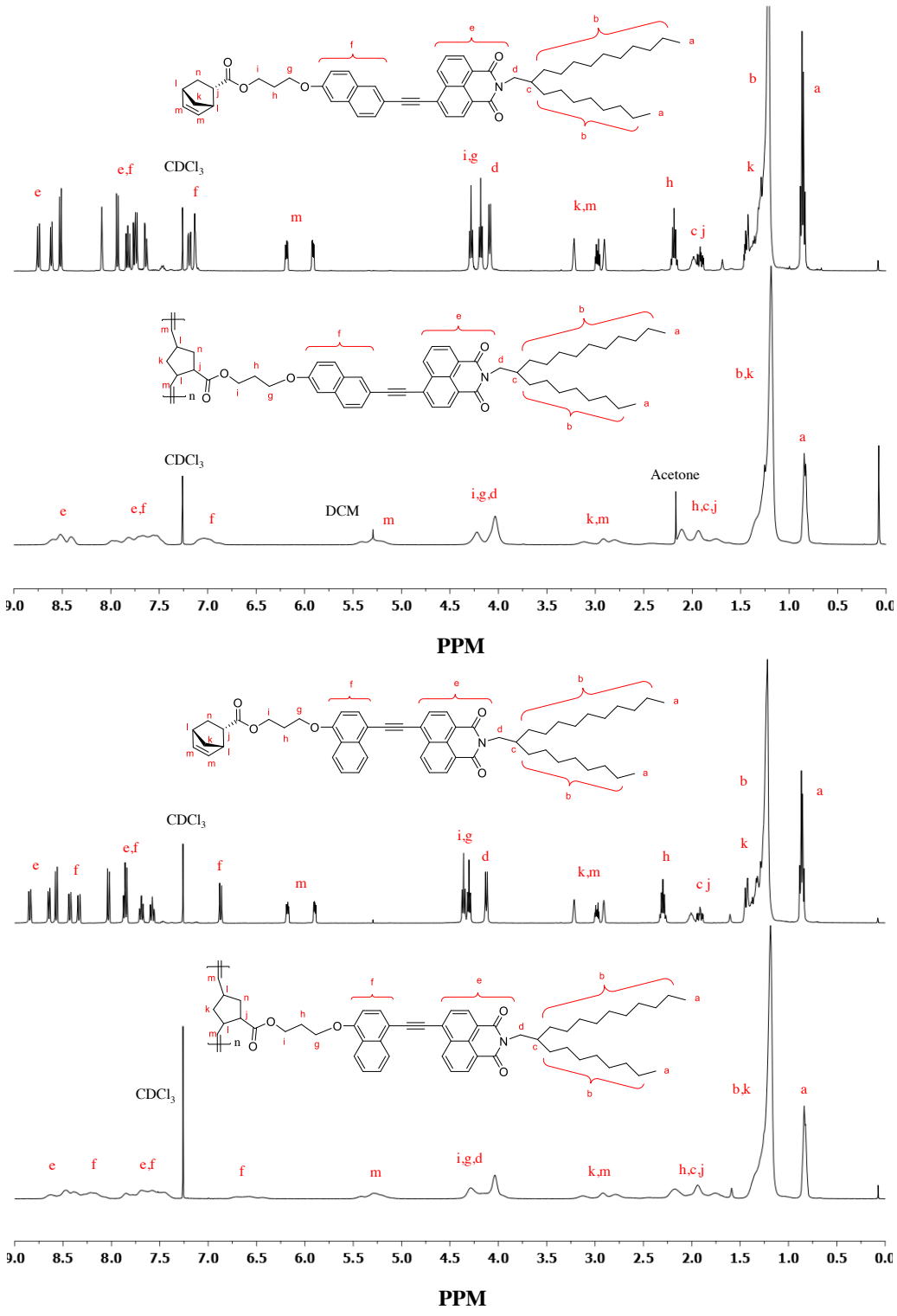

Figure 5.6 ^{1}H NMR spectra of (a) **M5.3** (top) and **P5.3** (bottom) and (b) **M5.4** (top) and **P5.4** (bottom) in $CDCl_3$.

5.3.4 Polymer thermal properties

The glass transition (T_g) temperatures of the polymers were investigated by differential scanning calorimetry (DSC) (scan rate of 10 °C/ min) (see Figure 5.7). While polymers **P5.1** and **P5.2** (both bearing octyl side chains) had T_g's at 99 and 98 °C, respectively, **P5.3** and **P5.4** (bearing the larger dodecyl octyl side chains) both showed lower T_g's at 52 and 45 °C. The thermal decomposition of the polymers at 5% (Td) were all fairly consistent between 402 – 418 °C.

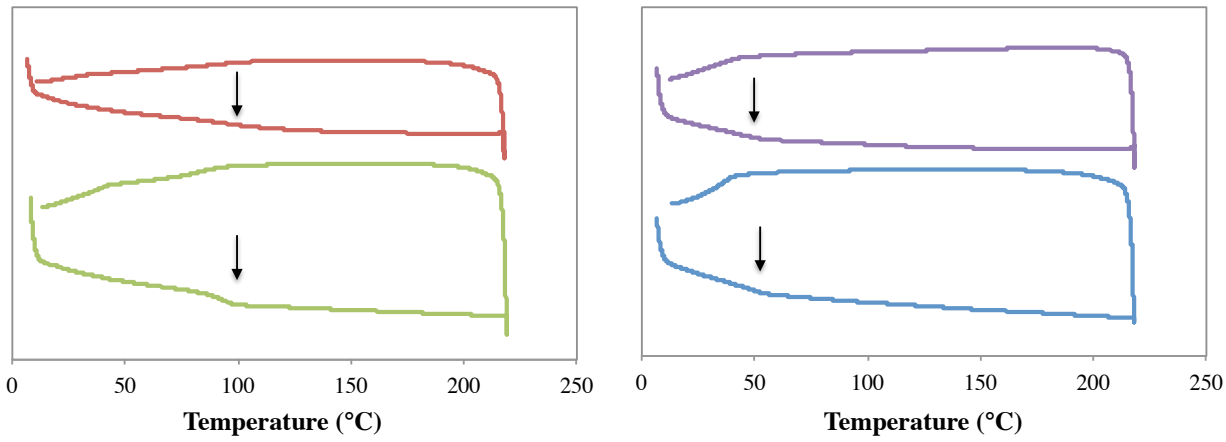

Figure 5.7 Differental scanning calorimetry curves for **P5.1** (red), **P5.2** (green), **P5.3** (purple) and **P5.4** (blue). Scans were performed at a rate of 10 °C per minute. The second heating and cooling cycles are shown.

5.3.5 Polymer optical properties

All collected photophysical data for **P5.1** - **P5.4** are located in Table 5.2. The normalized absorbance of **P5.1** - **P5.4** in CH_2Cl_2 are shown in Figure 5.8. In solution, **P5.1** and **P5.3** (2,6-donor orientations) both show λ_{max} Abs at 402 nm, **P5.2** and **P5.4** (1,4-donor orientations) show λ_{max} Abs at 420 and 421 nm, respectively. As a thin-film (drop-cast from CH_2Cl_2 onto glass slides) the polymers showed similar λ_{max} Abs with **P5.1** and **P5.3** λ_{max} Abs both at 400 nm and **P5.1** and **P5.3** at 422 and 423 nm, respectively. The absorption peaks for the polymer thin-films were slightly broader when compared to their solution state absorption peaks.

State	Property	P5.1	P5.2	P5.3	P5.4
Thin-film*	Absorbance	400	422	400	423
	Fluorescence	523	541	517	541
Solution**	Absorbance	402	420	402	421
	Fluorescence	541	560	536	556

*Drop cast from CH_2Cl_2 solution on glass slide. **CH_2Cl_2 solution.

Table 5.2 Collected photophysical data for **P5.1** - **P5.4** in solution and in as thin-films.

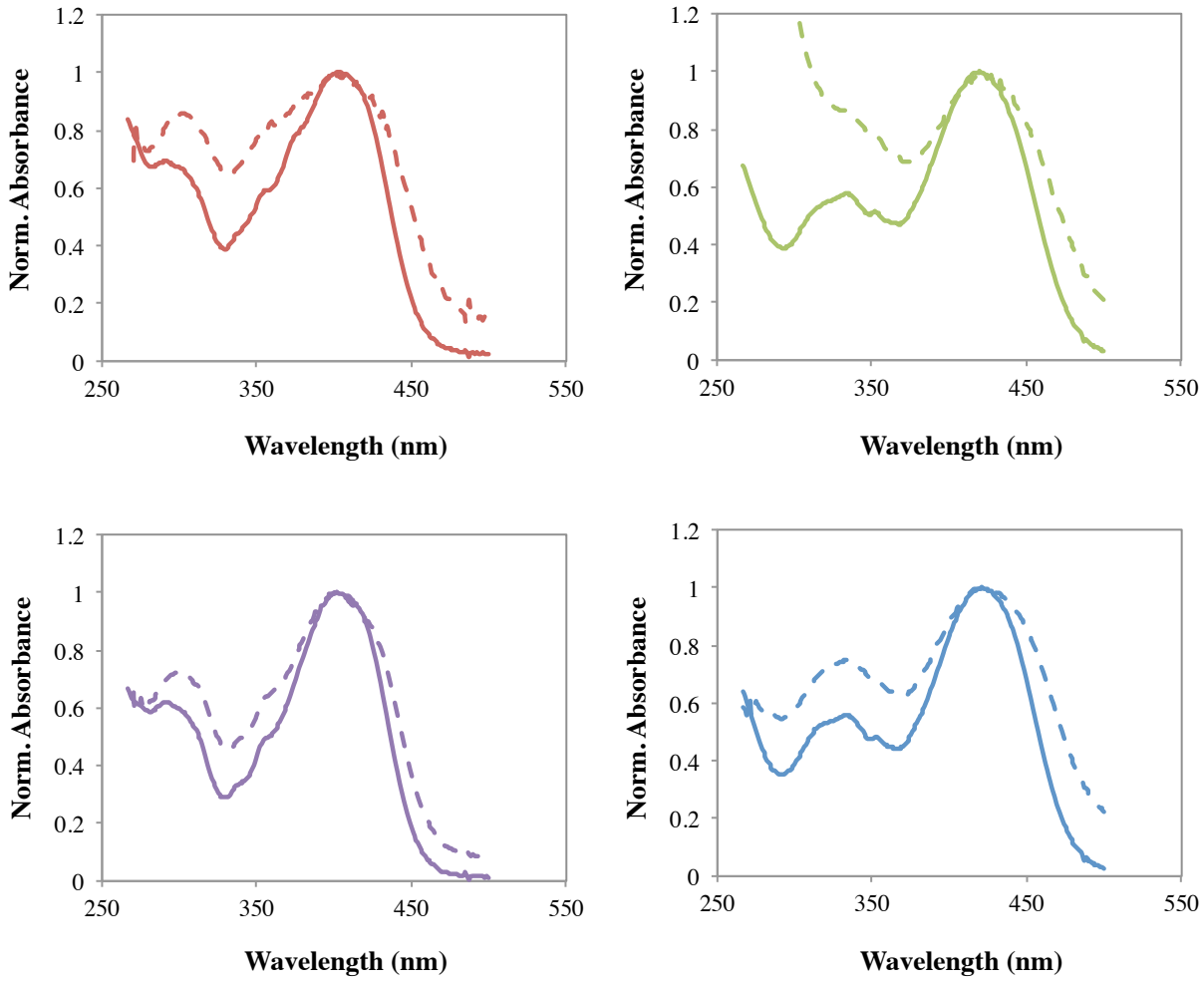

Figure 5.8 Normalized UV absorbance plots for **P5.1** (red), **P5.2** (green), **P5.3** (purple) and **P5.4** (blue) in solution (solid line, CH_2Cl_2) and as thin-films (dashed line, drop-cast from CH_2Cl_2 onto glass slides).

The normalized solution state emission for the polymers in CH_2Cl_2 are shown in Figure 5.9. While **P5.1** and **P5.3** show λ_{max} Em at 541 and 536 nm, respectively, **P5.2** and **P5.4** show λ_{max} Em at 560 and 556, respectively. Solid state fluorescence measurements for thin-films of **P5.1** and **P5.3** show λ_{max} Em of 523 and 517 nm, respectively, while **P5.2** and **P5.4** were both further red-shifted at 541 nm (Figure 5.9). Interestingly, for all polymers the solution state λ_{max} Em are bathochromically shifted 15 - 19 nm when compared to their thin-film λ_{max} Em spectra.

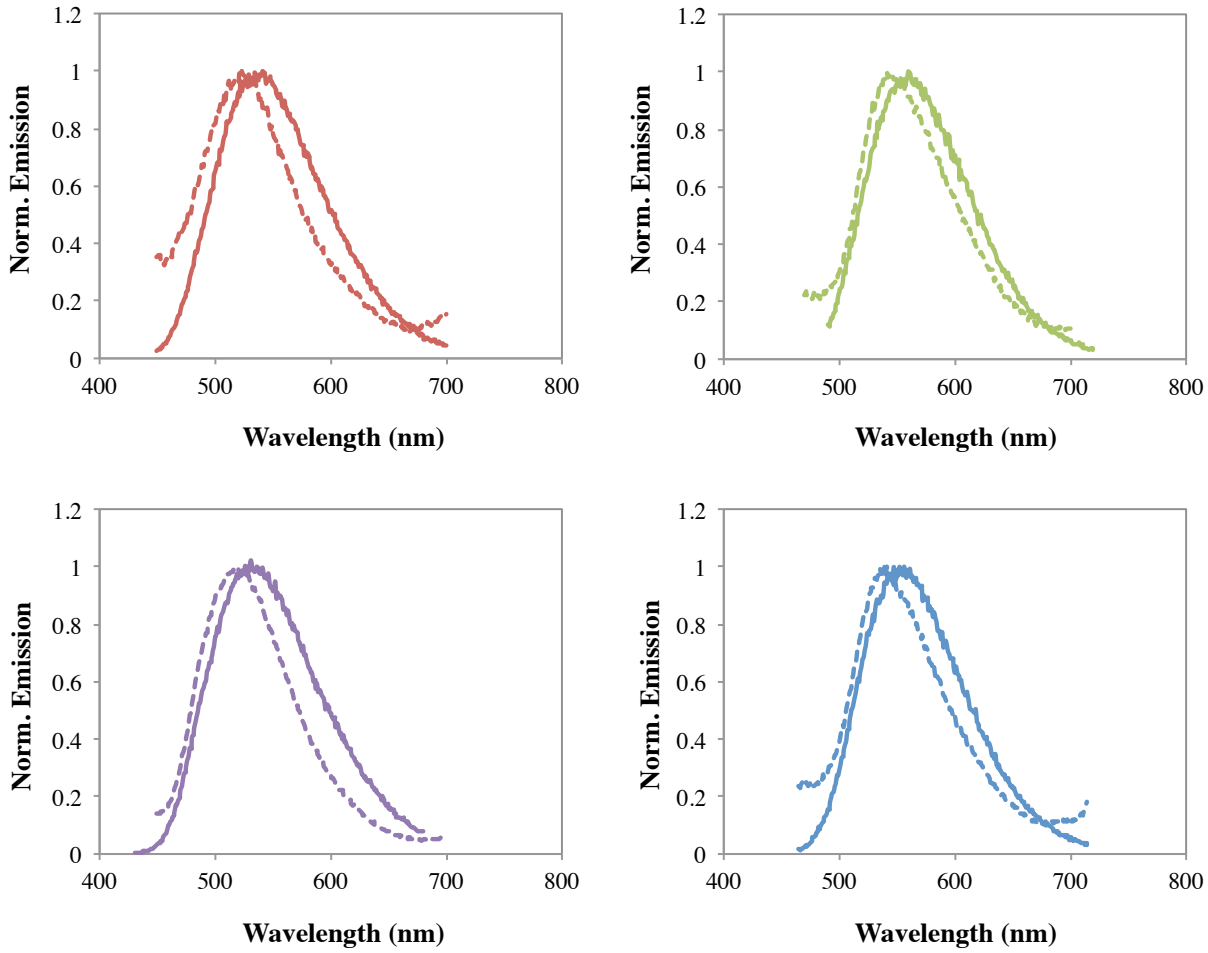

Figure 5.9 Normalized emission plots for **P5.1** (red), **P5.2** (green), **P5.3** (purple) and **P5.4** (blue) in solution (solid line, CH_2Cl_2) and as thin-films (dashed line, drop-cast from CH_2Cl_2 onto glass slides).

5.3.6 Polymer thin-film morphologies

Thin-film morphology of the polymers was analyzed using powder XRD (see Figure 5.10). Samples were prepared by drop-casting solutions of **P5.1** - **P5.4** in CH_2Cl_2 onto glass slides and drying overnight under vacuum. One large halo peak was relatively consistent in all four XRD patterns that corresponded to *d*-spacings of 3.9, 3.8, 4.1 and 3.8 Å for **P5.1**, **P5.2**, **P5.3** and **P5.4**, respectively. For each polymer a shoulder to these peaks at two theta = 32.0 ° is attributed to the glass slide diffraction (data not shown). Samples that were annealed at

temperatures above the polymer Tg's gave the same patterns as for those that were not heated. For **P5.1**, a peak at two theta = 2.56 ° was investigated by SAXS and the peak corresponded to a *d*-spacing of 34.6 Å.

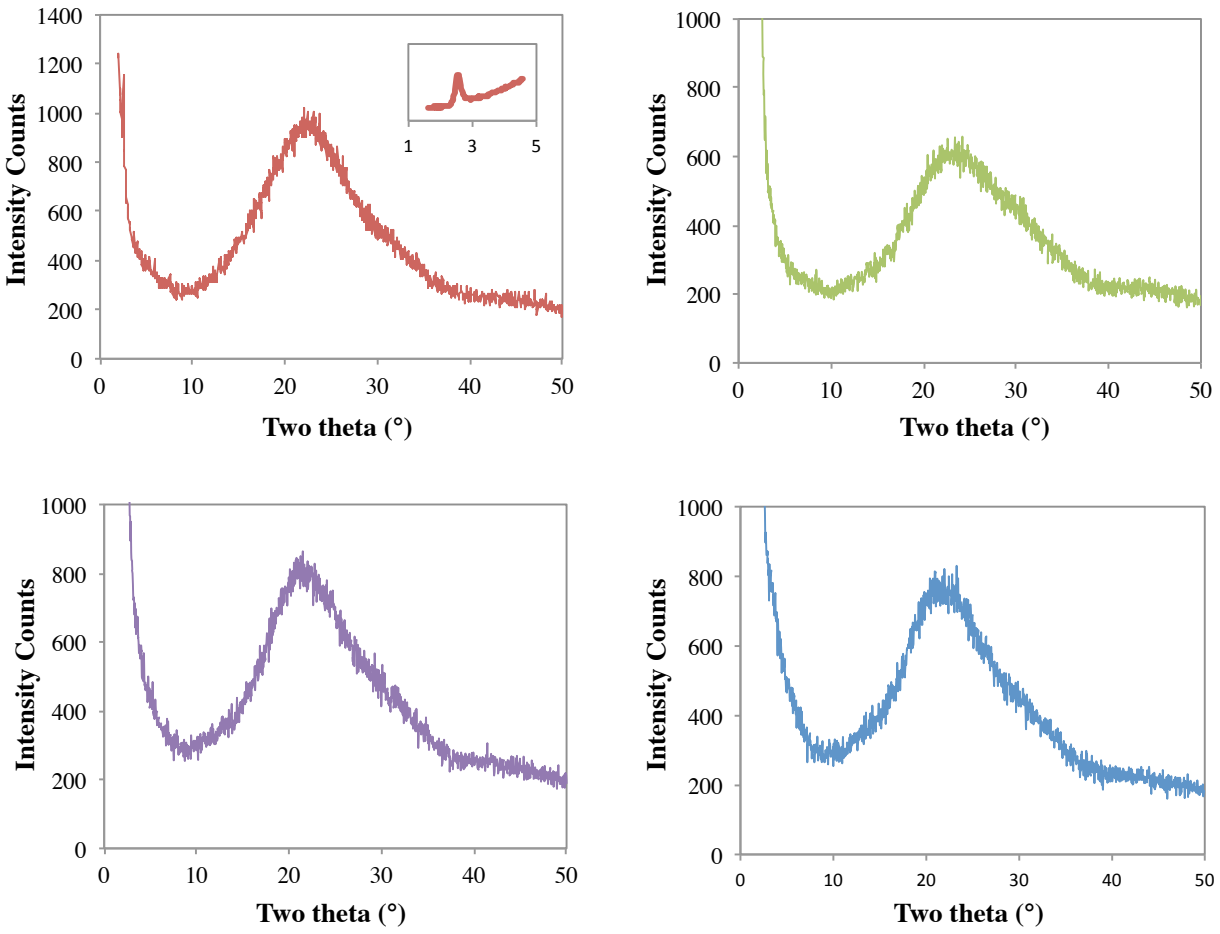

Figure 5.10 Polymer thin-film XRD patterns for **P5.1** (red), **P5.2** (green), **P5.3** (purple) and **P5.4** (blue). Inset plot for **P5.1** represents the SAXS for the peak observed at two theta = 2.56 °.

5.3.7 Liquid crystalline textures

The liquid crystalline properties of the polymers were investigated by polarized optical microscopy (Figure 5.11) using the same samples that were used for XRD analysis. All polymers

displayed birefringence under cross-polarized light at room temperature indicating some degree of alignment upon drop-casting onto glass. Unexpectedly, **P5.1** displayed a distinctive liquid crystalline mesophase Smectic A texture while **P5.2** and **P5.3** displayed nematic-like liquid crystalline mesophase textures. **P5.4** did not show any recognizable liquid crystalline mesophase textures although there was observable birefringence. Upon heating all polymers above their respective glass transition temperatures the liquid crystalline birefringence disappeared and the material became mobile with no textures under cross-polarized light. Cooling the samples back down to room temperature did not result in the immediate return of the birefringence.

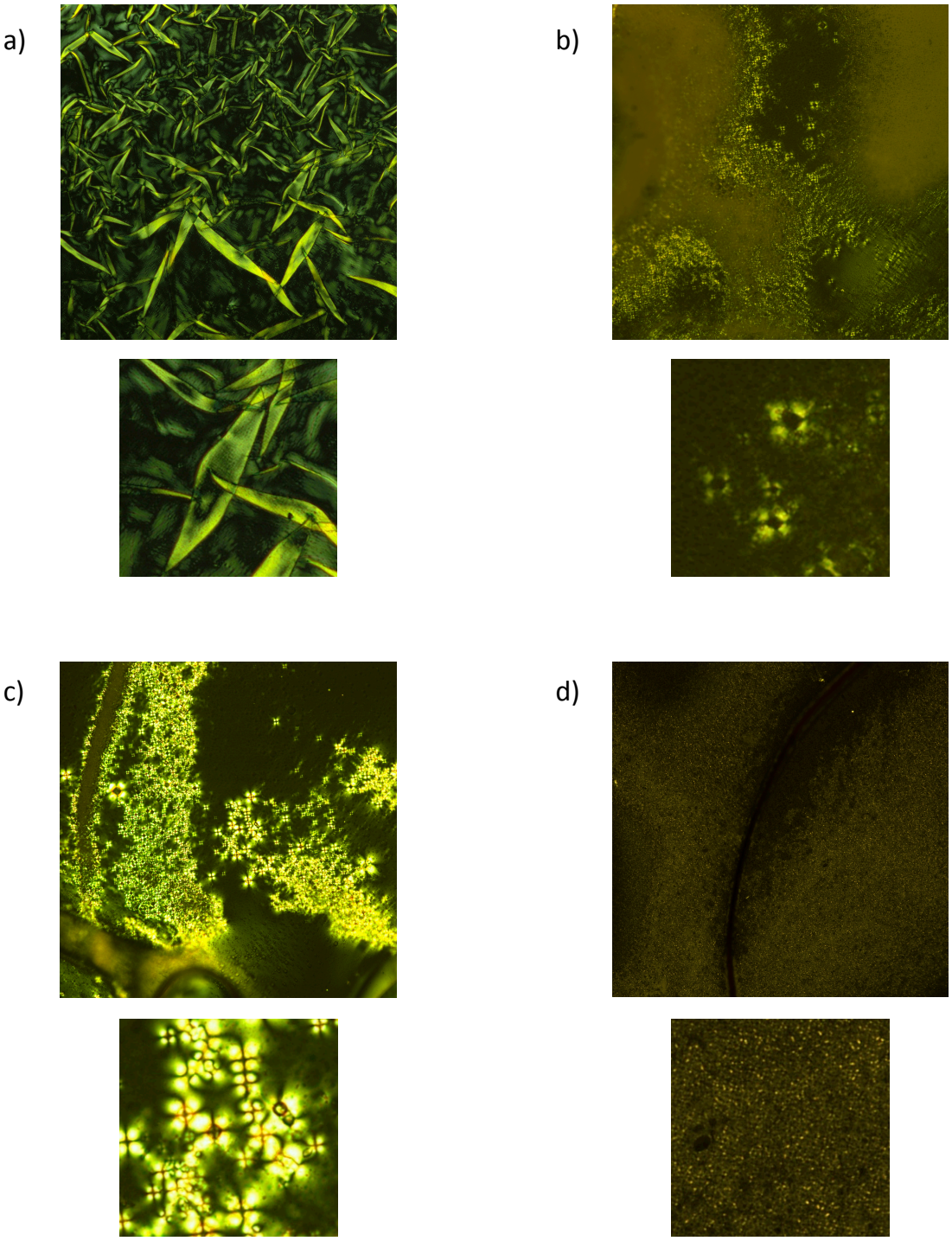

Figure 5.11 Cross-polarized optical microscope images of (a) **P5.1**, (b) **P5.2**, (c) **P5.3** and (d) **P5.4**. Bottom images are magnified sections of the top image.

5.3.8 Polymer electrochemical properties

Electrochemical data for **P5.1** - **P5.4** were collected for the thin-film and solution state using cyclic voltammetry (CV) analysis. All electrochemical data can be found in Table 5.3. Solution state CV was performed over a window of +0.50 to -2.50 V (vs Fc/Fc+) at a scan rate of 100 mV/s in 0.1M TBAF/anhydrous CH_2Cl_2 to determine the reduction and oxidation potentials of the polymers. A standard three electrode cell with a Pt working electrode, Pt counter electrode and $Ag/AgNO_3$ reference electrode was used. In the case of solid state measurements, the polymers were deposited as thin-films onto the Pt working electrode and measurements were conducted in a 0.1M TBAF/anhydrous MeCN solution at a scan rate of 100 mV/s.

	λ onset (nm)		**Eg^{opt} (eV)**		**Eg^{CV} (eV)**	**$E_{1/2}$ Red (V)**	**$E_{1/2}$ Ox (V)**	**CV (eV)**		**DFT (eV)**	
	Sol	Film	Sol	Film	Sol	Sol	Sol	LUMO	HOMO	LUMO	HOMO
P5.1	456	481	2.72	2.58	2.34	-1.49	0.85	-3.31	-5.65	-2.51	-5.60
P5.2	480	536	2.58	2.31	2.29	-1.53	0.76	-3.27	-5.56	-2.48	-5.46
P5.3	455	466	2.72	2.66	2.31	-1.50	0.81	-3.30	-5.61	-2.51	-5.60
P5.4	479	502	2.60	2.47	2.30	-1.55	0.75	-3.25	-5.55	-2.48	-5.46

Table 5.3 Summary of electrochemical properties of **P5.1** – **P5.4**. Values were estimated using the vacuum ferrocene reference value of -4.8 eV at 0.0 V.

5.3.9 Solution state CV

LUMO energy levels were determined from the $E_{1/2}$ values of the one-electron reduction peak and were found to be relatively consistent among the polymers with values between -3.25 and -3.31 eV (see Figure 5.12). For **P5.1** and **P5.3**, where the orientation of the MAN is 2,6-NI,

the LUMO values are slightly lower (-3.31 and -3.30 eV, respectively) than those for **P5.2** and **P5.4** (-3.27 and -3.25 eV, respectively).

HOMO energy levels were determined using two methods: 1) as estimates of the difference between the E_g^{opt} and the calculated LUMO energy levels from the $E_{1/2}$ reduction values, and 2) as calculated as the difference between the $E_{1/2}$ values of the one-electron reduction and $E_{1/2}$ values of the one-electron oxidation peaks. E_g^{opt} was estimated using the maximum solution state absorption edge and values for **P5.1**, **P5.2**, **P5.3** and **P5.4** were estimated at 2.72, 2.58, 2.72 and 2.60 eV, respectively. Using estimates from the E_g^{opt} values HOMO energy levels for **P5.1**, **P5.2**, **P5.3** and **P5.4** were found to be -6.03, -5.85, -6.02 and -5.85 eV, respectively. HOMO energy levels calculated from the oxidative $E_{1/2}$ values for **P5.1**, **P5.2**, **P5.3** and **P5.4** were determined to be -5.65, -5.56, -5.62 and-5.55 eV, respectively. E_g^{CV} values for **P5.1**, **P5.2**, **P5.3** and **P5.4** were then found to be 2.34, 2.29, 2.31, 2.30 eV, respectively. The E_g as estimated by thin-film absorbance maximum (E_g^{film}) gave values of 2.58, 2.31, 2.66 and 2.47 eV for **P5.1**, **P5.2**, **P5.3** and **P5.4**, respectively.

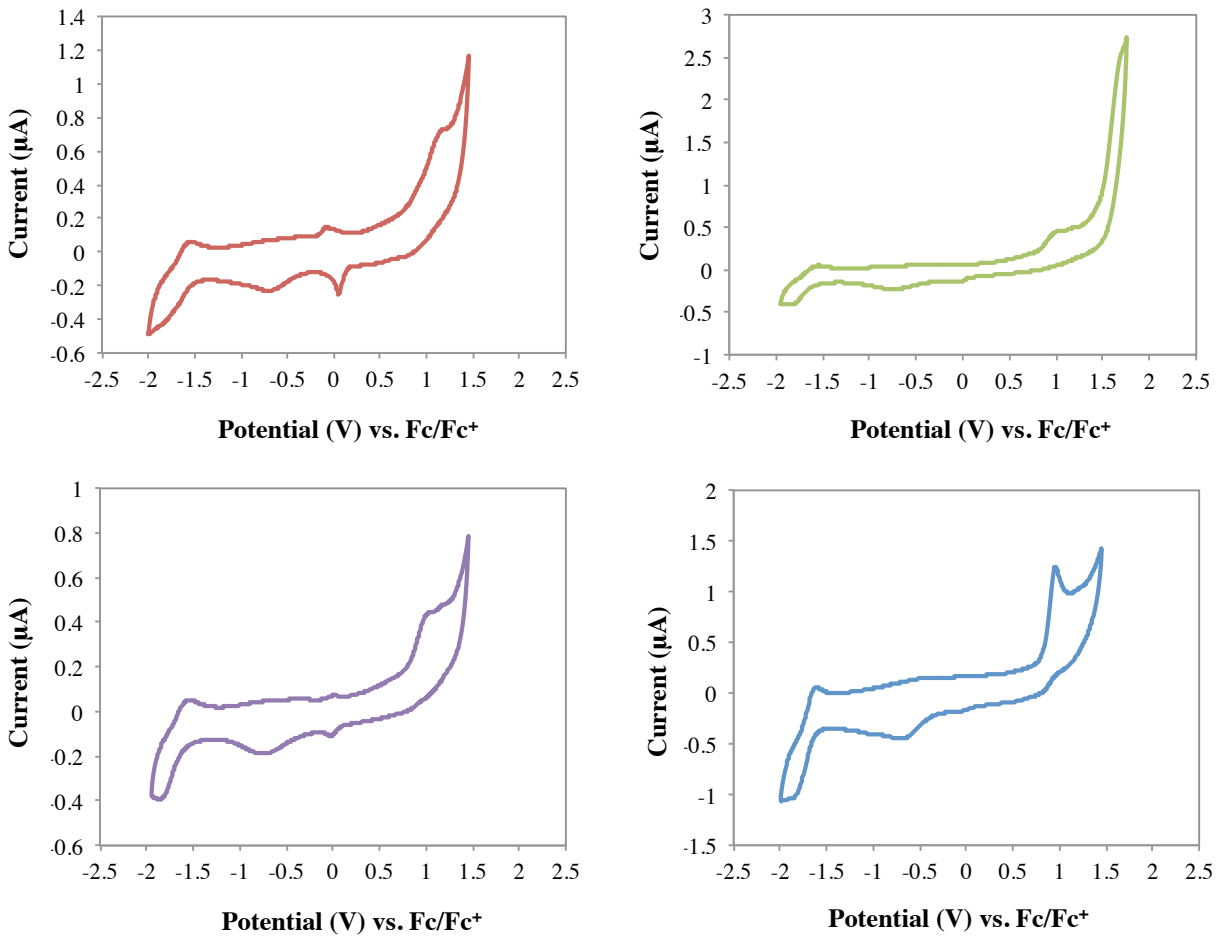

Figure 5.12 Cyclic voltammograms for **P5.1** (red), **P5.2** (green), **P5.3** (purple) and **P5.4** (blue) in 0.1M TBAF/anhydrous CH_2Cl_2 solution at a scan rate of 100 mV/s.

5.3.10 Solid state CV

To investigate the solid state electrochemistry of **P5.1** - **P5.4** the polymers were deposited as thin-films onto working electrodes and run as stated above in anhydrous acetonitrile (polymers not soluble) (see Figure 5.13). Close examination of the **P5.1** cathodic sweep shows a peak that could be a single electron reduction occurring at around -1.5 eV. Unfortunately, **P5.2** - **P5.4** did not show any oxidation peaks during the anodic sweep or any reduction peaks during the cathodic sweep.

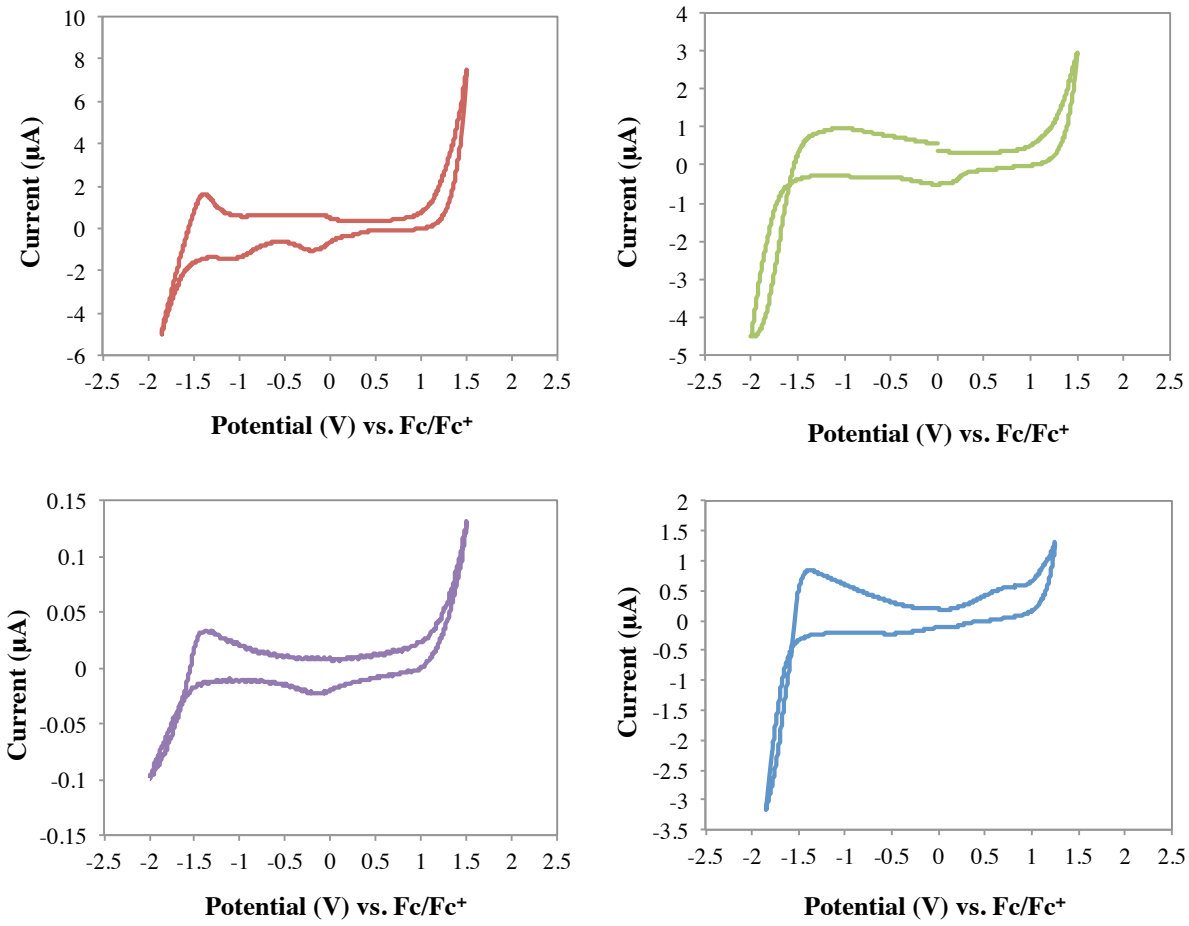

Figure 5.13 Cyclic voltammograms for **P5.1** (red), **P5.2** (green), **P5.3** (purple) and **P5.4** (blue) as a thin-films on platinum electrodes in 0.1M TBAF/anhydrous MeCN solution at a scan rate of 100 mV/s.

5.3.11 DFT calculated CV

E_g values were also estimated using DFT calculations (E_g^{DFT}) in Spartan 08 on the starting monomers **M5.1** - **M5.4** in vacuum and found to be 3.09, 2.98, 3.09 and 2.98 eV, respectively. As expected, the LUMO is predominantly located on the NI portion of the dyad with the HOMO located on the MAN portion. These values are thought to be representative for the E_g^{DFT} of **P5.1** - **P5.4**.

5.4 DISCUSSION

5.4.1 Polymer characterization

Four new polymers incorporating conjugated MAN-NI side chains onto a polynorbornene backbone were synthesized and characterized. The key synthetic steps include an esterification between the MAN and norbornene counterparts and a Sonogashira coupling between the MAN and NI aromatic units. The PDI of the polymers were relatively consistent (1.38 - 1.56). Differential scanning calorimetry (DSC) studies revealed that polymer T_g's were correlated to their solubilizing side chains: **P5.1** and **P5.2** (with octyl side chains) had T_g's of ~ 100 °C while **P5.3** and **P5.4** (with dodecyloctyl side chains) showed T_g's of ~ 50 °C. The lower T_g of **P5.3** and **P5.4** are consistent with being appended to larger, more dynamic side chains.

5.4.2 Polymer optical properties

Absorption peaks for solid-state thin-films of the polymers are slightly broadened when compared to solution-state absorption peaks. Interestingly, upon comparing polymer and monomer solution-state absorbance data there is no change in respect to peak width suggesting that the extent of dyad aggregation is the same between the monomeric and polymeric states. Additionally, the similarities between the absorption structural bands and maximums in the solution and solid state suggest that the polymers adopt similar structural conformations in both states.

A slight shoulder peak at 370 nm exists for the solution state and thin-film absorbance of **P5.1** and **M5.1** but is not present for **P5.3** and **M5.3**. Considering the only difference between the two sets of molecules is the solubilizing side chains a change in the organization of the polymer in both states must be occurring.

A hypsochromic shift of ~15-20 nm in λ_{max} Em occurred for each polymer upon going from the solution state to the solid state. Interestingly, most conjugated polymers display bathochromic emission shifts upon going from solution to the solid state indicative of favorable

polymer organization in the solid state (170, 171). The hypsochomic shifts of **P5.1** - **P5.4** indicate that the solid state organization of the polymers disrupts the extent of conjugation in the thin films (172). One possible explanation for this could be the enhanced conformational flexibility of the polynorbornene backbone in solution. This would allow the side mesogens to organize in a preferred geometry when compared to the ability of the mesogens to organize from the less dynamically flexible polynorbornene backbone in the solid state. Unfortunately, such an interpretation suggests that these polymers may not be good candidates for organic electronics due to disrupted stacking in the solid state.

Due to the alkyne linker between the MAN and NI components, an internal photo-induced electron transfer process should occur between the MAN and NI components. This charge separation in the excited state should result in varied solute-solvent stabilization in different solvents making the polymer solvatochromatic. Further studies should investigate this behavior and relate these polymer's photophysical phenomena to their monomeric components. It would also be interesting to study aggregation-induced emission (AIE) in the polymeric materials as well as investigate changes in polymer solution-state fluorescence as a consequence of polymer concentration. This behavior has been previously investigated for polymers made in our group (39). Additionally, even though no color change was detected during the electrochemical testing of the polymers, further studies should look at the potential of this molecule to undergo electrochemical color changing.

5.4.3 Polymer liquid crystal properties

Freezing the anisotropic alignment of the LCP below the T_g of the polymer is generally accomplished by electric, magnetic or mechanical fields (173). Interestingly, although most LCPs can only display LC mesophases above the T_g of the polymer, **P5.1** - **P5.3** displayed LC mesophase textures at room temperature without any applied stimuli. This should be further investigated as it may be a rarely observed phenomenon in LCPs. Additionally, although not

reported in the above section, when thin-films of **P5.1** - **P5.4** were heated just above their T_g's and a paperclip dragged along the polymer surface birefringence occurred along the edges of the paperclip trail. When this was attempted at room temperature (60 min after having cooled down from the T_g when no birefringence was observable) lasting birefringence could be observed where the paperclip was dragged. This strongly indicates that shearing these polymers can induce anisotropic alignment below their respective T_g temperatures. Considering that applications of SCLCPs for optoelectronic devices or "smart" plastics will take advantage of the potential to freeze their anisotropic alignment below the polymer T_g temperature (173), **P5.1** - **P5.4** may be promising materials for these applications.

Modeling a short oligomer of **P5.1** in Spartan 08 gave a distance of ~ 35 Å between the polymer backbone and the end of the solubilizing alkyl chain which exactly matches the small angle peak *d*-spacing. This XRD pattern is characteristic of Smectic A (SmA) liquid crystal mesophases in liquid crystalline polymers. From the XRD data the low intensity of the small angle peak relative to the halo peak the polymer thin-film does not display high crystallinity. For LCPs, the relationship between the layer spacing in a smectic polymer and the packing of the polymer side chains is not straightforward (174). Thus the following packing model for **P5.1** in the solid state is a rough estimate and further XRD studies (especially 2D- and VT-XRD) should help clarify this. However, based on the similarity between the small angle diffraction peak and the length of **P5.1** we can propose at least two 2D packing scenarios: a side chain to backbone packing and a side chain to side chain packing (see Figure 5.14). The amorphous halo peak centered around ~ 20 two theta (~ 4.0 A *d*-spacing) for all polymers could be indicative of a aromatic stacking between distances between the MAN-NI mesogens and/or interaction distances between the alkyl solubilizing tails (175). Our model is in agreement with other studies that have investigated the thin film packing of SCLCPs displaying Smectic A liquid crystal mesophases (174, 176).

Further research into the liquid crystalline nature of these polymers is necessary. Although liquid crystal textures can be observed by POM for **P5.2** and **P5.3**, XRD diffraction

patterns of these materials reveal no higher order packing morphology. As noted previously, after heating and cooling to room temperature the birefringence of the polymer disappeared. Future studies should investigate the kinetics of the LC stages and determine how the relaxation time of the polymers are correlated to their LC forming temperatures.

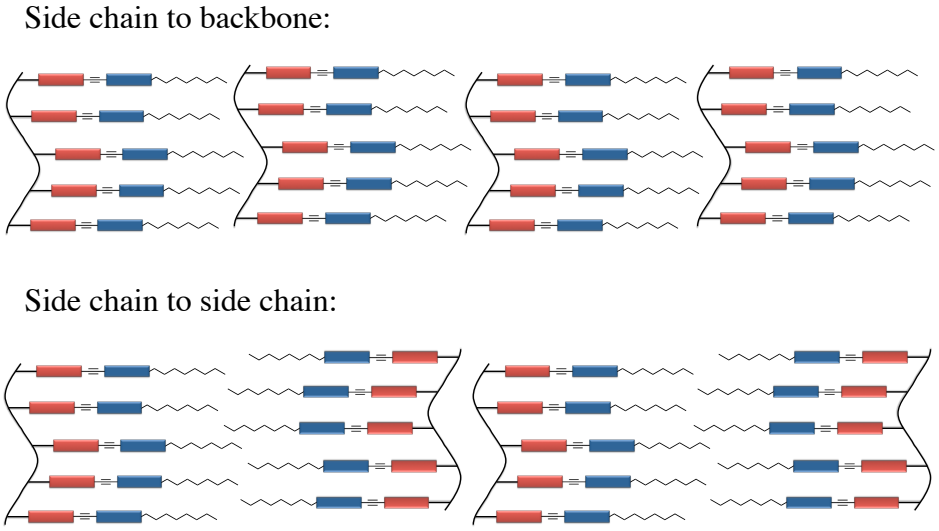

Figure 5.14 Two proposed models for the molecular packing for **P5.1**. The MAN component is shown in red and the NI component is shown in blue.

5.4.4 Polymer electrochemical properties

Each polymer exhibited a reversible one-electron reduction peak and an irreversible one-electron oxidation peak characteristic of other 1,8-naphthalimide-donor molecules (165, 166, 177, 178, 179). Interestingly, while the first reductive scans of each polymer showed only the residual ferrocene and one-electron reductive peaks of the NI moiety, additional reductive scans showed an increasingly large broad peak located between -0.5 and -1.0 eV. This peak is characteristic of electropolymerization occurring on the working electrode.

For each method of estimating and calculating the electrochemical bandgap (E_g^{DFT}, E_g^{opt} solution, E_g^{opt} thin-film, E_g^{CV} solution) the values for **P5.1** and **P5.3** were both relatively larger than for **P5.2** and **P5.4**. While the LUMO level of the polymers (-3.25 to -3.31 eV) were higher

than for the commonly used organic electron-acceptor PCBM (-3.7 eV) (3), the HOMO levels were lower than the commonly used organic electron-donor P3HT (-4.8 eV). Although the bandgap levels of the polymers (2.29 to 2.34 eV by CV) are currently too high for conventional organic photovoltatics (E_g <2.0 eV), additional derivitization of the polymer side chains may lower their bandgap. Our polymers were similar in respect to HOMO and LUMO energy levels and E_g^{CV} and E_g^{opt} values for other NI-donor polymers (177, 165, 166). The calculated E_g^{opt} values (for both solution and thin-film state) for the polymers were higher than the calculated E_g^{CV} values and is consistent with other NI-donor polymers (165, 166).

The thin-film CV of **P5.1** showed a potential reversible one-electron reduction peak at around -1.5 eV. The enhanced thin-film molecular ordering of **P5.1** (as observed by XRD) could be responsible for the possible redox activity observed by thin-film CV. Further studies should direct attention at trying to enhance the thin-film activity of **P5.1**.

We can attribute the lack of redox potential for thin-films of the polymers to at potentially three things: 1) The thin-films could be acting as insulators, 2) electropolymerization of the polymers may be happening, 3) the restricted motion of the thin-film polymers as compared to the polymers in solution (much more dynamic). More studies investigating the thin-film electrochemical behavior of these polymers should be conducted to verify their redox properties. Specifically, more attempts should be made to organize the polymers in the solid state (heating, surface treatment, etc.) followed by solid state conductive measurements.

5.5 CONCLUSIONS

Although the research presented in this Chapter is incomplete, it provides substantial groundwork towards better understanding MAN-NI side chain polymers. While the interpretation of the solid state electrochemical and fluorescence studies may suggest these polymers are not suitable as organic electronic materials, the interesting liquid crystalline mesophases warrant further investigation of these polymers.

5.6 EXPERIMENTAL

General Methods

Absorption spectra were taken on an Agilent 8453 UV-Vis spectrometer (50 μM concentrations for solution-state measurements). Fluorescence spectroscopy was performed on a PTI fluorimeter (100 nM concentrations for solution-state, 0.5 mm slits for solution-state, 2.00 mm slits for solid-state) equipped with a 814 photomultiplier detection system using a 75W xenon short arc lamp. IR spectroscopy was performed on a PerkinElmber Spectrum 100 FT-IR equppied with a universal ATR (UATR) accessory. Differential scanning calorimetry (DSC) was performed on a DSC Q100 from TA Instruments Waters (USA) at a scan rate of 5 °C/min under a Nitrogen airflow. Thermal gravitational analysis (TGA) was performed on a TA Instruments-Waters LLC TGA Q500 instrument. Powder X-ray diffraction (XRD) was obtained using a Scintag X1 theta-theta diffractometer equipped with a Cu X-ray tube and solid-state X-ray detector set to count Cu Kα radiation. X-ray crystallography was performed on a Nonius Kappa CCD diffractometer using a Bruker AXS Apex II detector and a graphite monochromator with Mo Kα radiation (λ = 0.71075 Å). Polarized optical microscopy was performed on an Olympus BX60 microscope equipped with a Mettler FP82HT hot stage and Leica digital camera. An ice-water cooling apparatus was attached to the hot stage to maintain a steady cool down rate while analyzing samples.

Electrochemical analysis

Electrochemical studies were performed in a dry-box under a nitrogen atmosphere using a GPES system from Eco. Chemie B. V. All the electrochemical experiments were carried out in a three-electrode cell with a Ag/AgNO3 reference (silver wire dipped in a 0.01 M silver nitrate solution with 0.1 M Bu4NPF6 in CH3CN), a Pt button working electrode, and a Pt wire coil counter electrode. Ferrocene was used as an external reference to calibrate the reference electrode before and after experiments were preformed and that value was used to correct the

measured potentials. The supporting electrolyte was 0.1 M TBAF that was purified by recrystallization three times from hot ethanol before being dried for three days at 100-150 C under vacuum.

Monomer and polymer synthesis

Scheme 5.1 Synthesis of **P5.1** – **P5.4**.

3-((6-bromonaphthalen-2-yl)oxy)propan-1-ol (1): 2-bromo-6-naphthol (5.0 g, 22.4 mmol), 1-bromobutanol (3.85 mL, 44.0 mmol), K_2CO_3 (12.4 g, 88.0 mmol) added to RBF with 200 mL MeCN and then Argon bubbled through for 10 min. Reaction refluxed at 90 °C overnight (18 hrs). Reaction brought to RT, MeCN concentrated, K_2CO_3 filtered through celite plug using DCM, loaded onto silica and columned (100% DCM) to yield **1** (4.49 g, 15.6 mmol, 70%) as a white crystalline solid. ^{1}H NMR ($CDCl_3$, 400 MHz): 7.92 (d, 1H), 7.64 (d, 1H), 7.59 (d, 1H), 7.50 (dd, 1H), 7.15 (tt, 2H), 4.23 (t, 2H), 3.92 (q, 2H), 2.12 (q, 2H), 1.70 (t, 1H). ^{13}C NMR ($CDCl_3$, 400 MHz): 157.16, 133.15, 130.19, 129.79, 128.67, 128.53, 120.00, 117.26, 65.82, 60.53, 32.08. IR: 3388, 3307, 3052, 2944, 2869, 2354, 1828, 1589, 1506, 1452, 1371, 1259, 1079, 980, 908, 811, 755.

3-((4-bromonaphthalen-1-yl)oxy)propan-1-ol (5): 1-bromo-4-napthol (5.71 g,25.6 mmol), 1-bromobutanol (4.37 mL, 50.0 mmol), K_2CO_3 (13.8 g, 100.0 mmol) added to RBF with 200 mL MeCN and then Argon bubbled through for 10 min. Reaction refluxed at 90 °C overnight (18 hrs). Reaction brought to RT, MeCN concentrated, K_2CO_3 filtered through celite plug using DCM, loaded onto silica and columned (100% DCM) to yield **5** (4.29 g, 15.3 mmol, 60%) as a light brown oil. ^{1}H NMR ($CDCl_3$, 400 MHz): 8.25 (d, 1H), 8.17 (d, 1H), 7.61 (tt, 2H), 7.51 (tt, 1H), 6.71 (d, 1H), 4.28 (t, 2H), 3.97 (q, 2H), 2.20 (q, 2H), 1.63 (t, 1H). ^{13}C NMR ($CDCl_3$, 400 MHz): 154.47, 132.57, 129.60, 127.88, 127.05, 126.12, 122.39, 113.47, 105.55, 72.59, 72.51, 65.74, 60.26, 32.16. HRMS (ESI+): calc. 346.1568, found. 369.1461 (M+Na). IR: 3404, 3354, 3084, 2960, 2891, 2370, 1840, 1585, 1504, 1454, 1369, 1261, 1227, 1076, 980, 908, 812, 756.

4-(6-(3-hydroxypropoxy)naphthalen-2-yl)-2-methylbut-3-yn-2-ol (2): 1 (4.19 g, 14.96 mmol), dry TEA (150mL), mebynol (4.4 mL, 45.0 mmol) added to RBF and Argon bubbled through for 10 min. CuI (140 mg, 5 mol %), PPh_3 (196 mg, 5 mol %), $PdCl_2(PPh_3)_2$ (500 mg, 5 mol %) added and reaction brought to reflux overnight (17 hrs). After cooling to RT, the TEA was concentrated in vacuo, the metals filtered off and rinsed with DCM, the crude residue loaded

onto silica and columned (5% acetone in DCM) to yield **2** (3.97 g, 14.0 mmol, 98%) as a light brown solid. ^{1}H NMR ($CDCl_3$, 400 MHz): 7.86 (s, 1H), 7.66 (dd, 2H), 7.42 (dd, 1H), 7.13 (dd, 2H), 4.24 (t, 2H), 3.91 (dd, 2H), 2.11 (t, 2H), 1.65 (s, 6H). ^{13}C NMR ($CDCl_3$, 400 MHz): 157.54, 134.18, 131.45, 129.43, 129.19, 128.58, 126.89, 119.60, 117.80, 106.80, 93.53, 84.13, 82.72, 65.82, 60.53, 32.08, 31.73, 31.19. HRMS (ESI+): calc. 284.1412, found. 307.1309 (M+Na). IR: 3286, 2987, 2970, 2366, 1599, 1441, 1363, 1254, 1211, 1169, 1057, 953, 891, 852, 723, 725.

4-(4-(3-hydroxypropoxy)naphthalen-1-yl)-2-methylbut-3-yn-2-ol (6): 5 (4.28 g, 15.3 mmol), dry TEA (150mL), mebynol (4.4 mL, 45.0 mmol) added to RBF and Argon bubbled through for 10 min. CuI (140 mg, 5 mol %), PPh_3 (196 mg, 5 mol %), $PdCl_2(PPh_3)_2$ (500 mg, 5 mol %) added and reaction brought to reflux overnight (17 hrs). After cooling to RT, the TEA was concentrated in vacuo, the metals filtered off and rinsed with DCM, the crude residue loaded onto silica and columned (5% acetone in DCM) to yield **6** (3.30 g, 11.6 mmol, 76%) as a dark brown solid. ^{1}H NMR ($CDCl_3$, 400 MHz): 8.24 (d, 2H), 7.66 (tt, 3H), 6.70 (d, 1H), 4.24 (t, 2H), 3.94 (t, 2H), 2.16 (t, 2H), 1.71 (s, 6H). HRMS (ESI+): calc. 284.1412, found. 307.1315 (M+Na). IR: 3286, 2987, 2985, 2966, 2368, 1585, 1460, 1363, 1207, 1167, 1138, 955, 891, 723, 717.

3-((6-ethynylnaphthalen-2-yl)oxy)propan-1-ol (3): 2 (2.0 g, 7.04 mmol), ground NaOH (0.4 g, 10.0 mmol), dry toluene (50 mL) added to RBF and Argon was bubbled through for 10 min. The reaction was then brought to reflux overnight (28 hrs). After cooling to RT, the toluene layer was washed with H_20 and brine then dried over Na_2SO_4. The organic layer was filtered, loaded onto silica and columned (100% DCM to 5% acetone in DCM) to yield **3** (733.3 mg, 3.24 mmol, 46%) as a light brown solid. ^{1}H NMR ($CDCl_3$, 400 MHz): 7.93 (s, 1H), 7.66 (dd, 2H), 7.49 (dd, 1H), 7.13 (tt, 2H), 4.21 (t, 2H), 3.88 (t, 2H), 3.12 (s, 1H), 2.09 (q, 2H). ^{13}C NMR ($CDCl_3$, 400 MHz): 157.69, 134.44, 132.15, 129.44, 129.25, 128.40, 126.94, 119.67, 117.07, 106.74, 84.29, 76.90, 65.65, 60.29, 32.03. HRMS (ESI+): calc. 226.0993, found. 226.0997. IR: 3296, 2958, 2893, 2366, 1624, 1597, 1468, 1387, 1261, 1225, 1173, 1032, 951, 858, 823.

3-((6-ethynylnaphthalen-2-yl)oxy)propan-1-ol (7): 6 (1.09 g, 3.84 mmol), ground KOH (0.86 g, 15.3 mmol), dry isopropanol (20 mL) added to RBF and Argon was bubbled through for 10 min. The reaction was then brought to reflux overnight (20 hrs). After cooling to RT the crude solution was passed through a short silica plug. The resulting eluent was concentrated under reduced pressure, loaded onto silica and columned (100% DCM to 5% acetone in DCM) to yield **7** (468.0 mg, 2.1 mmol, 54.7%) as a light brown solid. ^{1}H NMR ($CDCl_3$, 400 MHz): 8.28 (dd, 2H), 7.66 (d, 1H), 7.59 (tt, 1H), 7.51 (tt, 1H), 6.74 (d, 1H), 4.24 (t, 2H), 3.93 (t, 2H), 3.41 (s, 1H), 2.15 (q, 2H). ^{13}C NMR ($CDCl_3$, 400 MHz): 155.49, 134.52, 132.02, 127.53, 125.97, 125.90, 125.33, 122.23, 111.93, 104.33, 82.15, 50.50, 65.51, 60.07, 32.09. HRMS (ESI+): calc. 226.0993, found 249.0877 (M+Na). IR: 3300, 2960, 2920, 2372, 2102, 1743, 1579, 1510, 1458, 1379, 1323, 1240, 1220, 1086, 976, 820, 764.

3-((6-ethynylnaphthalen-2-yl)oxy)propyl(1S,2S,4S)-bicyclo[2.2.1]hept-5-ene-2 carboxylate (4-*endo*): 3 (204.8 mg, 0.906 mmol), 5-norbornene-2-carboxylic acid (0.2 mL, 1.80 mmol, mix. of *endo* and *exo*, 97/3), DMAP (25 mg, cat.) and dry DCM (15 mL) added to RBF and Argon bubbled through for 10 min. Reaction was brought down to 0 °C and allowed to cool for 20 min. To this stirring solution at 0 °C was then added DCC (230 mg, 1.1 mmol) and the reaction was stirred at 0 ° for an addition 20 min before being stirred at RT overnight (22 hrs). The insoluble DCC precipitate was filtered off, rinsed with DCM, and the organic layer was washed with H_2O and brine, dried over Na_2SO_4, and loaded onto silica. The crude material was purified via a column (50/50 Hex/ DCM) and the **4-*endo*** (190 mg, 0.548 mmol, 61%) and **4-*exo*** (13.6 mg, 0.039 mmol, 4.5%) isomers were separately isolated as a yellow oil and clear oil, respectively. **4-*endo***: ^{1}H NMR ($CDCl_3$, 400 MHz): 7.95 (s, 1H), 7.68 (dd, 2H), 7.50 (dd, 1H), 7.15 (dd, 1H), 7.09 (d, 1H), 6.18 (dd, 1H), 5.92 (dd, 1H), 4.27 (t, 2H), 4.15 (t, 2H), 3.22 (b, s, 1H), 3.13 (s, 1H), 2.96 (m, 1H), 2.90 (b, s, 1H), 2.16 (q, 2H), 1.91 (tt, 1H), 1.42 (m, 2H), 1.26 (d, 1H). ^{13}C NMR ($CDCl_3$, 400 MHz): 174.78, 157.69, 137.94, 134.41, 132.33, 132.15, 129.45, 129.23, 128.39,

126.88, 119.73, 117.06, 106.57, 84.26, 76.84, 64.53, 61.04, 49.73, 45.84, 43.42, 42.61, 29.31, 28.71. HRMS (ESI+): calc. 346.1568, found. 369.1461 (M+Na). IR: 3277, 2976, 2920, 2361, 1724, 1603, 1470, 1392, 1335, 1228, 1174, 1053, 957, 852, 820, 712. **4-*exo***: ^{1}H NMR ($CDCl_3$, 400 MHz): 7.95 (s, 1H), 7.67 (dd, 2H), 7.49 (dd, 1H), 7.15 (dd, 1H), 7.10 (d, 1H), 6.11 (qq, 2H), 4.33 (t, 2H), 4.17 (t, 3H), 3.12 (s, 1H), 3.05 (b, s, 1H), 2.92 (b, s, 1H), 2.20 (m, 3H), 1.93 (tt, 1H), 1.53 (d, 1H), 1.38 (m, 2H). ^{13}C NMR ($CDCl_3$, 400 MHz): 176.31, 157.71, 138.18, 135.79, 134.43, 132.17, 129.47, 129.26, 128.42, 126.90, 119.76, 117.09, 106.63, 84.28, 76.84, 64.60, 61.34, 46.74, 46.47, 43.25, 41.74, 30.47, 28.77. HRMS (ESI+): calc. 346.1568, found 369.1461 (M+Na). IR: 3276, 3062, 2973, 2873, 1724, 1625, 1602, 1469, 1390, 1226, 1157, 1051, 956, 890, 852, 821.

3-((4-ethynylnaphthalen-1-yl)oxy)propyl(1S,2S,4S)-bicyclo[2.2.1]hept-5-ene-2-carboxylate (8-*endo*): **7** (211.7 mg, 0.937 mmol), 5-norbornene-2-carboxylic acid (194 mg, 1.4 mmol, mix. of *endo* and *exo*, 97/3), DMAP (30 mg, cat.) and dry DCM (15 mL) added to RBF and Argon bubbled through for 10 min. Reaction was brought down to 0 °C and allowed to cool for 20 min. To this stirring solution at 0 °C was then added DCC (288 mg, 1.4 mmol) and the reaction was stirred at 0 ° for an addition 20 min before being stirred at RT overnight (24 hrs). The insoluble DCC precipitate was filtered off, rinsed with DCM, and the organic layer was washed with H_2O and brine, dried over Na_2SO_4, and loaded onto silica. The crude material was purified via a column (40/60 Hex/ DCM) and the **8-*endo*** (175 mg, 0.51 mmol, 54%) and **8-*exo*** (50.2 mg, 0.015 mmol, 16%) isomers were separately isolated as a yellow oil and clear oil, respectively. **8-*endo***: ^{1}H NMR ($CDCl_3$, 400 MHz): 8.31 (t, 2H), 7.67 (d, 1H), 7.61 (t, 1H), 7.52 (t, 1H), 6.75 (d, 1H), 6.17 (dd, 1H), 5.90 (dd, 1H), 4.33 (t, 2H), 4.23 (dd, 2H), 3.41 (s, 1H), 3.21 (b, s, 1H), 2.97 (m, 1H), 2.90 (b, s, 1H), 2.25 (q, 2H), 1.91 (tt, 1H), 1.44 (d, 2H), 1.28 (d, 1H). ^{13}C NMR ($CDCl_3$, 400 MHz): 174.80, 155.44, 137.97, 134.54, 132.32, 131.93, 127.57, 125.91, 125.36, 122.36, 112.05, 104.16, 82.12, 80.49, 64.83, 61.13, 49.75, 45.86, 43.44, 42.62, 29.33, 28.76. HRMS (CI): calc. 346.1568, found. 346.1564 (M+Na)+. IR: 3279, 3045, 2949, 2866, 2359, 1724, 1579,

1508, 1458, 1379, 1321, 1283, 1236, 1167, 1080, 766. **8-*exo***: ^{1}H NMR ($CDCl_3$, 400 MHz): 8.30 (t, 2H), 7.67 (d, 1H), 7.61 (tt, 1H), 7.52 (tt, 1H), 6.75 (d, 1H), 6.11 (qq, 2H), 4.40 (t, 2H), 4.25 (t, 2H), 3.41 (s, 1H), 3.04 (b, s, 1H), 2.92 (b, s, 1H), 2.29 (m, 3H), 1.94 (m, 1H), 1.52 (d, 1H), 1.37 (m, 2H). ^{13}C NMR ($CDCl_3$, 400 MHz): 176.34, 155.44, 138.18, 135.80, 134.55, 131.93, 127.59, 125.93, 125.37, 122.37, 112.06, 104.66, 104.20, 82.13, 80.50, 64.90, 61.44, 46.74, 46.46, 43.24, 41.73, 30.48, 28.80. HRMS (ESI+): calc. 346.1568, found 369.1461 (M+Na)+. IR: 3253, 3054, 2973, 2956, 2873, 1720, 1583, 1459, 1380, 1322, 1276, 1170, 1091, 1052, 1018, 862, 755.

6-bromo-2-octyl-1H-benzo[de]isoquinoline-1,3(2H)-dione (9): This molecule synthesized and characterized following the same method found in Chapter 3.

2-octyldodecyl methanesulfonate (10): To a dry round bottom flask was added 2-octyl-1-dodecanol (12.1 mL, 34.0 mmol) and pyridine (150 mL) at which point the solution was brought to 0 °C and stirred for 5 min. Methanesulfonyl chloride (3.0 mL, 38.8 mmol) was added to the above solution drop wise over several minutes, allowed to stir at 0 °C for 30 min, and then brought to room temperature to stir for 23 hrs. Pyridine was removed under reduced pressure, DCM was added to the round bottom and the organic layer washed with H_2O. The organic layer was then washed again with aqueous CuSO4, collected, dried, loaded onto silica and columned (100% hexanes to 60%/40% DCM/hexanes) to yield **10** as a yellow oil (10.25 g, 28.3 mmol, 83%). ^{1}H NMR ($CDCl_3$, 400 MHz): 4.11 (d, 2H), 2.98 (s, 3H), 1.70 (t, 1H), 1.25 (b, s, 30H), 0.87 (t, 6H) ^{13}C NMR ($CDCl_3$, 400 MHz): 72.65, 37.88, 37.24, 30.75, 29.95, 29.73, 29.67, 26.67, 22.80, 22.78, 14.22. IR: 2921, 2852, 2358, 1459, 1351, 1174, 941, 815, 719.

2-(2-octyldodecyl)isoindoline-1,3-dione (11): To a dry round bottom flask was added **10** (7.245 g, 19.2 mmol), potassium phthalimide (7.125 g, 38.4 mmol) and dry DMF (100 mL) and Argon was bubbled through the mixture for 10 minutes. The reaction was brought to reflux overnight (12 hrs) and after complete disappearance of **10** (as shown by TLC) the DMF was removed

under reduced pressure. The resulting pinkish suspension was extracted with DCM (100 mL), and washed with H_2O and saturated aqueous NaCl. The DCM layer was then dried over Na_2SO_4, filtered, loaded onto silica and columned (30%/70% DCM/Hexanes) to yield **11** as a clear oil (7.0226 g, 16.4 mmol, 86% yield). ^{1}H NMR ($CDCl_3$, 400 MHz): 7.83 (dd, 2H), 7.70 (dd, 2H), 3.56 (d, 2H), 1.86 (t, 1H), 1.22 (b, s, 30H), 0.85 (tt, 6H). ^{13}C NMR ($CDCl_3$, 400 MHz): 168.81, 133.91, 132.24, 123.25, 42.43, 37.13, 32.04, 32.01, 31.59, 30.09, 29.76, 29.73, 26.41, 22.80, 14.25. IR: 2919, 2850, 2335, 1772, 1712, 1465, 1394, 1357, 1186, 1047, 892, 786, 721.

2-octyldodecan-1-amine (12): To a dry round bottom flask was added **11** (7.0226 g, 16.4 mmol), hydrazine hydrate (4.78 mL, 98.4 mmol) and dry EtOH (60 mL) and Argon was bubbled through the mixture for 10 minutes. The reaction was brought to reflux for 3.5 hrs and after complete disappearance of **12** (as shown by TLC) the EtOH was removed under reduced pressure. The resulting white suspension was dissolved in DCM and washed with KOH (10% w/v solution). The combined aqueous layers were washed with DCM and then the organic layers combined and washed with saturated aqueous NaCl. The DCM layer was then dried over Na_2SO_4 to yield **12** as a light yellow oil (4.8733 g, 16.4 mmol, 100% yield). ^{1}H NMR ($CDCl_3$, 400 MHz): 2.57 (d, 2H), 1.40 (m, 1H), 1.24 (b, s, 30H), 0.95 (b, s, 2H), 0.86 (t, 6H). ^{13}C NMR ($CDCl_3$, 400 MHz): 45.38, 41.07, 32.04, 31.67, 30.24, 19.81, 29.77, 29.48, 26.92, 22.80, 14.22. IR: 2917, 2854, 2337, 1558, 1457, 1336, 1290, 811, 723.

6-bromo-2-(2-octyldodecyl)-1H-benzo[de]isoquinoline-1,3(2H)-dione (13): To a solution of 4-bromo-1,8-naphthalic anhydride (500 mg, 1.8 mmol) and dry EtOH (20 mL) was added **12** (644.3 mg, 2.16 mmol) at room temperature. Argon was bubbled through the solution for 10 min and then the mixture was heated to reflux overnight (20 hrs). The EtOH was removed under reduced pressure and the crude material was loaded onto silica and columned (20%/80% DCM/hexanes) to yield **13** as a dark yellow oil after drying (951.8 mg, 1.7 mmol, 95%). ^{1}H NMR ($CDCl_3$, 400 MHz): 8.61 (dd, 1H), 8.50 (dd, 1H), 8.36 (d, 1H), 7.99 (d, 1H), 7.80 (dd, 1H),

4.11 (d, 2H), 1.96 (m, 1H), 1.19 (b, s, 30H), 0.83 (dd, 6H). ^{13}C NMR ($CDCl_3$, 400 MHz): 163.99, 163.97, 133.14, 132.12, 131.31, 131.15, 130.64, 130.17, 129.07, 128.14, 123.23, 122.37, 44.76, 32.04, 32.01, 31.82, 30.15, 29.76, 29.73, 29.69, 29.47, 26.61, 22.81, 22.79, 14.25. HRMS (CI+): calc. 555.2712, found 555.2703 (M). IR: 2925, 2850, 2368, 1702, 1664, 1589, 1463, 1344, 1230, 1174, 1045, 848, 779, 750, 748.

3-((6-((2-octyl-1,3-dioxo-2,3-dihydro-1H-benzo[de]isoquinolin-6yl)ethynyl)naphthalen-2-yl)oxy)propyl(1S,2S,4S)-bicyclo[2.2.1]hept-5-ene-2-carboxylate (M5.1): **4-*endo*** (94.6 mg, 0.273 mmol), **9** (106.0 mg, 0.273 mmol), dry TEA (3.5 mL) were added to RBF and Argon bubbled through for 10 min. CuI (5 mg, 5 mol %), PPh_3 (7 mg, 5 mol %), $PdCl_2(PPh_3)_2$ (18 mg, 5 mol %) added and reaction brough to reflux overnight (17 hrs). After cooling to RT, the TEA was concentrated under reduced pressure, the crude material passed through a plug of silica to remove the metals (using DCM), loaded onto silica and columned (40/60 Hex/DCM) to yield **M5.1** (60.3 mg, 0.092 mmol, 33%) as a bright green solid. ^{1}H NMR ($CDCl_3$, 400 MHz): 8.72 (d, 1H), 8.62 (d, 1H), 8.52 (d, 2H), 8.09 (s, 1H), 7.93 (d, 1H), 7.82 (t, 1H), 7.74 (dd, 2H), 7.64 (d, 1H), 7.20 (dd, 1H), 7.13 (s, 1H), 6.18 (dd, 1H), 5.91 (dd, 1H), 4.28 (t, 2H), 4.17 (m, 4H), 3.22 (b, s, 1H), 2.98 (m, 1H), 2.91 (b, s, 1H), 2.19 (q, 2H), 1.92 (tt, 1H), 1.73 (q, 2H), 1.35 (m, 13H), 0.87 (t, 3H). ^{13}C NMR ($CDCl_3$, 400 MHz): 174.84, 164.07, 163.80, 158.12, 138.00, 134.80, 132.46, 132.35, 132.15, 131.66, 131.62, 130.67, 130.46, 129.70, 128.91, 128.55, 127.87, 127.44, 127.24, 123.10, 122.01, 120.05, 117.19, 106.74, 100.05, 86.30, 64.67, 61.07, 49.78, 45.78, 43.48, 42.66, 40.69, 31.95, 29.47, 29.36, 28.78, 28.26, 27.30, 22.77, 14.23. HRMS (CI+): calc. 653.3141, found 653.3170. IR: 2937, 2868, 2202, 1738, 1699, 1659, 1587, 1466, 1394, 1356, 1261, 1186, 1066, 849, 781, 712. MP (DSC): 117.5 °C.

3-((4-((2-octyl-1,3-dioxo-2,3-dihydro-1H-benzo[de]isoquinolin-6-yl)ethynyl)naphthalen-1-yl)oxy)propyl(1S,2S,4S)-bicyclo[2.2.1]hept-5-ene-2-carboxylate (M5.2): **8-*endo*** (134.7 mg, 0.389 mmol), **9** (151 mg, 0.389 mmol), dry TEA (5 mL) added to RBF and Argon bubbled

through for 10 min. CuI (10 mg, 10 mol %), PPh_3 (10 mg, 10 mol %), $PdCl_2(PPh_3)_2$ (26 mg, 10 mol %) were added and the reaction was brought to reflux overnight (24 hrs). After cooling to RT, the TEA was concentrated under reduced pressure, the crude material passed through a plug of silica to remove the metals (using DCM), loaded onto silica and columned (40/60 Hex/DCM) to yield **M5.2** (80.3 mg, 0.123 mmol, 32%) as a bright yellow solid. ^{1}H NMR ($CDCl_3$, 400 MHz): 8.83 (d, 1H), 8.64 (d, 1H), 856 (d, 1H), 8.42 (d, 1H), 8.33 (d, 1H), 8.02 (d, 1H), 7.85 (t, 2H), 7.67 (tt, 1H), 7.57 (tt, 1H), 6.87 (d, 1H), 6.18 (q, 1H), 5.90 (q, 1H), 4.36 (t, 2H), 4.30 (t, 2H), 4.18 (t, 2H), 3.21 (b, s, 1H), 2.98 (m, 1H), 2.91 (b, s, 1H), 2.30 (q, 2H), 1.91 (tt, 1H), 1.73 (q, 2H), 1.27 (m, 13H), 0.88 (t, 3H). ^{13}C NMR ($CDCl_3$, 400 MHz): 174.87, 164.17, 163.91, 156.21, 138.05, 134.25, 132.58, 132.33, 131.66, 131.63, 130.66, 128.30, 128.02, 127.50, 126.24, 125.84, 125.56, 123.17, 122.72, 112.22, 104.55, 98.15, 90.12, 65.07, 61.14, 49.81, 45.92, 43.50, 42.67, 40.73, 31.97, 29.50, 29.38, 28.82, 28.29, 27.32, 22.79, 14.25. HRMS (ESI+): calc. 653.3141, found 676.3048 (M+Na)**.** IR: 3049, 2921, 2850, 2356, 2186, 1729, 1697, 1654, 1579, 1508, 1361, 1349, 1234, 1170, 1087, 1027, 788, 754, 707. MP (DSC): 138.01 °C.

3-((6-((2-(2-octyldodecyl)-1,3-dioxo-2,3-dihydro-1H-benzo[de]isoquinolin-6-yl)ethynyl)naphthalen-2-yl)oxy)propyl(1S,2S,4S)-bicyclo[2.2.1]hept-5-ene-2-carboxylate (M5.3): **4-*endo*** (72.9 mg, 0.21 mmol), **13** (117 mg, 0.21 mmol), dry TEA (4 mL) were added to a RBF and Argon was bubbled through for 10 min. CuI (5 mg, 5 mol %), PPh_3 (8 mg, 10 mol %), $PdCl_2(PPh_3)_2$ (16 mg, 10 mol %) were added and the reaction was brought to reflux overnight (17 hrs). After cooling to RT, the TEA was concentrated under reduced pressure, the crude material passed through a plug of silica to remove the metals (using DCM), loaded onto silica and columned (50/50 Hex/DCM) to yield **M5.3** (69.0 mg, 0.0839 mmol, 40%) as a yellow oil which solidified to a yellow solid overnight. ^{1}H NMR ($CDCl_3$, 400 MHz): 8.75 (dd, 1H), 8.61 (dd, 1H), 8.52 (dd, 1H), 8.09 (s, 1H), 7.93 (d, 1H), 7.82 (dd, 1H), 7.75 (dd, 2H), 7.64 (dd, 1H), 7.19 (dd, 1H), 7.13 (d, 1H), 6.19 (q, 1H), 5.91 (q, 1H), 4.28 (t, 2H), 4.18 (t, 2H), 4.09 (t, 2H), 3.22 (b, s, 1H), 2.97 (m, 1H), 2.91 (b, s, 1H), 2.19 (q, 2H), 1.99 (m, 1H), 1.92 (tt, 1H), 1.21 (b, s,

33H), 0.85 (dd, 6H). ^{13}C NMR ($CDCl_3$, 400 MHz): 174.84, 164.44, 164.17, 158.11, 138.00, 134.79, 132.36, 132.15, 131.68, 131.65, 130.67, 130.53, 129.70, 128.92, 128.55, 128.20, 127.82, 127.45, 127.23, 123.10, 121.99, 120.05, 117.20, 106.73, 100.01, 86.30, 64.66, 61.07, 49.78, 45.89, 44.70, 43.48, 42.66, 32.04, 32.01, 30.16, 29.76, 29.47, 29.43, 26.63, 22.82, 22.79, 14.26. HRMS (CI-): calc. 821.5019, found 821.5020 (M)**.** IR: 2921, 2850, 2196, 1731, 1697, 1660, 1587, 1463, 1392, 1348, 1259, 1182, 1130, 1064, 887, 848, 782, 754, 707. MP (DSC): 55.9 °C.

3-((4-((2-(2-octyldodecyl)-1,3-dioxo-2,3-dihydro-1H-benzo[de]isoquinolin-6-yl)ethynyl)naphthalen-1-yl)oxy)propyl(1S,2S,4S)-bicyclo[2.2.1]hept-5-ene-2-carboxylate (M5.4): **8-*endo*** (149.9 mg, 0.433 mmol), **13** (240.4 mg, 0.433 mmol), dry TEA (6.0 mL) were added to a RBF and Argon was bubbled through for 10 min. CuI (10 mg, 5 mol %), PPh_3 (12 mg, 10 mol %), $PdCl_2(PPh_3)_2$ (30 mg, 10 mol %) were added and the reaction was brought to reflux overnight (20 hrs). After cooling to RT, the TEA was concentrated under reduced pressure, the crude material passed through a plug of silica to remove the metals (using DCM), loaded onto silica and columned (50/50 Hex/DCM) to yield **M5.4** (211.5 mg, 0.259 mmol, 59%) as an oil which solidified to a bright orange solid overnight. ^{1}H NMR ($CDCl_3$, 400 MHz): 8.84 (dd, 1H), 8.65 (dd, 1H), 8.57 (dd, 1H), 8.43 (d, 1H), 8.34 (d, 1H), 8.03 (d, 1H), 7.86 (t, 2H), 7.69 (tt, 1H), 7.58 (tt, 1H), 6.87 (d, 1H), 6.18 (q, 1H), 5.90 (q, 1H), 4.32 (tt, 3H), 4.12 (d, 2H), 3.22 (b, s, 1H), 2.98 (m, 1H), 2.91 (b, s, 1H), 2.30 (m, 2H), 2.01 (m, 1H), 1.92 (tt, 1H), 1.22 (b, s, 32H), 0.87 (m, 6H). ^{13}C NMR ($CDCl_3$, 400 MHz): 174.88, 164.56, 164.30, 156.21, 138.07, 134.26, 132.34, 131.75, 131.64, 130.68, 128.35, 128.26, 128.02, 127.52, 126.24, 125.85, 125.57, 123.17, 122.72, 121.88, 112.24, 104.54, 98.11, 90.12, 65.06, 61.14, 49.81, 45.92, 44.75, 43.50, 42.67, 32.04, 31.86, 30.19, 29.78, 29.72, 29.45, 26.66, 22.84, 22.82, 14.28. HRMS (CI-): calc. 821.5012, found 821.5011 (M)**.** IR: 2927, 2850, 2192, 1737, 1695, 1654, 1579, 1328, 1236, 1178, 1081, 754, 711. MP (DSC): 91.61 °C.

P5.1: To a vigorously stirring solution of **M5.1** (31 mg, 0.0474 mmol) in dry THF (1 mL) was added a solution of Grubbs 2 (1.0 mg, 2.5 mol %) in dry THF (1 mL) at RT under Argon. The solution remained green in color throughout the duration of the reaction. After 2.5 hrs (complete disappearance of **M5.1** by TLC) ethyl vinyl ether (1 mL) was added to the solution to quench the polymerization at which point a suspension immediately formed. The reaction was allowed to stir for an additional 15 min and then it was poured into stirring MeOH, the precipitate filtered, thoroughly rinsed with MeOH, precipitated once more from THF using MeOH, and collected to yield **P5.1** (27.0 mg, 87% yield) as a green, fluffy solid. ^{1}H NMR ($CDCl_3$, 400 MHz): 8.48 (b, s, 3H), 7.63 (b, m, 6 H), 7.00 (b, s, 2H), 5.30 (b, t, 2H), 4.21-4.06 (b, d, 6 H), 3.10 (b, s, 1H), 2.84 (b, d, 2H), 2.10 (b, s, 2H), 1.67 (b, s, 2H), 1.24 (b, m, 9H), 0.84 (b, s, 3H). IR: 2927, 2858, 2368, 2206, 1731, 1699, 1656, 1589, 1465, 1349, 1263, 1172, 1056, 854, 782, 755. Mn = 394,100 D, Mw = 602,912 D, PDI = 1.53, 5% decomposition at 413 °C, T_g at 99 °C.

P5.2: To a vigorously stirring solution of **M5.2** (48.6 mg, 0.0743 mmol) in dry THF (1 mL) was added a solution of Grubbs 2 (1.0 mg, 2.5 mol %) in dry THF (1 mL) at RT under Argon. The solution remained yellow in color throughout the duration of the reaction. After 2.5 hrs (complete disappearance of **M5.2** by TLC) ethyl vinyl ether (0.5 mL) was added to the solution to quench the polymerization at which point a suspension immediately formed. The reaction was allowed to stir for an additional 15 min and then it was poured into stirring MeOH, the precipitate filtered, thoroughly rinsed with MeOH, precipitated once more from THF using MeOH, and collected to yield **P5.2** (42.6.0 mg, 89% yield) as a yellow, powdery solid. ^{1}H NMR ($CDCl_3$, 400 MHz): 8.41 (b, m, 5H), 7.56 (b, m, 5 H), 6.59 (b, s, 2H), 5.28 (b, d, 3H), 4.27-4.06 (b, d, 6 H), 3.11 (b, s, 1H), 2.90 (b, s, 1H), 2.77 (b, s, 1H), 1.90 (b, m, 7H), 1.25 (b, s, 10H), 0.84 (b, s, 3H). IR: 2917, 2848, 2185, 1704, 1662, 1654, 1577, 1467, 1461, 1351, 1236, 1168, 1085, 1020, 790, 754, 728. Mn = 288,896 D, Mw = 429,610 D, PDI = 1.49, 5% decomposition at 402 °C, T_g at 98 °C.

P5.3: To a vigorously stirring solution of **M5.3** (54.9 mg, 0.0668 mmol) in dry THF (2.5 mL) was added a solution of Grubbs 2 (1.0 mg, 2.5 mol %) in dry THF (1 mL) at RT under Argon. The solution remained yellow-green in color throughout the duration of the reaction. After 5 hrs (complete disappearance of **M5.3** by TLC) ethyl vinyl ether (0.5 mL) was added to the solution to quench the polymerization. The reaction was allowed to stir for an additional 30 min and then it was poured into stirring MeOH, the precipitate filtered, thoroughly rinsed with MeOH, precipitated once more from THF using MeOH, and collected to yield **P5.3** (45.7 mg, 83% yield) as a yellow solid. ^{1}H NMR ($CDCl_3$, 400 MHz): 8.52 (b, m, 3H), 7.67 (b, m, 6H), 7.03 (b, m, 2H), 5.29 (b, m, 2H), 4.22-4.03 (b, d, 5H), 3.11 (b, s, 1H), 2.92-2.80 (b, d, 2H), 2.41 (b, s, 1H), 2.11 (b, s, 2H), 1.94 (b, s, 2H), 1.75 (b, s, 2H), 1.19 (b, s, 24H), 0.84 (b, s, 5H). IR: 2923, 2850, 2358, 2202, 1753, 1699, 1658, 1589, 1465, 1384, 1351, 1236, 1170, 1054, 854, 782, 754. Mn = 221,374 D, Mw = 346,137 D, PDI = 1.56, 5% decomposition at 417 °C, T_g at 52 °C.

P5.4: To a vigorously stirring solution of **M5.4** (134.2 mg, 0.163 mmol) in dry THF (4.0 mL) was added a solution of Grubbs 2 (2.0 mg, 2.5 mol %) in dry THF (1 mL) at RT under Argon. The solution remained yellow-green in color throughout the duration of the reaction. After 5 hrs (complete disappearance of **16** by TLC) ethyl vinyl ether (1.0 mL) was added to the solution to quench the polymerization. The reaction was allowed to stir for an additional 30 min and then it was poured into stirring MeOH, the precipitate filtered, thoroughly rinsed with MeOH, precipitated once more from THF using MeOH, and collected to yield **P5.4** (115.0 mg, 86% yield) as a bright yellow solid. ^{1}H NMR ($CDCl_3$, 400 MHz): 8.39 (b, m, 5H), 7.658 (b, m, 5H), 6.58 (b, m, 2H), 5.29 (b, m, 2H), 4.29-4.03 (b, d, 5H), 3.12 (b, s, 1H), 2.92-2.79 (b, d, 2H), 2.17 (b, s, 2H), 1.94 (b, s, 2H), 1.76 (b, s, 1H), 1.19 (b, s, 22H), 0.84 (b, s, 5H). IR: 2922, 2859, 2359, 2187, 1728, 1699, 1659, 1579, 1508, 1458, 1383, 1323, 1234, 1169, 1086, 958, 762. Mn = 351,538 D, Mw = 483,919 D, PDI = 1.38, 5% decomposition at 418 °C, T_g at 45 °C.

APPENDIX

Single Crystal Data for Dyads 3.1f, 3.1s and 3.4s

DYAD 3.1F

Crystal data and structure refinement for **Dyad 3.1f**.

Empirical formula	C27 H18 Cl3 N O3	
Formula weight	510.77	
Temperature	153(2) K	
Wavelength	0.71073 Å	
Crystal system	Triclinic	
Space group	P-1	
Unit cell dimensions	a = 9.294(2) Å	a= 99.545(12)°.
	b = 10.2523(17) Å	b= 105.418(16)°.
	c = 12.700(3) Å	g = 93.466(13)°.
Volume	1143.5(4) $Å^3$	
Z	2	
Density (calculated)	1.484 Mg/m^3	
Absorption coefficient	0.433 mm^{-1}	
F(000)	524	
Crystal size	0.57 x 0.08 x 0.08 mm	
Theta range for data collection	1.69 to 27.50°.	
Index ranges	-12<=h<=12, -13<=k<=13, -16<=l<=16	
Reflections collected	31327	
Independent reflections	5117 [R(int) = 0.1152]	
Completeness to theta = 27.50°	97.3 %	
Absorption correction	Semi-empirical from equivalents	
Max. and min. transmission	1.00 and 0.852	
Refinement method	Full-matrix least-squares on F^2	
Data / restraints / parameters	5117 / 0 / 309	
Goodness-of-fit on F^2	1.033	
Final R indices [I>2sigma(I)]	R1 = 0.0624, wR2 = 0.1284	
R indices (all data)	R1 = 0.1497, wR2 = 0.1644	
Largest diff. peak and hole	1.054 and -0.965 $e.Å^{-3}$	

Atomic coordinates (x 10^4) and equivalent isotropic displacement parameters (Å^{2}x 10^3) for **Dyad 3.1f**. U(eq) is defined as one third of the trace of the orthogonalized U^{ij} tensor.

	x	y	z	U(eq)
C1	4772(4)	2046(3)	7818(3)	19(1)
C1A	2298(4)	9123(4)	8630(3)	31(1)
C2	5538(4)	1212(3)	7123(3)	16(1)
C3	5761(4)	-65(3)	7271(3)	22(1)
C4	6499(4)	-852(3)	6621(3)	21(1)
C5	7006(4)	-384(3)	5812(3)	18(1)
C6	6798(4)	938(3)	5638(3)	16(1)
C7	7284(4)	1491(3)	4832(3)	22(1)
C8	7045(4)	2756(4)	4688(3)	25(1)
C9	6344(4)	3554(3)	5367(3)	22(1)
C10	5860(4)	3054(3)	6167(3)	17(1)
C11	5150(4)	3917(3)	6890(3)	21(1)
C12	6058(4)	1734(3)	6306(3)	16(1)
C13	4050(4)	4211(4)	8464(3)	27(1)
C14	7726(4)	-1224(3)	5135(3)	22(1)
C15	8295(4)	-1929(3)	4555(3)	20(1)
C16	8951(4)	-2810(3)	3858(3)	19(1)
C17	9532(4)	-2366(3)	3077(3)	19(1)
C18	10203(4)	-3224(3)	2406(3)	17(1)
C19	10838(4)	-2796(3)	1608(3)	21(1)
C20	11517(4)	-3636(3)	995(3)	21(1)
C21	11607(4)	-4958(3)	1150(3)	20(1)
C22	10994(4)	-5420(3)	1902(3)	20(1)
C23	10276(4)	-4568(3)	2545(3)	18(1)
C24	9644(4)	-4998(3)	3342(3)	22(1)
C25	8996(4)	-4147(3)	3979(3)	24(1)
C26	12520(5)	-7020(4)	648(3)	33(1)
N1	4688(3)	3350(3)	7699(2)	18(1)
O1	4254(3)	1617(2)	8502(2)	27(1)
O2	4966(3)	5062(2)	6820(2)	29(1)
O3	12349(3)	-5682(2)	507(2)	27(1)

Cl1	1893(2)	9463(1)	9907(1)	68(1)
Cl2	662(1)	8853(1)	7517(1)	58(1)
Cl3	3286(1)	7726(1)	8554(1)	50(1)

Bond lengths [Å] and angles [°] for **Dyad 3.1f**.

C1-O1	1.227(4)	C13-H13A	0.98
C1-N1	1.374(4)	C13-H13B	0.98
C1-C2	1.475(4)	C13-H13C	0.98
C1A-Cl1	1.746(4)	C14-C15	1.193(5)
C1A-Cl2	1.750(4)	C15-C16	1.435(5)
C1A-Cl3	1.751(4)	C16-C17	1.374(5)
C1A-H1A	1.00	C16-C25	1.406(5)
C2-C3	1.374(5)	C17-C18	1.410(4)
C2-C12	1.419(4)	C17-H17	0.95
C3-C4	1.396(5)	C18-C19	1.415(4)
C3-H3	0.95	C18-C23	1.420(4)
C4-C5	1.380(4)	C19-C20	1.360(5)
C4-H4	0.95	C19-H19	0.95
C5-C6	1.426(5)	C20-C21	1.406(5)
C5-C14	1.434(5)	C20-H20	0.95
C6-C7	1.407(4)	C21-O3	1.361(4)
C6-C12	1.417(4)	C21-C22	1.366(5)
C7-C8	1.362(5)	C22-C23	1.415(5)
C7-H7	0.95	C22-H22	0.95
C8-C9	1.402(5)	C23-C24	1.413(4)
C8-H8	0.95	C24-C25	1.366(5)
C9-C10	1.373(4)	C24-H24	0.95
C9-H9	0.95	C25-H25	0.95
C10-C12	1.411(4)	C26-O3	1.425(4)
C10-C11	1.479(5)	C26-H26A	0.98
C11-O2	1.210(4)	C26-H26B	0.98
C11-N1	1.408(4)	C26-H26C	0.98
C13-N1	1.469(4)		

O1-C1-N1	120.3(3)	Cl2-C1A-Cl3	109.3(2)
O1-C1-C2	122.0(3)	Cl1-C1A-H1A	108.5
N1-C1-C2	117.7(3)	Cl2-C1A-H1A	108.5
Cl1-C1A-Cl2	111.5(2)	Cl3-C1A-H1A	108.5
Cl1-C1A-Cl3	110.5(2)	C3-C2-C12	119.9(3)

C3-C2-C1	120.1(3)	H13A-C13-H13C	109.5
C12-C2-C1	120.0(3)	H13B-C13-H13C	109.5
C2-C3-C4	120.3(3)	C15-C14-C5	178.6(4)
C2-C3-H3	119.9	C14-C15-C16	178.3(4)
C4-C3-H3	119.9	C17-C16-C25	119.7(3)
C5-C4-C3	121.5(3)	C17-C16-C15	120.9(3)
C5-C4-H4	119.3	C25-C16-C15	119.3(3)
C3-C4-H4	119.3	C16-C17-C18	121.0(3)
C4-C5-C6	119.8(3)	C16-C17-H17	119.5
C4-C5-C14	120.4(3)	C18-C17-H17	119.5
C6-C5-C14	119.8(3)	C17-C18-C19	122.6(3)
C7-C6-C12	118.3(3)	C17-C18-C23	119.2(3)
C7-C6-C5	123.3(3)	C19-C18-C23	118.2(3)
C12-C6-C5	118.4(3)	C20-C19-C18	121.4(3)
C8-C7-C6	121.2(3)	C20-C19-H19	119.3
C8-C7-H7	119.4	C18-C19-H19	119.3
C6-C7-H7	119.4	C19-C20-C21	120.2(3)
C7-C8-C9	120.5(3)	C19-C20-H20	119.9
C7-C8-H8	119.8	C21-C20-H20	119.9
C9-C8-H8	119.8	O3-C21-C22	125.2(3)
C10-C9-C8	120.1(3)	O3-C21-C20	114.3(3)
C10-C9-H9	119.9	C22-C21-C20	120.6(3)
C8-C9-H9	119.9	C21-C22-C23	120.3(3)
C9-C10-C12	120.2(3)	C21-C22-H22	119.8
C9-C10-C11	119.4(3)	C23-C22-H22	119.8
C12-C10-C11	120.3(3)	C24-C23-C22	122.2(3)
O2-C11-N1	119.9(3)	C24-C23-C18	118.3(3)
O2-C11-C10	123.4(3)	C22-C23-C18	119.4(3)
N1-C11-C10	116.7(3)	C25-C24-C23	121.3(3)
C10-C12-C6	119.6(3)	C25-C24-H24	119.3
C10-C12-C2	120.2(3)	C23-C24-H24	119.3
C6-C12-C2	120.2(3)	C24-C25-C16	120.4(3)
N1-C13-H13A	109.5	C24-C25-H25	119.8
N1-C13-H13B	109.5	C16-C25-H25	119.8
H13A-C13-H13B	109.5	O3-C26-H26A	109.5
N1-C13-H13C	109.5	O3-C26-H26B	109.5

H26A-C26-H26B	109.5
O3-C26-H26C	109.5
H26A-C26-H26C	109.5
H26B-C26-H26C	109.5
C1-N1-C11	124.9(3)
C1-N1-C13	117.6(3)
C11-N1-C13	117.6(3)
C21-O3-C26	117.1

Anisotropic displacement parameters ($Å^2 x\ 10^3$) for **Dyad 3.1f**. The anisotropic displacement factor exponent takes the form: $-2p^2[\ h^2\ a^{*2}U^{11} + ... + 2\ h\ k\ a^*\ b^*\ U^{12}\ ]$

	U^{11}	U^{22}	U^{33}	U^{23}	U^{13}	U^{12}
C1	16(2)	20(2)	20(2)	-1(2)	6(2)	1(2)
C1A	37(2)	25(2)	34(2)	12(2)	12(2)	-1(2)
C2	12(2)	17(2)	16(2)	0(1)	3(2)	0(1)
C3	22(2)	25(2)	19(2)	3(2)	9(2)	-1(2)
C4	22(2)	16(2)	22(2)	2(2)	4(2)	3(2)
C5	16(2)	22(2)	13(2)	-2(1)	2(2)	1(2)
C6	12(2)	21(2)	13(2)	-1(1)	1(2)	1(1)
C7	17(2)	28(2)	19(2)	-3(2)	8(2)	1(2)
C8	26(2)	32(2)	19(2)	7(2)	10(2)	-1(2)
C9	22(2)	22(2)	22(2)	7(2)	6(2)	-1(2)
C10	13(2)	21(2)	15(2)	3(2)	1(2)	2(2)
C11	17(2)	21(2)	22(2)	2(2)	3(2)	3(2)
C12	12(2)	20(2)	12(2)	1(1)	0(2)	0(1)
C13	28(2)	26(2)	26(2)	-6(2)	12(2)	5(2)
C14	19(2)	23(2)	23(2)	6(2)	4(2)	1(2)
C15	16(2)	22(2)	20(2)	2(2)	5(2)	2(2)
C16	15(2)	22(2)	17(2)	-2(2)	1(2)	2(2)
C17	18(2)	14(2)	23(2)	2(2)	4(2)	2(2)
C18	12(2)	17(2)	19(2)	3(2)	1(2)	1(1)
C19	20(2)	18(2)	23(2)	8(2)	3(2)	0(2)
C20	19(2)	27(2)	18(2)	6(2)	5(2)	1(2)
C21	16(2)	24(2)	20(2)	0(2)	6(2)	4(2)
C22	19(2)	16(2)	25(2)	2(2)	5(2)	3(2)
C23	15(2)	19(2)	19(2)	2(2)	3(2)	1(2)
C24	22(2)	17(2)	28(2)	7(2)	8(2)	2(2)
C25	25(2)	25(2)	25(2)	5(2)	12(2)	2(2)
C26	37(3)	27(2)	40(2)	1(2)	23(2)	8(2)
N1	18(2)	18(2)	16(2)	-1(1)	6(1)	0(1)
O1	35(2)	27(1)	25(1)	4(1)	20(1)	2(1)
O2	36(2)	23(1)	32(2)	9(1)	14(1)	11(1)
O3	29(2)	25(1)	31(2)	3(1)	18(1)	5(1)

Cl1	128(1)	38(1)	59(1)	9(1)	62(1)	9(1)
Cl2	50(1)	34(1)	78(1)	24(1)	-12(1)	-1(1)
Cl3	50(1)	42(1)	64(1)	14(1)	20(1)	19(1)

Hydrogen coordinates (x 10^4) and isotropic displacement parameters ($Å^2$x 10^3) for **Dyad 3.1f**.

	x	y	z	U(eq)
H1A	2942	9906	8564	37
H3	5412	-414	7817	26
H4	6655	-1730	6739	25
H7	7788	973	4380	26
H8	7356	3099	4124	30
H9	6204	4442	5273	26
H13A	2983	3909	8317	41
H13B	4161	5130	8351	41
H13C	4581	4168	9233	41
H17	9481	-1466	2988	23
H19	10789	-1904	1498	25
H20	11931	-3329	462	25
H22	11051	-6319	1993	24
H24	9671	-5897	3437	26
H25	8574	-4460	4506	28
H26A	13086	-7025	1418	49
H26B	13064	-7436	141	49
H26C	11528	-7518	483	49

Torsion angles [°] for **Dyad 3.1f**.

O1-C1-C2-C3	-3.4(5)
N1-C1-C2-C3	174.7(3)
O1-C1-C2-C12	177.1(3)
N1-C1-C2-C12	-4.8(5)
C12-C2-C3-C4	0.1(5)
C1-C2-C3-C4	-179.4(3)
C2-C3-C4-C5	-0.7(5)
C3-C4-C5-C6	0.9(5)
C3-C4-C5-C14	-178.3(3)
C4-C5-C6-C7	179.9(3)
C14-C5-C6-C7	-0.9(5)
C4-C5-C6-C12	-0.4(5)
C14-C5-C6-C12	178.8(3)
C12-C6-C7-C8	-0.4(5)
C5-C6-C7-C8	179.3(3)
C6-C7-C8-C9	1.9(5)
C7-C8-C9-C10	-1.5(5)
C8-C9-C10-C12	-0.3(5)
C8-C9-C10-C11	178.8(3)
C9-C10-C11-O2	0.0(5)
C12-C10-C11-O2	179.1(3)
C9-C10-C11-N1	-179.5(3)
C12-C10-C11-N1	-0.4(5)
C9-C10-C12-C6	1.8(5)
C11-C10-C12-C6	-177.3(3)
C9-C10-C12-C2	-179.1(3)
C11-C10-C12-C2	1.7(5)
C7-C6-C12-C10	-1.4(5)
C5-C6-C12-C10	178.9(3)
C7-C6-C12-C2	179.5(3)
C5-C6-C12-C2	-0.2(5)
C3-C2-C12-C10	-178.7(3)
C1-C2-C12-C10	0.8(5)
C3-C2-C12-C6	0.3(5)

DYAD 3.1S

Crystal data and structure refinement for **Dyad 3.1s**

Empirical formula	C59 H42 N2 O6	
Formula weight	874.95	
Temperature	153(2) K	
Wavelength	0.71073 Å	
Crystal system	Triclinic	
Space group	P-1	
Unit cell dimensions	a = 8.1791(9) Å	a= 107.534(7)°.
	b = 14.041(2) Å	b= 95.216(6)°.
	c = 20.311(3) Å	g = 100.316(6)°.
Volume	2162.0(5) $Å^3$	
Z	2	
Density (calculated)	1.344 Mg/m^3	
Absorption coefficient	0.087 mm^{-1}	
F(000)	916	
Crystal size	0.38 x 0.27 x 0.03 mm	
Theta range for data collection	1.56 to 25.00°.	
Index ranges	-9<=h<=9, -16<=k<=16, -24<=l<=24	
Reflections collected	67638	
Independent reflections	7610 [R(int) = 0.1631]	
Completeness to theta = 25.00°	99.9 %	
Absorption correction	Semi-empirical from equivalents	
Max. and min. transmission	1.00 and 0.874	
Refinement method	Full-matrix least-squares on F^2	
Data / restraints / parameters	7610 / 0 / 608	
Goodness-of-fit on F^2	1.264	
Final R indices [I>2sigma(I)]	R1 = 0.0857, wR2 = 0.1561	
R indices (all data)	R1 = 0.2309, wR2 = 0.2054	
Largest diff. peak and hole	0.375 and -0.270 $e.Å^{-3}$	

Atomic coordinates (x 10^4) and equivalent isotropic displacement parameters (Å^{2}x 10^3) for **Dyad 3.1s**. U(eq) is defined as one third of the trace of the orthogonalized U^{ij} tensor.

	x	y	z	U(eq)
C1	6568(6)	2020(4)	11439(3)	31(2)
C2	6009(6)	1958(4)	10730(3)	22(1)
C3	5000(6)	2617(4)	10602(3)	32(2)
C4	4426(6)	2530(4)	9928(3)	27(1)
C5	4815(6)	1825(4)	9351(3)	27(2)
C6	5817(6)	1145(4)	9453(3)	24(1)
C7	6247(6)	381(4)	8914(3)	23(1)
C8	7206(7)	-253(4)	9046(3)	34(2)
C9	7795(6)	-166(4)	9731(3)	30(2)
C10	7409(6)	559(4)	10283(3)	22(1)
C11	8018(6)	600(4)	10999(3)	25(2)
C12	6418(6)	1230(4)	10168(3)	23(2)
C13	8019(7)	1336(5)	12257(3)	57(2)
C14	4183(6)	1774(4)	8662(3)	29(2)
C15	3623(6)	1779(4)	8101(3)	29(2)
C16	2917(6)	1767(4)	7420(3)	26(1)
C17	1988(6)	2456(4)	7340(3)	25(1)
C18	1297(6)	2423(4)	6672(3)	25(1)
C19	338(6)	3132(4)	6572(3)	27(1)
C20	-301(6)	3091(4)	5919(3)	29(1)
C21	-5(6)	2340(4)	5331(3)	30(1)
C22	916(6)	1653(4)	5398(3)	28(1)
C23	1597(6)	1678(4)	6077(3)	24(1)
C24	2556(7)	982(4)	6173(3)	32(2)
C25	3211(6)	1023(4)	6828(3)	31(2)
C26	-361(8)	1699(4)	4088(3)	47(2)
C27	9011(7)	4486(4)	11229(3)	29(2)
C28	8425(6)	4393(4)	10506(3)	23(1)
C29	7449(6)	5058(4)	10378(3)	29(2)
C30	6892(6)	4967(4)	9698(3)	29(2)
C31	7238(6)	4245(4)	9130(3)	26(1)

C32	8235(6)	3562(4)	9244(3)	21(1)
C33	8687(6)	2812(4)	8709(3)	25(1)
C34	9621(6)	2161(4)	8839(3)	28(1)
C35	10131(6)	2225(4)	9524(3)	26(1)
C36	9747(6)	2952(4)	10078(3)	20(1)
C37	10293(6)	2991(4)	10798(3)	24(1)
C38	8797(6)	3643(4)	9952(3)	20(1)
C39	10491(7)	3850(5)	12053(3)	46(2)
C40	6622(7)	4195(4)	8441(3)	32(2)
C41	6038(7)	4176(4)	7872(3)	33(2)
C42	5368(6)	4175(4)	7199(3)	27(1)
C43	4438(6)	4874(4)	7125(3)	30(2)
C44	3785(6)	4881(4)	6463(3)	27(1)
C45	2858(6)	5607(4)	6370(3)	32(2)
C46	2264(7)	5599(5)	5726(3)	38(2)
C47	2526(7)	4852(5)	5129(3)	32(2)
C48	3396(6)	4135(4)	5187(3)	31(2)
C49	4055(6)	4125(4)	5856(3)	28(2)
C50	5020(7)	3420(4)	5949(3)	33(2)
C51	5656(6)	3444(4)	6595(3)	32(2)
C52	2031(8)	4197(5)	3886(3)	52(2)
C53	3226(9)	167(6)	3745(4)	58(2)
C54	4433(8)	1078(6)	3985(4)	66(2)
C55	4553(11)	1742(7)	3603(6)	93(3)
C56	3381(13)	1510(8)	2982(5)	94(3)
C57	2204(11)	592(8)	2783(4)	84(3)
C58	2103(9)	-65(6)	3155(4)	70(2)
C59	3109(9)	-547(6)	4133(4)	97(3)
N1	7522(5)	1326(4)	11547(2)	30(1)
N2	9921(5)	3771(4)	11336(2)	29(1)
O1	6263(5)	2650(3)	11957(2)	51(1)
O2	8882(4)	47(3)	11131(2)	42(1)
O3	-714(5)	2391(3)	4708(2)	41(1)
O4	8748(5)	5156(3)	11737(2)	47(1)
O5	11061(4)	2387(3)	10933(2)	40(1)
O6	1867(5)	4941(3)	4516(2)	44(1)

Bond lengths [Å] and angles [°] for **Dyad 3.1s**

C1-O1	1.231(6)	C18-C19	1.420(7)
C1-N1	1.405(6)	C19-C20	1.361(7)
C1-C2	1.444(7)	C19-H19	0.95
C2-C12	1.395(7)	C20-C21	1.408(7)
C2-C3	1.409(7)	C20-H20	0.95
C3-C4	1.368(7)	C21-C22	1.355(7)
C3-H3	0.95	C21-O3	1.371(6)
C4-C5	1.392(7)	C22-C23	1.429(7)
C4-H4	0.95	C22-H22	0.95
C5-C6	1.412(7)	C23-C24	1.403(7)
C5-C14	1.424(7)	C24-C25	1.368(7)
C6-C7	1.404(7)	C24-H24	0.95
C6-C12	1.453(7)	C25-H25	0.95
C7-C8	1.355(7)	C26-O3	1.429(6)
C7-H7	0.95	C26-H26A	0.98
C8-C9	1.392(7)	C26-H26B	0.98
C8-H8	0.95	C26-H26C	0.98
C9-C10	1.372(7)	C27-O4	1.234(6)
C9-H9	0.95	C27-N2	1.407(6)
C10-C12	1.404(7)	C27-C28	1.462(7)
C10-C11	1.476(7)	C28-C38	1.390(7)
C11-O2	1.209(6)	C28-C29	1.397(7)
C11-N1	1.410(7)	C29-C30	1.374(7)
C13-N1	1.458(6)	C29-H29	0.95
C13-H13A	0.98	C30-C31	1.377(7)
C13-H13B	0.98	C30-H30	0.95
C13-H13C	0.98	C31-C40	1.419(7)
C14-C15	1.190(7)	C31-C32	1.421(7)
C15-C16	1.445(7)	C32-C33	1.395(7)
C16-C17	1.369(7)	C32-C38	1.434(7)
C16-C25	1.407(7)	C33-C34	1.359(6)
C17-C18	1.407(7)	C33-H33	0.95
C17-H17	0.95	C34-C35	1.386(7)
C18-C23	1.413(7)	C34-H34	0.95

C35-C36	1.377(7)	C48-H48	0.95
C35-H35	0.95	C49-C50	1.416(7)
C36-C38	1.411(6)	C50-C51	1.354(7)
C36-C37	1.472(7)	C50-H50	0.95
C37-O5	1.220(6)	C51-H51	0.95
C37-N2	1.395(6)	C52-O6	1.422(6)
C39-N2	1.453(6)	C52-H52A	0.98
C39-H39A	0.98	C52-H52B	0.98
C39-H39B	0.98	C52-H52C	0.98
C39-H39C	0.98	C53-C58	1.357(9)
C40-C41	1.201(7)	C53-C54	1.390(9)
C41-C42	1.426(8)	C53-C59	1.445(9)
C42-C43	1.378(7)	C54-C55	1.378(10)
C42-C51	1.412(7)	C54-H54	0.95
C43-C44	1.405(7)	C55-C56	1.427(11)
C43-H43	0.95	C55-H55	0.95
C44-C45	1.420(7)	C56-C57	1.386(10)
C44-C49	1.428(7)	C56-H56	0.95
C45-C46	1.349(7)	C57-C58	1.354(10)
C45-H45	0.95	C57-H57	0.95
C46-C47	1.407(7)	C58-H58	0.95
C46-H46	0.95	C59-H59A	0.98
C47-C48	1.359(7)	C59-H59B	0.98
C47-O6	1.361(6)	C59-H59C	0.98
C48-C49	1.421(7)		

O1-C1-N1	118.1(6)	C3-C4-H4	118.5
O1-C1-C2	123.7(6)	C5-C4-H4	118.5
N1-C1-C2	118.2(5)	C4-C5-C6	119.5(6)
C12-C2-C3	119.7(6)	C4-C5-C14	120.4(6)
C12-C2-C1	120.6(5)	C6-C5-C14	120.0(6)
C3-C2-C1	119.7(6)	C7-C6-C5	124.7(6)
C4-C3-C2	119.4(6)	C7-C6-C12	117.7(5)
C4-C3-H3	120.3	C5-C6-C12	117.6(5)
C2-C3-H3	120.3	C8-C7-C6	121.9(6)
C3-C4-C5	123.1(6)	C8-C7-H7	119.0

C6-C7-H7	119.0	C19-C20-C21	119.8(5)
C7-C8-C9	120.4(6)	C19-C20-H20	120.1
C7-C8-H8	119.8	C21-C20-H20	120.1
C9-C8-H8	119.8	C22-C21-O3	124.9(5)
C10-C9-C8	120.7(6)	C22-C21-C20	121.5(5)
C10-C9-H9	119.7	O3-C21-C20	113.6(5)
C8-C9-H9	119.7	C21-C22-C23	119.8(5)
C9-C10-C12	120.7(6)	C21-C22-H22	120.1
C9-C10-C11	118.7(6)	C23-C22-H22	120.1
C12-C10-C11	120.6(5)	C24-C23-C18	118.9(5)
O2-C11-N1	119.9(5)	C24-C23-C22	121.9(5)
O2-C11-C10	123.7(6)	C18-C23-C22	119.2(5)
N1-C11-C10	116.5(5)	C25-C24-C23	121.1(5)
C2-C12-C10	120.7(5)	C25-C24-H24	119.5
C2-C12-C6	120.7(5)	C23-C24-H24	119.4
C10-C12-C6	118.6(5)	C24-C25-C16	120.1(5)
N1-C13-H13A	109.5	C24-C25-H25	120.0
N1-C13-H13B	109.5	C16-C25-H25	120.0
H13A-C13-H13B	109.5	O3-C26-H26A	109.5
N1-C13-H13C	109.5	O3-C26-H26B	109.5
H13A-C13-H13C	109.5	H26A-C26-H26B	109.5
H13B-C13-H13C	109.5	O3-C26-H26C	109.5
C15-C14-C5	176.3(7)	H26A-C26-H26C	109.5
C14-C15-C16	178.8(6)	H26B-C26-H26C	109.5
C17-C16-C25	120.0(5)	O4-C27-N2	119.6(6)
C17-C16-C15	121.8(5)	O4-C27-C28	123.2(6)
C25-C16-C15	118.3(5)	N2-C27-C28	117.2(5)
C16-C17-C18	120.8(5)	C38-C28-C29	120.2(5)
C16-C17-H17	119.6	C38-C28-C27	120.9(5)
C18-C17-H17	119.6	C29-C28-C27	118.9(5)
C17-C18-C23	119.1(5)	C30-C29-C28	118.9(5)
C17-C18-C19	122.2(5)	C30-C29-H29	120.5
C23-C18-C19	118.6(5)	C28-C29-H29	120.5
C20-C19-C18	121.0(5)	C29-C30-C31	123.3(6)
C20-C19-H19	119.5	C29-C30-H30	118.3
C18-C19-H19	119.5	C31-C30-H30	118.3

C30-C31-C40	120.3(6)	C42-C43-H43	119.3
C30-C31-C32	119.0(5)	C44-C43-H43	119.3
C40-C31-C32	120.7(5)	C43-C44-C45	122.7(5)
C33-C32-C31	124.1(5)	C43-C44-C49	118.9(6)
C33-C32-C38	118.0(5)	C45-C44-C49	118.4(5)
C31-C32-C38	117.9(5)	C46-C45-C44	121.2(6)
C34-C33-C32	122.3(5)	C46-C45-H45	119.4
C34-C33-H33	118.8	C44-C45-H45	119.4
C32-C33-H33	118.8	C45-C46-C47	120.4(6)
C33-C34-C35	119.5(5)	C45-C46-H46	119.8
C33-C34-H34	120.2	C47-C46-H46	119.8
C35-C34-H34	120.2	C48-C47-O6	125.2(6)
C36-C35-C34	121.4(5)	C48-C47-C46	120.9(6)
C36-C35-H35	119.3	O6-C47-C46	113.9(6)
C34-C35-H35	119.3	C47-C48-C49	120.4(6)
C35-C36-C38	119.7(5)	C47-C48-H48	119.8
C35-C36-C37	119.9(5)	C49-C48-H48	119.8
C38-C36-C37	120.3(5)	C50-C49-C48	122.9(5)
O5-C37-N2	120.2(5)	C50-C49-C44	118.3(5)
O5-C37-C36	122.7(5)	C48-C49-C44	118.7(6)
N2-C37-C36	117.0(5)	C51-C50-C49	121.4(5)
C28-C38-C36	120.4(5)	C51-C50-H50	119.3
C28-C38-C32	120.6(5)	C49-C50-H50	119.3
C36-C38-C32	119.0(5)	C50-C51-C42	120.8(6)
N2-C39-H39A	109.5	C50-C51-H51	119.6
N2-C39-H39B	109.5	C42-C51-H51	119.6
H39A-C39-H39B	109.5	O6-C52-H52A	109.5
N2-C39-H39C	109.5	O6-C52-H52B	109.5
H39A-C39-H39C	109.5	H52A-C52-H52B	109.5
H39B-C39-H39C	109.5	O6-C52-H52C	109.5
C41-C40-C31	176.7(7)	H52A-C52-H52C	109.5
C40-C41-C42	178.7(6)	H52B-C52-H52C	109.5
C43-C42-C51	119.2(5)	C58-C53-C54	121.4(8)
C43-C42-C41	121.2(5)	C58-C53-C59	118.2(8)
C51-C42-C41	119.6(6)	C54-C53-C59	120.3(8)
C42-C43-C44	121.4(5)	C55-C54-C53	119.7(8)

C55-C54-H54	120.1	C53-C59-H59A	109.5
C53-C54-H54	120.1	C53-C59-H59B	109.5
C54-C55-C56	119.5(9)	H59A-C59-H59B	109.5
C54-C55-H55	120.2	C53-C59-H59C	109.5
C56-C55-H55	120.2	H59A-C59-H59C	109.5
C57-C56-C55	117.0(10)	H59B-C59-H59C	109.5
C57-C56-H56	121.5	C1-N1-C11	123.4(5)
C55-C56-H56	121.5	C1-N1-C13	119.2(5)
C58-C57-C56	123.3(9)	C11-N1-C13	117.4(5)
C58-C57-H57	118.4	C37-N2-C27	124.0(5)
C56-C57-H57	118.4	C37-N2-C39	118.3(5)
C57-C58-C53	118.9(8)	C27-N2-C39	117.6(5)
C57-C58-H58	120.5	C21-O3-C26	116.6(4)
C53-C58-H58	120.5	C47-O6-C52	117.6(5)

Anisotropic displacement parameters ($Å^2 x\ 10^3$) for **Dyad 3.1s**. The anisotropic displacement factor exponent takes the form: $-2p^2[\ h^2\ a^{*2}U^{11} + ... + 2\ h\ k\ a^*\ b^*\ U^{12}\ ]$

	U^{11}	U^{22}	U^{33}	U^{23}	U^{13}	U^{12}
C1	23(3)	25(4)	40(4)	1(3)	9(3)	4(3)
C2	16(3)	19(4)	29(4)	12(3)	-1(3)	-5(3)
C3	25(3)	18(4)	49(5)	8(3)	0(3)	-3(3)
C4	20(3)	22(4)	40(4)	12(3)	1(3)	5(3)
C5	18(3)	29(4)	37(4)	18(3)	2(3)	0(3)
C6	15(3)	23(4)	35(4)	14(3)	2(3)	-3(3)
C7	19(3)	24(3)	25(4)	7(3)	3(3)	3(3)
C8	30(3)	33(4)	39(4)	11(3)	9(3)	5(3)
C9	26(3)	23(4)	36(4)	9(3)	3(3)	-1(3)
C10	24(3)	14(3)	24(4)	4(3)	7(3)	-2(3)
C11	12(3)	26(4)	42(4)	22(3)	4(3)	-1(3)
C12	18(3)	24(4)	20(4)	7(3)	-2(3)	-8(3)
C13	54(4)	86(6)	25(4)	26(4)	-11(3)	-5(4)
C14	26(3)	26(4)	32(4)	12(3)	-6(3)	-1(3)
C15	30(3)	21(4)	34(4)	9(3)	0(3)	2(3)
C16	27(3)	29(4)	18(3)	11(3)	4(3)	-6(3)
C17	22(3)	28(4)	22(4)	6(3)	3(3)	3(3)
C18	22(3)	24(4)	26(4)	10(3)	2(3)	-3(3)
C19	31(3)	20(3)	26(4)	4(3)	5(3)	5(3)
C20	32(3)	26(4)	31(4)	8(3)	6(3)	12(3)
C21	25(3)	34(4)	25(4)	10(3)	-1(3)	-2(3)
C22	36(4)	24(4)	20(4)	4(3)	7(3)	0(3)
C23	27(3)	20(3)	27(4)	10(3)	6(3)	1(3)
C24	40(4)	27(4)	31(4)	9(3)	9(3)	9(3)
C25	32(3)	26(4)	38(4)	14(3)	1(3)	8(3)
C26	75(5)	37(4)	25(4)	10(3)	-1(3)	6(4)
C27	27(4)	25(4)	31(4)	6(3)	8(3)	0(3)
C28	16(3)	22(4)	29(4)	7(3)	-3(3)	0(3)
C29	27(3)	23(4)	31(4)	1(3)	8(3)	4(3)
C30	22(3)	26(4)	40(4)	13(3)	4(3)	7(3)
C31	28(3)	18(4)	26(4)	6(3)	1(3)	-3(3)

C32	15(3)	15(3)	33(4)	10(3)	1(3)	-3(3)
C33	26(3)	25(4)	26(4)	13(3)	4(3)	5(3)
C34	32(3)	29(4)	28(4)	11(3)	8(3)	10(3)
C35	25(3)	22(4)	34(4)	12(3)	4(3)	5(3)
C36	10(3)	23(4)	24(4)	11(3)	-3(3)	-2(3)
C37	16(3)	22(4)	31(4)	7(3)	-4(3)	-1(3)
C38	14(3)	17(4)	27(4)	7(3)	5(3)	-1(3)
C39	53(4)	48(4)	27(4)	12(3)	-8(3)	-11(3)
C40	28(3)	28(4)	42(4)	16(3)	4(3)	3(3)
C41	30(4)	21(4)	50(4)	17(3)	3(3)	1(3)
C42	21(3)	31(4)	28(4)	15(3)	-8(3)	-4(3)
C43	27(3)	36(4)	23(4)	8(3)	2(3)	3(3)
C44	19(3)	28(4)	28(4)	7(3)	2(3)	-4(3)
C45	28(3)	34(4)	37(4)	11(3)	11(3)	15(3)
C46	39(4)	43(4)	37(4)	21(4)	-2(3)	9(3)
C47	29(3)	39(4)	25(4)	19(3)	-5(3)	-8(3)
C48	28(3)	33(4)	30(4)	10(3)	2(3)	0(3)
C49	23(3)	26(4)	33(4)	9(3)	6(3)	0(3)
C50	37(4)	31(4)	26(4)	1(3)	10(3)	7(3)
C51	31(4)	26(4)	39(4)	8(3)	10(3)	4(3)
C52	66(5)	62(5)	22(4)	18(4)	-2(3)	-6(4)
C53	61(5)	61(6)	69(6)	26(5)	36(4)	35(4)
C54	48(5)	38(5)	86(6)	-12(5)	25(4)	-5(4)
C55	79(7)	51(6)	134(9)	-2(7)	60(7)	7(5)
C56	98(7)	85(8)	96(8)	7(7)	53(6)	34(7)
C57	100(7)	97(8)	53(6)	7(6)	30(5)	39(7)
C58	66(5)	84(7)	55(6)	8(5)	15(5)	27(5)
C59	80(6)	108(8)	100(7)	18(6)	33(5)	29(6)
N1	27(3)	40(3)	18(3)	10(3)	-7(2)	-3(3)
N2	31(3)	31(3)	20(3)	9(3)	-3(2)	-7(2)
O1	60(3)	46(3)	35(3)	-3(2)	6(2)	12(2)
O2	34(2)	48(3)	56(3)	31(2)	1(2)	15(2)
O3	51(3)	41(3)	24(2)	7(2)	-6(2)	5(2)
O4	54(3)	46(3)	35(3)	3(2)	8(2)	13(2)
O5	35(2)	44(3)	45(3)	22(2)	-5(2)	13(2)
O6	46(3)	58(3)	30(3)	23(2)	-1(2)	5(2)

Hydrogen coordinates (x 10^4) and isotropic displacement parameters (Å^{2}x 10^3)
for **Dyad 3.1s**.

	x	y	z	U(eq)
H3	4722	3119	10981	39
H4	3729	2971	9851	33
H7	5854	307	8442	28
H8	7478	-760	8668	41
H9	8471	-612	9817	36
H13A	9171	1738	12432	86
H13B	7966	633	12257	86
H13C	7255	1643	12559	86
H17	1808	2962	7742	30
H19	140	3642	6967	32
H20	-945	3567	5860	35
H22	1109	1157	4994	34
H24	2754	474	5777	39
H25	3866	550	6883	37
H26A	858	1810	4092	70
H26B	-896	1819	3677	70
H26C	-804	993	4069	70
H29	7175	5565	10755	35
H30	6235	5425	9616	35
H33	8329	2754	8238	30
H34	9923	1665	8464	34
H35	10758	1757	9613	32
H39A	9516	3697	12280	69
H39B	11136	4546	12307	69
H39C	11207	3361	12056	69
H43	4234	5362	7531	36
H45	2652	6108	6769	38
H46	1666	6100	5676	46
H48	3565	3638	4778	38
H50	5225	2919	5551	39

H51	6304	2964	6642	39
H52A	3226	4225	3854	78
H52B	1490	4338	3486	78
H52C	1491	3514	3884	78
H54	5173	1242	4411	79
H55	5409	2350	3752	112
H56	3406	1964	2716	112
H57	1431	414	2365	101
H58	1259	-679	3006	84
H59A	3526	-175	4629	145
H59B	3788	-1049	3955	145
H59C	1933	-900	4078	145

Torsion angles [°] for **Dyad 3.1s**

O1-C1-C2-C12	179.3(5)	C25-C16-C17-C18	1.0(7)
N1-C1-C2-C12	-0.3(7)	C15-C16-C17-C18	-179.3(5)
O1-C1-C2-C3	-2.6(8)	C16-C17-C18-C23	-1.1(7)
N1-C1-C2-C3	177.8(5)	C16-C17-C18-C19	-179.5(5)
C12-C2-C3-C4	0.4(7)	C17-C18-C19-C20	179.3(5)
C1-C2-C3-C4	-177.7(5)	C23-C18-C19-C20	0.8(7)
C2-C3-C4-C5	-1.2(8)	C18-C19-C20-C21	-0.3(8)
C3-C4-C5-C6	1.5(8)	C19-C20-C21-C22	-0.4(8)
C3-C4-C5-C14	-179.7(5)	C19-C20-C21-O3	-179.7(5)
C4-C5-C6-C7	177.8(5)	O3-C21-C22-C23	179.8(5)
C14-C5-C6-C7	-0.9(8)	C20-C21-C22-C23	0.6(8)
C4-C5-C6-C12	-0.9(7)	C17-C18-C23-C24	0.9(7)
C14-C5-C6-C12	-179.7(5)	C19-C18-C23-C24	179.4(5)
C5-C6-C7-C8	-179.6(5)	C17-C18-C23-C22	-179.1(5)
C12-C6-C7-C8	-0.8(7)	C19-C18-C23-C22	-0.6(7)
C6-C7-C8-C9	0.3(8)	C21-C22-C23-C24	179.9(5)
C7-C8-C9-C10	0.3(8)	C21-C22-C23-C18	-0.1(7)
C8-C9-C10-C12	-0.3(8)	C18-C23-C24-C25	-0.7(8)
C8-C9-C10-C11	178.1(5)	C22-C23-C24-C25	179.4(5)
C9-C10-C11-O2	2.0(8)	C23-C24-C25-C16	0.5(8)
C12-C10-C11-O2	-179.6(5)	C17-C16-C25-C24	-0.7(8)
C9-C10-C11-N1	-177.1(5)	C15-C16-C25-C24	179.6(5)
C12-C10-C11-N1	1.3(7)	O4-C27-C28-C38	178.1(5)
C3-C2-C12-C10	-179.4(5)	N2-C27-C28-C38	-1.6(7)
C1-C2-C12-C10	-1.3(7)	O4-C27-C28-C29	-3.3(8)
C3-C2-C12-C6	0.1(7)	N2-C27-C28-C29	177.0(5)
C1-C2-C12-C6	178.2(5)	C38-C28-C29-C30	-1.1(7)
C9-C10-C12-C2	179.2(5)	C27-C28-C29-C30	-179.7(5)
C11-C10-C12-C2	0.8(7)	C28-C29-C30-C31	0.4(8)
C9-C10-C12-C6	-0.3(7)	C29-C30-C31-C40	-180.0(5)
C11-C10-C12-C6	-178.7(5)	C29-C30-C31-C32	-0.7(8)
C7-C6-C12-C2	-178.7(5)	C30-C31-C32-C33	-179.0(5)
C5-C6-C12-C2	0.2(7)	C40-C31-C32-C33	0.3(8)
C7-C6-C12-C10	0.8(6)	C30-C31-C32-C38	1.7(7)
C5-C6-C12-C10	179.7(5)	C40-C31-C32-C38	-179.1(5)

C31-C32-C33-C34	-178.9(5)	C45-C44-C49-C50	178.2(5)
C38-C32-C33-C34	0.4(7)	C43-C44-C49-C48	-179.9(5)
C32-C33-C34-C35	1.0(8)	C45-C44-C49-C48	0.4(7)
C33-C34-C35-C36	-1.7(8)	C48-C49-C50-C51	178.7(5)
C34-C35-C36-C38	0.8(7)	C44-C49-C50-C51	1.0(8)
C34-C35-C36-C37	179.4(5)	C49-C50-C51-C42	0.3(8)
C35-C36-C37-O5	-1.4(8)	C43-C42-C51-C50	-0.5(8)
C38-C36-C37-O5	177.2(5)	C41-C42-C51-C50	179.3(5)
C35-C36-C37-N2	177.5(5)	C58-C53-C54-C55	-3.1(10)
C38-C36-C37-N2	-3.9(7)	C59-C53-C54-C55	178.7(6)
C29-C28-C38-C36	-178.4(5)	C53-C54-C55-C56	3.0(11)
C27-C28-C38-C36	0.2(7)	C54-C55-C56-C57	-2.3(11)
C29-C28-C38-C32	2.1(7)	C55-C56-C57-C58	1.5(11)
C27-C28-C38-C32	-179.3(5)	C56-C57-C58-C53	-1.6(11)
C35-C36-C38-C28	-178.9(5)	C54-C53-C58-C57	2.3(10)
C37-C36-C38-C28	2.6(7)	C59-C53-C58-C57	-179.5(6)
C35-C36-C38-C32	0.7(7)	O1-C1-N1-C11	-177.0(5)
C37-C36-C38-C32	-177.9(5)	C2-C1-N1-C11	2.6(7)
C33-C32-C38-C28	178.2(5)	O1-C1-N1-C13	3.8(7)
C31-C32-C38-C28	-2.4(7)	C2-C1-N1-C13	-176.6(5)
C33-C32-C38-C36	-1.3(7)	O2-C11-N1-C1	177.8(5)
C31-C32-C38-C36	178.1(5)	C10-C11-N1-C1	-3.1(7)
C51-C42-C43-C44	-0.6(8)	O2-C11-N1-C13	-3.0(7)
C41-C42-C43-C44	179.6(5)	C10-C11-N1-C13	176.1(5)
C42-C43-C44-C45	-178.4(5)	O5-C37-N2-C27	-178.5(5)
C42-C43-C44-C49	1.9(7)	C36-C37-N2-C27	2.5(7)
C43-C44-C45-C46	179.3(5)	O5-C37-N2-C39	0.9(7)
C49-C44-C45-C46	-1.0(8)	C36-C37-N2-C39	-178.0(5)
C44-C45-C46-C47	1.2(8)	O4-C27-N2-C37	-179.6(5)
C45-C46-C47-C48	-0.9(8)	C28-C27-N2-C37	0.2(7)
C45-C46-C47-O6	-179.6(5)	O4-C27-N2-C39	1.0(7)
O6-C47-C48-C49	178.9(5)	C28-C27-N2-C39	-179.3(5)
C46-C47-C48-C49	0.3(8)	C22-C21-O3-C26	-3.7(7)
C47-C48-C49-C50	-177.8(5)	C20-C21-O3-C26	175.6(5)
C47-C48-C49-C44	-0.1(7)	C48-C47-O6-C52	3.2(7)
C43-C44-C49-C50	-2.0(7)	C46-C47-O6-C52	-17

DYAD 3.4S

Crystal data and structure refinement for **Dyad 3.4s**.

Empirical formula	C40 H45 N O3	
Formula weight	587.77	
Temperature	298(2) K	
Wavelength	1.54180 Å	
Crystal system	Monoclinic	
Space group	Cc	
Unit cell dimensions	a = 4.6720(10) Å	a= 90°.
	b = 43.934(8) Å	b= 96.876(9)°.
	c = 15.519(3) Å	g = 90°.
Volume	3162.5(11) $Å^3$	
Z	4	
Density (calculated)	1.234 Mg/m^3	
Absorption coefficient	0.596 mm^{-1}	
F(000)	1264	
Theta range for data collection	6.69 to 60.00°.	
Index ranges	-5<=h<=5, -48<=k<=45, -15<=l<=17	
Reflections collected	10094	
Independent reflections	3689 [R(int) = 0.1978]	
Completeness to theta = 60.00°	99.2 %	
Absorption correction	Semi-empirical from equivalents	
Max. and min. transmission	1.00 and 0.227	
Refinement method	Full-matrix least-squares on F^2	
Data / restraints / parameters	3689 / 266 / 399	
Goodness-of-fit on F^2	1.226	
Final R indices [I>2sigma(I)]	R1 = 0.1905, wR2 = 0.2675	
R indices (all data)	R1 = 0.3422, wR2 = 0.3377	
Largest diff. peak and hole	0.295 and -0.267 $e.Å^{-3}$	

Atomic coordinates (x 10^4) and equivalent isotropic displacement parameters (Å^{2}x 10^3) for **Dyad 3.4s**. U(eq) is defined as one third of the trace of the orthogonalized U^{ij} tensor.

	x	y	z	U(eq)
N1	-3360(30)	4144(4)	5695(12)	65(5)
O1	-1710(30)	4227(3)	7132(10)	90(5)
O2	-4780(30)	4054(3)	4326(9)	92(5)
O3	15440(30)	6291(3)	4423(9)	76(4)
C1	13440(50)	6056(5)	4572(15)	73(7)
C2	12080(40)	5888(5)	3945(15)	88(8)
C3	10210(40)	5678(5)	4237(13)	80(7)
C4	9910(30)	5631(4)	5082(12)	38(5)
C5	11480(40)	5796(4)	5739(14)	62(6)
C6	11320(40)	5756(5)	6667(16)	86(7)
C7	12910(40)	5913(4)	7250(14)	72(7)
C8	14800(40)	6137(5)	6956(14)	84(7)
C9	15130(40)	6180(5)	6132(15)	83(7)
C10	13380(40)	6016(4)	5491(14)	57(6)
C11	7800(50)	5415(5)	5258(13)	76(7)
C12	6320(50)	5212(5)	5498(14)	80(7)
C13	4270(40)	4998(5)	5772(16)	72(6)
C14	4000(30)	4913(4)	6565(11)	48(5)
C15	2050(40)	4687(4)	6770(13)	59(6)
C16	380(30)	4538(4)	6194(11)	29(4)
C17	580(40)	4598(4)	5316(13)	57(6)
C18	-1190(50)	4444(5)	4622(16)	75(7)
C19	-1120(40)	4523(4)	3760(14)	73(7)
C20	680(30)	4743(4)	3548(12)	53(6)
C21	2330(40)	4890(4)	4146(13)	63(6)
C22	2460(40)	4835(4)	5040(13)	52(6)
C23	-1750(60)	4294(6)	6350(18)	95(8)
C24	-3200(50)	4209(5)	4823(15)	74(7)
C25	15920(40)	6353(4)	3544(12)	69(6)
C26	17680(40)	6637(4)	3527(11)	61(6)
C27	15970(40)	6918(4)	3721(12)	55(5)

C28	17700(40)	7213(4)	3666(14)	84(7)
C29	15700(40)	7508(4)	3769(13)	78(7)
C30	17290(40)	7802(4)	3677(13)	70(6)
C31	15290(40)	8075(4)	3801(13)	86(7)
C32	16810(40)	8382(4)	3697(12)	94(8)
C33	-5160(40)	3903(4)	5941(12)	68(6)
C34	-3600(40)	3594(4)	5983(12)	81(7)
C35	-5550(30)	3330(4)	6124(11)	59(6)
C36	-3860(40)	3036(4)	6143(11)	61(6)
C37	-5700(40)	2752(4)	6207(13)	77(7)
C38	-3980(40)	2458(4)	6168(12)	71(6)
C39	-5650(40)	2173(4)	6237(12)	70(6)
C40	-3940(40)	1880(4)	6172(11)	75(6)

Bond lengths [Å] and angles [°] for **Dyad 3.4s**.

N1-C23	1.36(3)	C16-C23	1.50(3)
N1-C24	1.39(2)	C17-C18	1.45(2)
N1-C33	1.434(19)	C17-C22	1.46(2)
O1-C23	1.25(2)	C18-C19	1.39(2)
O2-C24	1.21(2)	C18-C24	1.45(2)
O3-C1	1.43(2)	C19-C20	1.35(2)
O3-C25	1.435(19)	C19-H19	0.9300
C1-C2	1.32(2)	C20-C21	1.30(2)
C1-C10	1.44(2)	C20-H20	0.9300
C2-C3	1.38(2)	C21-C22	1.40(2)
C2-H2	0.9300	C21-H21	0.9300
C3-C4	1.35(2)	C25-C26	1.50(2)
C3-H3	0.9300	C25-H25A	0.9700
C4-C5	1.39(2)	C25-H25B	0.9700
C4-C11	1.42(2)	C26-C27	1.52(2)
C5-C10	1.40(2)	C26-H26A	0.9700
C5-C6	1.46(3)	C26-H26B	0.9700
C6-C7	1.30(2)	C27-C28	1.54(2)
C6-H6	0.9300	C27-H27A	0.9700
C7-C8	1.43(2)	C27-H27B	0.9700
C7-H7	0.9300	C28-C29	1.62(2)
C8-C9	1.32(2)	C28-H28A	0.9700
C8-H8	0.9300	C28-H28B	0.9700
C9-C10	1.41(2)	C29-C30	1.51(2)
C9-H9	0.9300	C29-H29A	0.9700
C11-C12	1.22(2)	C29-H29B	0.9700
C12-C13	1.44(3)	C30-C31	1.55(2)
C13-C14	1.31(2)	C30-H30A	0.9700
C13-C22	1.51(2)	C30-H30B	0.9700
C14-C15	1.408(19)	C31-C32	1.54(2)
C14-H14	0.9300	C31-H31A	0.9700
C15-C16	1.294(18)	C31-H31B	0.9700
C15-H15	0.9300	C32-H32A	0.9600
C16-C17	1.40(2)	C32-H32B	0.9600

C32-H32C	0.9600	C37-C38	1.529(19)
C33-C34	1.539(19)	C37-H37A	0.9700
C33-H33A	0.9700	C37-H37B	0.9700
C33-H33B	0.9700	C38-C39	1.49(2)
C34-C35	1.51(2)	C38-H38A	0.9700
C34-H34A	0.9700	C38-H38B	0.9700
C34-H34B	0.9700	C39-C40	1.525(19)
C35-C36	1.51(2)	C39-H39A	0.9700
C35-H35A	0.9700	C39-H39B	0.9700
C35-H35B	0.9700	C40-H40A	0.9600
C36-C37	1.527(19)	C40-H40B	0.9600
C36-H36A	0.9700	C40-H40C	0.9600
C36-H36B	0.9700		

C23-N1-C24	123(2)	C6-C7-C8	118(2)
C23-N1-C33	117(2)	C6-C7-H7	121.1
C24-N1-C33	121(2)	C8-C7-H7	121.1
C1-O3-C25	118.1(16)	C9-C8-C7	124(2)
C2-C1-O3	123(2)	C9-C8-H8	118.1
C2-C1-C10	127(2)	C7-C8-H8	118.1
O3-C1-C10	110(2)	C8-C9-C10	119(2)
C1-C2-C3	113(2)	C8-C9-H9	120.6
C1-C2-H2	123.2	C10-C9-H9	120.6
C3-C2-H2	123.3	C5-C10-C9	120(2)
C4-C3-C2	124(2)	C5-C10-C1	116(2)
C4-C3-H3	117.9	C9-C10-C1	124(2)
C2-C3-H3	117.9	C12-C11-C4	170(2)
C3-C4-C5	122(2)	C11-C12-C13	173(2)
C3-C4-C11	116(2)	C14-C13-C12	127(2)
C5-C4-C11	122(2)	C14-C13-C22	118(2)
C4-C5-C10	117(2)	C12-C13-C22	115(2)
C4-C5-C6	125(2)	C13-C14-C15	124(2)
C10-C5-C6	118(2)	C13-C14-H14	118.2
C7-C6-C5	122(2)	C15-C14-H14	118.2
C7-C6-H6	119.0	C16-C15-C14	124(2)
C5-C6-H6	119.0	C16-C15-H15	118.2

C14-C15-H15	118.2	C27-C26-H26A	109.3
C15-C16-C17	118.0(19)	C25-C26-H26B	109.3
C15-C16-C23	127(2)	C27-C26-H26B	109.3
C17-C16-C23	114.6(18)	H26A-C26-H26B	107.9
C16-C17-C18	122(2)	C26-C27-C28	112.3(15)
C16-C17-C22	122.3(19)	C26-C27-H27A	109.1
C18-C17-C22	115(2)	C28-C27-H27A	109.1
C19-C18-C17	122(2)	C26-C27-H27B	109.2
C19-C18-C24	118(2)	C28-C27-H27B	109.2
C17-C18-C24	120(2)	H27A-C27-H27B	107.9
C20-C19-C18	120(2)	C27-C28-C29	110.9(16)
C20-C19-H19	119.9	C27-C28-H28A	109.5
C18-C19-H19	120.0	C29-C28-H28A	109.5
C21-C20-C19	121(2)	C27-C28-H28B	109.5
C21-C20-H20	119.5	C29-C28-H28B	109.5
C19-C20-H20	119.5	H28A-C28-H28B	108.1
C20-C21-C22	125(2)	C30-C29-C28	112.4(16)
C20-C21-H21	117.6	C30-C29-H29A	109.1
C22-C21-H21	117.6	C28-C29-H29A	109.1
C21-C22-C17	117(2)	C30-C29-H29B	109.1
C21-C22-C13	128(2)	C28-C29-H29B	109.1
C17-C22-C13	115(2)	H29A-C29-H29B	107.9
O1-C23-N1	124(3)	C29-C30-C31	109.9(16)
O1-C23-C16	113(2)	C29-C30-H30A	109.7
N1-C23-C16	123(2)	C31-C30-H30A	109.7
O2-C24-N1	114(2)	C29-C30-H30B	109.7
O2-C24-C18	128(2)	C31-C30-H30B	109.7
N1-C24-C18	118(2)	H30A-C30-H30B	108.2
O3-C25-C26	108.9(16)	C32-C31-C30	111.8(15)
O3-C25-H25A	109.9	C32-C31-H31A	109.3
C26-C25-H25A	109.9	C30-C31-H31A	109.2
O3-C25-H25B	109.9	C32-C31-H31B	109.3
C26-C25-H25B	109.9	C30-C31-H31B	109.3
H25A-C25-H25B	108.3	H31A-C31-H31B	107.9
C25-C26-C27	111.7(15)	C31-C32-H32A	109.5
C25-C26-H26A	109.3	C31-C32-H32B	109.5

H32A-C32-H32B	109.5	C37-C36-H36B	108.8
C31-C32-H32C	109.5	H36A-C36-H36B	107.7
H32A-C32-H32C	109.5	C36-C37-C38	112.6(15)
H32B-C32-H32C	109.5	C36-C37-H37A	109.1
N1-C33-C34	111.8(15)	C38-C37-H37A	109.1
N1-C33-H33A	109.3	C36-C37-H37B	109.1
C34-C33-H33A	109.3	C38-C37-H37B	109.1
N1-C33-H33B	109.3	H37A-C37-H37B	107.8
C34-C33-H33B	109.2	C39-C38-C37	115.1(15)
H33A-C33-H33B	107.9	C39-C38-H38A	108.5
C35-C34-C33	113.1(15)	C37-C38-H38A	108.5
C35-C34-H34A	109.0	C39-C38-H38B	108.5
C33-C34-H34A	109.0	C37-C38-H38B	108.5
C35-C34-H34B	109.0	H38A-C38-H38B	107.5
C33-C34-H34B	109.0	C38-C39-C40	114.8(15)
H34A-C34-H34B	107.8	C38-C39-H39A	108.6
C34-C35-C36	109.7(14)	C40-C39-H39A	108.6
C34-C35-H35A	109.7	C38-C39-H39B	108.6
C36-C35-H35A	109.7	C40-C39-H39B	108.6
C34-C35-H35B	109.7	H39A-C39-H39B	107.6
C36-C35-H35B	109.7	C39-C40-H40A	109.5
H35A-C35-H35B	108.2	C39-C40-H40B	109.5
C35-C36-C37	113.7(15)	H40A-C40-H40B	109.5
C35-C36-H36A	108.8	C39-C40-H40C	109.5
C37-C36-H36A	108.8	H40A-C40-H40C	109.5
C35-C36-H36B	108.8	H40B-C40-H40C	109.5

Anisotropic displacement parameters ($Å^2 x\ 10^3$) for **Dyad 3.4s**. The anisotropic displacement factor exponent takes the form: $-2p^2[\ h^2\ a^{*2}U^{11} + ... + 2\ h\ k\ a^*\ b^*\ U^{12}\ ]$

	U^{11}	U^{22}	U^{33}	U^{23}	U^{13}	U^{12}
N1	69(9)	61(9)	69(9)	12(7)	23(7)	-19(7)
O1	102(8)	84(8)	83(8)	-7(7)	6(7)	-5(7)
O2	101(8)	87(8)	92(9)	-4(7)	23(7)	3(7)
O3	86(7)	69(7)	73(8)	-6(7)	19(6)	-8(7)
C1	73(10)	71(10)	79(10)	2(8)	24(8)	2(8)
C2	88(11)	88(11)	92(11)	-8(9)	24(9)	0(9)
C3	86(10)	77(10)	81(10)	5(8)	20(9)	1(8)
C4	35(8)	42(9)	40(8)	3(7)	18(7)	-7(7)
C5	65(10)	50(9)	68(10)	-15(8)	4(8)	-2(8)
C6	89(10)	84(10)	88(10)	-14(9)	23(8)	16(8)
C7	72(10)	75(10)	68(10)	-6(8)	5(8)	4(8)
C8	85(11)	83(10)	85(10)	-7(8)	18(9)	-3(8)
C9	85(11)	79(10)	87(11)	0(9)	12(9)	3(8)
C10	59(9)	51(10)	64(10)	4(8)	19(8)	6(8)
C11	82(10)	62(10)	89(10)	-14(8)	30(8)	1(8)
C12	83(11)	76(11)	87(11)	1(9)	33(8)	-3(8)
C13	70(10)	73(10)	76(10)	9(8)	25(8)	9(8)
C14	45(9)	55(9)	51(9)	21(7)	24(7)	-6(8)
C15	66(9)	51(9)	63(9)	-16(8)	20(8)	-13(8)
C16	26(8)	29(8)	34(8)	-12(7)	8(7)	-11(7)
C17	57(9)	56(10)	61(9)	0(8)	16(8)	21(8)
C18	68(10)	73(10)	87(10)	-7(8)	25(9)	5(8)
C19	70(10)	71(10)	80(10)	-11(8)	14(8)	-5(8)
C20	53(9)	48(9)	56(9)	-15(8)	4(7)	-9(8)
C21	69(9)	63(10)	61(9)	-6(8)	20(8)	-6(8)
C22	55(9)	50(9)	57(9)	-11(8)	27(8)	17(8)
C23	95(11)	95(11)	98(11)	3(9)	20(9)	6(9)
C24	76(10)	73(10)	77(10)	4(9)	21(8)	-3(8)
C25	75(10)	71(10)	65(9)	10(8)	21(8)	-11(8)
C26	58(9)	61(9)	66(10)	-4(8)	16(8)	-6(8)
C27	47(9)	52(9)	68(9)	6(8)	18(7)	-32(8)

C28	87(10)	83(10)	85(10)	5(8)	23(8)	-3(9)
C29	81(10)	78(10)	76(10)	2(8)	16(8)	-8(9)
C30	66(10)	75(10)	68(9)	11(8)	6(8)	-5(8)
C31	84(10)	87(10)	91(10)	-9(8)	23(8)	-5(9)
C32	92(11)	98(11)	92(11)	5(8)	16(8)	-8(9)
C33	61(10)	70(10)	75(10)	8(8)	21(8)	0(8)
C34	83(10)	79(10)	84(10)	6(8)	22(8)	-1(9)
C35	58(9)	60(9)	63(9)	-7(8)	18(8)	3(8)
C36	61(9)	60(9)	65(9)	-5(8)	24(8)	-3(8)
C37	70(10)	76(10)	83(10)	-4(8)	2(8)	5(8)
C38	72(10)	70(9)	75(9)	0(8)	27(8)	0(8)
C39	69(10)	67(10)	74(9)	-8(8)	15(8)	3(8)
C40	72(10)	71(10)	86(10)	2(8)	24(8)	-5(8)

Hydrogen coordinates (x 10^4) and isotropic displacement parameters (Å^{2}x 10^3)
for **Dyad 3.4s**.

	x	y	z	U(eq)
H2	12351	5909	3364	106
H3	9087	5561	3825	97
H6	10045	5613	6846	103
H7	12824	5882	7839	87
H8	15855	6259	7369	100
H9	16506	6317	5977	100
H14	5164	5006	7019	58
H15	1957	4643	7353	71
H19	-2325	4424	3327	88
H20	745	4791	2967	63
H21	3504	5042	3966	76
H25A	14091	6379	3186	83
H25B	16932	6184	3316	83
H26A	18332	6659	2960	73
H26B	19369	6621	3954	73
H27A	15384	6900	4298	65
H27B	14232	6928	3310	65
H28A	18465	7221	3112	101
H28B	19317	7214	4122	101
H29A	14037	7501	3331	94
H29B	15010	7503	4333	94
H30A	17939	7813	3107	84
H30B	18976	7811	4108	84
H31A	13591	8062	3378	104
H31B	14672	8065	4375	104
H32A	18365	8406	4157	141
H32B	15456	8545	3721	141
H32C	17566	8387	3148	141
H33A	-6881	3890	5524	81
H33B	-5762	3948	6504	81

H34A	-2770	3563	5446	97
H34B	-2027	3599	6453	97
H35A	-7132	3323	5660	71
H35B	-6343	3356	6669	71
H36A	-2367	3040	6635	73
H36B	-2915	3023	5620	73
H37A	-7266	2753	5734	92
H37B	-6550	2758	6747	92
H38A	-3144	2454	5625	85
H38B	-2400	2460	6635	85
H39A	-7266	2173	5780	83
H39B	-6440	2174	6788	83
H40A	-3374	1863	5599	113
H40B	-5111	1709	6285	113
H40C	-2250	1885	6590	113

Torsion angles [°] for **Dyad 3.4s**.

C25-O3-C1-C2	2(3)	C23-C16-C17-C22	177.8(16)
C25-O3-C1-C10	176.7(15)	C16-C17-C18-C19	174.9(17)
O3-C1-C2-C3	-178.9(16)	C22-C17-C18-C19	-1(3)
C10-C1-C2-C3	7(3)	C16-C17-C18-C24	-2(3)
C1-C2-C3-C4	-4(3)	C22-C17-C18-C24	-178.3(16)
C2-C3-C4-C5	1(3)	C17-C18-C19-C20	2(3)
C2-C3-C4-C11	177.4(17)	C24-C18-C19-C20	178.9(17)
C3-C4-C5-C10	1(3)	C18-C19-C20-C21	-2(3)
C11-C4-C5-C10	-176.2(16)	C19-C20-C21-C22	1(3)
C3-C4-C5-C6	-178.8(18)	C20-C21-C22-C17	-1(3)
C11-C4-C5-C6	4(3)	C20-C21-C22-C13	-178.8(18)
C4-C5-C6-C7	178.2(19)	C16-C17-C22-C21	-175.5(15)
C10-C5-C6-C7	-1(3)	C18-C17-C22-C21	1(2)
C5-C6-C7-C8	2(3)	C16-C17-C22-C13	3(2)
C6-C7-C8-C9	-4(3)	C18-C17-C22-C13	179.1(15)
C7-C8-C9-C10	5(3)	C14-C13-C22-C21	178.6(18)
C4-C5-C10-C9	-176.8(17)	C12-C13-C22-C21	-8(3)
C6-C5-C10-C9	3(3)	C14-C13-C22-C17	1(2)
C4-C5-C10-C1	2(3)	C12-C13-C22-C17	174.4(16)
C6-C5-C10-C1	-178.6(17)	C24-N1-C23-O1	-175(2)
C8-C9-C10-C5	-5(3)	C33-N1-C23-O1	2(3)
C8-C9-C10-C1	176.6(18)	C24-N1-C23-C16	-1(3)
C2-C1-C10-C5	-6(3)	C33-N1-C23-C16	176.0(16)
O3-C1-C10-C5	179.0(15)	C15-C16-C23-O1	-4(3)
C2-C1-C10-C9	172(2)	C17-C16-C23-O1	174.3(17)
O3-C1-C10-C9	-2(3)	C15-C16-C23-N1	-178.2(19)
C12-C13-C14-C15	-175.8(18)	C17-C16-C23-N1	0(3)
C22-C13-C14-C15	-3(3)	C23-N1-C24-O2	180(2)
C13-C14-C15-C16	2(3)	C33-N1-C24-O2	3(3)
C14-C15-C16-C17	2(2)	C23-N1-C24-C18	1(3)
C14-C15-C16-C23	179.7(17)	C33-N1-C24-C18	-176.1(16)
C15-C16-C17-C18	179.9(18)	C19-C18-C24-O2	5(3)
C23-C16-C17-C18	2(2)	C17-C18-C24-O2	-178(2)
C15-C16-C17-C22	-4(2)	C19-C18-C24-N1	-176.4(17)

C17-C18-C24-N1	1(3)	C23-N1-C33-C34	-91(2)
C1-O3-C25-C26	170.7(14)	C24-N1-C33-C34	87(2)
O3-C25-C26-C27	-70.1(19)	N1-C33-C34-C35	-172.4(16)
C25-C26-C27-C28	-177.5(16)	C33-C34-C35-C36	179.0(14)
C26-C27-C28-C29	173.6(14)	C34-C35-C36-C37	-175.1(14)
C27-C28-C29-C30	-177.3(15)	C35-C36-C37-C38	176.5(14)
C28-C29-C30-C31	-178.7(15)	C36-C37-C38-C39	179.4(14)
C29-C30-C31-C32	-179.0(15)	C37-C38-C39-C40	178.3(1

REFERENCES

1. Sheu, S. Y.; Yang, D.-S. Y.; Selzle, H. L.; Schlag, E. W. *Proc. Natl. Acad. Sci.* **2003,** *100,* 12683.

2. Romulus, J.; Weck, M. *Macromol. Rapid Commun.* **2013,** *34,* 1518.

3. Yang, H.; McLaughlin, C. K.; Aldaye, F. A.; Hamblin, G. D.; Rys, A. Z.; Rouiller, I.; Sleiman, H. *Nat. Chem.* **2009,** *1,* 390.

4. Cochran, A. G.; Skelton, N. J.; Starovasnik, M. A. *Proc. Natl. Acad. Sci.* **2001,** *98,* 5578.

5. Gazit, E. *FASEB* **2002,** *16,* 77.

6. Gazit, E. *Prion* **2007,** *1,* 32.

7. Chen, Y.; Feng, Y.; Gao, J. J.; Bouvet, M. J. *Coll. Inter. Sci.* **2012,** *368,* 387.

8. Avinash, M. B.; Govindaraju, T. *Nanoscale* **2011,** *3,* 2536.

9. Shao, H.; Gao, M.; Kim, S. H.; Jaroniec, C. P.; Parquette, J. R. *Chem. Eur. J.* **2011,** *17,* 12882.

10. Das, A.; Molla, M. R.; Maity, B.; Koley, D.; Ghosh, S. *Chem. Eur. J.* **2012,** *18,* 9849.

11. Hunter, C. A.; Sanders, J. K. M. *J. Am. Chem. Soc.* **1990,** *112,* 5525.

12. Hori, A. *The importance of pi-interactions in crystal engineering: Frontiers in crystal engineering;* John Wiley & Sons, Ltd., 2012.

13. Cox, E. G.; Cruickshank, D. W.; Smith, J. A. *Proc. R. Soc. London Ser. A* **1958,** *247,* 1.

14. Patrick, C. R.; Prosser, G. S. *Nature* **1960,** *187,* 1021.

15. Williams, J. H.; Cockcroft, J. K.; Fitch, A. N. *Angew. Chem. Int. Ed.* **1992,** *31,* 1655.

16. Rashkin, M. J.; Waters, M. L. *J. Am. Chem. Soc.* **2002,** *124,* 1860.

17. Wheeler, S. E.; Houk, K. N. *J. Am. Chem. Soc.* **2008,** *130,* 10854.

18. Wheeler, S. E.; McNeil, A. J.; Müller, P.; Swager, T. M.; Houk, K. N. *J. Am. Chem. Soc.* **2010,**

132, 3304.

19. Wheeler, S. E. *J. Am. Chem. Soc.* **2011,** *133,* 10262.

20. Wheeler, S. E. *Acc. Chem. Res.* **2013,** *46,* 1029.

21. Ringer, A. L.; Sinnokrot, M. O.; Lively, R. P.; Sherrill, C. D. *Chem. Eur. J.* **2006,** *12,* 3821.

22. Sinnokrot, M. O.; Sherrill, C. D. *J. Phys. Chem. A* **2003,** *107,* 8377.

23. Arnstein, S. A.; Sherrill, C. D. *Phys. Chem. Chem. Phys.* **2008,** *10,* 2646.

24. Parrish, R. M.; Sherrill, C. D. *J. Am. Chem. Soc.* **2014,** *136,* 17386.

25. Snyder, S. E.; Huang, B.-S.; Chu, Y. W.; Lin, H.-S.; Carey, J. R. *Chem. Eur. J.* **2012,** *18,* 12663.

26. Lee, E. C.; Kim, D.; Jurečka, P.; Tarakeshwar, P.; Hobza, P.; Kim, K. S. *J. Phys. Chem. A* **2007,** *111,* 3446.

27. Grimme, S. *Angew. Chem. Int. Ed.* **2008,** *47,* 3430.

28. Cubberely, M. S.; Iverson, B. L. *J. Am. Chem. Soc.* **2001,** *123,* 7560.

29. Reczek, J. J.; Villazor, K. R.; Lynch, V.; Swager, T. M.; Iverson, B. L. *J. Am. Chem. Soc.* **2006,** *128,* 7995.

30. Molla, M. R.; Ghosh, S. *Chem. Eur. J.* **2012,** *18,* 9849.

31. Kar, H.; Molla, M. R.; Ghosh, S. *Chem. Commun.* **2013,** *49,* 4220.

32. Das, A.; Molla, M. R.; Ghosh, S. *Chem. Eur. J.* **2011,** *123,* 963.

33. Das, A.; Ghosh, S. *Macromolecules* **2013,** *46,* 3939.

34. Au-Yeung, H. Y.; Pantoş, G. D.; Sanders, J. K. *Proc. Natl. Acad. Sci.* **2009,** *106,* 10466.

35. Cougnon, F. B.; Au-Yeung, H. Y.; Pantoş, G. D.; Sanders, J. K. *J. Am. Chem. Soc.* **2011,** *133,* 3198.

36. Au-Yeung, H. Y.; Pantoş, G. D.; Sanders, J. K. *Proc. Natl. Acad. Sci.* **2009,** *106,* 10466.

37. Gabriel, G. J.; Iverson, B. L. *J. Am. Chem. Soc.* **2002,** *124,* 15174.

38. Reczek, J. J.; Iverson, B. L. *Macromolecules* **2006,** *39,* 5601.

39. Alvey, P. M.; Ono, R. J.; Bielawski, C. W.; Iverson, B. L. *Macromolecules* **2013,** *46,* 718.

40. Shao, H.; Nguyen, T.; Romano, N. C.; Modarelli, D. A.; Parquette, J. R. *J. Am. Chem. Soc.* **2009,** *131,* 16374.

41. Shao, H.; Seifret, J.; Romano, N. C.; Gao, M.; Helmus, J. J.; Jaroniec, C. P.; Modarelli, D. A.; Parquette, J. R. *Angew. Chem. Int. Ed.* **2010,** *49,* 7688.

42. Avinash, M. B.; Govindaraju, T. *Adv. Func. Mater.* **2011,** *21,* 3875.

43. de Rouville, H.-P. J.; Iehl, J.; Bruns, C. J.; McGrier, P. L.; Frasconi, M.; Sarjeant, A. A.; Stoddart, J. R. *Org. Lett.* **2012,** *14,* 5188.

44. Dey, S. K.; Coskun, A.; Fahrenbach, A. C.; Barin, G.; Basuray, A. N.; Trabolsi, A.; Botros, Y. Y.; Stoddart, J. F. *Chem. Sci.* **2011,** *2,* 1046.

45. Talukdar, P.; Bollot, G.; Mareda, J.; Sakai, N.; Matile, S. *J. Am. Chem. Soc.* **2005,** *127,* 6528.

46. Sakai, N.; Talukdar, P.; Matile, S. *Chirality* **2006,** *18,* 91.

47. Bhosdale, S.; Sisson, A. L.; Talukdar, P.; Fürstenberg, A.; Banerji, N.; Vauthey, E.; Bollot, G.; Mareda, J.; Röger, C.; Würthner, F.; Sakai, N.; Matile, S. *Science* **2006,** *313,* 84.

48. Molla, M. R.; Das, A.; Ghosh, S. *Chem. Eur. J.* **2010,** *16,* 10084.

49. Das, A.; Molla, M. R.; Banerjee, A.; Paul, A.; Ghosh, S. *Chem. Eur. J.* **2011,** *17,* 6061.

50. Alvey, P. M.; Reczek, J. J.; Lynch, V.; Iverson, B. L. *J. Org. Chem.* **2010,** *75,* 7682.

51. Sakai, N.; Mareda, J.; Vauthey, E.; Matile, S. *Chem. Commun.* **2010,** *46,* 4225.

52. Bhosdale, S. V.; Jani, C. H.; Langford, S. J. *Chem. Soc. Rev.* **2008,** *37,* 331.

53. Flood, A. H.; Stoddart, J. F.; Steuerman, D. W.; Heath, J. R. *Science* **2004,** *306,* 2055.

54. Champin, B.; Mobian, P.; Sauvage, J.-P. *Chem. Soc. Rev.* **2007,** *36,* 358.

55. Baldwin, A. J.; Knowles, T. P. J.; Tartaglia, G. G.; Fitzpatrick, A. W.; Devlin, G. L.; Shammas, S. L.; Waudby, C. A.; Mossuto, M. F.; Meehan, S.; Gras, S. L.; Christodoulou, J.; Anthony-Cahill, S. J.; Barker, P. D.; Vendruscolo, M.; Dobson, C. M. *J. Am. Chem. Soc.* **2011,** *133,* 14160.

56. Jarrett, J. T.; Berger, E. P.; Lansbury, P. T. *Biochemistry* **1993,** *32,* 4693.

57. Jarrett, J. T.; Lansbury, P. T. *Cell* **1993,** *73,* 1055.

58. Kumar, S.; Udgaonkar, J. B. *Curr. Sci.* **2010,** *98,* 639.

59. Goure, W. F.; Krafft, G. A.; Jerecic, J.; Hefti, F. *Alzheimer's Res. and Ther.* **2014,** *6,* 41.

60. Chiti, F.; Dobson, C. M. *Annu. Rev. Biochem.* **2006,** *75,* 333.

61. Makin, O. S.; Atkins, E.; Sikorski, P.; Johansson, J.; Serpell, L. C. *Proc. Natl. Acad. Sci.* **2005,** *102,* 315.

62. Adamcik, J.; Mezzenga, R. *Macromolecules* **2012,** *45,* 1137.

63. Aggeli, A.; Nyrkova, I. A.; Bell, M.; Harding, M.; Carrick, L.; McLeish, T. C. B.; Semenov, A.; Boden, N. *Proc. Natl. Acad. Sci.* **2001,** *98,* 11857.

64. Petkova, A. T.; Ishii, Y.; Balbach, J. J.; Antzukin, O. N.; Leapman, R. D.; Delaglio, F.; Tycko, R. A. *Proc. Natl. Acad. Sci.* **2002,** *99,* 16742.

65. Nelson, R.; Sawaya, M. R.; Balbirnie, M.; Madsen, A. Ø. *Nature* **2005,** *435,* 773.

66. Sawaya, M.; Sambashivan, S.; Nelson, R.; Ivanova, M. I.; Sievers, S. A.; Apostol, M. I.; Thompson, M. J.; Balbirnie, M.; Wiltzius, J. J. W.; McFarlane, H. T.; Madsen, A. Ø. *Nature* **2007,** *447,* 453.

67. Marshall, K. E.; Morris, K. L.; Charlton, D.; O'Reilly, N.; Lewis, L.; Walden, H.; Serpell, L. C. *Biochemistry* **2011,** *50,* 2061.

68. Rubin, N.; Perugia, E.; Goldschmidt, M.; Fridkin, M.; Addadi, L. *J. Am. Chem. Soc.* **2008,** *130,* 4602.

69. Dong, M.; Hovgaard, M. B.; Mamdouh, W.; Xu, S.; Otzen, D. E.; Bosenbacher, F. *Nanotechnology* **2008,** *19,* 1.

70. Paravastu, A. K.; Leapman, R. D.; Yau, W. M.; Tycko, R. *Proc. Natl. Acad. Sci.* **2008,** *105,* 18349.

71. Arimon, M.; Díez-Pérez, I.; Kogan, M. J.; Durany, N.; Giralt, E.; Sanz, F.; Fernàndez-Busquets, X. *FASEB* **2005,** *10,* 1344.

72. Porat, Y.; Mazor, Y.; Efrat, S.; Gazit, E. *Biochemistry* **2004,** *43,* 14454.

73. Tenidis, K.; Walder, M.; Bernhagen, J.; Fischle, W.; Bergmann, M.; Weber, M.; Merkle, M.-L.; Voelter, W.; Brunner, H.; Kapurniotu, A. *J. Mol. Bio.* **2000,** *295,* 1055.

74. Reches, M.; Gazit, E. *J. Protein Folding Disord.* **2004,** *11,* 81.

75. Reches, M.; Gazit, E. *J. Bio. Chem.* **2002,** *277,* 25475.

76. Balbach, J. J.; Ishii, Y.; Antzutkin, O. N.; Leapman, R. D. *Biochemistry* **2000,** *39,* 13748.

77. Balbirnie, M.; Grothe, R.; Eisenberg, D. S. *Proc. Natl. Acad. Sci.* **2001,** *98,* 2375.

78. Lokey, R. S.; Iverson, B. L. *Nature* **1995,** *375,* 303.

79. Nguyen, J. Q.; Iverson, B. L. *J. Am. Chem. Soc.* **1999,** *121,* 2639.

80. Bradford, V. J.; Iverson, B. L. *J. Am. Chem. Soc.* **2008,** *130,* 1517.

81. Gawroński, M.; Brzostowska, M.; Kacprzak, K.; Kolbon, H.; Skowronek, P. *Chirality* **2000,** *12,* 263.

82. Shao, H.; Parquette, J. R. *Chem. Commun.* **2010,** *46,* 4285.

83. Bhosdale, S.; Matile, S. *Chirality* **2006,** *18,* 849.

84. Jiménez, J. L.; Nettleton, E. J.; Bouchard, M.; Robinson, C. V.; Dobson, C. M.; Saibil, H. R. *Proc. Natl. Acad. Sci.* **2002,** *99,* 9196.

85. Pandeeswar, M.; Avinash, M. B.; Govindaraju, T. *Chem. Eur. J.* **2012,** *18,* 4818.

86. Talukdar, P.; Bollot, G.; Mareda, J.; Sakai, N.; Matile, S. *Chem. Eur. J.* **2005,** *11,* 6525.

87. Tartaglia, G. G.; Cavalli, A.; Pellarin, R.; Caflisch, A. *Protein Science* **2004,** *13,* 1939.

88. Shao, H.; Parquette, J. R. *Angew. Chem. Int. Ed.* **2009,** *48,* 2525.

89. Peebles, C.; Piland, R.; Iverson, B. L. *Chem. Eur. J.* **2013,** *19,* 11598.

90. Zych, A.; Iverson, B. L. *J. Am. Chem. Soc.* **2000,** *122,* 8898.

91. Wang, M.; Wudl, F. *J. Mater. Chem* **2012,** *22,* 24297-24314.

92. Dössel, L. F.; Kamm, V.; Howard, I. A.; Laquai, F.; Pisula, W.; Feng, X.; Li, C.; Takase, M.; Kudernac, T.; Feyter, S. D.; Müllen, K. *J. Am. Chem. Soc.* **2012,** *134,* 5876-5886.

93. Brédas, J.-L.; Norton, J. E.; Cornil, J.; Coropceanu, V. *Acc. Chem. Res.* **2009,** *42,* 1691-1699.

94. Samorì, P.; Fechtenkötter, A.; Reuther, E.; Watson, M. D.; Severin, N.; Müllen, K.; Rabe, J. P. *Adv. Mater.* **2006,** *18,* 1317.

95. Venkataraman, D.; Yurt, S.; Venkatraman, B. H.; Gavvalapalli, N. *J. Phys. Chem. Lett.* **2010,** *1,* 947.

96. Mativetsky, J. M.; Kastler, M.; Savage, R. C.; Gentilini, D.; Palma, M.; Pisula, W.; Müllen, K.; Samorì, P. *Adv. Funct. Mater.* **2009,** *19,* 2486-2494.

97. Treier, M.; Liscio, A.; Mativetsky, J. M.; Kastler, M.; Müllen, K.; Palermo, V.; Samorì, P. *Nanoscale* **2012,** *4,* 1677-1681.

98. Wang, S.; Dössel, L.; Mavrinskiy, A.; Gao, P.; Feng, X.; Pisula, W.; Müllen, K. *Small* **2011,** *7,* 2841-2846.

99. Li, W.-S.; Yamamoto, Y.; Fukushima, T.; Saeki, A.; Seki, S.; Tagawa, S.; Masunaga, H.; Sasaki, S.; Takata, M.; Aida, T. *J. Am. Chem. Soc.* **2008,** *130,* 8886-8887.

100. Yamamoto, Y.; Zhang, G.; Jin, W.; Fukushima, T.; Ishii, N.; Saeki, A.; Seki, S.; Tagawa, S.; Minari, T.; Tsukagoshi, K.; Aida, T. *Proc. Nat. Acad. Sci.* **2009,** *106,* 21051-21056.

101. Benanti, T. L.; Saejueng, P.; Venkataraman, D. *Chem. Commun.* **2007,** 692-694.

102. Bheemaraju, A.; Pourmand, M.; Yang, B.; Surampudi, S. K.; Benanti, T. L.; Achermann, M.; Barnes, M. D.; Venkataraman, D. *J. of Macro. Science, Part A: Pure and Appl. Chem.* **2011,** *48,* 986-993.

103. Würthner, F.; Chen, Z.; Hoeben, F. J.; Osswald, P.; You, C.-C.; Jonkheijm, P.; Herrikhuyzen, J.; Schenning, A. P.; van der Schoot, P. P.; Meijer, E. W.; Beckers, E. H.; Meskers, S. C.; Janssen, R. A. *J. Am. Chem. Soc.* **2004,** *126,* 10611-10618.

104. Peebles, C.; Piland, R.; Iverson, B. L. *Chem. Eur. J.* **2013,** *19,* 11598-11602.

105. Au-Yeung, H. Y.; Pantos, G. D.; Sanders, J. K. *Proc. Natl. Acad. Sci.* **2009,** *106,* 10466-10470.

106. Cougnon, F. B.; Au-Yeung, H. Y.; Pantos, G. D.; Sanders, J. K. *J. Am. Chem. Soc.* **2011,** *133,* 3198-3207.

107. Vignon, S. A.; Jarrossonm, T.; Iijima, T.; Tseng, H.-R.; Sanders, J. K.; Stoddart, J. F. *J. Am. Chem. Soc.* **2004,** *126,* 9884-9885.

108. Zhang, Z.-J.; Han, M.; Zhang, H.-Y.; Yu, L. *Org. Lett.* **2013,** *15,* 1698-1701.

109. Kitamura, M.; Hara, Y. H. *J. Cryst. Growth* **2008,** *310,* 3067-3071.

110. Li, Y.-X.; Zhou, H.-B.; Miao, J.-L.; Sun, G.-X.; Li, G.-B.; Nie, Y.; Chen, C.-L.; Chen, Z.; Tao, X.-T. *CrystEngComm* **2012,** *14,* 8286-8291.

111. Forbes, C. C.; Beatty, A. M.; Smith, B. D. *Org. Lett.* **2001,** *3,* 3595-3598.

112. Gardner, R. R.; McKay, S. L.; Gellman, S. H. *Org. Lett.* **2000,** *2,* 2335-2338.

113. Yamasaki, R.; Tantatani, A.; Masu, H.; Yamaguchi, K.; Kagechika, H. *Cryst. Growth Des.* **2006,** *6,* 2007-2010.

114. Lee, A. Y.; Lee, I. S.; Myerson, A. S. *Chem. Eng. Technol.* **2006,** *29,* 281-285.

115. Alvey, P. M. *Self-Assembly of Electron-Rich and Electron-Poor Naphthalene Rings;* The University of Texas Press, 2013.

116. Ma, J.; Zhao, J.; Yang, P.; Huang, D.; Zhang, C.; Li, Q. *Chem. Commun.* **2012,** *48,* 9720-9722.

117. Liu, R.; Azenkeng, A.; Li, Y.; Sun, W. *Dalton Trans.* **2012,** *41,* 12353-12357.

118. McAdam, C. J.; Robinson, B. H.; Simpson, J.; Tagg, T. *Organometallics* **2010,** *29,* 2474-2483.

119. McAdam, C. J.; Robinson, B. H.; Simpson, J. *Organometallics* **2000,** *19,* 3644-3653.

120. McAdam, C. J.; Morgan, J. L.; Robinson, B. H.; Simpson, J.; Rieger, P. H.; Rieger, A. L. *Organometallics* **2003,** *22,* 5126-5136.

121. Bandela, A.; Chinta, J. P.; Hinge, V. K.; Dikundwar, A. G.; Row, T. N.; Rao, C. P. *J. Org. Chem.* **2011,** *76,* 1742-1750.

122. Cavigiolio, G.; Morgan, J. L.; Robinson, B. H.; Simpson, J. *Aust. J. Chem.* **2004,** *57,* 885-894.

123. Shao, H.; Parquette, J. R. *Chem. Commun.* **2010,** *46,* 4285-4287.

124. Shukla, D.; Nelson, S. F.; Freeman, D. C.; Rajeswaran, M.; Ahearn, W. G.; Meyer, D. M.; Carey, J. T. *Chem. Mater.* **2008,** *20,* 7486-7491.

125. Tomasulo, M.; Naistat, D. M.; White, A. J.; Williams, D. J.; Raymo, F. M. *Tet. Lett.* **2005,** *46,* 5695-5698.

126. Shao, H.; Nguyen, T.; Romano, N. C.; Modarelli, D. A.; Parquette, J. R. *J. Am. Chem. Soc.* **2009,** *131,* 16374-16376.

127. Durban, M. M.; Kazarinoff, P. D.; Luscombe, C. K. *Macromolecules* **2010,** *43,* 6348-6352.

128. Alvey, P. M.; Ono, R. J.; Bielawski, C. W.; Iverson, B. L. *Macromolecules* **2013,** *46,* 718-726.

129. Wheeler, S. E.; Houk, K. N. *J. Am. Chem. Soc.* **2008,** *130,* 10854-10855.

130. Gu, X.; Yao, J.; Zhang, G.; Yan, Y.; Zhang, C.; Peng, Q.; Liao, Q.; Wu, Y.; Xu, Z.; Zhao, Y.; Fu, H. *Adc. Funct. Mater.* **2012,** *22,* 4862.

131. Li, C. Y.; Luo, X.; Zhao, W.; Huang, Z.; Liu, Z. P.; Tong, B.; Dong, Y. Q. *Sci. China Chem.* **2013,** No. 56, 1173.

132. Gong, Y.; Tan, Y.; Liu, J.; Lu, P.; Feng, C.; Yuan, W. Y.; Lu, W.; Sun, J. Z.; He, G.; Zhang, Y. *Chem. Commun.* **2013,** *49,* 4009.

133. Lumb, I.; Hundal, M. S.; Corbella, M.; Gómez, V.; Hundal, G. *Eur. J. Inorg. Chem.* **2013,** 4799.

134. Sagara, Y.; Kato, T. *Nat. Chem.* **2009,** No. 1, 605.

135. Luo, W.; Zhao, W.; Shi, J.; Li, C.; Liu, Z.; Bo, Z.; Dong, Y. Q.; Tang, B. Z. J. *J. Phys. Chem. C* **2012,** No. 116, 21967.

136. Dou, C.; Han, L.; Zhao, S.; Zhang, H.; Wang, Y. *J. Phys. Chem. Lett.* **2011,** *2,* 666.

137. Shan, X.-C.; Zhang, H.-B.; Chen, L.; Wu, M.-Y.; Jiang, F.-L.; Hong, M.-C. *Cryst. Growth. Des.* **2013,** *13,* 1377.

138. Tsukuda, T.; Kawase, M.; Dairiki, A.; Matsumoto, K.; Tsubomura, T. *Chem. Commun.* **2010,** *46,* 1905.

139. Rao, S. M.; Liao, C.-W.; Su, W.-L.; Sun, S.-S. *J. Mater. Chem. C* **2013,** *1,* 5491.

140. Shan, X.-C.; Jiang, F.-J.; Chen, L.; Wu, M.-Y.; Pan, J.; Wan, X.-Y.; Hong, M.-C. *J. Mater. Chem. C* **2013,** *1,* 4339.

141. Zhang, Z.; Yao, D.; Zhou, T.; Zhang, H.; Wang, Y. *Chem. Commun.* **2011,** *47,* 7782.

142. Rao, S. M.; Liao, C.-W.; Su, W.-L.; Sun, S.-S. *J. Mater. Chem. C* **2013,** *1,* 6386.

143. Shan, G.-G.; Li, H.-B.; Cao, H.-T.; Zhu, D.-X.; Li, P.; Su, Z.-M.; Liao, Y. *Chem. Commun.* **2012,** *48,* 2000.

144. Ramachandran, D.; Urban, M. W. *Handbook of Stimuli-Responsive Materials,* 1st ed.; Wiley-VCH, 2011.

145. Shan, G.-G.; Li, H.-B.; Cao, H.-T.; Sun, H.-Z.; Zhu, S.-X.; Su, Z.-M. *Dyes Pigments* **2013,** *99,* 1082.

146. Sagara, Y.; Mutai, T.; Yoshikawa, I.; Araki, K. *J. Am. Chem. Soc.* **2007,** *129,* 1520.

147. Kunzelman, J.; Kinami, M.; Crenshaw, B. R.; Protasiewicz, J. D.; Weder, C. *Adv. Mater.* **2008,** *20,* 119.

148. Yagai, S.; Okamura, S.; Nakano, Y.; Yamauchi, M.; Kishikawa, K.; Karatsu, T.; Kitamura, A.; Ueno, A.; Kuzuhara, D.; Yamada, H.; Seki, T.; Ito, H. *Nat. Commun.* **2014,** *5*.

149. Ito; Ito, H.; Muromoto, M.; Kurenuma, S.; Ishizaka, S.; Kitamura, N.; Sato, H.; Seki, T. H. *Nat. Commun.* **2013,** *4*.

150. Peebles, C.; Alvey, P. M.; Lynch, V.; Iverson, B. L. *Cryst. Growth. Des.* **2014,** *14,* 290.

151. Chen, K.-F.; Chang, C.-W.; Lin, J.-L.; Hsu, Y.-C.; Yeh, M.-C. P.; Hsu, C.-P.; Sun, S.-S. *Chem. Eur. J.* **2010,** *16,* 12873.

152. Raikar, U. S.; Tangod, V. B.; Mannopantar, S. R.; Mastiholi, B. M. *Optics Commun.* **2010,** *283,* 4289.

153. Zhang, X.; Chi, Z.; Zhang, Y.; Liu, S.; Xu, J. *J. Mater. Chem. C* **2013,** *1,* 3376.

154. Lee, A. Y.; Lee, I. S.; Myerson, A. S. *Chem. Eng. Technol.* **2006,** *29,* 281.

155. Lou, X.; Zhao, W.; Shi, J.; Li, C.; Liu, Z.; Bo, Z.; Dong, Y. Q.; Tang, B. Z. *J. Phys. Chem. C* **2012,** *116,* 21967.

156. Ooyama, Y.; Harima, Y. *J. Mater. Chem.* **2011,** *21,* 8372.

157. Sun, W.; Zhou, C.; Xu, C.-H.; Zhang, Y.-Q.; Li, Z.-X.; Fang, C.-J.; Sun, L.-D.; Yan, C.-H. *J. Phys. Chem. A* **2009,** *113,* 8635.

158. Chen, R.; Zhao, G.; Yang, X.; Jiang, X.; Liu, J.; Tian, H.; Gao, Y.; Liu, X.; Han, K.; Sun, M.; Sun, L. J. *J. Mol. Struct.* **2008,** *876,* 102.

159. Shi, J.; Li, C.; Liu, Z.; Bo, Z.; Dong, Y. Q.; Tang, B. Z. *J. Phys. Chem. C* **2012,** *116,* 21967.

160. Threlfall, T. *Org. Process Res. Dev.* **2003,** *7,* 1017.

161. Komiya, Z.; Shrock, R. R. *Macromolecules* **2003,** *12,* 1393.

162. Zheng, J.-F.; Yu, Z.-Q.; Liu, X.; Chen, X.-F.; Yang, S.; Chen, E.-Q. *J. Poly. Sci. Part A: Poly. Chem.* **2012,** *50,* 5023.

163. Ganicz, T.; Stańczyk, W. *Materials* **2009,** *2,* 95.

164. Finkelmann, H.; Ringsdorf, H.; Wendorff, J. H. *Macromol. Chem.* **1978,** *179,* 273.

165. Ledwon, P.; Brzeczek, A.; Pluczyk, S.; Jarosz, T.; Kuznik, W.; Walczak, K.; Lapkowski, M. *Electrochim. Acta* **2014,** *128,* 420.

166. Koyuncu, F. B.; Koyuncu, S.; Ozdemir, E. *Electrochim. Acta* **2010,** *55,* 4925.

167. Karim, R.; Sheikh, R.; Yahya, R.; Salleh, N. M.; Azzahari, A. D.; Hassan, A.; Sarih, N. M. *L. Polym. Res.* **2013,** *20,* 259.

168. Maughon, B. R.; Weck, M.; Mohr, B.; Grubbs, R. H. *Macromolecules* **1997,** *30,* 257.

169. Lian, W.-R.; Wu, H.-Y.; Wang, K.-L.; Liaw, D.-L.; Lee, K.-R.; Lai, J.-Y. *J. Polym. Sci., Part A: Polym. Chem.* **2011,** *49,* 3673.

170. Bedi, A.; Zade, S. S. *Macromolecules* **2013,** *46,* 8864.

171. Damaceanu, M.-D.; Rusu, R.-D.; Bruma, M.; Jarzabek, B. *Polym. J.* **2010,** *42,* 663.

172. Bouffard, J.; Swager, T. M. *Macromolecules* **2008,** *41,* 5559.

173. Trimmel, G.; Riegler, S.; Fuchs, G.; Slugovc, C.; Stelzer, F. *Adv. Polym. Sci.* **2005,** *176,* 43.

174. Shi, H.; Zhao, Y.; Dong, X.; Zhou, Y.; Wang, D. *Chem. Soc. Rev.* **2013,** *42,* 2075.

175. Zhu, Y.-F.; Tian, H.-J.; Wu, H.-W.; Hao, D.-Z.; Zhou, Y.; Shen, Z.; Zou, D.-C.; Sun, P.-C.; Fan, X.-H.; Zhou, Q.-F. *J. Polym. Sci., Part A: Polym. Chem.* **2014,** *52,* 295.

176. Ujiie, S.; Miyazaki, W.; Iimura, K. *Polym. J.* **2012,** *44,* 561.

177. Ren, W.; Zhuang, H.; Bao, W.; Miao, S.; Li, H.; Lu, J.; Wang, L. *Dyes PIgments* **2014,** *100,* 127.

178. Freccero, M.; Fasani, E.; Albini, A. *J. Org. Chem.* **1993,** *58,* 1740.

179. Ulla, H.; Garudachari, B.; Satyanarayan, M. N.; Umesh, G.; Isloor, A. M. *Opt. Mat.* **2014,** *36,* 704.

180. Chu, C.-W.; Shrotriya, V.; Li, G.; Yang, Y. *App. Phys. Lett.* **2006,** *88,* 153504.

Vita

Cameron Peebles was born in the beautiful state of Vermont. His family (David, Giovanna, Stirling, Skye) are incredibly wonderful people. Do not hesitate to meet them if you are given the chance. After high school he attended Hampshire College where he studied photography and organic chemistry under Professor Rayane Moreira and Professor Dula Amarasiriwardena. After graduating from Hampshire in 2009, he entered the graduate program at The University of Texas at Austin in 2010 under the guidance of Professor Brent Iverson.

Permanent email: cameron.peebles@gmail.com

This dissertation was typed by Cameron Peebles.